

TALLINN UNIVERSITY OF TECHNOLOGY  
DOCTORAL THESIS  
31/2019

# **Development of Thermal Analysis Tools for Synchronous Reluctance Motors**

PAYAM SHAMS GHAHFAROKHI



TALLINN UNIVERSITY OF TECHNOLOGY  
School of Engineering  
Department of Electrical Power Engineering and Mechatronics  
This dissertation was accepted for the defence of the degree 10/05/2019

**Supervisor:** Prof. Anouar Belahcen  
School of Engineering  
Tallinn University of Technology  
Tallinn, Estonia

**Co-supervisor:** Dr. Ants Kallaste  
School of Engineering  
Tallinn University of Technology  
Tallinn, Estonia

**Opponents:** Dr. Avo Reinap  
Department of Industrial Electrical Engineering and  
Automation  
LUND University

Dr. Roman Pechánek  
Faculty of Electrical Engineering  
University of West Bohemia

**Defence of the thesis:** 18/06/2019, Tallinn

**Declaration:**

Hereby I declare that this doctoral thesis, my original investigation and achievement, submitted for the doctoral degree at Tallinn University of Technology has not been submitted for doctoral or equivalent academic degree.

Payam Shams Ghahfarokhi

-----  
signature



European Union  
European Regional  
Development Fund



Investing  
in your future

Copyright: Payam Shams Ghahfarokhi, 2019  
ISSN 2585-6898 (publication)  
ISBN 978-9949-83-446-4 (publication)  
ISSN 2585-6901 (PDF)  
ISBN 978-9949-83-447-1 (PDF)

TALLINNA TEHNIKAÜLIKOOL  
DOKTORITÖÖ  
31/2019

# **Soojusanalüüsi töövahendi väljaarendus sünkroon-reluktantsmootorile**

PAYAM SHAMS GHAHFAROKHI





# Contents

List of Publications .....	7
Author's Contribution to the Publications .....	8
List of Abbreviations .....	10
Symbols .....	11
1 Introduction .....	16
1.1 Importance of thermal design of the electrical machine .....	16
1.2 Different cooling methods .....	18
1.3 Latest trends in the cooling of electric machines .....	20
1.4 Objectives and scope of the thesis.....	21
1.5 Outline of the thesis.....	23
1.6 Scientific contributions .....	23
2 State of the art .....	25
2.1 Thermal design and analysis of an electrical machine .....	25
2.1.1 Analytical thermal design of the electrical machine .....	25
2.1.2 Numerical thermal design of the electrical machine .....	27
2.2 Heat transfer modeling .....	28
2.3 Critical parameters in the thermal model.....	29
2.3.1 The equivalent thermal conductivity of the slot .....	30
2.3.2 Interface gap heat transfer .....	30
2.3.3 Air gap heat transfer .....	31
2.3.4 Convection from the housing surface .....	31
2.3.5 End space cooling.....	33
2.4 Summary of Chapter 2 .....	34
3 Thermal analysis and modeling methods .....	35
3.1 Synchronous reluctance motor prototype.....	35
3.2 Lumped parameter thermal modeling.....	36
3.3 Calculation of the LPTN components .....	38
3.3.1 Conduction lumped parameter resistance .....	39
3.3.2 Radiation lumped parameter resistance.....	44
3.3.3 Convection lumped parameter resistances .....	45
3.4 Hybrid thermal model.....	53
3.5 Determination of the components of the hybrid model .....	55
3.6 Computation of power losses .....	56
3.6.1 Resistive losses.....	57
3.6.2 Iron losses .....	57
3.6.3 Mechanical losses .....	59
3.7 Steady-state thermal analysis of LPTN.....	59
3.8 Hybrid model analysis .....	60
3.9 Summary of Chapter 3 .....	61
4 Analytical and Numerical Results.....	62
4.1 Analytical data of convection from different basic shapes .....	62
4.2 Convection heat transfer from the housing surface of the TEFC machine .....	66
4.3 Experimental estimation of losses in SynRM .....	70
4.4 Steady-state temperature results of LPTN.....	74

4.5 Results of the hybrid thermal model .....	75
4.6 Summary of Chapter 4 .....	77
5 Validation and Discussion .....	78
5.1 Experimental validation of the convection coefficient .....	78
5.1.1 Convection coefficient from basic shapes.....	78
5.1.2 Natural heat transfer from the housing of the TEFC electrical machine .....	85
5.1.3 Forced heat transfer from the housing of the TEFC electrical machine .....	87
5.2 Experimental validation of thermal models.....	89
5.3 Summary of Chapter 5 .....	92
6 Conclusion and Future Work.....	93
6.1 Conclusion and summary of work.....	93
6.2 Future work.....	94
References .....	95
Acknowledgements.....	100
Abstract.....	101
Kokkuvõte .....	102
Appendix .....	103
Curriculum vitae.....	178
Elulookirjeldus.....	180

## List of Publications

The list of author's publications, on the basis of which the thesis has been prepared:

- I P. Shams Ghahfarokhi, A. Belahcen, A. Kallaste, T. Vaimann, L. Gerokov, and A. Rassolkin, "Thermal Analysis of a SynRM Using a Thermal Network and a Hybrid Model," in *2018 XIII International Conference on Electrical Machines (ICEM)*, 2018, pp. 2682–2688.
- II P. Shams Ghahfarokhi, A. Kallaste, T. Vaimann, A. Rassolkin, and A. Belahcen, "Determination of natural convection heat transfer coefficient over the fin side of a coil system," *Int. J. Heat Mass Transf.*, vol. 126, pp. 677–682, Nov. 2018.
- III P. Shams Ghahfarokhi, A. Kallaste, A. Belahcen, T. Vaimann, and A. Rassolkin, "Hybrid thermal model of a synchronous reluctance machine," *Case Stud. Therm. Eng.*, vol. 12, pp. 381–389, Sep. 2018.
- IV P. Shams Ghahfarokhi, A. Kallaste, T. Vaimann, A. Rassolkin, and A. Belahcen, "Steady-State Thermal Model of a Synchronous Reluctance Motor," in *2018 IEEE 59th International Scientific Conference on Power and Electrical Engineering of Riga Technical University (RTUCON)*, 2018, pp. 1–5.
- V P. Shams Ghahfarokhi, A. Kallaste, T. Vaimann, and A. Belahcen, "Natural convection from flat side's of coil system," in *2018 19th International Scientific Conference on Electric Power Engineering (EPE)*, 2018, pp. 1–5.
- VI P. Shams Ghahfarokhi, A. Kallaste, T. Vaimann, A. Rassolkin, and A. Belahcen, "Determination of forced convection coefficient over a flat side of coil," in *2017 IEEE 58th International Scientific Conference on Power and Electrical Engineering of Riga Technical University (RTUCON)*, 2017, pp. 1–4.
- VII P. Shams Ghahfarokhi, A. Kallaste, A. Belahcen, and T. Vaimann, "Steady state and transient thermal analysis of the stator coil of a permanent magnet generator," in *2017 18th International Scientific Conference on Electric Power Engineering (EPE)*, 2017, pp. 1–5.
- VIII P. Shams Ghahfarokhi, A. Kallaste, A. Belahcen, T. Vaimann, and A. Rassolkin, "Review of thermal analysis of permanent magnet assisted synchronous reluctance machines," in *2016 Electric Power Quality and Supply Reliability (PQ)*, 2016, pp. 219–224.
- IX P. Shams Ghahfarokhi, A. Kallaste, A. Belahcen, and T. Vaimann, "Thermal analysis of electromagnetic levitation coil," in *2016 17th International Scientific Conference on Electric Power Engineering (EPE)*, 2016, pp. 1–5.

## Author's Contribution to the Publications

Contribution to the papers in this thesis are:

- I Payam Shams Ghahfarokhi is the main author of the paper, proposed the LPTN and the hybrid thermal model for SynRM. He developed the test bench for the forced cooling test and validated the analytical and numerical results. He presented the paper at 2018 XIII International Conference on Electrical Machines (ICEM). The co-authors contributed through discussions and guidance.
- II Payam Shams Ghahfarokhi is the main author of the paper, proposed appropriate correlations to determine the convection coefficient over the large parallel rectangular fin arrays in horizontal and vertical directions. The co-authors contributed through discussions and guidance.
- III Payam Shams Ghahfarokhi is the main author of the paper, proposed the hybrid thermal model, which is coupling the FE 2D of the active part with the LPTN of the end regions of the machine. He used the FEMM and Matlab software for the hybrid thermal model. The co-authors contributed through discussions and guidance.
- IV Payam Shams Ghahfarokhi is the main author of the paper, proposed the LPTN for SynRM and evaluated different parameters of LPTN. He presented the paper at 2018 IEEE 59th International Scientific Conference on Power and Electrical Engineering of Riga Technical University (RTUCON).
- V Payam Shams Ghahfarokhi is the main author of the paper, proposed the appropriated empirical correlations for determining the convection coefficient during the passive cooling method from the flat plate on the horizontal and vertical directions. He presented the paper at 19th International Scientific Conference on Electric Power Engineering (EPE). The co-authors contributed through discussions and guidance.
- VI Payam Shams Ghahfarokhi is the main author of the paper, proposed the empirical correlation to determine the convection coefficient over the flat plate with unheated starting part under air forced cooling condition. He presented the paper at 2017 IEEE 58th International Scientific Conference on Power and Electrical Engineering of Riga Technical University (RTUCON). The co-authors contributed through discussions and guidance.
- VII Payam Shams Ghahfarokhi is the main author of the paper, proposed the LPTN to model the steady state and transient thermal behavior of coil module. He used the Matlab software and matrix iteration method to predict the final temperature of the coil module during the passive cooling method and using the Runge-Kutta 4th order iteration method and Matlab software to model the temperature rise for the transient analysis of the coil module. He presented the paper at 18th International Scientific Conference on Electric Power Engineering (EPE). The co-authors contributed through discussions and guidance.
- VIII Payam Shams Ghahfarokhi is the main author of the paper, proposed the thermal method concepts; he considered the different thermal methods and their challenges. He presented the paper at Electric Power Quality and Supply Reliability (PQ). The co-authors contributed through discussions and guidance.



- IX Payam Shams Ghahfarokhi is the main author of the paper, proposed analytical and numerical thermal analysis of three different toroidal coils levitated on an aluminum plate. He presented the paper at 17th International Scientific Conference on Electric Power Engineering (EPE). The co-authors contributed through discussions and guidance.

## List of Abbreviations

AC	Alternating Current
DC	Direct Current
FE	Finite Element
FEA	Finite Element Analysis
FT	Fourier Transformation
IPM	interior permanent magnet
LPTN	Lumped Parameter Thermal Network
NdFeB	Neodymium Iron Boron
PM	Permanent Magnet
PMaSRM	Permanent Magnet Assisted Synchronous Reluctance Motor
PMDC	Permanent Magnet Direct Current
SynRM	Synchronous Reluctance Motor
TE	Totally Enclosed
TEFC	Totally Enclosed Fan Cooled
TENV	Totally Enclosed Non-Ventilated
2D	Two Dimensional
3D	Three Dimensional

## Symbols

$A$	Surface area
$a$	Constant used in the calculation of Nusselt number
$A_{act}$	Actual outer surface of the active part of the machine
$A_c$	Cross section area of conductor
$A_{cr}$	Cross-section area
$A_{ec}$	External area of the end cap
$A_{elc}$	Electrical loading
$A_{ew}$	Total surface of the end winding in contact with inner air
$A_{fin}$	Surface area of the fin sections
$A_{plate}$	Surface area of the flat plate
$A_{slot}$	Interior slot surface
$A_T$	Total surface area
$A'_{act}$	Simplified outer surface of the active part of the machine
$b$	Constant used in the calculation of Nusselt number
$B$	Reverse thermal coefficient of electrical resistivity of copper at 0 [°C]
$B_{gmax}$	Magnetic loading
$B_n$	Magnetic flux density
$\hat{B}$	Peak flux density
$c$	Constant used in the calculation of Nusselt number
$C_{En}$	Loss coefficients related to eddy current
$C_{Hn}$	Loss coefficients related to hysteresis
$c_p$	Fluid specific heat capacity
$D$	Rotor diameter
$D_b$	Inner diameter of bearing
$D_h$	Hydraulic diameter
$D_{ir}$	Rotor inner diameter
$D_{is}$	Stator inner diameter
$D_{or}$	Rotor inner diameter
$D_{os}$	Stator outer diameter
$D_r$	Rotor diameter
$F$	View factor
$F_b$	<i>Bearing load</i>
$f$	Frequency
$f_1$	Volume fraction of the conductor
$f_2$	Volume fraction of the impregnation
$g$	Gravitational acceleration
$Gr$	Grashof number
$Gr'$	Modified Grashof number
$H$	Fin height

$H_{ag}$	Air-gap height
$H_{slot}$	Slot height
$I$	Electrical current
$h_c$	Convection heat transfer coefficient
$h_e$	Heat transfer coefficient
$h_{ec}$	Heat transfer coefficient between the inner air and endcap
$h_{ew}$	Heat transfer coefficient in the end space of the machine
$h_{fin}$	Convection coefficient from fin section
$h_{plate}$	Convection coefficient from the flat section
$h_r$	Radiation coefficient
$H_y$	Stator yoke height
$h_0$	Heat transfer coefficient from the machine housing to the ambient
$h_1$	Heat transfer coefficient from basic shape one
$h_2$	Heat transfer coefficient from basic shape two
$h'$	Modified heat transfer coefficient
$K$	Constant used in the calculation of machine torque
$k$	Thermal conductivity of the material
$k_{air}$	Thermal conductivity of air
$k_{al}$	Thermal conductivity of aluminium
$k_{cu}$	Thermal conductivity of copper
$k_{ed}$	Eddy current coefficient
$k_{exc}$	Excess losses coefficient
$k_f$	Slot filling factor
$k_{hyst}$	Hysteresis coefficient
$k_{ins}$	Equivalent thermal conductivity of insulation materials
$k_{ir}$	Thermal conductivity of electric steel M-350-50A
$k_R$	Skin effect factor
$k_{res}$	Thermal conductivity of resin
$k_{sh}$	Thermal conductivity of steel
$k_\rho$	Experimental factor
$k_1$	Curve fitting coefficient
$k_2$	Curve fitting coefficient
$k_3$	Curve fitting coefficient
$L$	Characteristic length
$l_{av}$	Average conductor length of half a turn
$L_{ec}$	Motor housing length
$L_f$	Fin length
$l_g$	Radial thickness of the air gap
$l_{ig}$	Interface gap between the stator and motor housing
$l_{sb}$	Perimeter of the stator slot

$L_{shaft}$	Length of the shaft
$l_r$	Rotor length
$L_s$	Stator core length
$I'$	Empirically determined constant
$m$	Number of machine phase
$N$	Number of turns in the slot
$N_{block}$	Number of block fins
$N_h$	Number of harmonics
$N_s$	Number of slots
$N_{total}$	Total number of fins
$P$	Perimeter of the surface
$P_{bearing}$	Bearing losses
$P_c$	Constant losses
$P_{cu}$	Resistive losses or winding copper losses
$P_{ec}$	Dynamic eddy current loss
$P_{eddy}$	Rotor iron losses
$P_{exc}$	Excess loss
$P_{ex}$	Amount of heat transfer from the end-windings to slots
$P_{Fe}$	Iron losses
$P_{hyst}$	Hysteresis loss
$P_{Ja}$	Joule losses in the active part
$P_{Je}$	Joule losses in end –winding
$P_{ir}$	Stator iron losses
$P_m$	Mechanical losses
$Pr$	Prandtl number
$\rho_{th}$	Reduction factor
$P_0$	Total input losses
$Q_{conv}$	Rate of the heat transfer by convection
$Q_{rad}$	Rate of the heat transfer by radiation
$Q_T$	Rate of the total heat transfer
$R$	Winding electrical resistance
$Ra$	Rayleigh number
$R_{conv}$	Convection resistance
$Re$	Reynold number
$R_e$	Equivalent thermal resistance
$R_{h1}$	Conduction thermal resistance between the midpoint of end-winding and the midpoint of coil side
$R_{h2}$	Conduction thermal resistance between the stator winding and the frame
$R_{h3}$	Convection thermal resistances between the stator end-winding and inner air of the end region

$R_{h4}$	Convection thermal resistance between the inner air and the end cap
$R_{h5}$	Total heat extraction thermal resistance from the frame to the ambient
$r_{in}$	Stator end-winding Joule losses
$r_{ir}$	Inner radius of the rotor
$r_{is}$	Inner stator radius
$r_{iy}$	Inner radius of stator yoke
$r_m$	Mean value of the stator yoke radius
$r_{or}$	Outer radius of the rotor
$r_{out}$	Outer radius
$r_{oy}$	Outer radius of the stator
$R_{rad}$	Radiation resistance
$R_r$	Total value of the rotor resistance
$R_{th}$	Conduction resistance
$R_T$	Actual average electrical resistance of the stator winding
$R_{T0}$	Stator winding resistance in the reference temperature
$R_0$	Forced Convection and radiation thermal resistance from frame surface to ambient
$R_1$	Interface gap conduction thermal resistance between the frame and the active part of the machine
$R_2$	Conduction thermal resistance of the upper half side of the stator yoke
$R_3$	Conduction thermal resistance of the lower half side of the stator yoke
$R_4$	Conduction thermal resistance of the stator teeth
$R_5$	Conduction thermal resistance between the stator winding and stator teeth
$R_6$	Conduction thermal resistance between the coil side and the end-windings
$R_7$	Conduction thermal resistance between the stator winding and the frame
$R_8$	Convection thermal resistances between the stator end-winding and the inner air of the end region
$R_9$	Convection thermal resistance between the inner air and the end cap
$R_{10}$	Convection thermal resistance of the air gap
$R_{11}$	Conduction thermal resistance of the upper half side of the rotor
$R_{12}$	Conduction thermal resistance of the lower half part of the rotor
$R_{13}$	Axial thermal conduction of the shaft
$s$	Fin space
$s_{cu}$	Copper section in the stator slot
$s_{slot}$	Slot area
$S_T$	Total area of machine housing
$S_1$	Area occupied by basic shape one

$S_2$	Area occupied by basic shape two
$T$	Temperature difference between radiating and absorbing surfaces
$Ta$	Taylor number
$T_a$	Temperature of the active part of the winding
$T_e$	Temperature of the end-windings
$t_{eq}$	Equivalent thickness of impregnation
$t_h$	Thickness of the motor housing
$T_s$	Surface temperature
$T_w$	Average temperature of the winding
$T_{w0}$	Stator winding resistance in the reference temperature
$T_0$	Fluid temperature
$V$	Voltage
$v$	Local fluid velocity
$v_r$	Surface speed of the rotor
$\alpha$	Channel aspect ratio
$\alpha_e$	Temperature coefficient of the electrical resistivity
$\beta$	Coefficient of volume expansion
$\gamma$	Reduction coefficient to implement the distance between the outer surface of the end winding and the internal part of the housing
$\xi$	Length of unheated part
$\varphi$	Angular span
$\omega$	Rotor angular speed
$\omega_r$	Angular frequency of the shaft
$\omega_s$	Angular frequency of the supply
$\rho$	Fluid density
$\rho_e$	Electrical resistivity of a material
$\rho_{e0}$	Electrical resistivity of a material at reference temperature
$\vartheta$	kinematic viscosity
$\mu$	Fluid dynamic viscosity
$\mu_b$	Friction coefficient
$\epsilon$	Relative emissivity
$\sigma$	Stefan-Boltzmann constant
$\eta$	Fan efficiency
$\tau_p$	Pole pitch
$\Delta T$	Temperature difference
$\partial T/\partial x$	Temperature gradients in x-direction

# 1 Introduction

This chapter gives the motivation for the current work and states the importance of thermal analysis during the design process of an electrical machine. It provides thermal issues in electrical machines and describes the different cooling methods. Finally, the main objectives and scientific contribution of research work are presented.

## 1.1 Importance of thermal design of the electrical machine

The negative ecological footprint of combustion engines, global warming and reducing CO<sub>2</sub> emission as well as fossil fuel shortage have a major impact on the research and development of the electrical machine [1].

The design of the electrical machine is an interdisciplinary process and multiphase problem, which consists of the electromagnetic, thermal and mechanical design as well as materials science. The thermal analysis of the electrical machine is one of the most important sections in the design process of the electrical machine, which plays a vital role in the performance, torque, power density and energy efficiency of the electrical machine.

The objective of any design of an electrical machine is to increase the torque density. The general expression of the torque in an electrical machine is defined as [2]:

$$T = KD^2L_sA_{elc}B_{gmax}, \quad (1.1)$$

where  $K$  is a constant,  $D$  represents the rotor diameter,  $L_s$  is the axial length of the electrical machine,  $A_{elc}$  is electric loading, and  $B_{gmax}$  is magnetic loading.

Accordingly, to increase the torque per unit of volume, the electric and magnetic loading must be increased. In reality, designers are confronted with some limitations to increase the magnetic loading because of the stator iron saturation during high flux density. According to the above description, the only flexible way to improve the torque is by increasing the electric loading, which can be achieved by increasing the current density. However, higher current density leads to higher copper losses and higher temperature. As a consequence, to achieve the required torque and performance, the thermal analysis of the electrical machine is essential. The main aspects of the thermal analysis are described hereafter.

**Winding insulation (Machine life):** according to "10 °C half-life rule" every 10 °C increase in operating temperature cuts insulation life by half [3]. Accordingly, higher current density leads to higher copper losses and higher temperature of the winding inside the slot, which reduces the lifetime of winding insulation materials and machine life.

Figure 1.1 shows the lifespan of different classes of insulation materials via temperature. Accordingly, the life aging of the slot insulation materials is inversely proportional to the temperature; consequently, by increasing the temperature, the lifespan of insulation materials starts to decrease. Finally, the maximum permissible operating temperature of each insulation class is illustrated in figure 1.1.



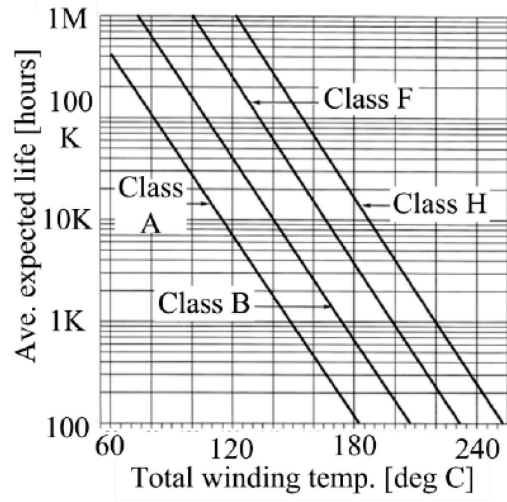


Figure 1.1. Effect of the slot temperature on different insulation classes.

**Copper loss:** Because the electrical resistivity of the conductor is temperature dependent, the value of copper loss increases by the temperature, which leads to a higher amount of the losses in the slot.

**Permanent magnet:** The performance of the permanent magnets is temperature dependent. Figure 1.2 shows the demagnetization curve of the NdFeB magnet. Accordingly, increasing the temperature has a direct effect on the magnetic characteristic of NdFeB and reduces its flux density. Besides, due to the overheated condition, the magnet operation point will be located in the knee point of the demagnetization curve; as a result, the magnet will be irreversibly demagnetized [4].

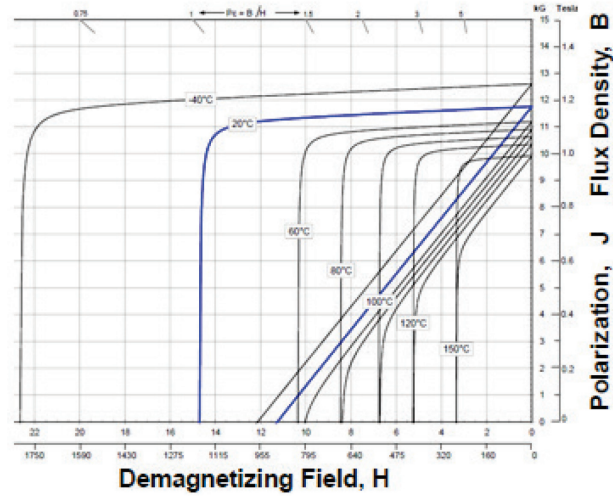


Figure 1.2. Demagnetization curves for the NdFeB type magnet [5].

**Thermal and electromagnetic effect of different materials:** From a material point of view, as Table 1.1 shows, by reducing the amount of the alloy content, the price of steels also starts to decrease and the thermal conductivity of the steel increases [6]. However, the iron loss in the steel with lower alloy content increases, which leads to higher temperature [6].

Table 1.1. Comparison between the steel lamination with the same thickness [6]

Material grade	M235	M250	M300	M330
k at 22 °C (pu)	1.00	1.04	1.15	1.32
k at 100 °C (pu)	1.46	1.55	1.60	1.73
k at 200 °C (pu)	1.63	1.73	1.78	1.85
Loss (W/kg)	2.35	2.50	3.00	3.30
% Si+ Al (pu)	1.00	0.91	0.74	0.58
Price (pu)	1.00	0.89	0.77	0.62

**Elevated temperatures:** From the mechanical point of view, at elevated temperatures, the electrical machine faces several problems such as the materials expansion, which induces mechanical stresses, bearing failure and thermal fatigue failure mechanism due to repetitive fluctuations in the temperature of the materials, which finally leads to the cracks in the materials [3].

Accordingly, the electromagnetic losses in the electrical machine appear in the form of heat, and since some of the machine materials are temperature dependent, the electrical machine faces several thermal constraints. To overcome these problems and protect the electrical machine from the mentioned failures and ensure reliable operation, the thermal design and analysis of the electrical machine during the design process for the required performance is essential.

## 1.2 Different cooling methods

Different applications of electrical machines require different cooling methods. The electrical machine faces several thermal constraints. These thermal drawbacks are modified and moderated by selecting an appropriate cooling method.

The appropriate cooling method of an electrical machine is selected according to several different parameters, e.g., machine application, machine topology, machine current density (Table 1.2), speed, the operational environment, cost and machine size [3], [7].

Table 1.2. Different cooling system based on the machine current density

Cooling System	Current Density [A/mm <sup>2</sup> ]
Totally enclosed non ventilated	1-5
Open air, fan cooled	5-10
Forced liquid cooled	10-30

Common cooling systems in different electrical machines are as follows [3]:

**Totally enclosed non-ventilated (TENV):** In this cooling method, most of the heat is removed by the passive cooling method (natural convection and radiation) [3], [8]. The housing provides the main path for the heat transfer from the inner sections of the machine to the ambient (figure 1.3) [9]. The amount of heat transfer depends on the machine dimensions, the viscous force, and the thermal diffusivity of the fluid [3].

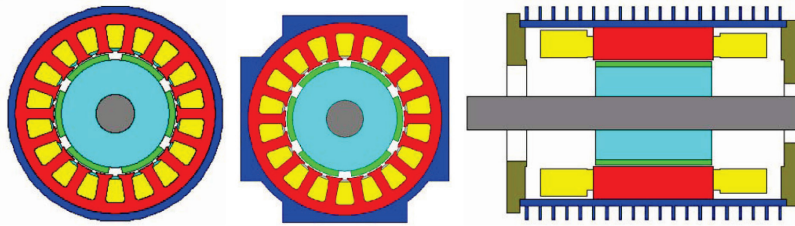


Figure 1.3. Different models of the housing for the TENV cooling method [8].

**Totally enclosed fan cooled (TEFC):** In this method, the external fan is attached to the non-driven part of the machine to blow the fluid (mostly air) into the fin channels of the housing (figure 1.4). In this approach, the fin channels over the housing are essential [3].

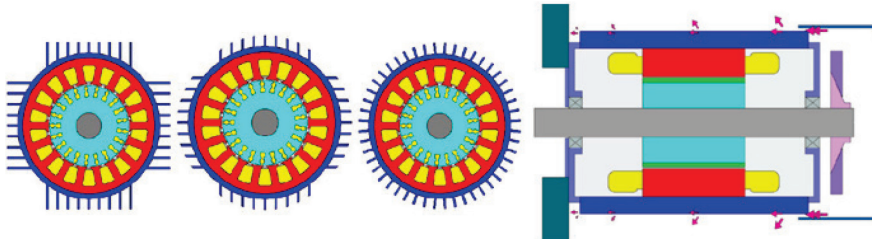


Figure 1.4. Different housing types for TEFC method [8].

**Through ventilation:** In this cooling method, the airflow is passed through the inner parts of the machine using three parallel paths (figure 1.5): axial and radial cooling duct in a stator, axial and radial cooling ducts in a rotor and air gap.

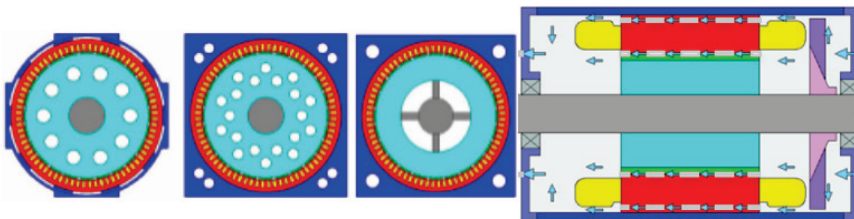


Figure 1.5. Through ventilation and different cooling ducts [8], [9].

**Housing water jackets with axial and circumferential ducts:** According to figure 1.6, in this method, the liquid cooling channels are located in the conductive frame of the machine above the stator laminations. Therefore, the heat generated in the machine is transferred by the conduction phenomenon to the machine housing and then it is extracted to the ambient by the convection employing the liquid fluid to the ambient [9].

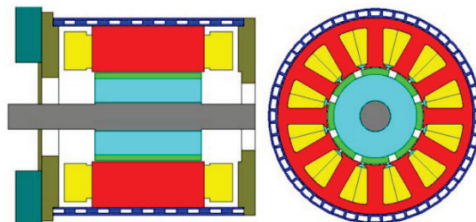


Figure 1.6. Housing water jack cooling method [8].

**Submersible cooling:** This cooling method is used for the machines that are working in a liquid environment such as a pump [3].

**Wet rotor and stator:** In this method, as figure 1.7 shows, the fluid (oil) is passed from the air gap, over the shaft to the end windings of the machine or it can be passed through the cooling slot channels inside the stator lamination [9].

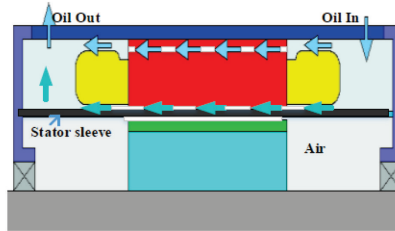


Figure 1.7. Example of wet stator cooling [9].

**Spray cooling:** According to figure 1.8, the target of this cooling approach is to directly cool the rotor and end windings by spraying the coolant fluid (oil) from the nozzles. This approach has a significant advantage for removing the heat whereas by applying this method, the conduction path for the heat generated within the windings decreases [9].

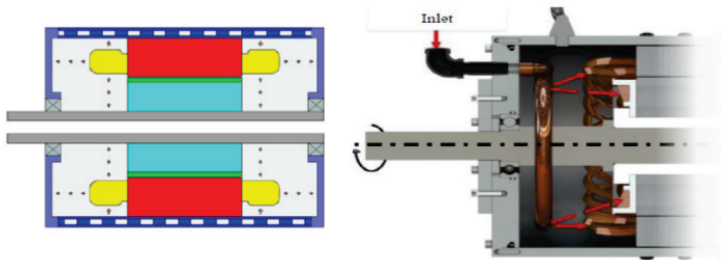


Figure 1.8. Spray cooling approach [9].

**Direct conductor cooling:** In this method, the fluid can be passed through the cooling tubes located inside the slot or the fluid is completely flowing between the conductors (figure 1.9).



Figure 1.9. Example of direct conductor cooling [10].

### 1.3 Latest trends in the cooling of electric machines

The manufacturers use different electrical motor topologies, e.g., Toyota, Nissan, BMW, and General Motor use permanent magnet synchronous motors; Tesla uses induction motors; Punch Power train starts to use switched reluctance motor; Renault uses wound-field synchronous motors and ABB starts to do experiments to implement the synchronous reluctance motors [9]. Furthermore, they use different cooling methods according to motor topologies and their cooling targets. In the following, motor topology

and cooling methodology of Nissan LEAF and Tesla Model S will be described in more detail.

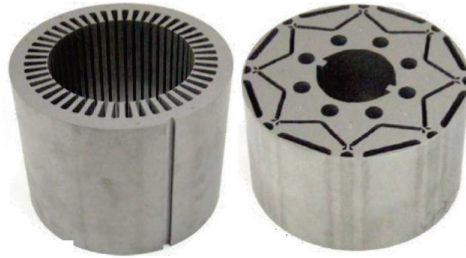


Figure 1.10. Nissan LEAF stator and rotor geometry [11].

Figure 1.10 shows the Nissan LEAF motor. Accordingly, Nissan Company uses the 48 slots, eight pole, three-phase brushless interior permanent magnet topology with two magnet layers in the form of flat and V shape [12], [11]. According to figure 1.11, for cooling purposes, it uses the water jacket cooling technology. For this purpose, three circumferential channels in the housing provide main cooling for the motor [12], [11].

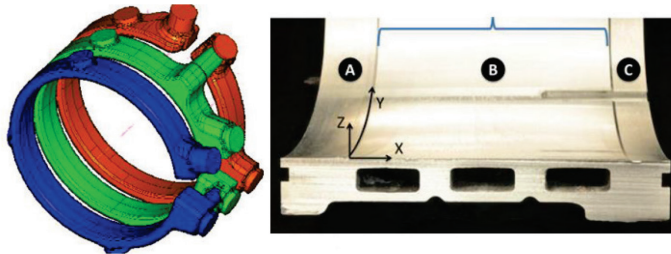


Figure 1.11. Nissan LEAF water jacket channels [12].

Tesla uses 60 slots, four poles, 74 rotor bars, two-layer windings, a 3-phase induction motor. As figure 1.12 shows, they use two different types of the cooling method: water jacket cooling by implementing the circumferential channels in the housing and additional rotor liquid cooling due to the rotor bar Joule losses [11].

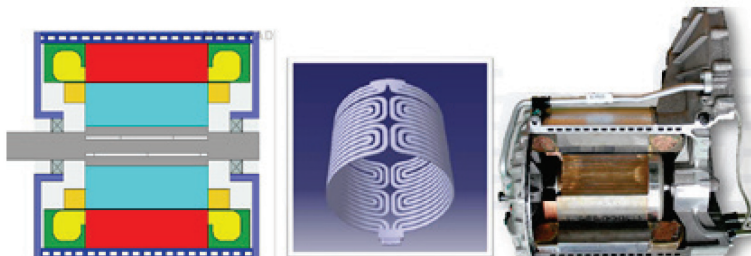


Figure 1.12. Tesla model S cross-section area [11].

## 1.4 Objectives and scope of the thesis

The objective of the PhD thesis was to enhance knowledge in thermal design and analysis of the electrical machine and develop the thermal analysis tools for electrical machines with a particular focus on SynRMs. The research focuses on existing challenges and problems in ongoing product development. The main objective is to develop scientifically sound methods that can be used in the thermal design and analysis of electrical machines, and then apply them for a specific machine. To clarify the research topic,

it mainly focuses on the thermal aspect including passive and active cooling. The passive cooling refers to the effectiveness of heat distribution within a machine, which is affected by material thermal properties, geometrical design and interfacial thermal resistances between machine components. For example, the passive thermal design of a stator slot strongly influences the temperature gradient of the coil. The active cooling refers to the effects of heat extraction from a machine to the coolant ultimately based on the convection phenomenon.

In this thesis, different thermal models of electrical machines with the focus on SynRM have been developed. Choosing the appropriate convective heat transfer cooling method has a significant effect on the amount of heat extraction from an electrical machine. Accordingly, the industrial motors in the medium power range are cooled by the TEFC method. As a result, the TEFC method was selected for cooling of the SynRM. In this cooling approach, the outer circumferential of the machine housing consists of the fin channels and the fan blades are mounted in the non-driven section of the machine shaft.

As the machine is used for variable speed purposes, most of the heat dissipates from the machine to the ambient by the mixture of convection (natural and forced) and radiation phenomena. According to the importance of the convection phenomenon in the total amount of the heat transfer, in the first step, the convection coefficient from different surfaces, e.g., flat plate, fin plate, in vertical and horizontal orientations under the natural cooling and air forced cooling condition, has been considered analytically by using empirical correlations and experimentally. Then, by the analysis and comparison of different analytical results by the experimental one, the appropriate correlation for each surface was selected. Finally, the analytical calculation method has been developed to find the convection coefficient from the complex shape of the TEFC machine housing during the natural and forced cooling.

The main target of this thesis is to provide analytical LPTN and numerical FE models to predict the temperature of the different components of the SynRM. For the analytical purpose, the LPTN has been developed to calculate the temperature of the key components of the electrical machine. The advantages of the developed LPTN are:

- Reducing the complexity of the LPTN of the electrical machine;
- Saving the accuracy to predict the temperature of the key components of the electrical machine;
- Decreasing the calculation time.

The thermal analysis of the electrical machine by applying 3D FEA has high setup and computation time. This approach is a beneficial method to model the heat distribution and conduction in solid materials. To reduce the setup and computation time and to use the benefit of the FEA in heat distribution and conduction in solid materials, the hybrid thermal model was applied. This method couples 2D FEA of the active part of the electrical machine by LPTN of the end region to capture all the key components of the electrical machine and provide the main paths of the heat transfer in the machine. The advantages of this method are:

- Using the FEM software without having access to the code itself;
- Reducing the time of the modeling process of the electrical machine by modeling only the active part of the machine whereas the end region of the machine is calculated by the LPTN;
- Using the advantages of the FEA to accurately model the conduction in the active part of the machine.

## 1.5 Outline of the thesis

The thesis is outlined as follows:

**Chapter 2** focuses on the state of the art. In the first part of this chapter, the different modern thermal analysis methods, their advantages, and drawbacks are considered in detail. In the second part, the various mechanisms of the heat transfer are described, and the critical parameters in the thermal modeling of the electrical machine are discussed in detail.

In **Chapter 3**, the analytical LPTN and the hybrid thermal model for the SynRM are developed. Next, the calculation procedures of the thermal components of the models are described. The source of losses in SynRM is considered, and the analytical and numerical methods are defined. In the final part, the analytical LPTN and the hybrid calculation method are described.

**Chapter 4** presents the results of the analytical and numerical calculation of the thermal model parameters. Finally, according to the calculated parameters, the thermal models are solved, and the results are presented.

**Chapter 5** contains the validation of the results of the developed models. It is divided into two main sections. In the first section, mainly the results of the convection coefficient from the basic shapes and machine housing are discussed and validated. In the second part, different measurement setups and procedures are described, and the accuracy of the thermal models is measured by comparing the thermal model results by the experimental results.

**Chapter 6** presents some conclusions and future work related to the thermal analysis of electrical machines.

## 1.6 Scientific contributions

### Scientific novelty

The scientific novelty of the doctoral thesis consists of the following:

- The critical parameters in the thermal modeling of the TEFC SynRM; different solutions to overcome these parameters; different equations to model the complex heat transfer phenomena.
- An LPTN for totally enclosed fan cooled electrical machines is proposed. The focus is on the critical parts of the SynRM machine, including the interfacial gap, the stator slots, end windings and heat transfer from the cooling machine system during the passive and active cooling methods.
- A new hybrid thermal modeling approach to model the heat transfer of the machine is proposed. This method benefits from the advantages of both LPTN and FEA. Particularly, the LPTN is applied to model the heat transfer of the end region of the machine. The proposed LPTN makes it simple to model the heat transfer of the end region of the machine and reduce the setup and calculation time instead of modeling the complex structure of the end region of the machine by FEA, and only the heat transfer and losses distribution of the active part of the machine are modeled by FEA method.
- A simplified method to calculate the radiation coefficient from the housing of the TEFC motor was applied. To reduce the complexity of the calculation and to save time, this parameter was calculated by using the hypothesis. Accordingly, the view factor of the surfaces without a clear view to the ambient is set to zero and the other ones with clear view to the ambient to one.

- The calculation methods to determine the total heat transfer coefficient from the housing of the TEFC machine for passive and active cooling were expanded.

**Practical novelty**

The thesis also has several practical novelties as described below:

- Created the calorimeter to confine the heat losses from the desired surface;
- Developed the test bench to consider the convection coefficient from different basic shapes during the natural and air forced cooling;
- Developed the passive and active test bench to validate the thermal models;
- Developed the test bench to measure the losses of SynRM.



## 2 State of the art

In this chapter, an overview of different types of thermal design and analysis is presented. The objective is to provide the reader with a picture of the state of the art regarding different thermal models with their advantages and drawbacks. It describes the challenges and provides the solutions to dominate them during thermal modeling of an electrical machine.

The thermal design and heat transfer have the same importance as electromagnetic design while it includes higher complexity and nonlinearity due to fluid flow nature [13]. Traditionally, the machine designers used  $D^*L$  equations or method sizing which is not the direct thermal analysis method and accordingly, limited the magnetic and current loads [3]. In some cases, they referred to the previous experimental results for the design of the machine, and in some others, they developed elementary resistance network that it could be calculated by hand; in some cases, this resistance network consists of only one resistance [3]. At the end of the twentieth century and beginning of the recent century, by expanding the role of the computer in the design process of the electrical machine, new thermal methods have been introduced, and the complexity of the thermal networks has been increased. As a result, it is possible to obtain more accurate results within a short computation time.

### 2.1 Thermal design and analysis of an electrical machine

The modern thermal design of an electrical machine is divided into two main categories: analytical and numerical methods [14],[15] and [16].

#### 2.1.1 Analytical thermal design of the electrical machine

In the analytical method, the lumped parameter thermal network (LPTN) is developed to predict the temperature of the key components of the electrical machine. As the electrical engineer is familiar with the electrical circuit concept, the LPTN is better understood for them [3]. The LPTN is equivalent to the electrical circuit [3]. Consequently, the nodal temperature is akin to voltage, the power loss is analogous to the current source, and the thermal resistances are analogous to electrical resistances [3]. This method has advantages, e.g., fast computation time [17]. However, in this method, thermal resistances are calculated by using semi-empirical correlations preparing by some simplification assumptions or experiments may lead to uncertainty results [18]. To prevent the LPTN from uncertainty results, the LPTN should be selected with care.

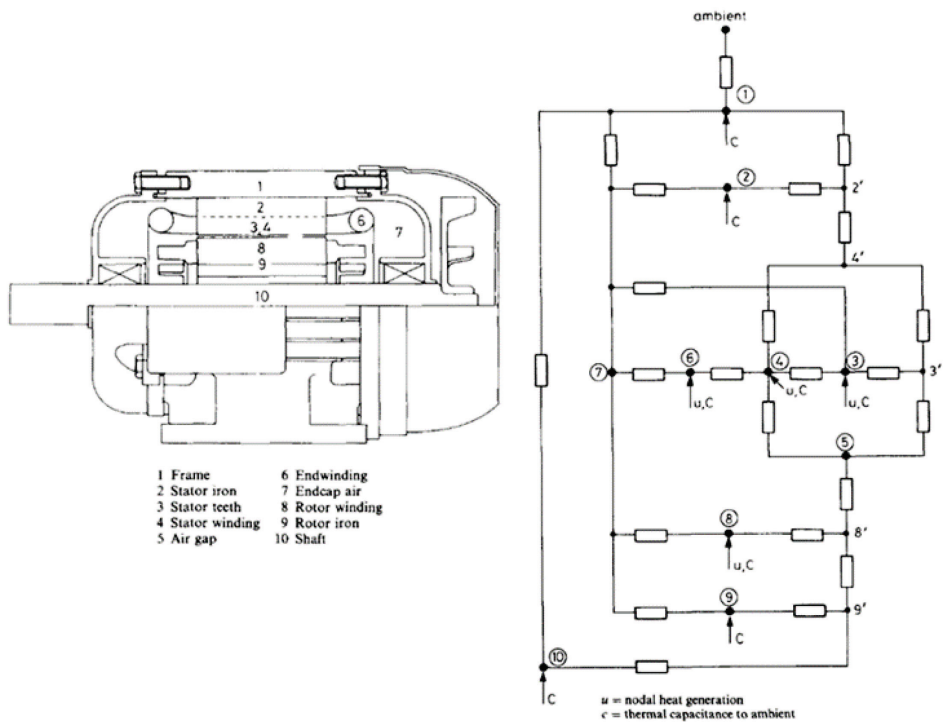


Figure 2.1. One of the earlier LPTN [19].

The thermal analysis of different electrical machines by this method has been reported in [19], [20], [21], [22] and [23]. One of the first studies in the field of thermal design of a totally enclosed fan cooled (TEFC) electrical machine is presented in [22]; where in 1991, Mellor developed the LPTN of the induction machine. To increase the accuracy of the model, he developed the LPTN in both axial and radial directions (figure 2.1) and finally validated it by doing the thermal test on two different induction machines in different power ranges from the medium (75-kW) to small power (5.5-kW). By calculating several convection heat transfer paths and developing the heat transfer paths in different directions, this model provides a very complex thermal network, which increases the computing process. In 2003, Boglietti [23] unveiled from his simplified thermal model for an induction machine and validated it by testing a 4-kW, 4-pole induction motor. By using some hypotheses, he reduced the complexity of the thermal model of the induction machine as well as computation time by saving the computation accuracy. However, in his model, he did not consider the radiation phenomenon and further, he determined some key parameters, e.g., equivalent thermal conductivity of slot, the length of the interface gap and natural convection resistance from the housing to the ambient by setting up a proper thermal test. Besides, he did not segregate the active and end winding parts.

One of the first to study thermal designs and analysis of permanent magnet synchronous machines was Lindstrom in 1999 [21]. He developed the LPTN for the surface mounted permanent magnet machine to analyze the thermal behavior of the machine during the steady-state and transient modes. His work contained no modeling the convection and radiation from the surface of the machine to the ambient and directly connected the thermal model of the machine to the ambient. In [22] El-Refaie developed a thermal model for the interior permanent magnet (IPM) synchronous machine based

on the proposed thermal model of Lindstrom. In 2012, Nategh presented his LPTN in [6] for directly cooled PMSRM. In addition, he proposed a new method to model the heat transfer of the stator slot. For this purpose, he assumed that the stator slot consists of a number of elliptical impregnation and copper layers and based on this assumption, he provided the final correlation for the temperature distribution in the stator slot.

### 2.1.2 Numerical thermal design of the electrical machine

The numerical method for the thermal analysis is divided into two main groups: finite element analysis (FEA) and computational fluid dynamics (CFD) [17]. These two approaches are applied to model heat transfer in complex structures [9]. In addition, these methods can model any geometry and shape.

The FEA is a suitable method for modeling the heat distribution and conduction heat transfer in the solid materials (figure 2.2) [9]. However, the CFD method is the most precise method to model heat transfer between two different media [9]. This method is employed to model the fluid flow distribution, to determine the coolant flow rate, velocity and the heat transfer coefficient (figure 2.3) [3], [9]. However, a weakness of both methods is that they have high setup and computation time [9]. Accordingly, the FEA or CFD can be used to analyze a specific part of the machine and for a complete analysis of the electrical machine, the coupling is needed [24].

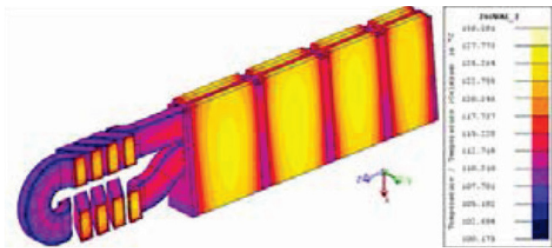


Figure 2.2. 3-D FEA of the stator section [25].

Many publications address the thermal analysis of the electrical machine by using these two approaches. For instance, Nair in [26] considered the thermal analysis of an induction machine using 3D FEA method, in [27] the thermal FEA method was applied to the surface mounted PM machine. In the thermal analysis of the electrical machine, Staton in [3] uses the CFD. In [23] and [28], Nategh presented a limited CFD and Partial FEA and coupled it by the lumped parameter model to reduce the computation and setup time of the numerical methods using the advantages of these methods.

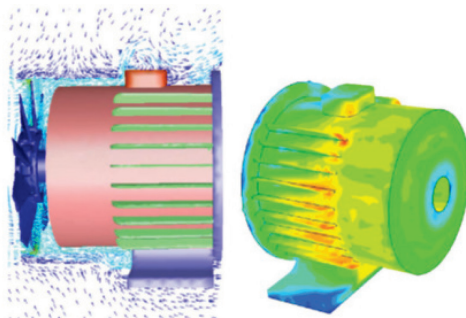


Figure 2.3. Thermal analysis of the TEFC machine utilizing the CFD method [14], [29].

## 2.2 Heat transfer modeling

The heat transfer mechanism in the machine is divided into three main heat transfer phenomena: conduction, convection, and radiation. Depending on the modeling method, these phenomena are described by the coefficients used either directly in the method or to calculate thermal resistances. Both of the coefficients and the resistances are calculated by the heat transfer correlations, which can be found in heat transfer literature and textbooks such as [3], [30] and [31]. The three heat transfer mechanisms are summarized below.

### 1. Conduction heat transfer

Two mechanisms have been defined for heat transfer by the conduction phenomenon; the first one is described according to the molecule vibration and the second one is based on free electrons [13]. In the first mechanism, the heat is transferred by the molecule interaction, which means that the molecule at a higher temperature with higher energy transfers its energy to the adjoining molecule by lattice vibration [13]. Accordingly, the materials with an excellent crystalline structure such as metals have high thermal conductivity [3], [13]. These types of materials like aluminum, copper, and steel have a high thermal conductivity in the range of 14-400 [W/(m K)] [3]. On the other hand, due to their weak crystalline structure, insulation materials, such as resin with the thermal conductivity in the range of 0.2-0.6 [W/(m K)], have low thermal conductivity.

In the second mechanism, the heat transfers between the free electrons. Based on this definition, the materials with a higher number of free electrons, such as pure metals, have better heat transfer conductivity [13]. Usually, a material with good electrical conductivity also has good thermal conductivity.

The general Fourier expression for heat conduction in a one-dimensional heat flow (x coordination) is [32]:

$$Q_{cond} = -kA_{cr} \frac{\partial T}{\partial x} \approx -kA_{cr} \frac{\Delta T}{x}, \quad (2.1)$$

where  $Q_{cond}$  is the rate of the heat conduction in x coordination [W],  $\partial T/\partial x$  is the temperature gradients in x-direction,  $k$  is the thermal conductivity of the material [W/(m K)],  $A_{cr}$  is the object cross-section area [m<sup>2</sup>],  $\Delta T$  is temperature difference across the object [K], and  $x$  is length [m].

### 2. Convection heat transfer

Convection occurs between the solid surface and the fluid. This phenomenon is a heat transfer process due to fluid motion [8]. In some cases, this process occurs by the buoyancy forces due to the difference in the density of hot and cold fluid molecules, which is called natural convection or in other cases, the fluid motion is generated by an external force, e.g., ventilator, fan, pump and blowers, which is known as the forced convection [8].

The amount of the heat transferred by the convection is calculated based on Newton's Law:

$$Q_{conv} = h_c A (T_s - T_0), \quad (2.2)$$

where  $Q_{conv}$  is the rate of the heat transfer by convection [W],  $h_c$  is the convection heat transfer coefficient [W/(m<sup>2</sup>K)],  $A$  is the surface area [m],  $T_s$  is the surface temperature [°C], and  $T_0$  is the fluid temperature [°C].

### 3. Radiation heat transfer

Both of the mentioned heat transfer phenomena in two previous sections need a medium to transfer the heat. Further, the heat transfer in these two phenomena occur

in the negative direction of the temperature gradients; in other words, heat is transferred from higher temperature to lower temperature part of the object or the fluid or gas medium [32].

In the third heat transfer phenomenon, its specifications are completely different from conduction and convection. Accordingly, it does not need the medium to exchange and transfer the heat; it can occur even in the vacuum area [13], [33]. Radiation is an electromagnetic phenomenon, and the heat is transferred by the electromagnetic waves [13], [33]. The amount of heat that can be emitted by this phenomenon completely depends on the absolute temperature of the body [33].

The amount of the heat transferred by radiation is calculated based on the Stefan-Boltzmann equation as in [32]:

$$Q_{rad} = A\varepsilon\sigma T^4, \quad (2.3)$$

where  $Q_{rad}$  is the amount of heat transferred by radiation [W],  $\varepsilon$  is the relative emissivity (in the range of zero to one),  $\sigma$  is the Stefan-Boltzmann constant equal to  $5.67 \times 10^{-8}$  [W/(m<sup>2</sup> K<sup>4</sup>)], and  $T$  is a temperature difference between radiating and absorbing surfaces [K].

Radiation is the latest heat transfer phenomenon in the thermal design and analysis of the electrical machine that has attracted attention of the experts. Information and experimental results about radiation in the electrical machine are scarce [17]. Further, most of the studies related to the thermal design and analysis of electrical machines have neglected the heat transfer by the radiation phenomenon according to the statement that the temperature of the stator housing of the motor is not high enough [17], [34]. However, this statement can be correct in the electrical machines such as TEFC machine cooling by the fan at high motor speed [34]. Nevertheless, in the electrical machine with natural cooling or with very low motor speeds, the above statement is incorrect and between 20 to 40% of the total heat is extracted by the radiation phenomenon [35], [36].

The radiation phenomenon occurs in both inside and outside of the electrical motor. However, it is very difficult to determine the radiation coefficient experimentally since it is a complex process. The radiation occurs in parallel by the convection, and it is difficult to segregate these two phenomena from each other. Accordingly, it is very common that thermal designers add the convection and the radiation coefficients together as the total heat transfer coefficient in their analysis. However, Boglietti in [34] and [37] has determined the radiation coefficient of the electric motor through the experiment. For this purpose, the motor was hanged using two thin plastic wires inside the vacuum chamber to minimize the conduction and neglect this phenomenon.

Further, the DC stator test was applied under vacuum condition. Based on his experiment, the amount of the radiation coefficient between the stator copper and iron laminations is 8.5 [W/(m<sup>2</sup>K)], between the end-winding and motor housing is 6.9 [W/(m<sup>2</sup>K)] and between the house of the motor to the ambient is 5.7 [W/(m<sup>2</sup>K)]. The results of these studies can be used as a good starting point for the thermal design and analysis of the electrical machine.

### 2.3 Critical parameters in the thermal model

The accuracy of the LPTN is highly dependent upon the accurate determination of the parameters. There are several critical parameters in the LPTN, which play an important role in the accuracy of the thermal model. In some cases, determining these thermal

model parameters in the complex part of the electrical machine cannot be calculated by the purely mathematical and analytical solution.

According to the different studies, e.g., [14], [17], [38] and [39], the critical parameters for the TEFC electrical machine are as follows:

- Winding model
- Interface gap between the stator lamination and the housing
- Air gap heat transfer
- Convection from the housing surface
- End space cooling

According to the role of these parameters in the accuracy of the thermal model, several studies such as [40] and [41] use the sensitivity analysis to clarify the effect of each parameter on the nodal temperature of the thermal model.

### 2.3.1 The equivalent thermal conductivity of the slot

The most critical part in the modeling of conduction heat transfer in the electrical machine is conduction inside the slot. This region consists of low thermal conductivity materials with high thermal sensitivity. In the thermal modeling of the slot, it is impossible and not essential to model the position of every single conductor. As figure 2.4 shows, there are three simplified methods to model the conduction heat transfer inside the slot. These methods are as follows [42]:

- Layer winding method: in this method, the slot is divided into several copper layers surrounded by impregnation and insulation [28]. Accordingly, the copper with the same temperature located at the same distance from the lamination, they lump and construct one layer [39]. Figure 2.4 (a) shows the scheme of this model.
- Cuboidal method: this model is based on the cuboidal winding and presents the 3-D heat transfer path of the windings [42].
- Equivalent insulation: in this approach, copper is located in the middle of the slot, and the insulation and impregnation material surrounds the copper as it has high thermal conductivity, it is neglected and only the equivalent thermal conductivity of the insulation materials is demonstrated, which depends on several factors such as the slot filling factor, the quality of the impregnation [42].

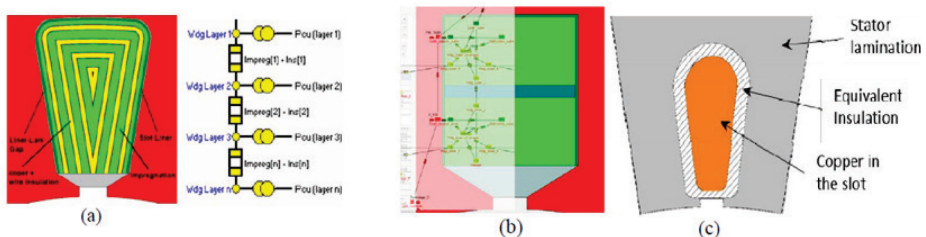


Figure 2.4. Different methods of stator slot modeling in the LPTN: (a) layered, (b) cuboidal, and (c) equivalent thermal conductivity [43].

### 2.3.2 Interface gap heat transfer

There are several different interface gaps in an electrical machine. However, the most important one in a TEFC machine is the interface gap between the stator laminations and the machine housing, as the total heat should be extracted from this part to the machine housing [17]. This gap is created mainly due to the imperfections between the surfaces of solid materials [38]. In the LPTN of an electrical machine, the interface gap is modeled

using the equivalent air gap. In this method, it is a challenging task to determine the equivalent length of the interface gap and it depends on different factors, e.g., surface roughness, material hardness, interface pressure and manufacture process [14].

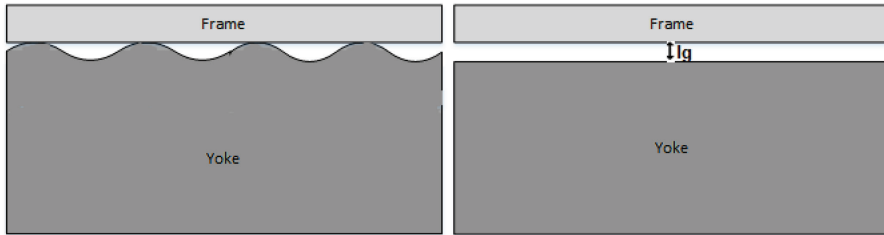


Figure 2.5. Effective air gap.

Different studies have addressed the problem of the interface gap in electrical machines [17]. For instance, Holman in [44] has defined the value of thermal resistances and conductances for various pressures and roughness; in [45] Miller defines the values of the interface gaps between different solid materials at the moderate pressure and usual finishes. Traditionally, in the thermal design of an electrical machine, they just evaluate the length of the gap according to the machine housing type and machine power [21]. However, several studies such as [39] and [46] show that the interface gap depends on the material properties, pressure and roughness surfaces, as well as on the manufacturing process that has direct impact on this parameter; consequently, in the advanced manufacturing process, the dimension of the interface gap has been reduced. Staton in [17] presented the typical values of the interface gap in a wide range of 4-pole TEFC induction motors.

### 2.3.3 Air gap heat transfer

The heat is transferred across the air gap by conduction, convection, and radiation [21]. As the temperature differences between the rotor surface and the stator surface are rather small, the heat transfer by the radiation is neglected [21]. To consider the impact of the rotational flow on the total heat transfer in the air gap, a set of empirical correlations based on the Taylor dimensionless number ( $Ta$ ) has been characterized. The initial correlations were developed by experiments on the concentrated rotating cylinder by Taylor in 1935, and In the following, Gazley in 1958 completed it [39]. The Taylor number depends on the air gap length, the rotational speed of the rotor, rotor length and the kinematic viscosity. Furthermore, the value of the Taylor number determined the flow type (laminar, vortex, or turbulent) [13].

### 2.3.4 Convection from the housing surface

Most of the heat is transferred to the ambient by the convection phenomenon; consequently, accurate calculation of the convection coefficient increases the accuracy of the thermal model.

In a TEFC machine with variable speed drives, at the low-speed performance, the natural convection is the dominated cooling method, which is the largest single resistance between the winding to the ambient [17] and [8]. The housing structure of the TEFC machine is designed for the forced cooling condition, and the fins channels on the outer circumferential of the housing provide the flow paths for the airflow. In most of the cases, these fin channels do not provide a good airflow into the depth of the fins during natural cooling [17].

Boglietti in [39] has presented an empirical correlation based on several DC stator experiments on different TEFC induction machines with different power ranges. However, the most accurate method to determine the natural convection coefficient is the area based composite correlation [17]. According to the complex shape of the housing of the TEFC machine, no single correlation exists. Consequently, the machine housing is segregated to different shapes with the known empirical correlation and then the total natural convection coefficient is determined by an area-based average [8].

The TEFC electrical machine is cooled by passing the airflow over spacing between the fins of the machine housing. In comparison to some forced cooling system, such as a liquid cooling system, in which the fluid flow speed can be estimated with reasonable accuracy, the prediction of the airflow speed from the housing of a TEFC machine is a challenging task [39].

There are several reasons to explain the above statement. The distribution of the airflow, which is produced by the fan, is not uniform in every fin channel [17], [39]. According to figure 2.6, due to the air leakage from semi-open fin channels, the airflow speed starts to drop in the axial direction [39]. Furthermore, in the housing of TEFC machines, some of the fin channels are blocked using the terminal box and bolt lugs, which results in the unbalanced distribution of the airflow around the machine housing [17].

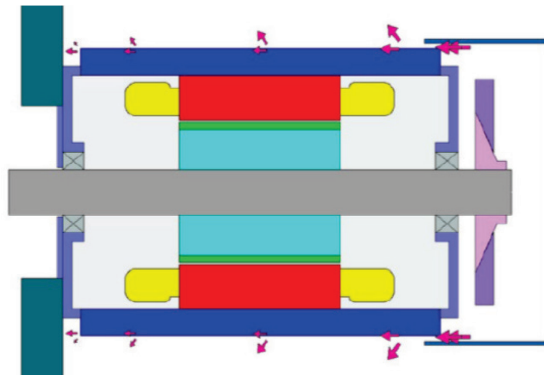


Figure 2.6. Air leakage flow in the axial direction [47].

Figure 2.7 provides a better overview of the typical reduction of the air velocity in the axial direction of the fin channels of different TEFC machines [8]. Accordingly, the air velocity in the driven part of the machine is lower than in the non-driven part, and the effect of this factor on the heat transfer from the machine housing to the surrounding must be included in the calculation. Furthermore, the rates of the reduction of the velocity versus the distance are different in all the machines and depend on the fan characteristics, fin designs, motor size, and rotational speed.



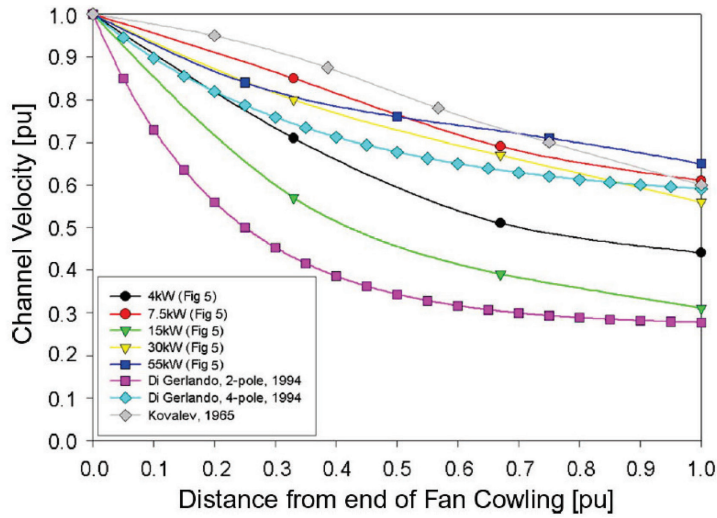


Figure 2.7. Air velocity in the fin channel versus distance from the fan side [8].

### 2.3.5 End space cooling

The end space cooling is one the most difficult and complex areas of machine cooling due to the airflow around the end winding [17]. Several studies have addressed the heat transfer in this region, and according to figure 2.8, they have proposed diverse correlations in the following format to determine the heat transfer coefficient in the end space of the machine[48], [49], [50],[51] and [52].

$$h_{ew} = k_1(1 + k_2v^{k_3}), \quad (2.4)$$

where  $h_{ew}$  is the total heat transfer coefficient in the end space [W/(m<sup>2</sup>K)],  $k_1$ ,  $k_2$  and  $k_3$  curve fitting coefficients and  $v$  is the local velocity [m/s]. The  $k_1$  term shows the value of the natural convection, and  $k_1 \times k_2 \times v^{k_3}$  term presents the forced convection.

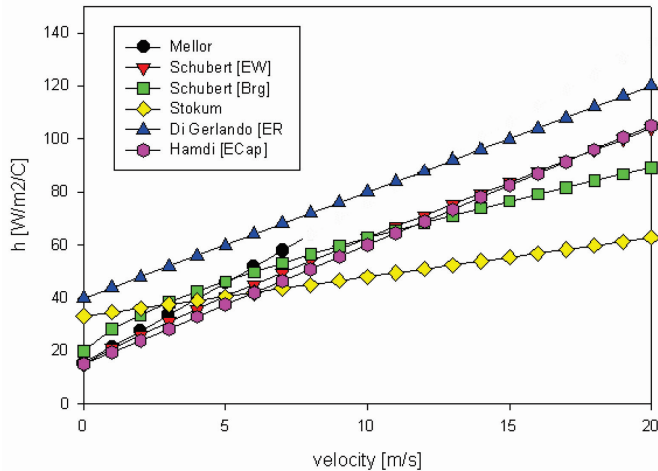


Figure 2.8. Heat transfer coefficient of end space via inner air velocity [17].

Table 2.1 shows different values of  $K_1$ ,  $K_2$  and  $K_3$  in these studies.

*Table 2.1. Different values of  $K_1$ ,  $K_2$  and  $K_3$*

<b>Name</b>	<b><math>K_1</math></b>	<b><math>K_2</math></b>	<b><math>K_3</math></b>
Mellor	15.5	0.39	1
Schubert (1)	15	0.4	0.9
Schubert (2)	20	0.425	0.7
Stokum	33.2	0.0445	1
DiGerlando	40	0.1	1
Hamdi	10	0.3	1

The turbulent flow in this area depends on several factors, such as shape and length of the end winding, fanning effects of internal fans, the number and the dimension of Wafers, end-rings and surface finish of the end section of the rotor [8].

## **2.4 Summary of Chapter 2**

Modern thermal analysis methods were addressed and advantages and weakness of these methods were analyzed. To achieve the objectives established in Chapter 1, the analytical LPTN and the hybrid thermal model were selected as ideal methods to analyze the heat transfer of the machine. The basic principles of heat transfer were presented. In addition, common correlations, as well as critical parameters in the thermal calculation, were demonstrated and summarized and different methods to overcome these challenges were proposed.

### 3 Thermal analysis and modeling methods

This chapter focuses on the development of the thermal models for the TEFC electrical machine. The developed thermal models are evaluated on a TEFC SynRM. In addition, the parameters of the thermal models, especially the heat transfer coefficient from the complex housing of this type of machine, are calculated. A more comprehensive explanation about the analytical LPTN and the hybrid thermal model, as well as the calculation of their components and the computation methodology are presented in papers [I] to [VII].

#### 3.1 Synchronous reluctance motor prototype

For the research purposes, the thermal models described in this study are applied to a four poles 10 kW, 400 V, 50 Hz, transverse-laminated radial flux SynRM with 'F' insulation class. Figure 3.1 shows a CAD drawing of the machine and its cross section. This machine is a totally enclosed fan cooled machine and it uses the air forced cooling method. Accordingly, the fin channel design is essential in the outer circumferential of the machine housing.

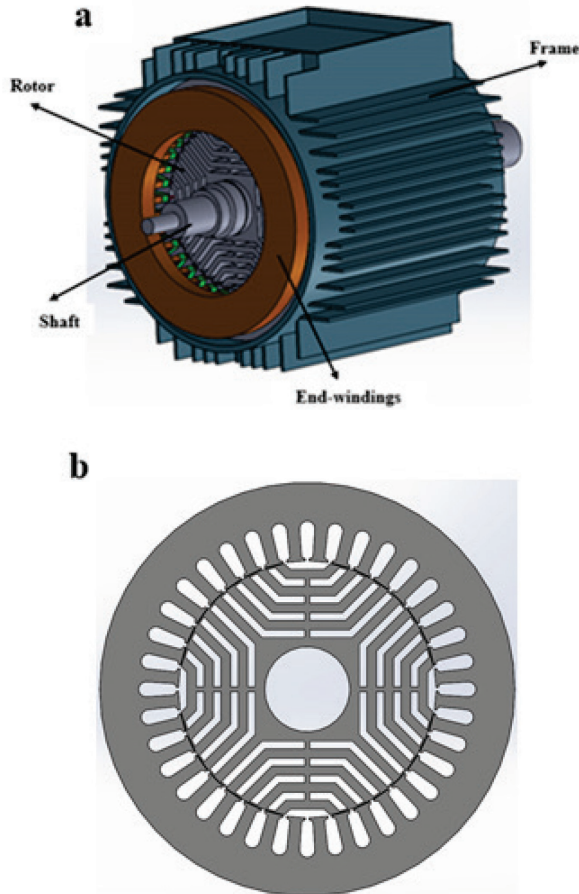


Figure 3.1. Structure and topology of the transverse-laminated SynRM.

Detailed information on the geometrical data of the motor is given in Table 3.1, and the material properties of the machine are presented in Table 3.2.

Table 3.1. Geometrical data of the transverse- laminated SynRM

Name	Symbol	Unit	Value
Stator core length	$L_s$	mm	156
Stator inner diameter	$D_{is}$	mm	136
Stator outer diameter	$D_{os}$	mm	219
Number of slots	$N_s$	-	36
Air-gap height	$H_{ag}$	mm	0.4
Rotor inner diameter	$D_{ir}$	mm	45
Rotor outer diameter	$D_{or}$	mm	135.2
Slot height	$H_{slot}$	mm	21
Slot filling factor	$k_f$	-	0.6
Slot area	$S_{lots}$	mm <sup>2</sup>	130.1

Table 3.2. Material data of transverse- laminated SynRM

Machine part	Material	Thermal conductivity symbols	Thermal conductivity [W/(mK)]
Frame	Aluminum	$k_{al}$	230
Laminations	M-350-50A	$k_{ir}$	28
Winding	Copper	$k_{cu}$	387
Impregnation	Resin	$k_{res}$	0.2
Air gap	Air	$k_{air}$	0.0257
Shaft	Steel	$k_{sh}$	41

### 3.2 Lumped parameter thermal modeling

In this section, the analytical LPTN applied for this research is presented. Due to the risk of high temperature inside the slot and damaging the slot insulation, which reduces the lifetime of the insulation materials as well as the machine life, precise prediction of the temperature distribution in the machine is necessary. To model the steady-state thermal behavior of the machine with the LPTN, the different heat transfer paths and power losses in the machine are represented using impedances and power sources respectively.

An electrical machine consists of complex geometries; to model the temperature distribution inside the machine with high accuracy and resolution, a large thermal network to involve all thermal paths is needed. However, the large thermal network with a high number of nodes enhances the computation time and the complexity of the model. Furthermore, some variable parameters such as convection coefficients require a complicated calculation process due to complex geometries and the unknown flow condition. As a result, during the design process of an electrical machine, a fast and compact model, which predicts the temperature of the key components of the electrical machine, is needed. Consequently, it is necessary to implement the geometrical symmetries and some hypothesis such as a uniform distribution of losses inside the

machine; focus of the heat transfer in the axial direction is on the shaft and the stator windings, uniform distribution of the temperature in the machine housing. The effect of these symmetries and hypotheses on the model is in reducing the number of thermal paths and nodes, calculating the conduction resistances to model the heat paths in the machine lamination easily by hollow cylinder correlation, and reducing the order and complexity of the LPTN

Figure 3.2 presents the steady-state LPTN developed for the machine under investigation. The model consists of six nodes that feature all the key thermal parameters and temperature rises. Node 1 is used to model the heat transfer between the machine housing and the cooling medium.

Further, two nodes (nodes 2 and 3) are used to model the stator yoke and teeth respectively. The most important component in SynRM electrical machines is the stator windings; major portion of the heat is generated inside the slot. The end-windings are usually the hottest parts of the machine. As a result, an accurate prediction of the temperature of the stator windings is of great importance. Accordingly, nodes 4 and 5 are defined in the thermal network to predict the temperatures of the active part of the stator windings and the stator end windings respectively. The rotor of the SynRM consists of the iron lamination and does not contain materials with high thermal sensitivity. Accordingly, it is modeled by one node only (node 6). In addition, among the different nodes, there are thermal resistances to model the heat transfer paths as well as heat sources to model the losses in the machine. In total, there are 14 thermal resistances and 4 heat sources. Table 3.3 gives the definitions of these resistances and sources.

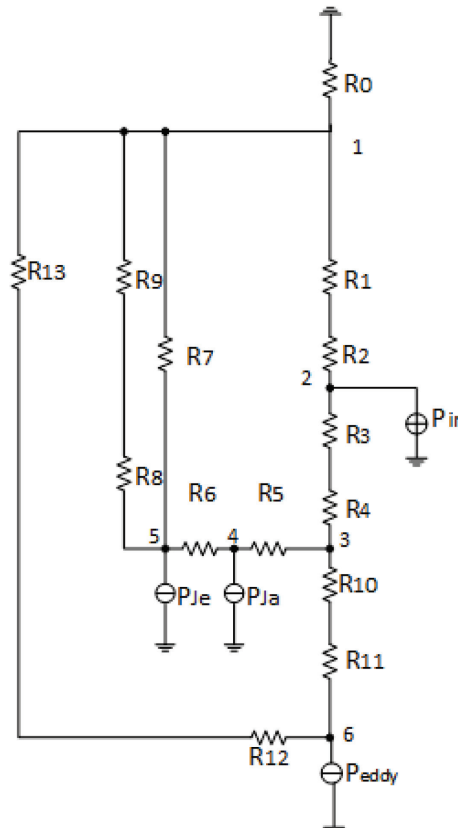


Figure 3.2. The developed LPTN model of SynRM.

Table 3.3. Definitions of the thermal model components

Component	Description
$R_0$	Forced convection and radiation thermal resistance from the frame surface to ambient
$R_1$	Conduction thermal resistance of the Interface gap between the frame and the active part of the machine
$R_2$	Conduction thermal resistance of the upper half side of the stator yoke
$R_3$	Conduction thermal resistance of the lower half side of the stator yoke
$R_4$	Conduction thermal resistance of the stator teeth
$R_5$	Conduction thermal resistance between the stator winding and the stator teeth
$R_6$	Conduction thermal resistance between the coil side and the end-windings
$R_7$	Conduction thermal resistance between the stator winding and the frame
$R_8$	Convection thermal resistance between the stator end-winding and the inner air of the end region
$R_9$	Convection thermal resistance between the inner air and the end cap
$R_{10}$	Convection thermal resistance of the air gap
$R_{11}$	Conduction thermal resistance of the upper half side of the rotor
$R_{12}$	Conduction thermal resistance of the lower half part of the rotor
$R_{13}$	Axial thermal conduction of the shaft
$P_{ir}$	Stator iron losses
$P_{Ja}$	Joule losses in the active part
$P_{Je}$	Joule losses in the end –winding
$P_{eddy}$	Rotor iron losses

### 3.3 Calculation of the LPTN components

In the LPTN analysis, the thermal resistances that are present in the conduction, convection and radiation phenomenon are determined. In this section, the computing methods of the thermal network resistances by using analytical and empirical correlations are described. For these purposes, some geometry simplifications are implemented, which are discussed below. The SynRM has the same stator structure as an induction machine. Accordingly, the stator thermal resistances can be evaluated by the same correlations as presented in [20]. First, this section focuses on the calculation of the conductive resistances in the stator and the rotor. Then, the radiation resistance is calculated, and finally, the calculation of the convection resistances from different machine surfaces is described.

### 3.3.1 Conduction lumped parameter resistance

In the equivalent thermal circuit, the purely conductive paths are represented using the conduction resistance. The conduction resistance according to the shape and direction of the heat flow transfer in an electrical machine is divided into conduction resistance for the plane slab (axial direction) and radial conduction resistance in hollow cylinder layers [32].

Figure 3.3 shows the calculation of the conduction resistance for the plane slab shape or the heat transfer in the axial direction in the electrical machine[32]:

$$R_{th} = \frac{L}{kA_{cr}} \quad (3.1)$$

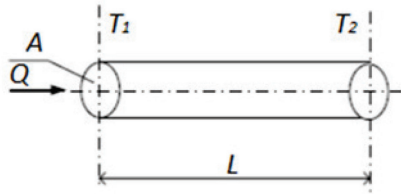


Figure 3.3. Conduction heat transfer in the axial direction.

According to (3.1), the conduction resistance depends on the thermal conductivity of the material and the dimension of the conduction path. For a high amount of the heat transfer by the conduction, the value of this resistance should be small. Accordingly, it occurs when the thermal conductivity of the material is high, or the ratio of the length to the cross-section path is minimized [3].

According to figure 3.4, the general equation for the calculation of the conduction resistance from the radial direction of the hollow cylinder is [30]:

$$R_{th} = \frac{\ln\left(\frac{r_{out}}{r_{in}}\right)}{2\pi kL}, \quad (3.2)$$

or a cylindrical section that occurs in a machine (2.3) is converted to [22]:

$$R_{th} = \frac{\ln\left(\frac{r_{out}}{r_{in}}\right)}{2\pi kL\varphi}, \quad (3.3)$$

where  $r_{out}$  is the outer radius [m],  $r_{in}$  is the inner radius [m], and  $\varphi$  is the angular span [rad].

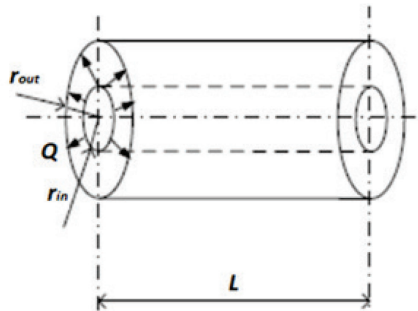


Figure 3.4. Conduction heat transfer in the radial direction.

By using equations (3.1), (3.2) and (3.3) and relevant geometric and thermal data represented in Tables 3.1 and 3.2, the values of conductive resistances in the thermal network in figure 3.2 are hereafter calculated and summarized.

**Interface gap conduction resistance ( $R_1$ ):**

The interface gap occurs during the assembling process of packing the stator to the housing and it is evaluated as [20]:

$$R_1 = \frac{l_{ig}}{k_{air}\pi D_{os}L_s}, \quad (3.4)$$

where  $l_{ig}$  is the interface gap between the stator and the motor housing [m], which is selected according to [39].

**Stator yoke conduction resistances ( $R_2$  and  $R_3$ ):**

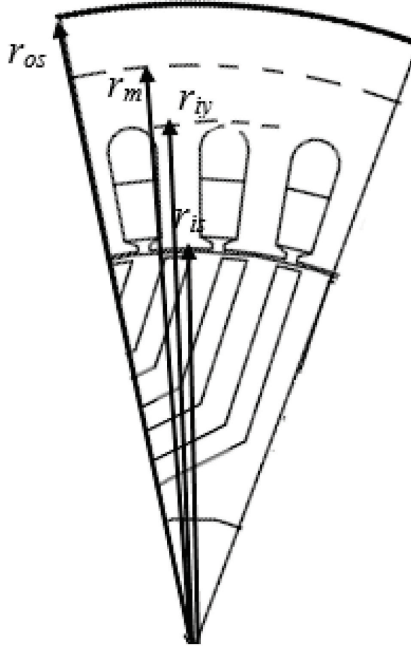


Figure 3.5. The stator core radial dimensions.

According to figure 3.5, the stator yoke is divided into two sections and the value of the radial conduction resistance of each part is evaluated by using (3.2) as follows [20]:

$$R_2 = \frac{\ln\left(\frac{r_{os}}{r_m}\right)}{2\pi k_{ir}L_s}, \quad (3.5)$$

$$R_3 = \frac{\ln\left(\frac{r_m}{r_{iy}}\right)}{2\pi k_{ir}L_s}, \quad (3.6)$$

where  $r_m$  is the mean value of the stator yoke radius [m],  $r_{oy}$  is the outer radius of the stator and  $r_{iy}$  is the inner radius of the stator yoke [m].



**Stator teeth conduction resistance ( $R_4$ ):**

To evaluate the equivalent thermal resistance of the stator teeth, the geometry of this motor portion is assumed as a cylinder. To reduce the slots section and evaluate the value of the thermal resistance of the teeth, one reduction factor ( $\rho_{th}$ ), which equals the percentage of teeth volume iron to the total volume of the teeth and slots is applied to the formula [20]

$$R_4 = \frac{\ln\left(\frac{r_{iy}}{r_{is}}\right)}{2\pi k_{ir} L_s \rho_{th}}, \quad (3.7)$$

where  $r_{is}$  is the inner stator radius [m].

**Conduction thermal resistance from stator windings ( $R_5$  and  $R_6$ )**

The stator winding is the most important section of thermal modeling. A major part of the heat is produced there. This section consists of several different materials with high thermal sensitivity, which increases the importance of accurate modeling of this part.

Heat fluxes in the slot are released in axial, radial and circumferential directions. The axial path presents the heat flow movement from end windings to the active part of slots or vice versa. Radial and circumferential paths represent the heat flow paths to coolant medium by means of the stator core. Consequently, the stator winding is divided into resistances  $R_5$  and  $R_6$  to model the circumferential and the axial heat transfer respectively.

$R_5$  presents the conduction paths for the heat flow in the radial and circumferential part of the stator slot and is evaluated as in [20]:

$$R_5 = \frac{t_{eq}}{k_{ins} A_{slot}}, \quad (3.8)$$

where  $t_{eq}$  is the equivalent thickness of impregnation insulation materials in the stator slot [m],  $k_{ins}$  is the equivalent thermal conductivity of insulation materials in the stator slot [W/(mK)], and  $A_{slot}$  is the interior slot surface [m<sup>2</sup>].

The thickness of air and insulation materials in the stator slot is calculated as:

$$t_{eq} = \frac{S_{slot} - S_{cu}}{l_{sb}}, \quad (3.9)$$

where  $S_{cu}$  is the copper section in the stator slot [m<sup>2</sup>], and  $l_{sb}$  is the perimeter of the stator slot [m].

The equivalent thermal conductivity of the slot can be calculated by three methods: layer winding, cuboidal and equivalent insulation. In this thesis, the equivalent insulation method is applied to find the equivalent conductivity of the slot. This method is a fast calculation method and can be easily used by knowing the slot-filling factor. Based on this method, Copper has high thermal conductivity and low conduction thermal resistance. Consequently, the copper thermal resistance can be neglected in the analytical model of the stator winding in the circumferential and radial direction. Figure 3.6 shows a simplified assumption to model the equivalent insulation method in the active part of the slot. As a result, the equivalent thermal conductivity of the insulation  $k_{ins}$  is calculated by using a liner empirical correlation as in [39]:

$$k_{ins} = 0.1076k_f + 0.029967. \quad (3.10)$$

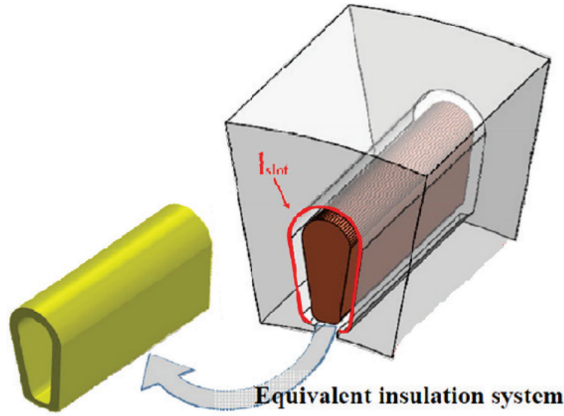


Figure 3.6. Equivalent insulation method in the stator slot [42].

$R_6$  presents the thermal conduction path from the end winding to the active part, and it is computed as in [21]:

$$R_6 = \frac{l_{av}}{6 N_s k_{cu} S_{cu}} . \quad (3.11)$$

where  $l_{av}$  is average conductor length of half a turn [m].

**Conduction thermal resistance between the end windings and the motor frame ( $R_7$ ):**

The distance between the outer surface of the end winding and the internal part of the machine housing is low; accordingly, the air speed in this region is very low, and the heat transfer from the end winding to the internal part of the housing is assumed as conduction and is calculated as:

$$R_7 = \frac{\ln\left(\frac{r_{os}}{r_{os}-\gamma H_y}\right)}{2\pi k_{air}(L_{ec}-L_s)} , \quad (3.12)$$

$H_y$  is the stator yoke height [m],  $\gamma$  is the reduction coefficient to implement the distance between the outer surface of the end winding, and the internal part of the housing and  $L_{ec}$  is the motor housing length [m].

The value of  $\alpha$  for ordinary induction machines with single layer windings is defined in the range of 0.4 to 0.7 [20]. However, this value for the machine by the double layer windings decreases to the range of 0.25 to 0.4.

**Conduction thermal resistances of the rotor ( $R_{11}$  and  $R_{12}$ ):**

Figure 3.7 shows the geometry of a half a pole of the rotor of SynRM. The rotor construction consists of the iron laminations, which makes the magnetic flux paths and air gaps in the laminations that are the magnetic flux barriers. Making the hypothesis that the heat transfer inside the flux barriers is carried out through natural convection according to the high thermal conductivity of the rotor iron laminations, the majority of the heat is transferred by the conduction phenomenon. Consequently, the heat transfer by the natural convection phenomenon from magnetic flux barriers can be neglected. As a result, the total heat fluxes inside the rotor are transferred through the iron laminations.

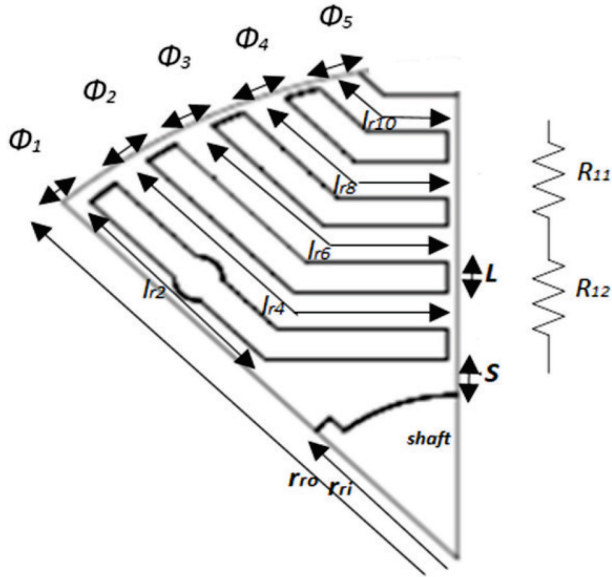


Figure 3.7. Cross section of 1/8 of the rotor.

Figure 3.8 shows the equivalent thermal circuit for the rotor by implementing the above simplified hypothesis. According to figure 3.8, the total value of the rotor resistance equals  $R_r$ , which consists of the series-parallel combinations of thermal resistances. To implement the rotor losses to the LPTN,  $R_r$  is divided into two equal resistances  $R_{11}$  and  $R_{12}$  illustrated in figure 3.7 and the LPTN of the SynRM.

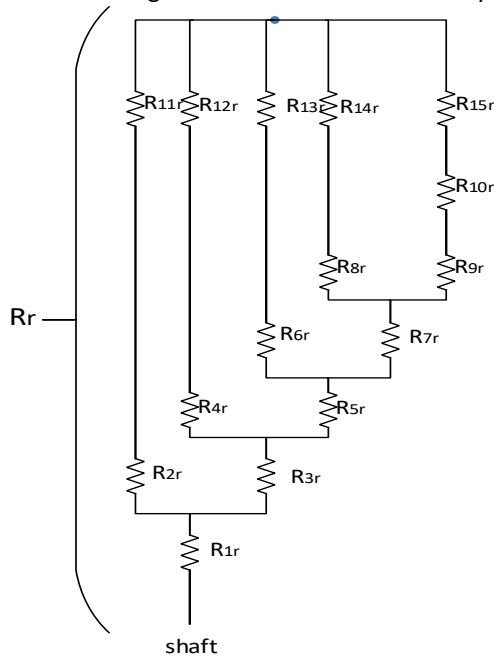


Figure 3.8. The equivalent thermal circuit of the rotor.

The value of the thermal resistances presented in figure 3.8 is calculated by (3.1) and (3.3). The values of  $R_{1r}$  and  $R_{11r}$  to  $R_{15r}$  are calculated by (3.3), and the rest are evaluated by (3.1). Tables 3.4 and 3.5 provide a better overview of the calculation of the thermal resistances.

Table 3.4. Calculation of the radial thermal resistance by (3.3)

<b>Resistance</b>	<b><math>r_{out}</math></b>	<b><math>r_{in}</math></b>	<b><math>k</math></b>	<b><math>\varphi</math></b>
$R_{1r}$	$r_{ir}+S$	$r_{ir}$	$k_{ir}$	$\pi/4$
$R_{11r}$	$r_{or}$	$r_{or}-1$	$k_{ir}$	$\Phi_1$
$R_{12r}$	$r_{or}$	$r_{or}-1$	$k_{ir}$	$\Phi_2$
$R_{13r}$	$r_{or}$	$r_{or}-1$	$k_{ir}$	$\Phi_3$
$R_{14r}$	$r_{or}$	$r_{or}-1$	$k_{ir}$	$\Phi_4$
$R_{15r}$	$r_{or}$	$r_{or}-1$	$k_{ir}$	$\Phi_5$

Table 3.5. Calculation of the thermal resistances by (3.1)

<b>Resistance</b>	<b><math>L</math></b>	<b><math>k</math></b>	<b><math>A</math></b>
$R_{2r}$	$l_{r2}$	$k_{ir}$	$A_{2r}$
$R_{3r}$	$L$	$k_{ir}$	$A_{3r}$
$R_{4r}$	$l_{r4}$	$k_{ir}$	$A_{4r}$
$R_{5r}$	$L$	$k_{ir}$	$A_{5r}$
$R_{6r}$	$l_{r6}$	$k_{ir}$	$A_{6r}$
$R_{7r}$	$L$	$k_{ir}$	$A_{7r}$
$R_{8r}$	$l_{r8}$	$k_{ir}$	$A_{8r}$
$R_{9r}$	$L$	$k_{ir}$	$A_{9r}$
$R_{10r}$	$l_{r10}$	$k_{ir}$	$A_{10r}$

Finally, the value of  $R_r$  is calculated by using the series-parallel resistances law in the electrical circuit. Further,  $R_{11}$  and  $R_{12}$  are defined as:

$$R_{11} = R_{12} = \frac{R_r}{2}. \quad (3.13)$$

### Axial conduction thermal resistance of the shaft ( $R_{13}$ ):

According to the hypothesis, the axial heat transfer in the rotor is considered in the shaft and by using the simplified assumption that the temperature distribution along the shaft is uniform,  $R_{13}$  is calculated as [20]:

$$R_{13} = \frac{1}{4} \left( \frac{0.5L_s}{k_{ir}\pi r_{ir}^2} \right) + \frac{1}{2} \left( \frac{0.5(L_{shaft}-L_s)}{k_{ir}\pi r_{ir}^2} \right). \quad (3.14)$$

where  $L_{shaft}$  is the length of the shaft [m] and  $r_{ir}$  is the inner radius of the rotor [m].

### 3.3.2 Radiation lumped parameter resistance

The radiation resistance  $R_{rad}$  [K/W] is calculated as [13], [33]:

$$R_{rad} = \frac{T_1 - T_2}{\varepsilon \sigma F (T_1^4 - T_2^4) A} = \frac{1}{h_r A}, \quad (3.15)$$

where  $F$  is the view factor; the value of this variable ranges from zero to one and indicates the quality of the view between the radiating and absorbing surfaces. In addition,  $h_r$  is the radiation coefficient [W/(m<sup>2</sup>K)] and calculated as in [53],[33] and [54]:

$$h_r = \varepsilon \sigma F \frac{T_1^4 - T_2^4}{T_1 - T_2} = \varepsilon \sigma F (T_1 + T_2)(T_1^2 + T_2^2). \quad (3.16)$$

Table 3.6 shows the emissivity of different materials.

Table 3.6. Total emissivity of various materials [33]

Material	Emissivity	Material	Emissivity
Aluminum		Iron	
Black anodised	0.86	Polished	0.07-0.38
Polished	0.03-0.1	oxidised	0.31-0.61
Heavily oxidised	0.2-0.3	Nickel	0.21
Sandblasted	0.41	Paints	
Alumina	0.2-0.5	White	0.80-0.95
Asbestos	0.96	Grey	0.84-0.91
Carbon	0.77-0.84	Black lacquer	0.96-0.98
Ceramic	0.58	Quartz, fused	0.93
Copper		Rubber	0.94
Polished	0.02	Silver, polished	0.02-0.03
Heavily oxidized	0.78	Stainless steel	0.07
Glass	0.95	Tin, bright	0.04

The radiation resistance can be calculated by (3.15). However, the radiation calculation of the fins housing of the electrical machine is more complicated and difficult than that of the smooth electrical machine housings. In particular, the calculation of the view factor is a challenging part of the calculation of the radiation coefficient ( $h_r$ ) [17]. To reduce the complexity of the radiation calculation, a simplified assumption is used. Staton has applied this assumption in his software Motor-CAD [47]. Accordingly, the whole surface with a clear view of the ambient such as fin base, end caps, and fin tips has a view factor equal to one and the other with no clear view of the ambient such as fin sides has the view factor equal to zero [47]. According to this assumption, the heat can be transferred to the ambient by radiation phenomenon only from the fin base, fin tips, and end caps. In this thesis, the same assumption was used to calculate the radiation coefficient from the machine housing.

### 3.3.3 Convection lumped parameter resistances

The challenging parameter in the calculation of the convection heat transfer is the accuracy of the calculation of the convection coefficient  $h_c$ . This parameter depends on several different factors, e.g., surface temperature, fluid properties, and materials, different cooling methods, shape and size of surfaces. The convection heat transfer coefficient for both natural and forced cases is often calculated by using the empirical correlations. These empirical correlations have been developed by using the dimensionless number, e.g., Rayleigh (Ra), Grashof (Gr), Prandtl (Pr) and Reynold (Re) numbers [9].

In the natural convection, the typical form of the Nusselt number is defined as [8]:

$$\text{Nu} = a(\text{GrPr})^b, \quad (3.17)$$

where  $a$  and  $b$  are constants, Gr and Pr are calculated respectively as [8]:

$$\text{Gr} = \frac{\beta g \Delta T \rho^2 L^3}{\mu^2}, \quad (3.18)$$

$$\text{Pr} = \frac{c_p \mu}{k}, \quad (3.19)$$

where  $\beta$  is the coefficient of cubical expansion [1/K],  $g$  is the gravitational acceleration [m/s<sup>2</sup>],  $\Delta T$  is the temperature difference between the surface and the fluid [°C],  $\rho$  is fluid density [kg/m<sup>3</sup>],  $L$  is the characteristic length of the surface [m],  $\mu$  is the fluid dynamic viscosity [kg/(s .m)],  $c_p$  is fluid specific heat capacity [kJ/(kg°C)], and  $k$  is fluid thermal conductivity [W/(m°C)].

The typical form of the Nusselt number for the forced convection is defined as [8]:

$$\text{Nu} = a(\text{Re})^b (\text{Pr})^c, \quad (3.20)$$

where  $a$ ,  $b$  and  $c$  are constants, and  $\text{Re}$  is calculated as [8]:

$$\text{Re} = \frac{\rho \cdot v \cdot L}{\mu}, \quad (3.21)$$

where  $v$  is fluid velocity [m/s].

Finally, the correlation between the convection coefficient  $h_c$  and the Nusselt number ( $\text{Nu}$ ) is defined as [8]:

$$h_c = \frac{\text{Nu} \cdot k}{L}. \quad (3.22)$$

The value of the convection resistance  $R_{conv}$  [K/W] is calculated as:

$$R_{conv} = \frac{1}{h_c A}, \quad (3.23)$$

### **Convection resistance from the machine housing to the ambient ( $R_o$ )**

A significant part of the heat in the TEFC machine is dissipated from the machine surface to the ambient by the convection phenomenon. Accordingly, the accurate prediction of the convection coefficient leads to the higher accuracy of the analytical LPTN and the FEA thermal model of the electrical machine.

There are several empirical correlations for the basic shapes and geometries for both natural and forced convection. In the first step, the various empirical correlations for natural and air forced cooling for different basic geometries are considered and then extended to the real frame of a TEFC electrical machine. For the next step, to validate the result and find an appropriate empirical correlation from among the numerous correlations, a test bench for some basic geometries like flat surface and fin surface was developed and by comparing experimental and theoretical results, appropriate empirical correlations were selected. In the final section, the natural and forced convection from the surface of the TEFC SynRM is studied in detail.

### **Analytical background of convection from basic shapes**

#### **1. Natural convection from a flat plate**

As figure 3.9 shows, the simplest housing of the TENV electrical machine consists of smooth blocks. The natural convection coefficients from these housing types are calculated by using empirical dimensionless correlations for flat plates [17]. Fortunately, there are different correlations for the convection heat transfer over the flat plate surface in the horizontal and the vertical orientations, which are considered in detail in the following.

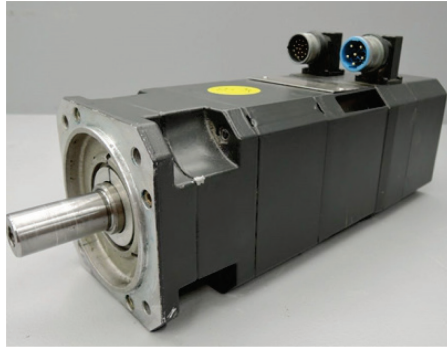


Figure 3.9. The TENV servo motor.

### A. Flat plate in the horizontal direction

As figure 3.10 shows, the empirical correlations for the flat plate in the horizontal direction according to the hot plate statue are divided into two main categories: upper face and lower face [31].

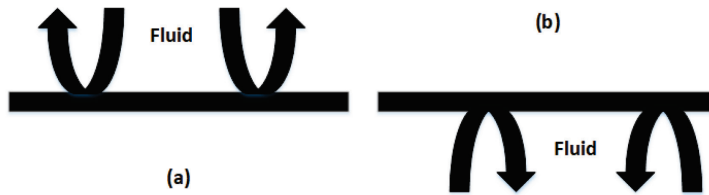


Figure 3.10. Natural convection on the horizontal flat a) hot surface facing up and b) hot surface facing down.

The empirical correlations for the upper face hot surface in the laminar and turbulent mode are respectively as [31]:

$$Nu = 0.54(GrPr)^{0.25}, \quad (3.24)$$

$$Nu = 0.15(GrPr)^{0.33}. \quad (3.25)$$

The empirical correlation for the lower hot surface is:

$$Nu = 0.27(GrPr)^{0.25}, \quad (3.26)$$

The characteristic length for the horizontal surface is calculated as [31]:

$$L = \frac{A}{P}, \quad (3.27)$$

where  $P$  is the perimeter of the surface [m].

### B. Flat plate in the vertical direction

There are different empirical correlations for the calculation of the average Nusselt number for the vertical flat plate. One of the first correlations to calculate the Nusselt number which covers laminar and turbulent mode was introduced by Mc Adams in 1954 [55]:

$$Nu = 0.59(GrPr)^{0.25}, \quad (3.28)$$

$$Nu = 0.10(GrPr)^{0.33}, \quad (3.29)$$

However, in 1975, Churchill and Chu found a new correlation, which can be applied to an entire range of  $Ra$  [55]:

$$\text{Nu} = \left\{ 0.825 + \frac{0.387(\text{GrPr})^{1/6}}{[1+(0.492/\text{Pr})^9/16]^{8/27}} \right\}^2, \quad (3.30)$$

Moreover, they recommended the correlation for the laminar mode as follows [55]:

$$\text{Nu} = 0.68 + \frac{0.67(\text{GrPr})^{1/4}}{[1+(0.492/\text{Pr})^9/16]^{4/9}}, \quad (3.31)$$

In this manner, the characteristic length is defined as the height of the vertical flat plate.

### 1. Natural convection from a rectangular isothermal fins plate

The extended surface, which is called a fin, is the preferred cooling method in the natural convection mode. Rectangular cross-section shaped plate fins on a flat base are the most common types of fins used in different electrical devices. In the natural convection mode, the characteristics of fins, e.g., length, height, and spacing between the fins, play an important role in the maximum heat transfer rate. There are many empirical correlations for the rectangular fin arrangement with a flat base. In this section, the empirical correlations based on the scientific research of Jones and Smith [56], Van Del Pol and Tierney [57] and Tari [58], [59] are discussed.

#### A. Rectangular isothermal fins on the horizontal surface

In 1970, Jones and Smith derived an empirical correlation to determine the natural heat transfer from horizontal fins [56]. Based on their assumption, the fins on the horizontal orientation areas have U-shape horizontal channels. In this case, they defined the fin space ( $S$ ) [m] as the characteristic length. According to (3.32), the Nusselt number is determined without considering the fins size.

$$\text{Nu} = 0.00067 \cdot \text{Gr} \cdot \text{Pr} \cdot \left\{ 1 - e^{(-7640/\text{Gr}\cdot\text{Pr})^{0.44}} \right\}^{1.7}. \quad (3.32)$$

In [58], Tari and Mehrtash defined an empirical correlation for the natural heat transfer from upward horizontal plate-fin heat sinks according to the fin characteristics. For this purpose, they defined a modified Grashof number ( $\text{Gr}'$ ) as:

$$\text{Gr}' = \text{Gr} \cdot \left( \frac{H}{L_f} \right)^{0.5} \cdot \left( \frac{S}{H} \right)^{0.3}, \quad (3.33)$$

where  $H$  [m] and  $L_f$  [m] are respectively the fin height and length. The Nusselt number is then expressed as:

$$\text{Nu} = 0.0915 \cdot (\text{Gr}' \cdot \text{Pr})^{0.436}. \quad (3.34)$$

#### B. Rectangular isothermal fins on the vertical surface

The rectangular isothermal fins on the vertical base plate are the common heat sink configuration. Many studies have addressed the calculation of the natural heat transfer from this configuration. One of the earliest studies about this configuration is by Van De Pol dated from 1973. In [57], he also described the vertical fin configuration as a U-shape vertical channel. In this case, the Nusselt number was defined as:

$$\text{Nu} = \frac{L_f}{H} \cdot \frac{\text{Gr}\cdot\text{Pr}}{Z} \cdot \left[ 1 - e^{-Z \cdot \left[ \frac{0.5}{(L_f/H) \cdot \text{Gr}\cdot\text{Pr}} \right]^{0.75}} \right], \quad (3.35)$$



where  $Z$  was defined as:

$$Z = 24 \cdot \frac{1 - 0.483 \cdot e^{-0.17/\alpha}}{\left[ (1 + \alpha/2) \cdot \left( 1 + \left( 1 - e^{-0.83\alpha} \right) \cdot \left( 9.14 \cdot \sqrt{\alpha} \cdot e^{-465 \cdot S} - 0.61 \right) \right) \right]^{\frac{1}{5}}}, \quad (3.36)$$

where  $\alpha$  is the channel aspect ratio.

In [59], Tari and Mehrtash introduced a new empirical correlation for the calculation of the Nusselt number from a vertical heat sink. They defined a new modified Grashof number as:

$$Gr' = Gr \cdot \left( \frac{H}{L_f} \right)^{0.5} \cdot \left( \frac{S}{H} \right), \quad (3.37)$$

and based on the modified Grashof number, they defined the Nusselt number as:

$$Nu = 0.0929 \cdot (Gr' \cdot Pr)^{0.5} \quad \text{for } Gr' \cdot Pr < 250, \quad (3.38)$$

$$Nu = 0.2413 \cdot (Gr' \cdot Pr)^{1/3} \quad \text{for } 250 < Gr' \cdot Pr < 106. \quad (3.39)$$

## 2. Air forced convection

One of the common methods to remove the heat from the electric motor is forced air-cooling, which is provided by adding a fan to the end part of the machine to provide the airflow over the motor housing.

### A. Forced convection from the flat plate

Figure 3.11 shows a PMDC motor with smooth surface cools by the air-forced cooling system. According to the flow mode, whether turbulent or laminar, the following well-known correlations for forced convection over the flat plate are applied to calculate the convection coefficient over the smooth surface of the motor [8].

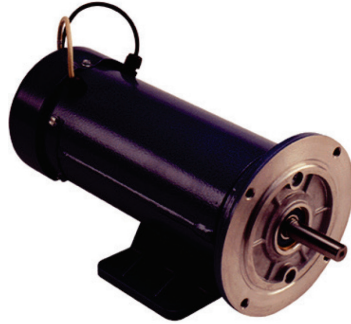


Figure 3.11. PMDC motor by air forced cooling system [60].

In the laminar mode ( $Re < 5 \times 10^5$ ), the Nusselt number is calculated as in [30]:

$$Nu = 0.664 \cdot Re^{0.5} \cdot Pr^{0.33}. \quad (3.40)$$

For the turbulent mode ( $Re > 5 \times 10^5$ ), the Nusselt number correlation is defined as [30]:

$$Nu = (0.037 \cdot Re^{0.8} - 871) \cdot Pr^{0.33}. \quad (3.41)$$

### B. Forced convection from a flat plate with an unheated starting part

The descriptions above involve a plate (horizontal cylinder) heated over the whole length. In many situations, the flat plates involve an unheated part (my case study)  $0 < x < \xi$ , as shown in figure 3.12. This part consists of an insulating material, and there is no heat generation beneath it. In such a case, the velocity boundary layer starts to develop from  $x=0$ , but the thermal boundary layer starts to develop from  $x=\xi$  [31], [61].

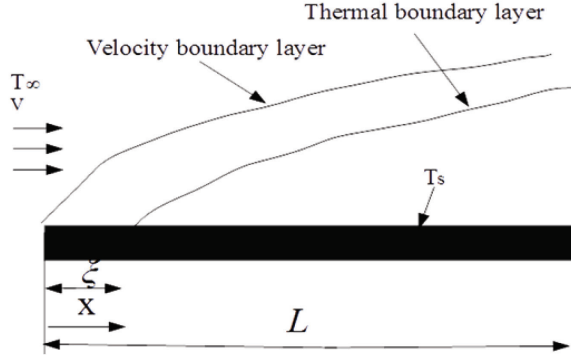


Figure 3.12. Illustration of the coolant flows over a flat plate with an unheated part.

In this situation, the Nusselt number for the laminar flow mode is calculated as follows [61]:

$$Nu_x = \frac{0.332 \cdot Re_x^{0.5} \cdot Pr^{\frac{1}{3}}}{\left[1 - \left(\frac{\xi}{x}\right)^{\frac{3}{4}}\right]^{\frac{1}{3}}}, \quad (3.42)$$

and for the turbulent mode it is calculated as in [61]:

$$Nu_x = \frac{0.0296 \cdot Re_x^{0.8} \cdot Pr^{\frac{1}{3}}}{\left[1 - \left(\frac{\xi}{x}\right)^{\frac{9}{10}}\right]^{\frac{1}{9}}}, \quad (3.43)$$

According to the above correlations, the average convection coefficient is calculated for the laminar and turbulent mode respectively as [61]:

$$h = 2 \cdot \frac{1 - \left(\frac{\xi}{L}\right)^{3/4}}{1 - \left(\frac{\xi}{L}\right)} \cdot h_{x=L}, \quad (3.44)$$

$$h = 1.25 \cdot \frac{1 - \left(\frac{\xi}{L}\right)^{9/10}}{1 - \left(\frac{\xi}{L}\right)} \cdot h_{x=L}. \quad (3.45)$$

### C. Forced convection from a flat plate with an unheated starting part inside a wind tunnel

In this manner, the model consists of the combination of the internal and external forced convection. The internal forced convection is defined as the fluid flows inside a confined space, e.g., a cylinder, tube or duct. In this case, the coolant fluid is completely bounded by the inner surface, and the boundary layer cannot expand freely [31], [30].

In this situation, the Reynolds number is defined as:

$$Re = \frac{v \cdot D_h}{\vartheta}, \quad (3.46)$$

where  $D_h$  is the hydraulic diameter of the internal flow [m] and  $\vartheta$  is the kinematic viscosity of the fluid [m<sup>2</sup>/s] [31].

In this manner, the range of Re to determine the laminar and turbulent modes of the flow is defined as [31], [30]:

$$\begin{cases} \text{Re} < 2300 & \text{laminar mode} \\ 2300 \leq \text{Re} \leq 10^4 & \text{transient mode} \\ 10^4 < \text{Re} & \text{turbulent mode} \end{cases}$$

while the convection from the flat plate side of the coil module represents the external forced convection.

## Convection heat transfer from the housing surface of the TEFC electrical machine

### 1. Natural convection

In the totally enclosed non-ventilated (TENV) or totally enclosed fan-cooled electrical machine working at low speed or close to the stall, the natural convection heat transfer is dominating the cooling phenomenon [17]. In this manner, generally, the thermal resistance from the housing of the electrical machine to the ambient is the largest thermal resistance from the stator winding to the ambient [17]. Accordingly, determining this thermal resistance with higher accuracy leads to an increase in the accuracy of the thermal model network to predict the temperature of the key components of an electrical machine. The mentioned thermal resistance is defined as:

$$R_0 = \frac{1}{S_T h_0}, \quad (3.47)$$

where  $S_T$  is the machine-housing area [ $\text{m}^2$ ] and  $h_0$  is the heat transfer coefficient from the housing to the ambient, which consists of the effect of the radiation and the natural convection phenomena [ $\text{W}/(\text{m}^2\text{K})$ ].

Determining  $h_0$  is a challenging task, especially for TEFC machines, which consist of complex shapes of the machine housing. In addition, the fins structure is not constructed for the natural convection purpose to provide effective natural cooling [39], [38]. To overcome the complex shape of the TEFC housing, the area-based composite correlations method is used to calculate the natural convection coefficient [17], [39]. Accordingly, the machine's housing is divided into several basic shapes with known empirical correlation to calculate the natural convection coefficient, and finally, the total amount of the natural convection heat transfer coefficient is calculated according to the average area occupied by each shape [8]. A positive aspect of using this method is that the total natural convection coefficient is more similar to the natural convection coefficient of the shape, which is dominated by the housing of the electrical machine surface [17].

### 2. Forced convection

There are different ways to determine the forced convection coefficient from the semi-open fin housing of the TEFC electrical machine, e.g., CFD, flow network analysis and empirical correlation [17]. Since the estimation of the forced convection coefficient by using the CFD and flow network analysis is a complex process, consisting of sophisticated computing, an empirical correlation is used to compute the forced convection coefficient. The common empirical correlation to calculate the amount of the forced convection coefficient from the semi-open fin housing was presented by Heiles [8]. This correlation is developed based on different experiments on the actual housing of induction motors. He used some hypothesis to develop his correlation. Based on his assumption, the airflow is always in a turbulent mode [8]. The correlation is defined as:

$$h = \frac{\rho c_p D_h v}{4L} (1 - e^{-m}), \quad (3.48)$$

$$m = 0.1448 \frac{L_f^{0.946}}{D_h^{1.16}} \left( \frac{k}{\rho c_p v} \right)^{0.214}, \quad (3.49)$$

where  $D_h$  is the hydraulic diameter [m],  $v$  is the air cooling speed [m/s], and  $L_f$  is the axial length of the fin channel [m]. According to Heiles's suggestion, the amount of the convection coefficient, which is calculated from (3.35), should multiply to a correction factor between 1.7 to 1.9 [8].

**Convection thermal resistance between the stator end windings and the inner air ( $R_8$ ):**  $R_8$  presents the thermal path from the end winding to the inner air by the convection and is calculated as:

$$R_8 = \frac{1}{A_{ew}h_{ew}}, \quad (3.50)$$

where  $A_{ew}$  is the total surface of the end winding in contact with the inner air [m<sup>2</sup>] and  $h_{ew}$  is the convection coefficient between the end windings and the inner air [W/(m<sup>2</sup>K)].

Since the inner section of the end winding is in contact with the inner air;  $A_{ew}$  is calculated as:

$$A_{ew} = (L_{ec} - L_s)2\pi r_{is}, \quad (3.51)$$

There are several different empirical correlations to calculate the convection coefficient of the end winding to the end region of the machine. According to [52], the best correlation that is in good agreement with the experimental results is :

$$h_{ew} = 41.4 + 6.6 v, \quad (3.52)$$

where  $v$  is defined as:

$$v = r_{or}\omega\eta, \quad (3.53)$$

where  $r_{or}$  is the outer radius of the rotor [m],  $\omega$  is the rotor angular speed [rad/s], and  $\eta$  is the fan efficiency and in most of the cases equals 0.5.

**Convection thermal resistance between the inner air and the end cap ( $R_9$ ):**

$R_9$  presents the thermal convection resistance between the inner air and the end cap and is evaluated as in [20] :

$$R_9 = \frac{1}{A_{ec}h_{ec}}, \quad (3.54)$$

where  $A_{ec}$  is the external area of the end cap [m<sup>2</sup>] and  $h_{ec}$  is the heat transfer coefficient between the inner air and the end cap [W/(m<sup>2</sup>K)] and equals the value of  $h_{ew}$ .

The motor consists of the two end caps, and for a simpler calculation, these parts are assumed to be circular. Accordingly,  $A_{ec}$  is defined as [20]:

$$A_{ec} = 2\pi(ros + t_h), \quad (3.55)$$

where  $t_h$  is the thickness of the motor housing [m].

**Convection thermal resistance of the air gap ( $R_{10}$ ):**

To model the heat transfer in the air gap of the motor by the LPTN, the traditional empirical correlation based on the Taylor number (Ta) is implemented as [39]:

$$Ta = Re \sqrt{\frac{l_g}{r_{or}}}, \quad (3.56)$$

where  $l_g$  is the radial thickness of the air gap [m].

The flow condition in the air gap (laminar or turbulent) and the Nusselt number are evaluated according to the range of the Taylor number (Ta) as [39]:

$$\begin{cases} Nu = 2 & Ta < 41 & \text{laminar mode} \\ Nu = 0.212 Ta^{0.63} Pr^{0.27} & 41 \leq Ta \leq 100 & \text{vortex mode} \\ Nu = 0.386 Ta^{0.5} Pr^{0.27} & Ta > 100 & \text{turbulent mode} \end{cases} \quad (3.57)$$

According to several experiments on different induction machines in the range of 4 [kW] to 55 [kW], the value of the  $T_a$  is always located in the laminar mode; also in this study, the value of  $T_a$  is located in the same mode [20]. In this condition, the heat transfer in the air gap occurs by the conduction phenomenon, and  $R_{10}$  is calculated as [20]:

$$R_{10} = \frac{\ln\left(\frac{r_{is}}{r_{or}}\right)}{2\pi k_{air} L_s}. \quad (3.58)$$

### 3.4 Hybrid thermal model

An electrical machine can be modeled with the FEA in a 2D or 3D approach [62]. Modeling the electrical machine by the 3D FEA is a very time-consuming process, consisting of several complex geometry setups, e.g., end-windings. Accordingly, to reduce the computation time and use the benefits of the FEA for monitoring the thermal behavior of the electrical machine, the 2D FEA is usually implemented. Many studies focus on the thermal modeling of electrical machines by 2D FEA [18], [62], [63], [64], [65] and [66] among others. However, there are some problems in the 2D FEA thermal models of electrical machines. For example, in [63], the author neglected the axial heat flow from the end-winding to the active part of the machine, and in [64], a 2D FEA is presented where the results are compared with a simplified LPTN that does not include the end-winding thermal effect. Since they applied the simplified assumption to neglect the heat transfer from the end-windings to the slots, they could not model the hottest spot of the electrical machine, and the whole temperature distribution is underestimated. As a result, these models cannot provide a correct view of the heat transfer and thermal analysis for an electrical machine. To remedy this simplification, as well as use the advantages of the 2D FEA, a hybrid thermal model is proposed. This approach consists of coupling the 2D FEA with the equivalent thermal circuit. Such an approach is very common in the electromagnetic analysis of electrical machines, where the end-winding impedance is added in the winding circuit equations and coupled with the 2D field equations.

The coupling methodology can be divided into two types: direct and indirect coupling. The direct coupling method requires access to the 2D system matrix assembly routine to add the circuit terms and solve all the equations simultaneously. Although fast, it is not possible to implement the approach in a general purpose software unless one has access to the code. In this research project, the indirect approach was selected, as explained in the methods section. My focus is on the application of this method in the steady-state thermal analysis of a SynRM. The temperature of the active part of the machine is modeled using a 2D FEA simulation software, and the temperature effect of the end-winding region of the machine is evaluated by an LPTN. The two models are coupled through an iterative procedure. The next paragraph explains the idea in more detail.

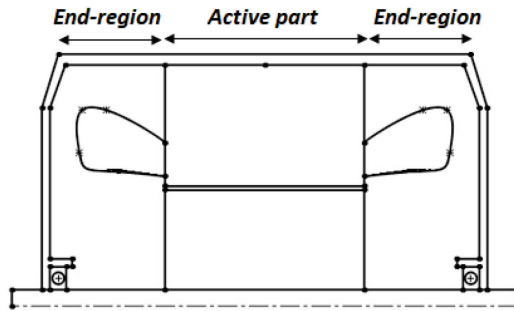


Figure 3.13. The axial cross-section of the electrical machine.

Figure 3.13 shows an illustration of the axial cross-section of an electrical machine. According to this figure, the construction of the electrical machine is divided into two main sections, the magnetic active part of the machine and the end-windings region. The 2D FEA can model only the heat transfer within the active part of the machine. It does not take into account the effect of heat transfer between the end-windings region and these active parts. One possibility to tackle this issue is to include the power losses in the end-windings in the slot losses while compiling the 2D model of the machine. However, this would result in an overestimation of the temperatures, as a part of the end-winding losses is flowing through the end-winding region and not transferred to the active parts. The proposed hybrid model is a better approach. According to figure 3.14, the hybrid thermal model is constructed by coupling the 2D FEA model of the active parts and the lumped parameters thermal network of the end-winding region.

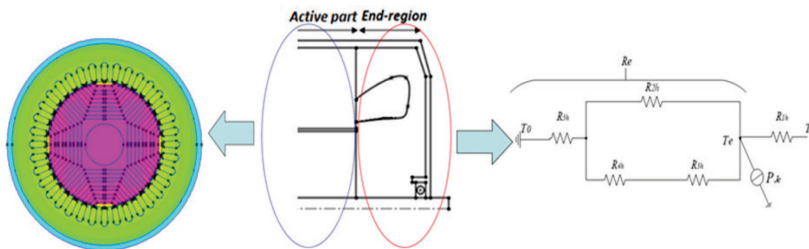


Figure 3.14. Construction of the hybrid thermal model.

### The FEA thermal model

In the hybrid thermal calculation method, the active parts of the machine are modeled by using a 2D FEA software. To model the heat transfer of the active part of the machine, the FEMM software was selected. This software has some advantages, e.g., free license software with a Matlab toolbox called OctaveFEMM to provide for operating the FEMM solver via Matlab functions [67]. This was a very important point in my selection, as the LPTN is also constructed in Matlab; thus, it is easy to operate and couple the two models from the same software.

### LPTN of the end-winding

To implement the effects of the end-windings on the total heat transfer of the machine and predict the temperature of its different parts, the LPTN of the end winding was developed in parallel to the 2D FE model. Figure 3.15 shows the steady-state LPTN of the end winding. This model consists of two nodes, five thermal resistances, and one loss source, which capture all the key thermal parameters and temperature rise as well as the main thermal heat transfer paths in the end regions of the machine.

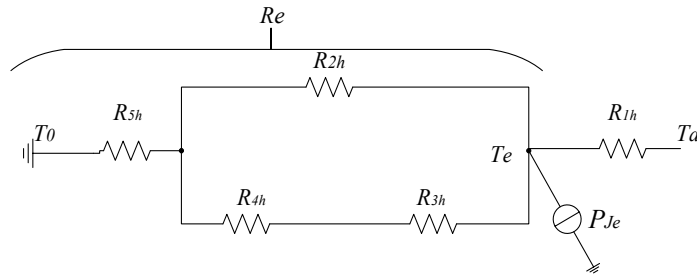


Figure 3.15. LPTN of the end winding.

The variables in the LPTN of figure 3.15 are  $T_a$  and  $T_e$ , which represent the average temperatures of the slots and the end windings respectively. Table 3.7 describes the definition of the thermal model components of the above LPTN. Accordingly,  $R_{1h}$  provides the axial conduction paths from the end winding to the active part of the slot and couples the 2D FE model with the LPTN of the end region of the machine.  $R_{2h}$  models the heat transfer by the conduction from the top side of the end windings to the machine housing. Also,  $R_{3h}$  and  $R_{4h}$  model the heat transfer by the convection mechanism to the inner air region in the end part of the machine; finally, the heat is extracted to the ambient by the convection using  $R_{5h}$ . The calculation methods of the components of the LPTN of the machine's end regions are described in detail in papers [I] and [III].

Table 3.7. Definition of thermal model components

Component	Description
$R_{1h}$	Conduction thermal resistance between the midpoint of the end-winding and the midpoint of coil side
$R_{2h}$	Conduction thermal resistance between the stator winding and the frame
$R_{3h}$	Convection thermal resistances between the stator end-winding and inner air of the end region
$R_{4h}$	Convection thermal resistance between the inner air and the end cap
$R_{5h}$	Total heat extraction thermal resistance from the frame to the ambient
$P_{Je}$	Stator end-winding Joule losses

### 3.5 Determination of the components of the hybrid model

#### FEA parameters

The main challenges with the FEA are how to define the thermal conductivity of the composite materials inside the slots such as the copper conductors, the conductor insulation, the impregnation material and the slot insulation; and how to implement the convection and radiation phenomena.

The slot area consists of different materials with different thermal conductivities. Due to the small dimensions of the materials layer in the slot, it is not practical to model each material separately. To solve this problem, an equivalent thermal conductivity of the slot area  $k_e$  is defined as in [4] :

$$k_e = k_2 \frac{(1+f_1)k_{cu}+(1-f_1)k_{ins}}{(1-f_1)k_{cu}+(1+f_1)k_{ins}}, \quad (3.59)$$

where  $f_1$  is the volume fraction of the conductor in the slot and  $f_2$  is the volume fraction of the impregnation in the slot (with  $f_1+f_2=1$ ). The other insulation materials are assumed equivalent to the impregnation material, which is a well-justified assumption, as explained in [4].

The heat is transferred from the exterior surface of the electrical machine to the ambient by the convection and radiation. These phenomena are implemented into the 2D FE model by defining the boundary condition on the outer surface of the model to describe the quality of the heat transfer from the outer surface of the machine to the ambient. In an actual machine, the outer surface consists of axial cooling fins, which can be modeled in the FEA analysis but this will result in a very dense mesh and thus very slow computations. According to figure 3.16, to reduce the model size, a modified smooth outer surface is used, and the effect of the cooling fins is accounted for through an equivalent heat transfer coefficient  $h'$ , which is calculated as in [66]:

$$h' = \frac{A_{act}}{A'_{act}} h, \quad (3.60)$$

where  $h$  is the actual heat transfer coefficient,  $A_{act}$  is the actual outer surface of the active part of the machine including the fins [ $m^2$ ] and  $A'_{act}$  is the simplified outer surface [ $m^2$ ].

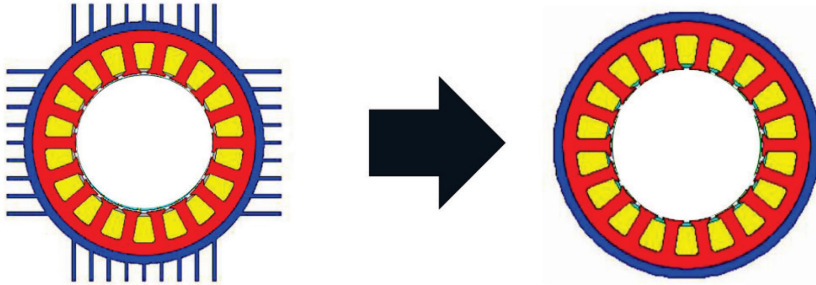


Figure 3.16. Simplified assumption to define the boundary layer in the 2D FE model.

### LPTN of the end winding

The parameters of the LPTN of the end windings are calculated by using the same formula presented in the LPTN parameters calculation in section 3.3 and are not described here

## 3.6 Computation of power losses

The losses in an electrical machine appear in the form of heat and cause an increase in the temperature of various parts of an electrical machine. Therefore, the amount of heat generated in the electrical machine depends on the amount of power losses. Accordingly, the accurate evaluation of power losses of the prototype under study plays an important role in the accuracy of the LPTN and the FEA to predict the final temperature of machine components. As figure 3.17 shows, the power losses in the SynRM are composed of:

- resistive losses in the stator windings
- iron losses
- mechanical losses



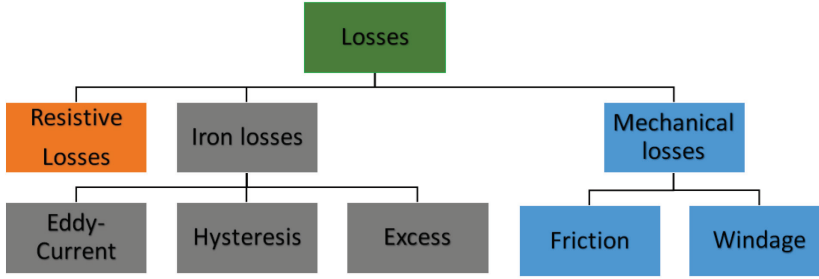


Figure 3.17. Power losses in a SynRM.

### 3.6.1 Resistive losses

Resistive losses or winding copper losses ( $P_{cu}$ ) are the major sources of losses in a SynRM. These types of losses are the function of the current ( $I$ ) and winding resistance ( $R$ ) and for  $m$  phase machine are calculated as in [13]:

$$P_{cu} = m RI^2, \quad (3.61)$$

Further, the resistance of each phase is calculated as in [13]:

$$R = k_R \rho_e \frac{2Nl_{av}}{A_c}, \quad (3.62)$$

where  $k_R$  is the skin effect factor for the resistance equation,  $\rho_e$  the electrical resistivity of the conductor material [ $\Omega \cdot m$ ],  $N$  the number of turns and  $A_c$  the cross section area of the conductor [ $m^2$ ].

The average length of the half turn  $l_{av}$  is calculated as [21]:

$$l_{av} = L_s + 1.2\tau_p + l', \quad (3.63)$$

where  $\tau_p$  is the pole pitch [ $m$ ] and  $l'$  is an empirically determined constant [ $m$ ], depending on the size of the machine.

The winding copper losses are temperature dependent and their value increases by increasing the temperature [68]. The reason for the variability of these losses by temperature is due to the temperature dependency of the electrical resistivity of the conductor material. The value of the electrical resistivity of the material with the temperature is evaluated as in [68]:

$$\rho_e = \rho_{e0}(1 + \alpha_e \Delta T), \quad (3.64)$$

where  $\rho_{e0}$  is the electrical resistivity of the conductor material at reference temperature  $T=20$  [ $^{\circ}C$ ], and  $\alpha_e$  is the temperature coefficient of the electrical resistivity. As an example for the copper conductor  $\rho_{e0}=1.724 \times 10^{-8}$  [ $\Omega m$ ] and  $\alpha_e = 0.00393$  [ $K^{-1}$ ]. Accordingly, if the temperature increases to 50 [ $^{\circ}C$ ] or 140 [ $^{\circ}C$ ] the value of the resistance increases respectively 20% or 50% [3].

### 3.6.2 Iron losses

The iron losses occur due to the magnetic field and include the hysteresis (static) losses and eddy current (dynamic) losses [3]. Iron losses have been considered for several decades and still have not reached a definitive conclusion [3]. The accurate calculation of the iron loss is the key point for the optimization and development of the electrical motors for high-speed application as these motors can operate up to high frequency in

the range of 500 Hz [69]. Further, the power electronic devices such as electrical machine drives and frequency converters are applied to supply the electrical motors, which leads to the higher value of losses in the electrical machine due to non-sinusoidal (pulse width modulator) voltage waveform [3].

Figure 3.18 provides an overview of the different approaches to evaluate the iron losses in the electrical machine.

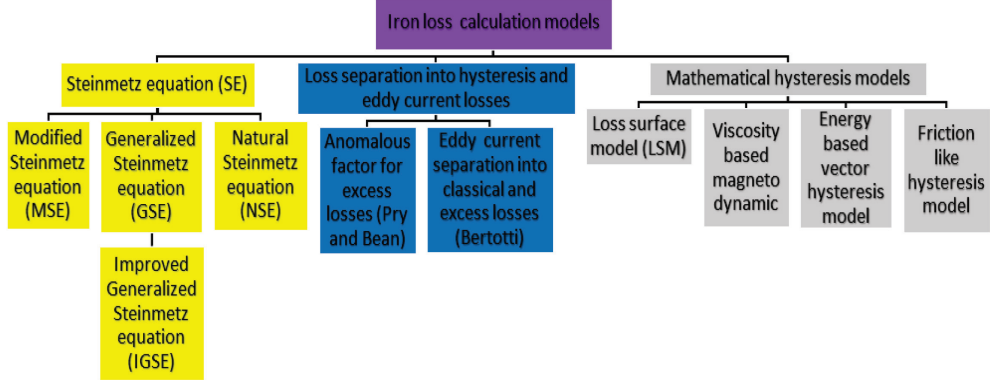


Figure 3.18. Different existing models for determining the iron losses in an electrical machine [70] and [71].

The first empirical correlation to model the iron loss was introduced by Steinmetz in 1894 [71]. According to his model, the core loss has an exponential function and depends on the peak flux density and frequency [70] and [71]. However, one of the best approaches to calculate the iron losses has been presented by a physical based model, called the segregation model [3]. Accordingly, the iron loss is segregated to static (hysteresis) and dynamic (eddy current) losses [3]. Further, Bertotti improved this model by adding the term called excess loss component into the original formula as follows [69]:

$$P_{Fe} = P_{hyst} + P_{ec} + P_{exc} = k_{hyst} f \hat{B}^2 + k_{ec} f^2 \hat{B}^2 + k_{exc} f^{1.5} \hat{B}^{1.5}, \quad (3.65)$$

where  $P_{Fe}$  is the total iron loss [W/kg],  $P_{hyst}$  is the hysteresis loss [W/kg],  $P_{ec}$  is the dynamic eddy current loss [W/kg],  $P_{exc}$  is the excess loss [W/kg],  $f$  is the frequency [Hz], and  $\hat{B}$  is the peak flux density [Tesla].  $k_{hyst}$ ,  $k_{ed}$  and  $k_{exc}$  are the hysteresis coefficient, eddy current coefficient and excess losses coefficient respectively. These coefficients are usually obtained from the measurements at a given frequency and the peak value of a unidirectional sinusoidal flux density [72].

This equation is valid for a sinusoidal variation of  $B$  and can calculate the iron losses for one frequency only. There are several extensions of this equation for the distorted waveforms; the most popular is to develop the flux density waveform into the Fourier series and apply the equation to each harmonic separately. The same principle can also be used with the two components method used in this thesis. The FEM software uses the frequency separation method to compute the iron losses in the electrical machine from the time stepping electromagnetic simulations. Accordingly, the software divides the machine surface into the small size mesh elements and applies the Fourier Transformation (FT) to determine the flux density related to each frequency [70]. After the FT, all the Fourier components of the magnetic flux density are calculated at the element level [73]. Finally, the value of the eddy current losses and hysteresis losses are integrated over the whole iron core respectively as in [73]:

$$P_{ec} = \int [\sum_{n=1}^{N_h} C_{En}(n\omega_s) B_n^2] dV, \quad (3.66)$$

$$P_{hyst} = \int [\sum_{n=1}^{N_h} C_{Hn} (n\omega_s)^2 B_n^2] dV, \quad (3.67)$$

where  $B_n$  is the magnetic flux density at the frequency order  $n$  after FT,  $N_h$  is the number of harmonics taken into account,  $\omega_s$  is the angular frequency of the supply [rad/s] and  $C_{En}$  and  $C_{Hn}$  are the loss coefficients related to eddy current and hysteresis respectively. The integration is carried out over the elements that belong to the iron core.

### 3.6.3 Mechanical losses

The mechanical losses contain the bearing friction losses and the windage losses [13]. These types of losses have not been widely addressed in the thermal design and analysis of electric machines [68]. Whereas these losses have the complex mechanism and there are no reliable computation approaches, they have been neglected or evaluated by some empirical correlations (based on the experiment) in most of relevant sources [68].

There are different bearings used in the electrical machine, e.g., ball bearing, magnet bearing and air bearings [68]. The ball bearing is used in the construction of the machine under study. Therefore, this section mainly describes the losses and empirical correlations for this specific type.

The bearing losses have a direct relation with the shaft speed, bearing types, the property of lubricant and the load on the bearing [13]. One of the most used empirical correlations to compute these losses was presented by SKF in 1994 as [13]:

$$P_{Bearing} = 0.5 \omega_r \mu_b F_b D_b, \quad (3.68)$$

where  $\omega_r$  is the angular frequency of the shaft [rad/s] supported by a bearing,  $\mu_b$  is the friction coefficient in the range of 0.001 to 0.005,  $F_b$  is the bearing load, and  $D_b$  is the inner diameter of bearing.

The windage losses are directly proportional to the rotational speed of the machine, which are more significant in the high-speed machine [13]. These losses result from friction between the surface of the rotational section of the rotor and the air around it [13]. There are several semi-empirical correlations with different accuracy to calculate these losses [13], [68], [74]. For a normal speed machine, the windage and ventilator losses are evaluated by the Schuisky empirical correlation as follows [13]:

$$P_p = k_p D_r (l_r + 0.6\tau_p) v_r^2, \quad (3.69)$$

where  $k_p$  is an experimental factor (Table 3.8),  $D_r$  is the rotor diameter,  $l_r$  is the rotor length,  $\tau_p$  is the pole pitch, and  $v_r$  is the surface speed of the rotor.

Table 3.8. The value of  $k_p$  for the calculation of windage losses

Cooling method	$k_p$
TEFC motors (small and medium-size machines)	15
Open-circuit cooling (small and medium-size machines)	10
Large machines	8
Air-cooled turbogenerators	5

## 3.7 Steady-state thermal analysis of LPTN

For the steady-state thermal analysis, the final nodal temperatures of the LPTN can be calculated by the matrix inversion theory. Accordingly, the nodal temperatures of the proposed thermal model are calculated as follows:

$$[T] = [G]^{-1}[P], \quad (3.70)$$

where  $[T]$  is the temperature column vector,  $[P]$  is the power column vector, which contains the losses at each node, and  $[G]$  is the thermal conductance square matrix defined as:

$$G = \begin{bmatrix} \sum_{i=1}^n \frac{1}{R_{1,i}} & -\frac{1}{R_{1,2}} & \cdots & -\frac{1}{R_{1,n}} \\ -\frac{1}{R_{2,1}} & \sum_{i=1}^n \frac{1}{R_{2,i}} & \cdots & -\frac{1}{R_{2,n}} \\ \vdots & \vdots & \ddots & \vdots \\ -\frac{1}{R_{n,1}} & -\frac{1}{R_{n,1}} & \cdots & \sum_{i=1}^n \frac{1}{R_{n,i}} \end{bmatrix}, \quad (3.71)$$

The  $G_{i,i}$  components in the main diagonal of the thermal conductance matrix are defined as the sum of the conductances connected to the  $i^{\text{th}}$  node and  $G_{i,j}$  is defined as the negative thermal conductances between nodes  $i$  and  $j$ .

### 3.8 Hybrid model analysis

In the hybrid thermal method, the temperature distribution and the heat transfer are modeled by the LPTN of the end region. The thermal network of the end region presented in figure 3.15 is further simplified, as shown in figure 3.19, by combining the thermal resistances  $R_{2h}$  to  $R_{5h}$  in a single equivalent resistance  $R_e$  as:

$$R_e = \frac{(R_{4h} + R_{3h})R_{2h}}{R_{2h} + R_{3h} + R_{4h}} + R_{5h}. \quad (3.72)$$

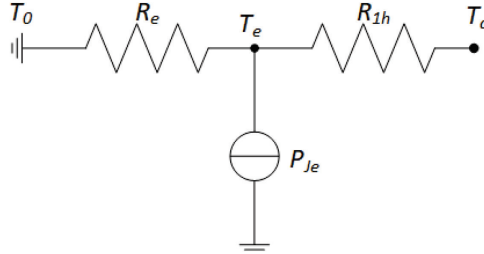


Figure 3.19. The final equivalent thermal circuit after lumping  $R_{2h}$  to  $R_{5h}$  into  $R_e$ .

The end-windings and slot copper loss are evaluated from the total copper loss based on the length of the copper conductors in the slots and the end-windings. The temperature of the end-windings  $T_e$  and the amount of heat transfer from the end-windings to slots  $P_{ex}$  are evaluated by applying the Kirchhoff current rule as follows:

$$T_e = \left( P_{Je} + \frac{T_0}{R_e} + \frac{T_a}{R_{1h}} \right) (R_{1h} + R_e), \quad (3.73)$$

$$P_{ex} = \frac{T_e - T_a}{R_{1h}}. \quad (3.74)$$

where the temperature of the active parts  $T_a$  is evaluated by the FEA and  $P_{ex}$  is the amount of losses added to the slot losses in the FEA at each iteration. Note that  $P_{ex}$  can be negative in some cases.

Figure 3.20 shows the flowchart of the hybrid model calculation. After the construction of the FE model and the definition of the materials, the copper losses are inserted in the model. In the first iteration step, the FEA calculates the temperature of the active part of the machine and predicts the average value of the slot temperature  $T_a$ .  $T_e$  and  $P_{ex}$  are then calculated by (3.73) and (3.74) respectively. In the next iteration,  $P_{ex}$  is added to the active copper losses in the FE model. This iteration process will

continue until the difference between the previous  $T_e$  and the new one is smaller than an arbitrary defined accuracy  $\varepsilon$ , which was 0.01 [K] in our case.

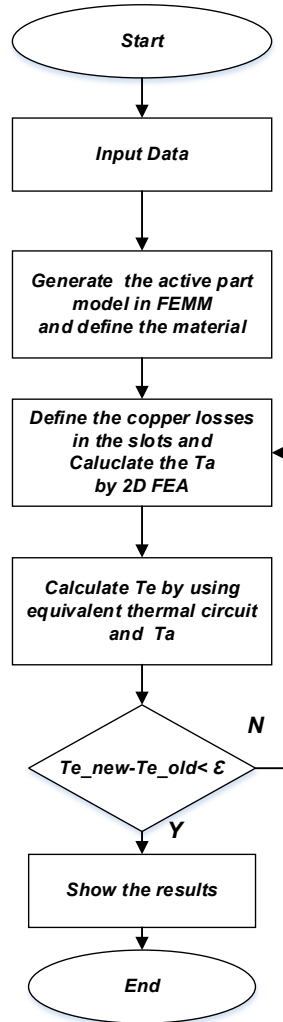


Figure 3.20. The flow chart of the hybrid model calculation.

### 3.9 Summary of Chapter 3

The principles of lumped parameter thermal networks and hybrid thermal models of the SynRM were presented in this chapter. Different empirical correlations to calculate the convection coefficients from several basic shapes in different directions during the natural and air forced cooling were considered. The area-based composite correlations method to determine the natural and forced convection coefficients from the machine-housing surface is presented in detail.

The simplified method to calculate the radiation coefficient from the complex surface of TEFC machine is described. Well-proven formulations were employed to calculate the critical parameters of the LPTN. The different sources of losses in this machine type were addressed.

## 4 Analytical and Numerical Results

The analytical and numerical analyses are presented in this chapter. This chapter describes the results obtained. A more comprehensive explanation of the analytical and numerical results and their analysis can be found in papers [I] to [VII]

### 4.1 Analytical data of convection from different basic shapes

Figure 4.1 shows the actual shape of the coil module used in the analytical calculations to investigate the convection coefficient from basic shapes. This coil module consists of six different faces. In this study, two sides with the largest cross-section areas with and without fins are used to consider the convection coefficient from flat plate and fin surface in different directions. The width of the coils module is  $W=222$  [mm] and its length  $L_{coil}=419$  [mm]. The fin side is divided into two sections: the fin section and the flat plate surface. The fin side of the module consists of two fins spaced by  $S=86$  [mm]. The fin's height is  $H=62.7$  [mm], its thickness is  $D_{fin}=10$  [mm], and its length is  $L_{fin}=265$  [mm]. The width of the L-shaped plate on top of the fin is  $W_L=38$  [mm].

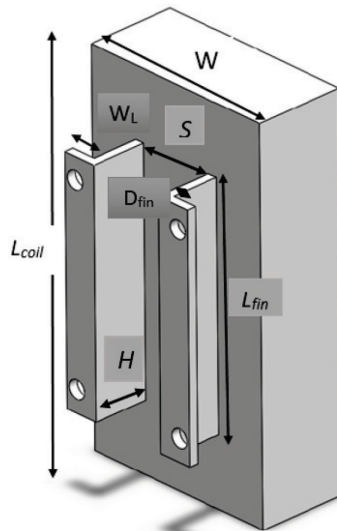


Figure 4.1. Illustration of the actual coil module setup.

#### Natural convection from the flat plate

The natural convection coefficient over the flat surface was calculated using correlations presented in paper [V] for both the horizontal upper side and the vertical orientations respectively.

##### 1. Horizontal flat plate

Table 4.1 shows theoretical results based on the empirical correlations. According to Table 4.1, by increasing the surface temperature, the amount of the convection heat transfer starts to increase by increasing the temperature.

Table 4 .1. Analytical results for the horizontal flat plate

$l$ [A]	$T_s$ [°C]	$T_a$ [°C]	$h_e$ [W/(m <sup>2</sup> K)]	$h_r$ [W/(m <sup>2</sup> K)]	$h_c$ [W/(m <sup>2</sup> K)]
10	40	23	9.22	3.53	5.37
12	46.6	23	9.78	3.63	5.80
15	60.3	23	10.70	3.73	6.44
17	71.6	24	11.30	3.83	6.79
18	77.3	24	11.58	4.03	6.94

## 2. Vertical flat plate

Tables 4.2, 4.3, and 4.4 show the analytical data for the vertical case for the calculation of the natural convection coefficients based on Mac Adams, Churchill I and II empirical correlations respectively.

Table 4 .2. Analytical results for the vertical flat plate based on Mac Adams correlation

$l$ [A]	$T_s$ [°C]	$T_a$ [°C]	$h_e$ [W/(m <sup>2</sup> K)]	$h_r$ [W/(m <sup>2</sup> K)]	$h_c$ [W/(m <sup>2</sup> K)]
10	42.3	24	8.42	3.91	4.45
12	49.6	24	8.90	4.05	4.86
15	62.4	24	9.67	4.32	5.35
17	74.3	24	10.25	4.58	5.67
18	81.0	25	10.54	4.75	5.79

Table 4.3. Analytical results for the vertical flat plate based on Churchill I correlation

$l$ (A)	$T_s$ [°C]	$T_a$ [°C]	$h_e$ [W/(m <sup>2</sup> K)]	$h_r$ [W/(m <sup>2</sup> K)]	$h_c$ [W/(m <sup>2</sup> K)]
10	42.3	24	8.22	3.91	4.31
12	49.6	24	8.76	4.05	4.71
15	62.4	24	9.55	4.32	5.23
17	74.3	24	10.16	4.58	5.58
18	81.0	25	10.45	4.75	5.70

Table 4 .4. Analytical results for the vertical flat plate based on Churchill II correlation

$l$ [A]	$T_s$ [°C]	$T_a$ [°C]	$h_e$ [W/(m <sup>2</sup> K)]	$h_r$ [W/(m <sup>2</sup> K)]	$h_c$ [W/(m <sup>2</sup> K)]
10	42.3	24	8.17	3.91	4.26
12	49.6	24	8.66	4.05	4.60
15	62.4	24	9.36	4.32	5.04
17	74.3	24	9.92	4.58	5.34
18	81.0	25	10.20	4.75	5.45

### Natural convection from rectangular isothermal fins

Figure 4.2 shows the modified shape used in the theoretical calculations. It should be noted that the actual setup consists of L-shaped fins. However, the upper part of the fin is for mechanical support only. The effect of this part on the heat convection coefficient was estimated through 2D finite element computations. It turns out that this part participated in the heat transfer, as it dissipated 13.8% of the total heat on average, resulting in a temperature difference of 3.7%. Therefore, this shape was replaced in the experimental calculations by an equivalent increased length of the fins, so that the same amount of heat is dissipated through the additional length. However, this change in the length affected very little the calculation of the heat transfer coefficient (less than 1% difference, which is lower than the measurement uncertainty).

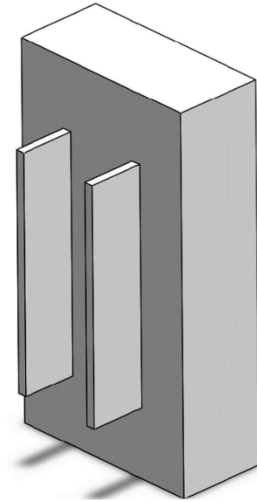


Figure 4.2. The simplified format of the coil module.

The actual fin is divided into two sections: the fin section and the flat plate surface. Therefore, the convection coefficient for each section is calculated separately and finally, the equivalent convection coefficient was calculated according to the area of each section as follows:

$$h_c = \frac{h_{fin} \cdot A_{fin} + h_{plate} \cdot A_{plate}}{A_T}, \quad (4.1)$$

where  $h_{fin}$  [W/(m<sup>2</sup>K)] is the convection coefficient from fin section,  $h_{plate}$  [W/(m<sup>2</sup>K)] is the convection coefficient from the flat section,  $A_{fin}$  [m<sup>2</sup>] is the surface area of the fin sections, and  $A_{plate}$  [m<sup>2</sup>] is the surface area of the flat plate.  $A_T$  [m<sup>2</sup>] is the total surface area.

#### 1. Rectangular isothermal fins on the horizontal surface

Tables 4.5 and 4.6 show the analytical data for the horizontal case for which the natural convection coefficients for the fin section were calculated based on Jones and Tari empirical correlations respectively presented in paper [11]. According to the tables, by increasing the temperature, the amount of the convection and radiation coefficient started to increase. However, the value of the radiation coefficient slightly increased, as the temperature difference was not high.



Table 4.5. Analytical results for the horizontal orientation based on the Jones empirical correlation

$l$ [A]	$T_s$ [°C]	$T_a$ [°C]	$h_e$ [W/(m <sup>2</sup> K)]	$h_r$ [W/(m <sup>2</sup> K)]	$h_c$ [W/(m <sup>2</sup> K)]
10	27.7	18.2	8.87	3.53	5.34
12	32.4	18.9	9.47	3.63	5.84
15	38.6	18.2	10.16	3.73	6.43
17	43.9	18.3	10.66	3.83	6.83
20	53.4	19	11.36	4.03	7.33

Table 4.6. Analytical results for the horizontal orientation based on the Tari empirical correlation

$l$ [A]	$T_s$ [°C]	$T_a$ [°C]	$h_e$ [W/(m <sup>2</sup> K)]	$h_r$ [W/(m <sup>2</sup> K)]	$h_c$ [W/(m <sup>2</sup> K)]
10	27.7	18.2	10.07	3.53	6.54
12	32.4	18.9	11.02	3.63	7.39
15	38.6	18.2	12.15	3.73	8.42
17	43.9	18.3	12.96	3.83	9.13
20	53.4	19	14.05	4.03	10.03

## 2. Rectangular isothermal fins on the vertical surface

Tables 4.7 and 4.8 show the analytical data for the vertical case for which the natural convection coefficients  $h_1$  for the fin section were calculated based on Van De Pol and Tari respectively.

Table 4.7. Analytical results for the vertical orientation based on the Van De Pol correlation

$l$ [A]	$T_s$ [°C]	$T_a$ [°C]	$h_e$ [W/(m <sup>2</sup> K)]	$h_r$ [W/(m <sup>2</sup> K)]	$h_c$ [W/(m <sup>2</sup> K)]
10	28.6	19	7.12	3.56	3.56
12	33.1	19.3	7.56	3.65	3.91
15	40.7	19.2	8.17	3.79	4.38
17	45.9	18.4	8.54	3.87	4.67
20	55.4	18.6	9.08	4.07	5.01

Table 4.8. Analytical results for the vertical orientation based on the Tari correlation

$l$ [A]	$T_s$ [°C]	$T_a$ [°C]	$h_e$ [W/(m <sup>2</sup> K)]	$h_r$ [W/(m <sup>2</sup> K)]	$h_c$ [W/(m <sup>2</sup> K)]
10	28.6	19	8.02	3.56	4.46
12	33.1	19.3	8.63	3.65	4.98
15	40.7	19.2	9.47	3.79	5.68
17	45.9	18.4	10.00	3.87	6.13
20	55.4	18.6	10.71	4.07	6.64

### Forced convection over the flat plate with an unheated starting part inside the wind tunnel

The objective of this section is to consider the effect of airflow speed over the flat plate on the estimation of the forced convection coefficient. More explanations can be found in paper [V].

For the analytical calculation, flat plate side of the coil module with an unheated starting part was located inside the wind tunnel; its boundary layers did not extend such as the free stream mode and the characteristic of the wind tunnel directly affects the fluid flow mode over the plate. Accordingly, the critical Reynold number for this case study was defined based on the critical Reynolds number in the internal flow. As a result, the fluid was in turbulent mode.

Table 4.9 shows the analytical calculation based on mentioned correlations for the forced convection coefficient over the flat plate with the unheated part in a combination of the external and internal forced convection mode. However, Table 4.10 shows the analytical result based on the external forced convection flow mode calculation.

Table 4.9. Analytical results based on the combination of external and internal forced convection

$v$ [m/s]	$T_s$ [°C]	$T_a$ [°C]	$h_e$ [W/(m <sup>2</sup> K)]	$h_r$ [W/(m <sup>2</sup> K)]	$h_c$ [W/(m <sup>2</sup> K)]
4.1	63	18.0	26.97	4.22	21.95
6.1	52	18.0	34.64	4.01	30.63
7.1	50	18.0	38.62	3.97	34.65
8.2	47	18.0	45.91	3.90	42.01
10.5	43	18.0	49.98	3.83	46.15

Table 4.10. Analytical results based on external convection flow mode boundary

$v$ [m/s]	$T_s$ [°C]	$T_a$ [°C]	$h_e$ [W/(m <sup>2</sup> K)]	$h_r$ [W/(m <sup>2</sup> K)]	$h_c$ [W/(m <sup>2</sup> K)]
4.1	63	18.0	18.16	4.22	13.94
6.1	52	18.0	21.08	4.01	17.07
7.1	50	18.0	22.39	3.97	18.42
8.2	47	18.0	23.72	3.90	19.82
10.5	43	18.0	25.37	3.83	22.45

## 4.2 Convection heat transfer from the housing surface of the TEFC machine

For this case study, the machine was installed in the horizontal direction. As the axial length of the fins, spaces between the fins and the height of the fins are different, the mean value of fins parameters for each side of the housing was calculated. Table 4.11 shows the characteristic data of the fin section of the machine housing at the axial length of 222.5 [mm] and a diameter of 230 [mm].

Table 4.11. Characteristic data of the fin section

	Mean fin's length [mm]	Mean fin's height [mm]	Mean fin's spacing [mm]	Number of fins
Fins on top of the housing	34.38	24.37	11.86	12
Fins on the underside of the housing	184.25	24.37	11.86	12
Fins on the sides of the housing	180.75	24.83	9.70	30

### 1. Natural cooling

According to the area-based composite method, machine housing is divided into several different basic shapes: the cylinder shape for the fin channel base, horizontal U-shape channel for fins on the top and underside of the housing and a horizontal flat plate with a hot plate on top or bottom for fins mounted on the side of the housing and the vertical flat plate to model the end cap of the housing.

Table 4.12 shows the segregation of the machine housing under study according to the area-based composite correlations method. Accordingly, the natural convection coefficient from each section was calculated by using the relevant empirical correlation for convection. The radiation coefficient was calculated by using the simplification assumption presented in Chapter 3.

Table 4.12. Segregation of the housing of the TEFC electrical machine

Component	Convection Correlation	Emissivity	View Factor	Area [m <sup>2</sup> ]
Fin base	Horizontal cylinder	0.8	1	0.0918
Fins on top of the housing	Horizontal fin channel	0.8	0	0.0201
Fins on undersides of the housing	Horizontal fin channel	0.8	0	0.1078
Fins on the sides of the housing	Horizontal flat plate (upper face and lower face)	0.8	0	0.2692
Fin tips	Horizontal and vertical flat plate	0.8	1	0.0209
End caps	Vertical flat plate	0.8	1	0.0831

After the calculation of the natural convection and the radiation coefficient of each segregated shape of the machine housing, the total heat transfer coefficient ( $h_0$ ) is calculated as:

$$h_0 = \frac{h_1 S_1 + h_2 S_2 + \dots}{S_T}, \quad (4.2)$$

where  $h_1$  is the heat transfer coefficient from basic shape one [W/ (m<sup>2</sup>K)],  $S_1$  is the area occupied by basic shape one [m<sup>2</sup>],  $h_2$  is the heat transfer coefficient from basic shape two [W/ (m<sup>2</sup>K)], and  $S_2$  is the area occupied by basic shape two [m<sup>2</sup>].

Table 4.13 shows the analytical calculation of the natural convection, radiation, and heat transfer coefficient.

Table 4.13. Analytical results

$V$ [V]	$I$ [A]	$T_s$ [°C]	$T_a$ [°C]	$h_o$ [W/(m <sup>2</sup> K)]
15	6.45	42	20.5	6.91
17	7.12	47	21.6	7.14
19	7.79	51.5	20.8	7.39
22	8.71	61	21.6	7.78
25	9.57	64.5	21.2	7.93

## 2. Air forced cooling

### A. Air cooling speed

According to (3.48), the only unknown parameter with the highest effect on the calculation of the forced convection coefficient is the airflow speed along the semi-open fin channels. To use the empirical correlation, accurate estimation of the speed of the cooling airflow in each fin is necessary. Accordingly, the amount of the speed of the cooling air is measured using a digital hot wire anemometer.

According to figure 4.3, to evaluate the mean speed of an air-cooling flow in the circumference of the machine housing, the air flow speed was measured in three different positions along the axial direction of the cooling fins: at the beginning, in the middle and at the end of the fins.

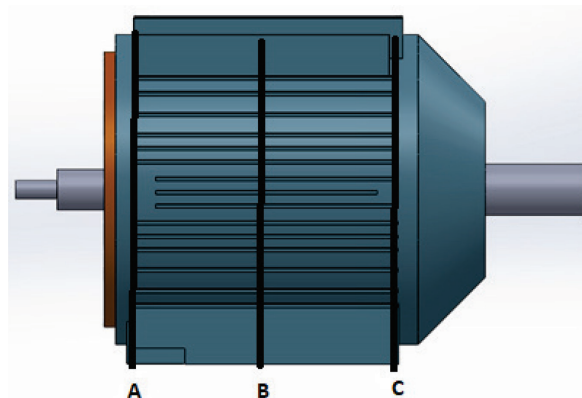


Figure 4.3. Different locations of the air-cooling speed measurement.

Figures 4.4 and 4.5 show the air-cooling speed for five different fan rotational speeds from 600 rpm to 1800 rpm. As expected and according to figure 4.5, by increasing the distance from the fan, the air-cooling speed starts to decrease due to the leakage. The average amount of the reduction in the air-cooling speed is around 0.4% of the inlet velocity.

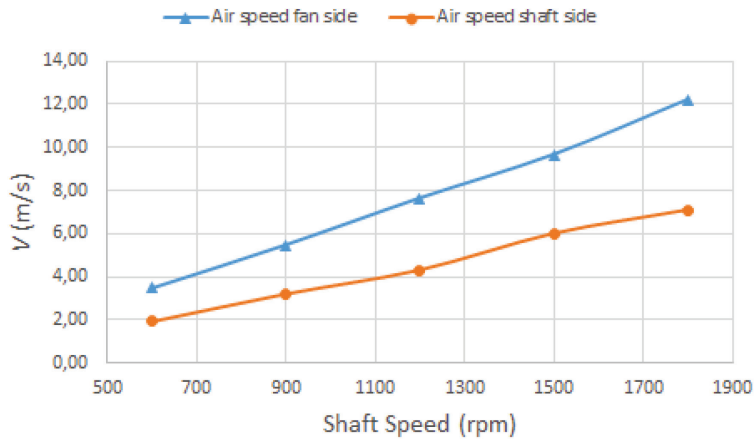


Figure 4.4. Air velocity along the axial direction versus the fan speed in the fan and shaft sides.

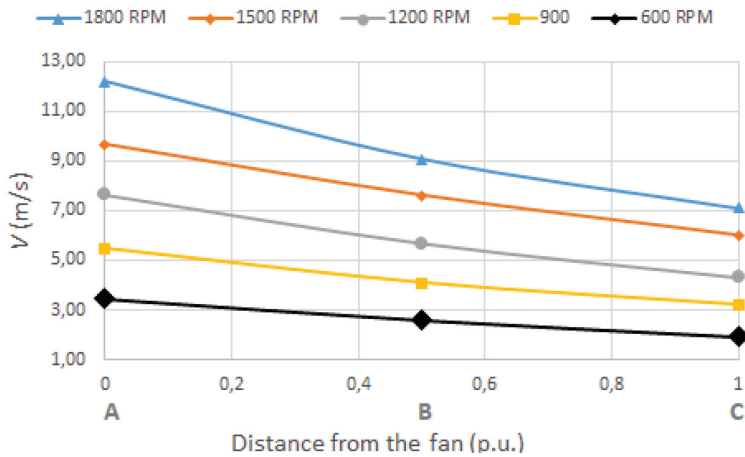


Figure 4.5. Air velocity along the axial direction versus the distance from the fan.

### B. Analytical calculation

To calculate the forced convection coefficient from the housing surface of the TEFC electrical machine by using the empirical correlations and applying the leakage effect on the air-cooling speed during the computation process, the housing of the machine is divided into three main sections: rear section near the fan, active part, and front section. Then, the amount of the force convection coefficient is calculated based on the appropriate empirical correlation. Furthermore, the amount of radiation is calculated by using the same method discussed in the previous chapter. Table 4.14 shows the segmentation of the machine housing and related empirical correlation for calculating the value of the forced convection coefficient and the radiation phenomenon.

Table 4.14. Segmentation of the housing of the TEFC for the forced convection coefficient

Component	Empirical Correlation	Air velocity [p.u]	Emissivity	View Factor	Area [m <sup>2</sup> ]
End cap (rear)	Flat plate	1	0.8	1	0.0415
Fins base (rear)	Fin channel	1	0.8	1	0.0128
Fin side (rear)	Horizontal fin channel	1	0.8	0	0.0585
Fin tips (rear)	Flat plate	1	0.8	1	0.0031
Fins base (active)	Fin channel	0.8	0.8	1	0.0908
Fin side (active)	Horizontal fin channel	0.8	0.8	0	0.4150
Fin tips (active)	Flat plate	0.8	0.8	1	0.0219
Fins base (front)	Fin channel	0.6	0.8	1	0.0128
Fin side (front)	Horizontal fin channel	0.6	0.8	0	0.0128
Fin tips (front)	Flat plate	0.6	0.8	1	0.0031
End cap (front)	Flat plate	0.5	0.8	1	0.0415

To apply the effect of fin blockage in the calculation of the forced convection coefficient, the blockage factor is defined based on the total number of fins ( $N_{total}$ ) and the number of block fins ( $N_{block}$ ) as in [39]:

$$\frac{N_{total} - N_{block}}{N_{total}}, \quad (4.3)$$

Finally, the amount of the total heat transfer coefficient is calculated by using (4.2).

Table 4.15 shows the analytical data of the total heat transfer coefficient from the housing of the TEFC electrical machine.

Table 4.15. Analytical data for the air forced cooling

Shaft speed [rpm]	Inlet speed [m/s]	$T_s$ [°C]	$T_a$ [°C]	$h_e$ [W/(m <sup>2</sup> K)]
600	3.5	32.3	22.3	20.3
900	5.5	29	21.2	27.9
1200	7.6	29.1	22.3	35.4
1500	9.7	28.4	22.2	41.9
1800	12.2	27.3	21.8	49.8

### 4.3 Experimental estimation of losses in SynRM

This section presents the measurement results of losses on the three-phase SynRM.

Copper losses are calculated from the value of the DC resistance of the stator windings [13]. The amount of stator winding resistance is measured by the DC resistance test at a specified temperature [13]. For these purposes, the amount of the stator winding resistance of each phase was measured by performing the DC test. Accordingly, the DC current was applied to the stator windings of each phase separately, and the voltage and current of the stator winding of each phase were measured (figure 4.6). This process continued for several different currents in the range of 1 to 2.5 [A] by step of 0.5 [A]. Then the value of the resistance of the stator winding was simply calculated by using the

Ohm's law. Finally, the winding resistance will be equal to the average value of the resistances calculated by Ohm's law in different input currents.

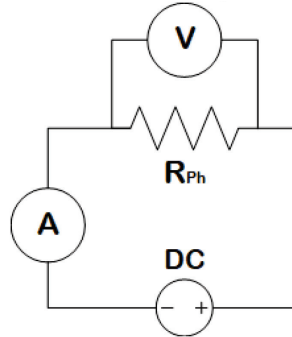


Figure 4.6. The schematic of measuring the phase resistance of the stator winding.

Table 4.16 shows the average value of the resistance of each phase. Accordingly, the value of resistance is 0.665 Ω.

Table 4.16. The value of the resistance of each phase

Phase	$R_{ph}$ [Ω]
U	0.669
V	0.663
W	0.663

The no-load test is a common method for measuring the iron losses in an electrical machine. For this purpose, the electrical machine was operated in the rated voltage and frequency until it reached its thermal steady state mode (According to the standard when the temperature varies less than one Kelvin when measured during the two successive 60-minute intervals). Since the machine under study is the SynRM, it needs the external prime mover to accelerate the rotor of the motor to reach the synchronous speed. In this manner, it takes into account that the rotational direction of the rotor should be the same as the direction of rotating the magnetic field of the stator; in other words, the prime mover and the SynRM should have the same phase sequences. After the SynRM reaches the synchronous speed, simultaneously, the prime mover should be separated from the SynRM, and the rated voltage should be applied to it. According to figure 4.7, an induction machine is operated as the prime mover. It is coupled to the SynRM by a belt, and the frequency converter is controlling the speed of the induction machine.



Figure 4.7. No-load experiment.

After separating the prime mover from the SynRM, the motor operates with the rated voltage and frequency until its steady-state mode. When the motor reaches a thermal state of equilibrium, the measurement process is started. In this step, the measurement occurs based on the voltage step in the range of 20% to 110% of the rated voltage in the descending order. Accordingly, the values of three-phase stator currents, stator voltages, power factors, and the motor input power, as well as the stator windings temperature, were measured.

Since the machine operated in no-load, the mechanical power was zero; therefore, the total input power equals the total losses generated inside the machine. The amount of the stator winding losses was evaluated by using the measured value of the stator winding resistance and current by using (3.61). As mentioned, the winding resistance starts to increase by increasing the temperature; therefore, the new value of the slot winding resistance was determined as in [43]:

$$R_T = R_{T0} \frac{B+T_w}{B+T_{w0}}, \quad (4.4)$$

where  $R_T$  is the actual average electrical resistance of the stator winding [ $\Omega$ ],  $T_w$  is the average temperature of the winding [ $^{\circ}\text{C}$ ],  $T_{w0}$  is the initial temperature [ $^{\circ}\text{C}$ ],  $R_{T0}$  is the stator winding resistance in the reference temperature [ $\Omega$ ] and  $B$  is the reverse thermal coefficient of the electrical resistivity of copper at 0 [ $^{\circ}\text{C}$ ].



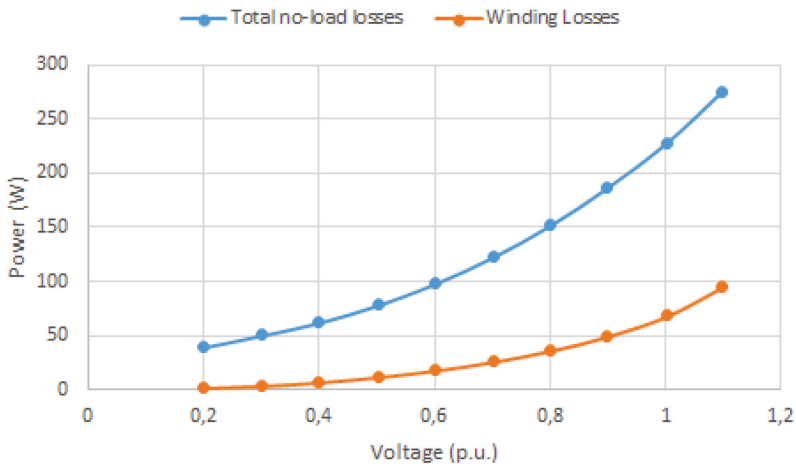


Figure 4.8. The measured value of the total input losses and winding losses vs. supply voltage.

Figure 4.8 shows the total input losses ( $P_0$ ) and the stator winding losses ( $P_{cu}$ ). As mentioned, the losses in SynRM consist of winding copper losses, iron losses, and mechanical losses. The sum of iron losses ( $P_{Fe}$ ) and mechanical losses ( $P_m$ ) is called constant losses ( $P_c$ ). According to (4.5), the value of the constant losses  $P_c$  is evaluated by subtracting the stator winding losses from the total input power.

$$P_c = P_{Fe} + P_m = P_0 - P_{cu} . \quad (4.5)$$

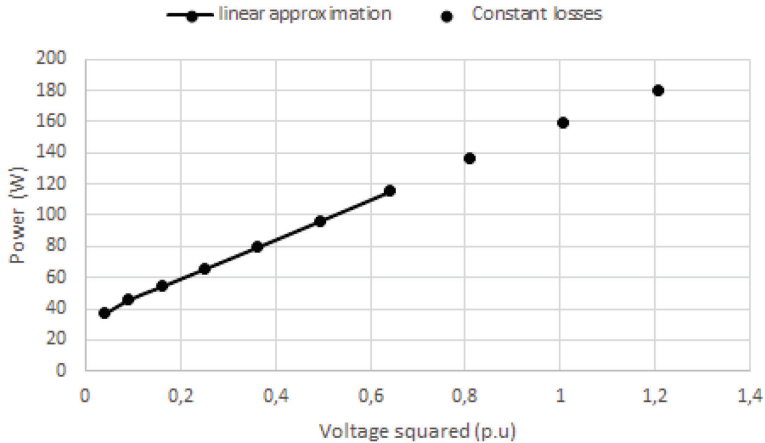


Figure 4.9. Constant power loss via voltage squared.

Figure 4.9 shows the constant power losses via voltage squared. To determine the mechanical losses from constant losses, the linear behavior appeared in the area without saturation is selected. In this mode, the point of the intersection of the liner region with the vertical axis in zero voltage is defined as mechanical losses. Finally, the iron losses (figure 4.10) are computed from subtracting the mechanical losses from the constant losses.

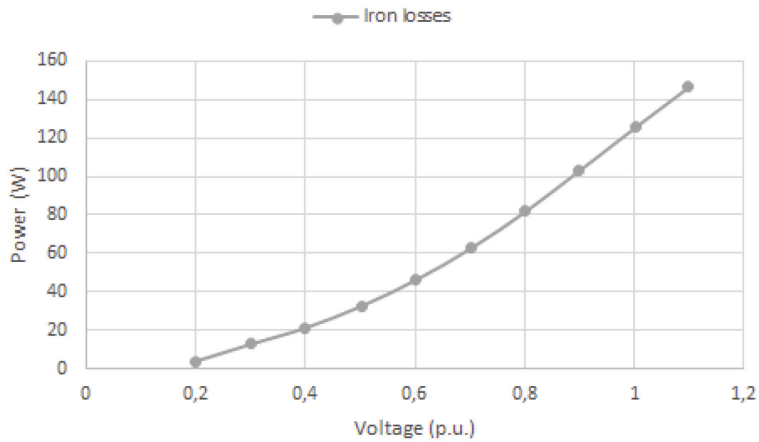


Figure 4.10. Iron losses via voltage.

Table 4.17 shows the value of losses for the rated voltage and frequency. In addition, these values will be used as the losses sources in the LPTN and thermal analysis of the machines.

Table 4.17. Experimental results of losses at the rated voltage and frequency

Name	Symbol	Unite	Value
Stator winding losses	$P_{cu}$	[W]	68.50
Iron losses	$P_{Fe}$	[W]	125.98
Mechanical losses	$P_m$	[W]	33.47

#### 4.4 Steady-state temperature results of LPTN

Table 4.18 shows the value of the thermal resistances of the LPTN during the active cooling test. These values were applied to model the heat transfer and predict the nodal temperature of the LPTN by using the matrix inversion method. Accordingly, the value of the  $R_0$  consists of the effect of forced convection and radiation during the nominal speed of the machine.

Table 4.18. Thermal resistances of the model during the air forced cooling

Thermal resistances	Value [K/W]
$R_0$	0.0231
$R_1$	0.0272
$R_2$	0.0036
$R_3$	0.0040
$R_4$	0.0196
$R_5$	0.0415
$R_6$	0.0492
$R_7$	10.694
$R_8$	0.4558
$R_9$	0.1617
$R_{10}$	0.2342
$R_{11}$	0.0790
$R_{12}$	0.0790
$R_{13}$	1.3221

To consider the accuracy and performance of the LPTN, it was run under passive (DC test) and active cooling (AC test). The passive cooling refers to the effectiveness of heat spreading within a machine, which is affected by the thermal properties of the material, geometrical design and interfacial thermal resistances between the machine components. The active cooling refers to the effects of heat removal from a machine to the coolant ultimately based on the convection phenomenon.

Table 4.19 shows the analytical results for the passive cooling and active cooling. During the passive cooling, the machine is in stall mode, and the only source of losses is the stator copper losses equal to 191.16 [W], and  $R_o$  equals 0.2056 [°C/W].

Table 4.19. Analytical LPTN results

Machine components	Passive cooling	Active cooling
Frame surface [°C]	59.4	25.9
Winding [°C]	70.8	33.2
End winding [°C]	76.7	33.7

#### 4.5 Results of the hybrid thermal model

To consider the performance of the hybrid model, it was run to model the heat transfer in different parts of the machine during the passive and active cooling condition. For these purposes, the different parameters of the hybrid thermal model were calculated according to the cooling method.

Table 4.20 shows the values of the LPTN components of the end region of the machine for the passive cooling condition. Furthermore, the modified total heat extraction coefficient, the equivalent thermal conductivity of the slot and copper losses produced in the slots implemented in the FE 2D parts of the hybrid model are 27 [W/(Km<sup>2</sup>)], 0.79 [W/(Km)] and 92.8 [W] respectively.

Table 4.20. The values of the thermal model components of the end region during the passive cooling

Component	Value	Unit
$R_{1h}$	0.05	[K/W]
$R_{2h}$	10.7	[K/W]
$R_{3h}$	2.3	[K/W]
$R_{4h}$	0.8	[K/W]
$R_{5h}$	0.6	[K/W]
$P_{Je}$	98.3	[W]

For the active cooling, the parameters of the LPTN of the end-winding are presented in Table 4.21. In addition, the values of the modified heat transfer coefficient, equivalent thermal conductivity of the slot and active copper losses implemented in the FE parts of the hybrid model are 171.6 [W/(Km<sup>2</sup>)], 0.79 [W/(Km)] and 33.26 [W] respectively.

Table 4.21. The values of the thermal model components of the end region during the active cooling

Component	Value	Unit
$R_{1h}$	0.05	[K/W]
$R_{2h}$	10.7	[K/W]
$R_{3h}$	0.46	[K/W]
$R_{4h}$	0.16	[K/W]
$R_{5h}$	0.08	[K/W]
$P_{Je}$	35.24	[W]

Table 4.22 shows the steady-state temperature results of SynRM by the hybrid thermal model in the passive and active cooling mode. Further, figures 4.11 and 4.12 show the temperature distribution in the active part of the machine computed with the hybrid thermal model during the passive and active cooling respectively.

Table 4.22. Results of temperature calculated by the hybrid thermal model during the passive and active cooling

Machine components	Passive cooling	Active cooling
Frame surface [°C]	68.6	29.1
Winding [°C]	72.9	33.2
End winding [°C]	78.5	33.7

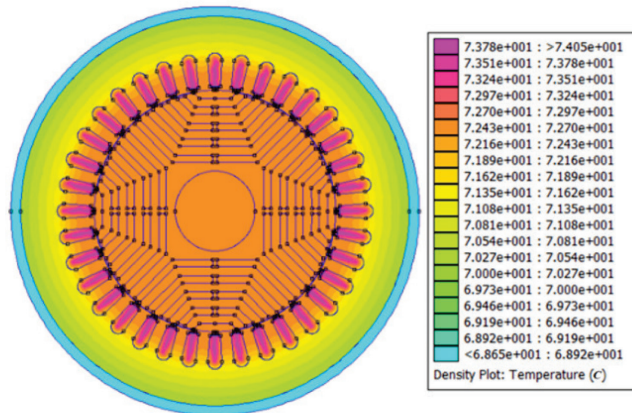


Figure 4.11. Temperature distribution in the active part of the machine by using the hybrid model during passive cooling.

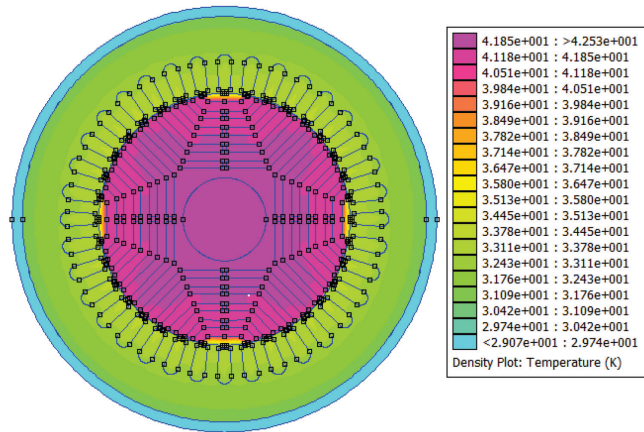


Figure 4.12. Temperature distribution in the active part of the machine by using the hybrid model during active cooling.

#### 4.6 Summary of Chapter 4

According to the effect of the correct prediction of the heat transfer coefficient on the accuracy of the thermal model, in the first section of this chapter, the analytical calculation of the heat transfer coefficient from several basic shapes was considered in different directions during the natural and forced cooling by using various empirical correlations. Then the analytical calculations were expanded to determine the heat transfer coefficient from the TEFC housing during the passive and active cooling.

During the passive cooling, heat is transferred from the machine housing to the surrounded area by natural convection and radiation. The value of the heat transfer coefficient was calculated by using the area-based composite method. During the active cooling in the TEFC machine, the correct prediction or measuring of the airflow speed around the machine housing plays an important part in the accuracy of the calculation of the heat transfer coefficient. Accordingly, the airflow speed was measured in different locations for several fan rotational speeds, and the value of the heat transfer coefficient was calculated by using the Heiles correlation.

In the next step, the machine losses were determined experimentally, and different parameters of the LPTN and the hybrid model were calculated and presented. Finally, the results of the analytical LPTN and the hybrid thermal model during the passive and active cooling are presented.

## 5 Validation and Discussion

The validations and experimental methodology were conducted to select the precise empirical correlation from among the several varieties of these correlations for different basic shapes and to validate the calculation method of the heat transfer coefficient from the machine housing as well as the thermal models. In this chapter, the experimental procedures and validation of the results are divided into two sections, in the first section, the experimental procedure and validation for the convection coefficient from different surfaces are described, and in the second part, the experimental procedures and validation of the thermal methods of the SynRM are provided. A more comprehensive explanation about the experimental methodology and the validation results and their analysis can be found in papers [I] to [VII].

### 5.1 Experimental validation of the convection coefficient

#### 5.1.1 Convection coefficient from basic shapes

To effectively consider the performance of different empirical correlations for predicting the convection coefficient from different surfaces and gain the most accurate correlation for use in the determination of the convection coefficient from the TEFC machine housing, several experimental verifications were carried out.

##### Experimental methodology

For experimental purposes, a stator coil of the permanent magnet generator was selected. According to figure 5.1, the stator coil used in this investigation consists of six different faces. To consider the convection from the flat side or fins side, the heat flux flow should be confined only to the desired surface. To achieve this, an insulation box according to the dimensions of the coil was created using foam insulation boards with a thickness of 10 [cm]. Since the foam insulation material has low thermal conductivity  $k = 0.3$  [W/(mK)], the thermal flux flow is restricted to the open surface. Therefore, the box is operating as a closed calorimeter. Another important point about the box is the temperature operation point; as the foam insulation board can handle temperatures up to 90 [°C], during the experiments, the coil temperature should not exceed that temperature.

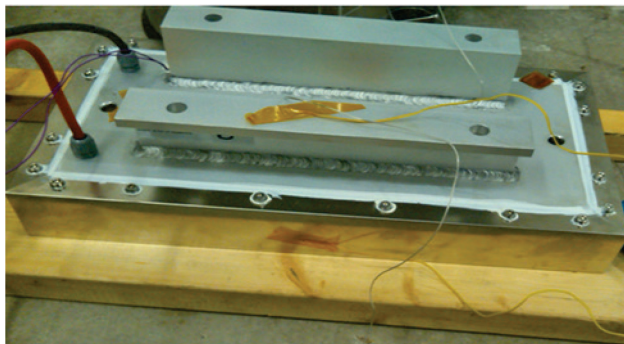


Figure 5.1. The coil module used in the experimental work.

Figure 5.2 depicts the experimental setup to consider the forced convection over the flat side of the stator coil. A wind tunnel was constructed of a cylindrical steel pipe with the length of 300 [cm] and the diameter of 80 [cm]. A four pole 7.5 [kW] squirrel cage induction motor was connected to the fan blades as the fan section. It was placed in front

of the wind tunnel to blow the air through the tunnel and provide airflow at different speed ranges. The induction motor is controlled with a frequency converter to regulate the coolant flow. Further, the coil insulation box was used as a calorimeter, and a DC power source was used to heat the coil. The system is protected with the temperature controller sensor to limit the temperature to the 90°C. In addition, the airflow velocity was measured by hot wire anemometer.

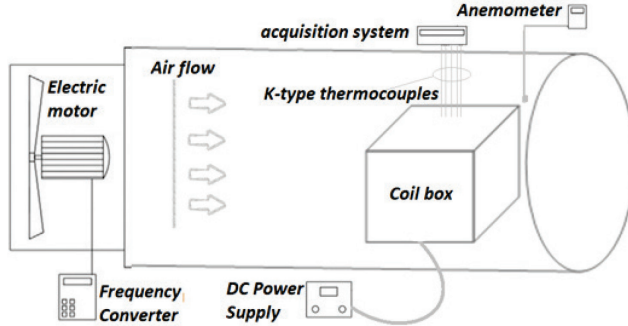


Figure 5.2. Schematic diagram of the main part of the experimental setup during the forced cooling.

The DC test is a common experimental method to evaluate the convection coefficient [54]. In this test, the loss of the coil is confined to the joule loss of the coil winding and the power can be easily calculated from the measured electric quantities. In the calculations, I accounted for the variations in the winding electrical resistance, as the winding resistivity is temperature dependent.

The total heat produced in the coil is equal to the total input power. Thus, the total heat in Watts [W] is defined as:

$$Q_T = V \cdot I, \quad (5.1)$$

where  $V$  [V] is the input voltage and  $I$  [A] the input current.

Accordingly, the total heat is extracted using the convection and radiation phenomena. Thus, the total heat can be described as:

$$Q_T = Q_{conv} + Q_{rad}, \quad (5.2)$$

where  $Q_{conv}$  [W] is the amount of heat extracted by convection and  $Q_{rad}$  [W] is the amount of heat extracted by radiation.

According to [54] and [53], the heat transfer coefficient  $h_e$  is calculated as:

$$h_e = \frac{Q_T}{(T_s - T_a)A}, \quad (5.3)$$

where  $T_s$  [°C] is the mean surface temperature,  $T_a$  [°C] is the ambient temperature, and  $A$  [m<sup>2</sup>] is the surface area.

The heat transfer coefficient is defined as the sum of the convection ( $h_c$ ) and radiation ( $h_r$ ) coefficients, whereas the radiation coefficient is calculated by (3.16):

$$h_e = h_c + h_r. \quad (5.4)$$

### Validation and analysis of convection results

The validation of the empirical correlations for different basic surfaces was made by comparing experimental data for different configurations.

### 1. Natural convection from a flat plate

Figure 5.3 shows the flat side of the stator coil module inside the coil box, which was used for the experiment. Accordingly, to study the effect of natural convection from a flat plate, the heat flux flow was confined to the flat side of the stator coil.

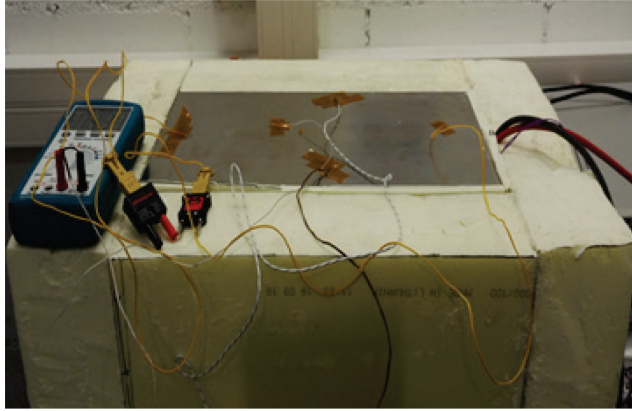


Figure 5.3. The used configuration for the flat plate experiment.

Table 5.1 shows the experimental results based on the DC test for five different DC input currents.

Table 5.1. Experimental results for the horizontal flat plate

$I$ [A]	$T_s$ [°C]	$T_a$ [°C]	$Q_T$ [W]	$h_e$ [W/(m <sup>2</sup> K)]	$h_r$ [W/(m <sup>2</sup> K)]	$h_c$ [W/(m <sup>2</sup> K)]
10	40	23	15.76	10.09	3.53	6.56
12	46.6	23	23.47	10.37	3.63	6.74
15	60.3	23	38.64	11.07	3.73	7.34
17	71.6	24	51.68	11.58	3.83	7.75
18	77.3	24	59.33	12.44	4.03	8.41

Figure 5.4 shows the variation of the heat transfer coefficient  $h_e$  with the temperature difference for five different input currents in the horizontal configuration. The analytical and experimental data were found to have an average relative difference of 6%, and the maximum relative difference based on this correlation is 9%. According to figure 5.4, it is clearly shown that by increasing the temperature, the relative difference of the analytical data compared with the experimental data decreases.



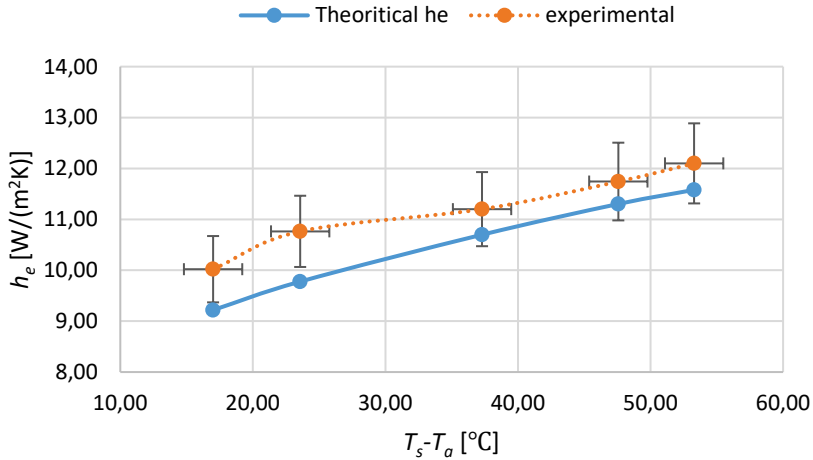


Figure 5.4. Variation of the heat transfer coefficient with the temperature difference for the horizontal direction.

Table 5.2 shows the experimental data for the vertical configuration.

Table 5.2. Experimental results for the vertical flat plate

$I$ [A]	$T_s$ [°C]	$T_a$ [°C]	$Q_T$ [W]	$h_e$ [W/(m <sup>2</sup> K)]	$h_r$ [W/(m <sup>2</sup> K)]	$h_c$ [W/(m <sup>2</sup> K)]
10	42.3	24	15.89	8.81	3.91	5.48
12	49.6	24	23.62	9.98	4.05	5.93
15	62.4	24	38.90	10.94	4.32	6.62
17	74.3	24	52.21	11.22	4.58	6.64
18	81.0	25	59.78	11.54	4.75	6.79

Figure 5.5 shows the variation of the heat transfer coefficient ( $h_e$ ) with the temperature difference for five different input currents in a vertical orientation. Significant differences were found between the analytical data based on the Churchill II correlation and the experimental data. The mean relative difference of this empirical correlation is about 12%, and the maximum one is 14%. However, the amount of the mean difference of the analytical results based on the Mac Adams correlation is less than the analytical results based on the Churchill I correlation. The average relative differences based on the mentioned correlations are 9% and 10% respectively.

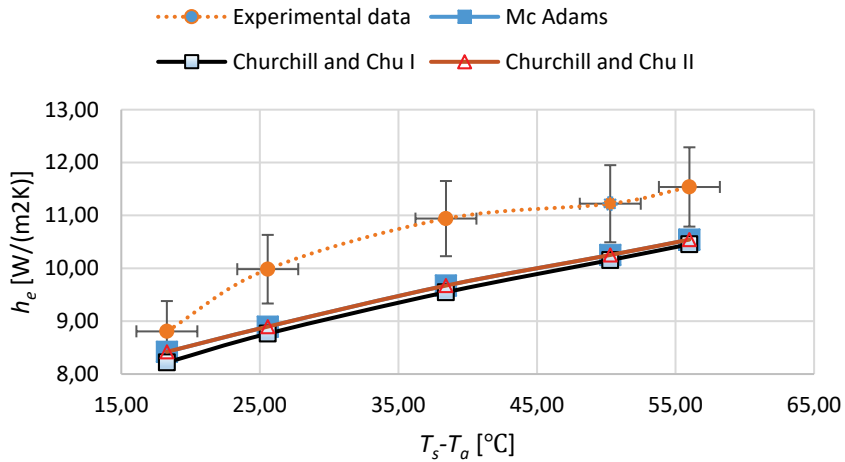


Figure 5.5. Variation of the heat transfer coefficient with the temperature difference for the vertical direction.

## 2. Natural convection from a rectangular isothermal fins plate

Figure 5.6 shows the coil box and the fins side of the coil in the vertical and the horizontal configurations. Accordingly, to consider the natural convection from the fin's side, the heat flux flow was confined to the fin side stator coil module.

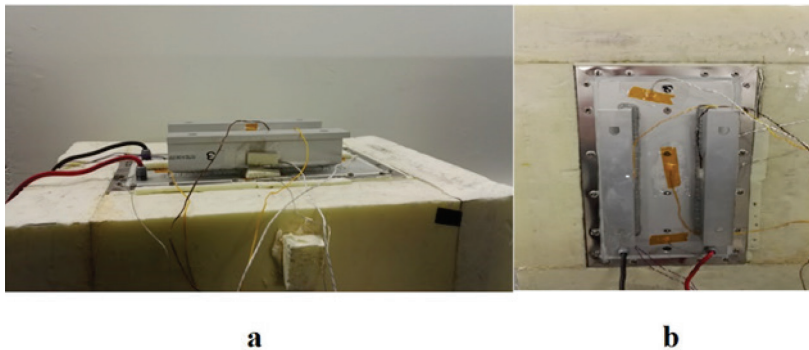


Figure 5.6. The used configurations in the experiment: a) Coil module inside the coil box in a horizontal position b) Coil module inside the coil box in a vertical position.

Table 5.3 shows the experimental data for the horizontal configuration by using the long term DC test.

Table 5.3. Experimental results for the horizontal configuration

$I$ [A]	$T_s$ [°C]	$T_a$ [°C]	$Q_T$ [W]	$h_e$ [W/(m <sup>2</sup> K)]	$h_r$ [W/(m <sup>2</sup> K)]	$h_c$ [W/(m <sup>2</sup> K)]
10	27.7	18.2	15.23	10.09	3.53	6.56
12	32.4	18.9	22.38	10.37	3.63	6.74
15	38.6	18.2	35.97	11.07	3.73	7.34
17	43.9	18.3	47.34	11.58	3.83	7.75
20	53.4	19	68.16	12.44	4.03	8.41

Figure 5.7 shows the variation of the heat transfer coefficient  $h_e$  with the temperature difference for five different input currents in the horizontal configuration. The average relative difference of the analytical data based on the Tari correlation in comparison with the experimental data is 8.1%, and the maximum relative difference based on this correlation is 12.9%. The average relative difference for the analytical data based on the Jones empirical correlation is 9.1%, and the maximum relative difference for these data is 12.1%. Accordingly, it is clearly shown that by increasing the temperature, the relative difference of the analytical data based on the Jones correlation compared with the experimental data decreases. For the temperature difference of 34.4 [°C], the relative difference is 9.5% with the Jones correlation while in the same situation it is 11.5% with the Tari correlation. Furthermore, figure 5.7 shows that by increasing the temperature, the analytical data curve based on Tari's correlation diverges from the experimental curve. It is interesting to note that the Jones empirical correlation has been developed without any dependence on the physical fin array's properties, e.g., fin's height ( $H$ ) and fin's length ( $L_{fin}$ ).

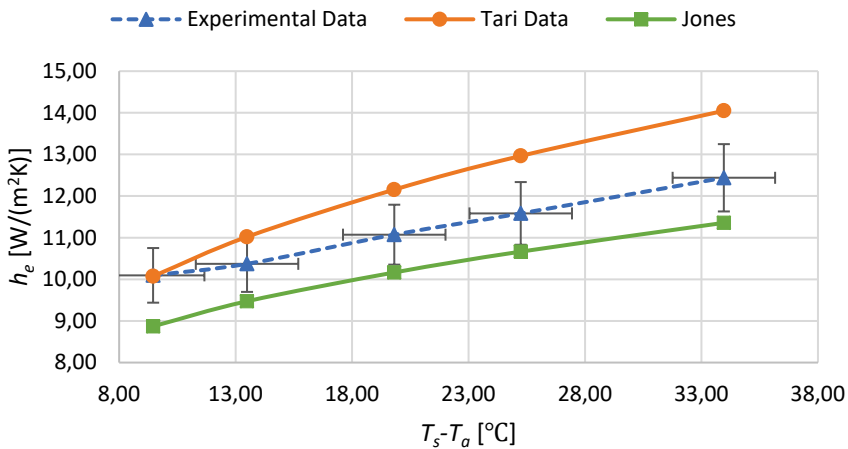


Figure 5.7. Variation of the heat transfer coefficient with the temperature difference for the horizontal orientation.

Table 5.4 shows the experimental data for the vertical configuration.

Table 5.4. Experimental results for the vertical configuration

$I$ [A]	$T_s$ [°C]	$T_a$ [°C]	$Q_T$ [W]	$h_e$ [W/(m <sup>2</sup> K)]	$h_r$ [W/(m <sup>2</sup> K)]	$h_c$ [W/(m <sup>2</sup> K)]
10	28.6	19	15.31	9.97	3.56	6.41
12	33.1	19.3	22.44	10.20	3.65	6.55
15	40.7	19.2	36.28	10.60	3.79	6.81
17	45.9	18.4	47.65	10.88	3.87	7.00
20	55.4	18.6	68.66	11.70	4.07	7.63

Figure 5.8 shows the variation of the heat extraction coefficient ( $h_e$ ) with the temperature difference in the vertical orientation. Significant differences were found between the analytical data based on Van Del Pol correlation and the experimental data. The mean relative difference of this empirical correlation is about 24%, and the

maximum one is 29%. The main reasons for this difference can be explained by the defined range for this correlation as well as by the fact that Van De Pol equations were derived for a periodical channel whereas Tari's equation is valid for a single channel too. According to [57] and [75], this correlation is fitted for rectangular fins in the range of  $0.33 < H/S < 4$  and  $42 < L_{fin}/S < 10.6$ . This case study is not located within these ranges. However, as Figure 5.8 shows, the difference between the analytical data based on Tari's correlation and the experimental data is significant at lower temperatures, but as the temperature difference increases, the analytical data curve converges toward the experimental one. Thus, the appropriateness of this correlation is better at high temperatures. The mean relative difference for this correlation is 12%. The maximum relative difference occurred at the low-temperature rise, amounting to 29%.

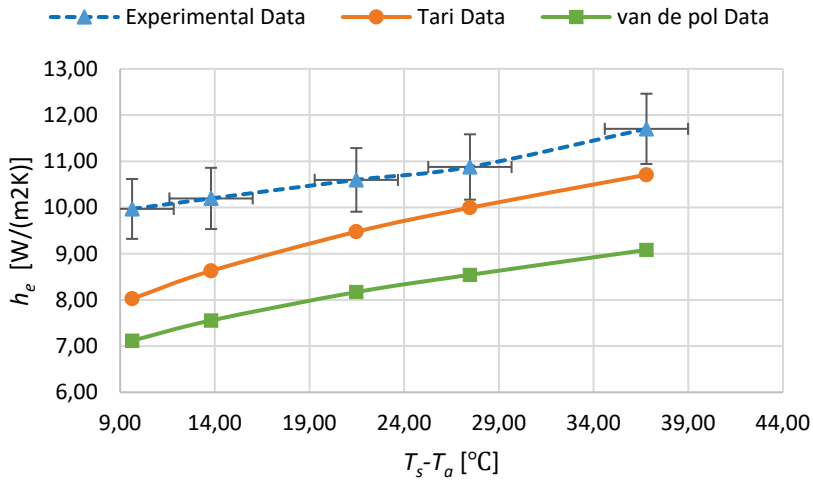


Figure 5.8. Variation of the heat transfer coefficient with the temperature difference for the vertical orientation.

### 3. Forced convection over the flat plate with the unheated starting part

Figure 5.9 shows the experimental setup where the flat side of the stator coil module inside the coil box is located inside the wind tunnel to study the effect of different airflows on the heat transfer coefficient.

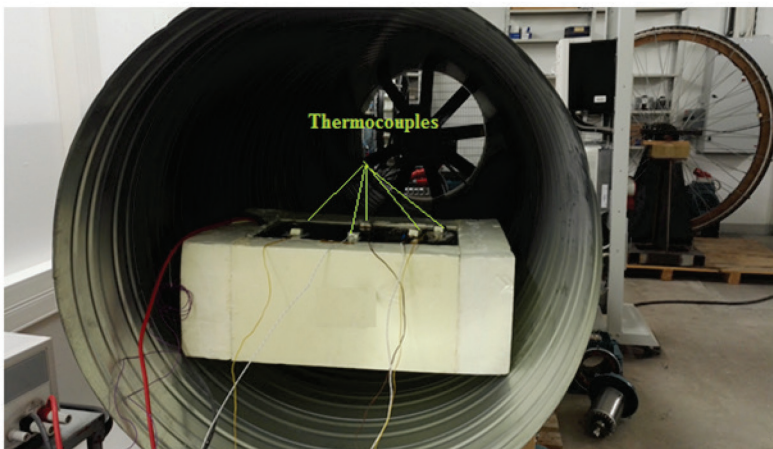


Figure 5.9. Coil box inside the wind tunnel.

Table 5.5 shows the experimental results for the flat side of the coil module under a fixed current with five different wind speeds.

Table 5.5. Experimental results

$v$ [m/s]	$T_s$ [ °C]	$T_a$ [ °C]	$Q_T$ [W]	$h_e$ [W/(m <sup>2</sup> K)]	$h_r$ [W/(m <sup>2</sup> K)]	$h_c$ [W/(m <sup>2</sup> K)]
4.1	62.7	18.6	137.4	33.70	4.22	29.48
6.1	52.4	18.5	133.0	42.36	4.01	38.36
7.1	50.5	18.7	131.7	44.80	3.97	40.83
8.2	47.2	18.3	130.2	48.96	3.90	45.05
10.5	43.5	18.3	128.4	55.09	3.83	51.26

Figure 5.10 shows the variations of the forced convection heat transfer via the airflow speed based on the experimental and analytical data. Accordingly, it is apparent that the convection coefficient heat transfer is proportional to the wind speed and it increases by increasing the speed. Furthermore, the graph proves the importance of accurate comprehension of the fluid flow mode during the calculation of the forced convection heat transfer. As expected, the fluid flow was in the turbulent mode. One interesting finding based on the analytical data is the linear correlation between the convection coefficient and the wind speed. Another important finding is that the convection coefficient at zero speed is not zero, which can be attributed to the natural convection. Finally, it shows that by increasing the wind speed, the experimental data converge toward turbulent analytical results. Thus, it can be expected that the precision of an analytical calculation is enhanced at high wind speed with high turbulent flow. However, in the calculation of the forced convection coefficient, 15% difference between the analytical and the experimental data is an acceptable relative difference [30].

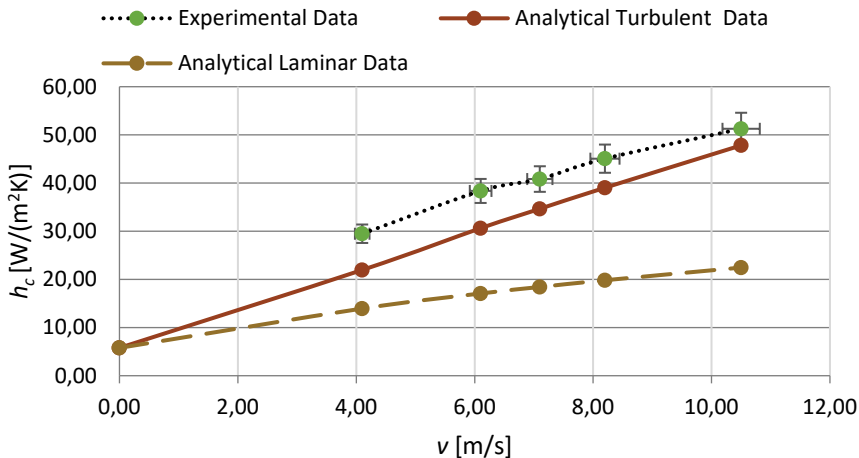


Figure 5.10. Convection heat transfer coefficient according to the wind speed.

### 5.1.2 Natural heat transfer from the housing of the TEFC electrical machine

To validate the performance of analytical methods for predicting the convection coefficient from the housing of the TEFC electrical machine during the natural cooling conditions, experimental verifications were conducted.

### Experimental methodology

A common experimental method to determine the total heat transfer coefficient of the machine housing during natural cooling is the DC stator test [76]. In this test, the losses of the machine are confined to the Joule loss of the stator windings where the electric power can be easily measured [40]. However, this is a long-term test and it takes several hours to reach a steady state condition.

For the DC test, the stator windings of the machine are connected in series, and during the experiment, the DC power applied to the motor and the surface temperature of the motor at different locations are measured. As shown in figure 5.11, four K-type thermocouples were installed by means of adhesive material in various locations on the frame surface of the motor. The ambient temperature was also measured by means of a K-type thermocouple. The average temperature of these four thermocouples assumed is the mean temperature of the motor frame surface. The experiment was carried out for each current input until the system reached its steady state condition. The experimental procedure was repeated for five different current inputs. The total heat transfer coefficient ( $h_0$ ) was calculated by (5.3), which is presented in below.

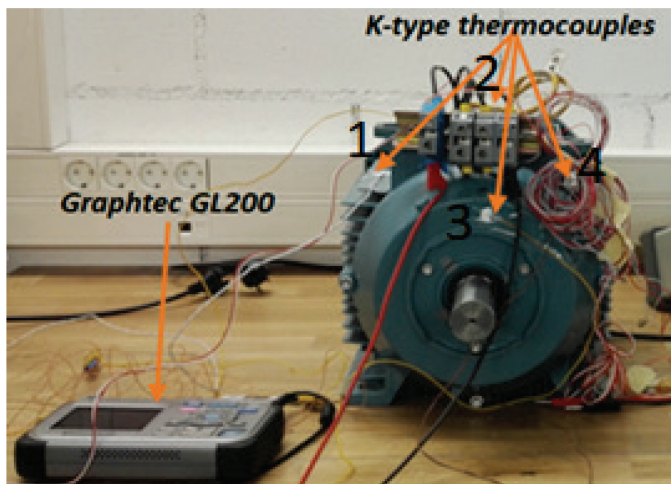


Figure 5.11. Test setup.

### Analysis and validation

Table 5.6 shows the experimental data for the horizontal configuration by using the long term DC test.

Table 5.6. Experimental results

$V$ [V]	$I$ [A]	$T_s$ [°C]	$T_a$ [°C]	$Q_T$ [W]	$h_0$ [W/(m <sup>2</sup> K)]
15	6.45	42	20.5	96.75	6.37
17	7.12	47	21.6	121.04	6.76
19	7.79	51.5	20.8	148.01	6.93
22	8.71	61	21.6	191.62	7.47
25	9.57	64.5	21.2	239.25	7.65

Figure 5.12 shows the variation of the total heat extraction coefficient ( $h_0$ ) via the temperature difference for experimental and analytical data. Accordingly, the relative difference between the analytical and the experimental data is about 5.5%, and the

maximum value is 8.2%. Figure 5.12 shows that by increasing the temperature, the accuracy of the analytical calculation increases.

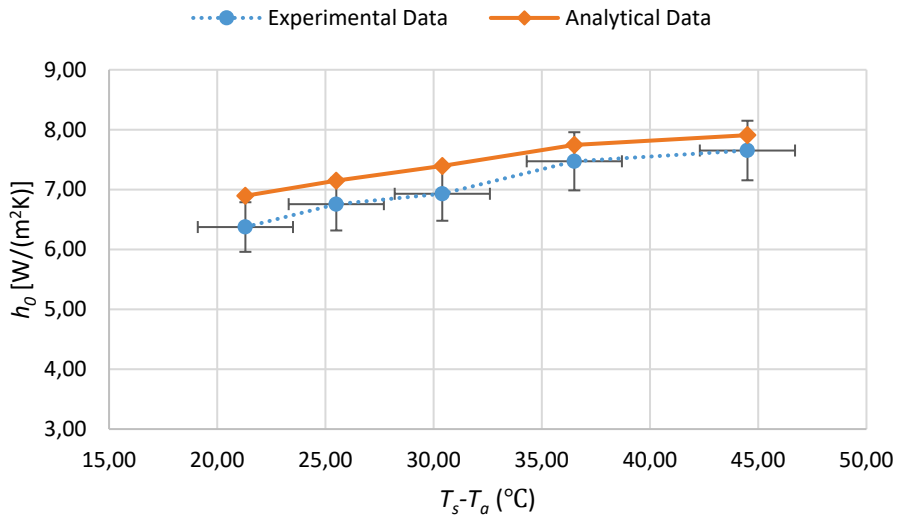


Figure 5.12. Variation of the heat transfer coefficient with the temperature difference.

### 5.1.3 Forced heat transfer from the housing of the TEFC electrical machine

The objective of the experimental work was to assess the total heat transfer coefficient from the housing of the TEFC electrical machine during air force cooling with different fan speeds. Another objective was to compare the analytical data to the experimental data for finding and verifying the accuracy of the analytical calculation.

#### Experimental methodology

Figure 5.13 shows the diagram of the test setup. Accordingly, to rotate the cooling fan, the shaft of SynRM was coupled to the shaft of an induction motor. For producing, different fan rotational speeds, the speed of the induction motor was adjusted by a frequency converter.

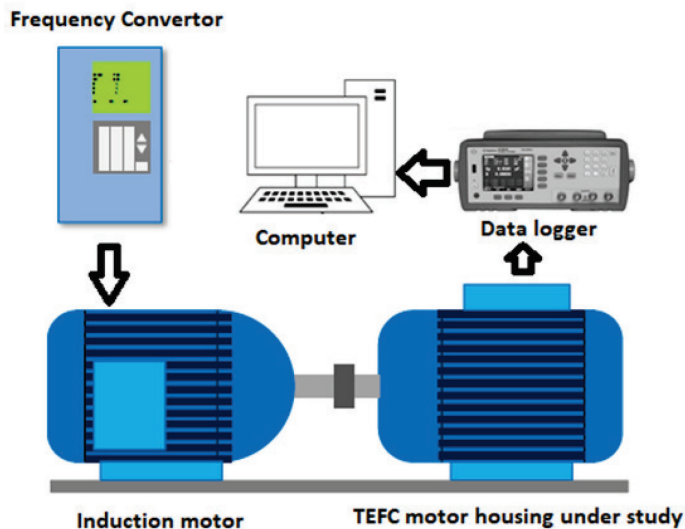


Figure 5.13. The diagram of the experimental setup.

To better identify convection phenomenon, it is important to define the system only based on the stator joule losses; accordingly, as shown in figure 5.14, the rotor of the SynRM machine was replaced by a shaft. Then the cooling fan was assembled at the end part of the shaft.



Figure 5.14. Replacement of the rotor of SynRM with the shaft.

Figure 5.15 shows the experimental setup. As mentioned, the DC stator test is a common experimental method for determining the convection coefficient. For this purpose, the three-phase stator windings of the SynRM were connected in series and were supplied through a digitally controlled DC power supply. During the experiments, in addition to the power input to the stator windings, the temperature of the machine housing and the air-cooling speed were measured at different locations. During the experiments, all the temperature data were collected using a Key sight logger. The experiment was carried out for each air-cooling speed until the system reached its steady state condition. The experimental procedure was repeated for five different fan rotational speeds: 600, 900, 1200, 1500 and 1800 rpm.

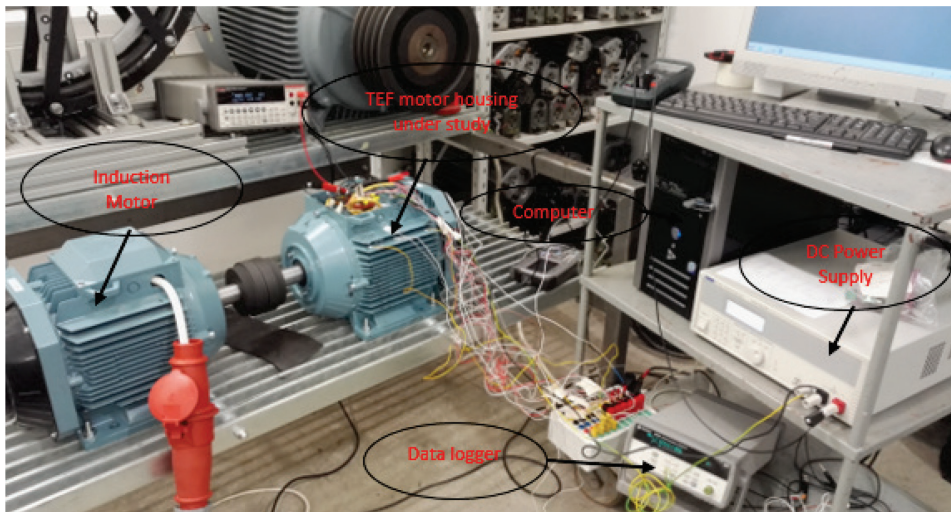


Figure 5.15. Experiment setup.

### Analysis and validation

Table 5.7 shows the experimental data of the heat transfer coefficient from the housing of the TEFC electrical machine. The heat transfer coefficient was calculated by using (5.3).



Table 5.7. Experimental data for the air forced cooling

Shaft speed [rpm]	Inlet speed [m/s]	$T_s$ [°C]	$T_a$ [°C]	$Q_T$ [W]	$h_e$ [W/(m <sup>2</sup> K)]
600	3.5	32.3	22.3	189.3	26.6
900	5.5	29	21.2	190.6	34.3
1200	7.6	29.1	22.3	190.7	39.3
1500	9.7	28.4	22.2	192	43.5
1800	12.2	27.3	21.8	192.2	49

Figure 5.16 shows the variation of the total heat transfer coefficient ( $h_e$ ) versus the fan rotational speed. According to the variation of the experimental value of  $h_e$  versus the fan rotational speed, it clearly shows the point when the flow is in turbulent mode. At 1500 rpm and after this point, a rapid increase occurred in the amount of the heat transfer coefficient. Also, according to the analytical data, by increasing the speed, the amount of the relative difference between the analytical and experimental data starts to decrease, and when the flow is in the turbulent mode, the analytical data merge to the experimental one. The amount of the relative mean difference between the experimental and analytical data is about 11%.

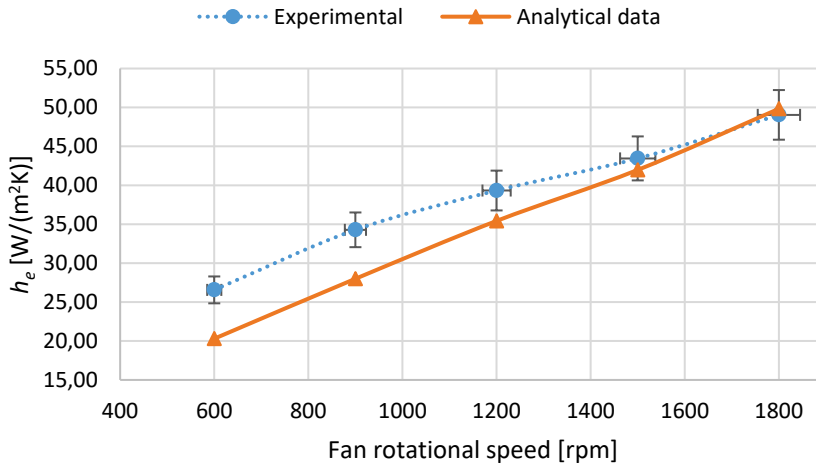


Figure 5.16. Variation of the heat extraction coefficient via the fan's rotational speed.

## 5.2 Experimental validation of thermal models

To effectively validate and evaluate the performance of the created SynRM LPTN and the hybrid thermal model and to gain details about the accuracy of the method in the prediction of temperature distribution across the machine's most important sections, an experimental verification stage was carried out. The experiments conducted for the validation of the model are described in brief hereafter.

### DC thermal test:

In this test, the machine loss was confined to the stator joule losses. The windings of stator phases were connected in series. As the motor is in stall condition, the air-cooling speed is zero, and the machine is cooled by the natural cooling method. Consequently,

to protect the machine from over-temperature condition and damage, the current applied to the machine is set to 40% of the rated current. In the steady state condition, the input power and the temperature of different parts of the machine, e.g., windings, end windings and the housing of the machine were measured. For measuring the temperature of the machine winding and the end-winding, thermal sensors (PT 100) were installed inside slots and the end windings of each phase. Furthermore, the mean temperature of the housing was evaluated by measuring the temperature of several locations of the machine housing.

Figure 5.17 shows the temperature comparison obtained using the LPTN, the hybrid thermal model and the measurements during the DC test. In the graph, the end winding, the winding, and housing temperatures are represented. The graph shows good agreement between the predicted and measured temperatures, but the only difference is in the housing temperature of the hybrid model and the experimental results. In the hybrid model, the housing temperature is defined as the mean frame temperature.

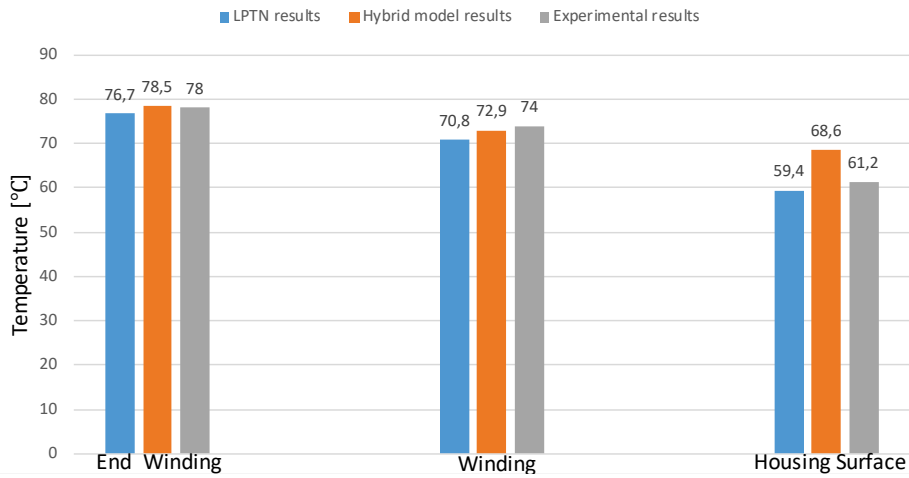


Figure 5.17. Temperature comparisons during the DC test.

**AC thermal test:**

For the AC experimental test, the SynRM is operated under no load condition. For this purpose, the SynRM is synchronized to the grid with an induction machine, which is disconnected from the SynRM after synchronization. The purpose is to operate the SynRM under sinusoidal grid supply as to conserve the same voltage and thus the same iron losses.

Figure 4.7 shows the experimental setup. During the experiment, the active power, the RMS value of the current and voltage, temperature and power factor of each phase were measured with a data acquisition system (Dewetron). The SynRM was equipped with six PT100 thermal sensors. Three sensors were located in the end winding section of each phase, and the other three were installed inside the slots. The motor surface temperature was measured by an infrared laser digital thermometer. During the experiment, when the machine reached its steady-state mode, the outer frame surface and ambient temperatures and total input power were measured.

Figure 5.18 shows the temperature comparison obtained using the LPTN, the hybrid thermal model and measurements during the AC test. The relative difference of the LPTN results for the surface temperature, slot winding, and end-winding are 3%, 3.3%, and

6.8% respectively. These difference in the LPTN arise from the hypothesis of the uniform distribution of losses in the machine as well as from the fact that the LPTN model predicts the mean temperature of the machine component while in the experimental part, the thermocouples show the temperatures at given positions. This fact is illustrated in Figure 5.19, which shows the temperature distribution over the frame surface of the SynRM in the steady-state mode. The figure gives a good overview of the temperature differences on the frame surface of the SynRM. The relative difference of the same components by the hybrid thermal model is 9%, 0.6%, and 0.3% respectively. The relative difference in the surface temperature arises from the assumption that the mean temperature of the active part of the frame is assumed as the surface temperature.

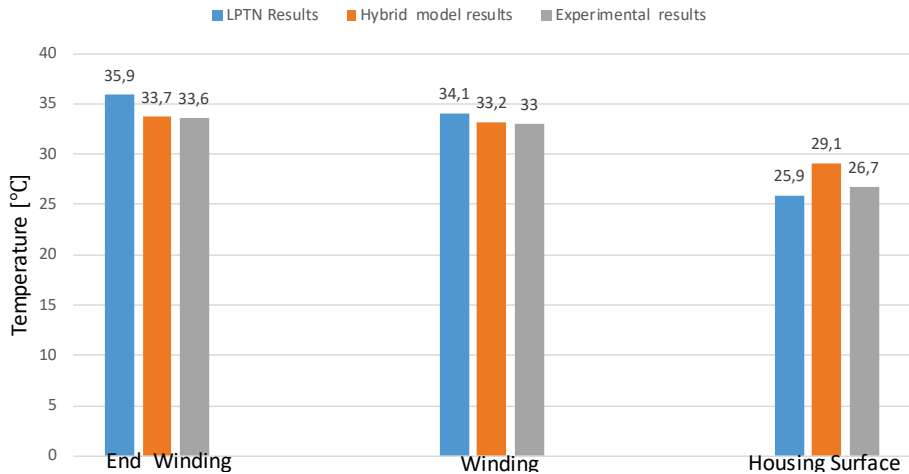


Figure 5.18. Temperature comparisons during the AC test.

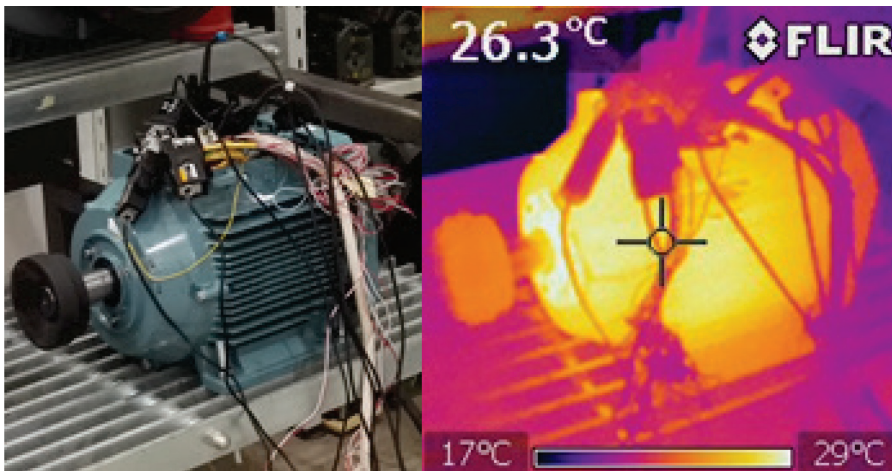


Figure 5.19. Temperature distribution over the frame surface.

The comparison of the LPTN results with the hybrid model indicates that the accuracy of the hybrid model in predicting the slots and the end winding temperature is higher than that of the LPTN.

### **5.3 Summary of Chapter 5**

In the first section of this chapter, the experimental procedures for measuring the heat transfer coefficient from basic shapes are presented. Next, the appropriate empirical correlation for each basic shape was selected by comparison with measurement results. Then the selected empirical correlations were used to calculate the heat transfer coefficient from the complex shape of the TEFC housing in the natural cooling. Finally, by measuring the airflow speed in different locations of the housing, the average airflow speed was evaluated, and the heat transfer coefficient of the machine via different cooling speed was determined.

In the second part, the experimental DC and AC tests constructed for the thermal analysis of the SynRM are described, followed by the thermal steady state results used to validate the LPTN and the hybrid thermal models presented in Chapter 3. The comparison shows close agreement between the thermal models and the measurements data, with a mean difference around 4 %.

## 6 Conclusion and Future Work

This chapter concludes the research during this scientific work and summarizes the research done for this study. Finally, this chapter presents some recommendations and a vision for future work.

### 6.1 Conclusion and summary of work

This research work has addressed different thermal issues during the design process of an electrical machine. Further, it has described the latest trends in the cooling of electric machines. In the following, different modern methods in the thermal analysis of the electrical machine and their advantages and drawbacks as well as the evolutionary history of the thermal analysis methods have been summarized. In addition, different heat transfer mechanisms in an electrical machine have been described, and several critical parameters in the thermal modeling of an electrical machine have been demonstrated, and several remedies were proposed to dominate these problems.

As established at the start of the thesis, the main objective of this study was to develop scientifically sound methods that can be applied in the thermal design and analysis of electrical machines and to implement them for a specific machine. For these purposes, the analytical LPTN and the hybrid thermal model were selected to model the heat transfer of the SynRM. As most of the heat is transferred from the machine to the ambient by the convection phenomenon and the importance of the convection heat transfer on the accuracy of the model, a great deal of this study was devoted to ensuring the accurate calculation of the convection coefficient from the machine surfaces. As the TEFC machine has a complex housing structure, the area based composite correlation method was implemented to determine the heat transfer from the machine housing during the passive cooling. Accordingly, the machine structure is segregated into several basic shapes with known empirical correlations to calculate the convection coefficient as there are several different empirical correlations to calculate the heat transfer coefficient from the basic shapes. First, the experimental setup was developed, and the experimental results and theoretical results from a variety of empirical correlations were compared for each basic shape. Finally, the most accurate correlation for each shape was selected. In the next step, according to the selected correlations, the convection coefficient of machine housing was calculated using the area based composite correlation. This thesis also provides a simplified method to calculate the radiation coefficient from the complex shape of the machine housing.

The Heiles correlation was applied to determine the heat transfer coefficient from the housing of the machine for the forced cooling method. Accordingly, the most important factor in determining the heat transfer coefficient from the machine surface is the airflow velocity. The measurement method was applied to determine the airflow velocity over the machine-housing surface and among the fin channels. In addition, the amount of leaking airflow from the semi-open fin channels was evaluated. Finally, to validate the methods the analytical results of the heat transfer coefficient from the machine housing during the active and passive cooling were compared to the experimental ones, which showed good agreement.

For the analytical thermal analysis of the electrical machine, the LPTN of the machine was developed and different components and how to calculate them were presented in details. For the numerical analysis, the hybrid thermal model of the machine was proposed. In this method, the active part of the machine was modeled by using 2D FEA,

and the heat transfer in the end region of the machine was modeled by the LPTN. Finally, these two methods were coupled to provide the heat transfer of the machine.

To validate the thermal models, the passive and active tests were conducted and the results were compared with the analytical and numerical results. Overall, the results provided by the LPTN and the hybrid thermal model were found in very good agreement with the experimental data. The analytical and numerical results are clearly within a mean difference of 4% for the steady state condition.

## **6.2 Future work**

Several additional investigations can be addressed in the future work. Accordingly, one of the challenging parameters in the thermal modeling of electrical machines is modeling the heat transfer of the end windings of an electrical machine. In this study, this parameter was calculated using an empirical correlation. However, this parameter depends on several different factors such as the number of the Wafers, size of the Wafers, etc. For further study, the end winding heat transfer model should be considered by using the CFD method to determine the effect of these factors on the heat transfer of the end windings. Furthermore, this study has provided the research only for the stranded winding. Therefore, the modeling of heat transfer for the hairpin windings and formed winding should be considered.

In the LPTN and the hybrid thermal model, the convection coefficient was determined by the empirical correlations. To enhance accuracy, it is required to develop the tools to coupling the CFD method to the LPTN and the hybrid thermal models to determine the heat transfer coefficient.

In this study, the hybrid thermal model was implemented for the TEFC cooling method. However, the possibility of modeling of other cooling methods by the hybrid thermal model should be investigated.

In the LPTN, it was assumed that the heat is distributed uniformly. To enhance the accuracy of the analytical thermal model, the iron loss distribution in different parts of laminations should be analyzed by applying the electromagnetic numerical method.

## References

- [1] T. Finken and K. Hameyer, "Design of Electric Motors for Hybrid-and Electric-Vehicle Applications," in *ICEMS*, 2009.
- [2] B. Mecrow, "Design of Machines and Drives," Newcastle upon tyne , 2011.
- [3] M. Rosu *et al.*, *Multiphysics simulation by design for electrical machines, power electronics and drives*, 1st ed. Wiley-IEEE Press, 2017.
- [4] M. Popescu, D. Staton, D. Dorrell, F. Marignetti, and D. Hawkins, "Study of the thermal aspects in brushless permanent magnet machines performance," in *2013 IEEE Workshop on Electrical Machines Design, Control and Diagnosis (WEMDCD)*, 2013, pp. 60–69.
- [5] "Arnold Magnetic Technologies | Global Magnet Manufacturer." [Online]. Available: <http://www.arnoldmagnetics.com>.
- [6] S. Nategh, A. Krings, Z. Huang, O. Wallmark, M. Leksell, and M. Lindenmo, "Evaluation of stator and rotor lamination materials for thermal management of a PMSRM," in *2012 XXth International Conference on Electrical Machines*, 2012, pp. 1309–1314.
- [7] Y. C. Chong, "Thermal Analysis and Air Flow Modelling of Electrical Machines," University of Edinburgh, 2015.
- [8] D. A. Staton and A. Cavagnino, "Convection Heat Transfer and Flow Calculations Suitable for Electric Machines Thermal Models," *IEEE Trans. Ind. Electron.*, vol. 55, no. 10, pp. 3509–3516, Oct. 2008.
- [9] Y. Gai *et al.*, "Cooling of automotive traction motors: Schemes, examples, and computation methods," *IEEE Trans. Ind. Electron.*, vol. 66, no. 3, pp. 1681–1692, Mar. 2019.
- [10] E. Nitsche and M. Naderer, "Internally Cooled Hollow Wires Doubling the Power Density of Electric Motors," *ATElektronik Worldw.*, vol. 12, no. 3, pp. 42–47, Jun. 2018.
- [11] D. Staton and J. Goss, "Open Source Electric Motor Models for Commercial EV & Hybrid Traction Motors," *CWIEME*, 2017.
- [12] E. Y. C. Chong, "Latest Trends in Cooling of Electric Traction Motors," in *Motor-design limited*, 2018, pp. 1–47.
- [13] J. Pyrhönen, T. Jokinen, and V. Hrabovcová, *Design of Rotating Electrical Machines*. Wiley, 2008.
- [14] A. Boglietti, A. Cavagnino, D. Staton, M. Shanel, M. Mueller, and C. Mejuto, "Evolution and Modern Approaches for Thermal Analysis of Electrical Machines," *IEEE Trans. Ind. Electron.*, vol. 56, no. 3, pp. 871–882, Mar. 2009.
- [15] C. Mejuto, "Improved lumped parameter thermal modelling of synchronous generators," The University of Edinburgh, 2010.
- [16] C. Micallef, "End winding cooling in electric machines," 2006.
- [17] A. Boglietti, A. Cavagnino, and D. Staton, "Determination of Critical Parameters in Electrical Machine Thermal Models," *IEEE Trans. Ind. Appl.*, vol. 44, no. 4, pp. 1150–1159, 2008.
- [18] S. LIPIŃSKI, K. Grunt, and J. Zawilak, "2D steady-state thermal analysis of a line-start, permanent magnet synchronous motor," *PRZEGLĄD ELEKTROTECHNICZNY*, vol. 1, no. 3, pp. 183–186, Mar. 2017.

- [19] P. H. Mellor, D. Roberts, and D. R. Turner, "Lumped parameter thermal model for electrical machines of TEFC design," *IEE Proc. B Electr. Power Appl.*, vol. 138, no. 5, p. 205, 1991.
- [20] A. Boglietti, A. Cavagnino, M. Lazzari, and M. Pastorelli, "A simplified thermal model for variable-speed self-cooled industrial induction motor," *IEEE Trans. Ind. Appl.*, vol. 39, no. 4, pp. 945–952, Jul. 2003.
- [21] J. Lindström, "Thermal Model of a Permanent-Magnet Motor for a Hybrid Electric Vehicle," CHALMERS UNIVERSITY OF TECHNOLOGY, Goteborg, 1999.
- [22] A. M. EL-Refaeie, N. C. Harris, T. M. Jahns, and K. M. Rahman, "Thermal Analysis of Multibarrier Interior PM Synchronous Machine Using Lumped Parameter Model," *IEEE Trans. Energy Convers.*, vol. 19, no. 2, pp. 303–309, Jun. 2004.
- [23] S. Nategh, Z. Huang, A. Krings, O. Wallmark, and M. Leksell, "Thermal Modeling of Directly Cooled Electric Machines Using Lumped Parameter and Limited CFD Analysis," *IEEE Trans. Energy Convers.*, vol. 28, no. 4, pp. 979–990, Dec. 2013.
- [24] G. Traxler-Samek, R. Zickermann, and A. Schwery, "Cooling airflow, losses, and temperatures in large air-cooled synchronous machines," *IEEE Trans. Ind. Electron.*, vol. 57, no. 1, pp. 172–180, Jan. 2010.
- [25] V. Fireteanu and V. CEDRAT, "FE Steady State Thermal Analysis of Squirrel Cage Induction Motors with Flux," *Flux News Altair*, pp. 6–9, 2016.
- [26] D. G. Nair, T. Jokinen, and A. Arkkio, "Coupled analytical and 3D numerical thermal analysis of a TEFC induction motor," in *2015 18th International Conference on Electrical Machines and Systems, ICEMS 2015*, 2016, pp. 103–108.
- [27] W. Jiang and T. M. Jahns, "Development of efficient electromagnetic-thermal coupled model of electric machines based on finite element analysis," in *2013 International Electric Machines & Drives Conference*, 2013, pp. 816–823.
- [28] S. Nategh, O. Wallmark, M. Leksell, and S. Zhao, "Thermal analysis of a PMaSRM using partial FEA and lumped parameter modeling," *IEEE Trans. Energy Convers.*, vol. 27, no. 2, pp. 477–488, Jun. 2012.
- [29] C. Mejuto, M. Mueller, D. Staton, S. Mebarki, and N. Al-Khayat, "Thermal modelling of TEFC alternators," in *IECON Proceedings (Industrial Electronics Conference)*, 2006, pp. 4813–4818.
- [30] F. P. Incropera, D. P. DeWitt, T. L. Bergman, and A. S. Lavine, *Fundamentals of Heat and Mass Transfer*. 2007.
- [31] Y. A. Cengel, *Heat Transfer: A Practical Approach*. New York : McGraw-Hill, 2004.
- [32] J. R. Simonson, *Engineering Heat Transfer*. London: Macmillan Education UK, 1988.
- [33] M. Popescu, D. A. Staton, A. Boglietti, A. Cavagnino, D. Hawkins, and J. Goss, "Modern Heat Extraction Systems for Power Traction Machines—A Review," *IEEE Trans. Ind. Appl.*, vol. 52, no. 3, pp. 2167–2175, May 2016.
- [34] A. Boglietti, A. Cavagnino, M. Parvis, and A. Vallan, "Evaluation of radiation thermal resistances in industrial motors," *IEEE Trans. Ind. Appl.*, vol. 42, no. 3, pp. 688–693, May 2006.
- [35] V. D. Rao, S. V. Naidu, B. G. Rao, and K. V. Sharma, "Heat transfer from a horizontal fin array by natural convection and radiation—A conjugate analysis," *Int. J. Heat Mass Transf.*, vol. 49, no. 19, pp. 3379–3391, 2006.
- [36] M. Ahmadi, G. Mostafavi, and M. Bahrani, "Natural convection from rectangular interrupted fins," *Int. J. Therm. Sci.*, vol. 82, pp. 62–71, 2014.



- [37] A. Boglietti and A. Vallan, "Measurement of housing thermal resistances in industrial motors," in *Conference Record - IEEE Instrumentation and Measurement Technology Conference*, 2006, pp. 1321–1325.
- [38] D. Staton and L. Šušnjić, "Induction Motors Thermal Analysis," *Strojarstvo*, vol. 51, no. 6, pp. 623–631, 2009.
- [39] D. Staton, A. Boglietti, and A. Cavagnino, "Solving the More Difficult Aspects of Electric Motor Thermal Analysis in Small and Medium Size Industrial Induction Motors," *IEEE Trans. Energy Convers.*, vol. 20, no. 3, pp. 620–628, Sep. 2005.
- [40] A. Boglietti, A. Cavagnino, and D. A. Staton, "TEFC induction motors thermal models: A parameter sensitivity analysis," *IEEE Trans. Ind. Appl.*, vol. 41, no. 3, pp. 756–763, May 2005.
- [41] A. Boglietti, A. Cavagnino, and D. A. Staton, "Thermal sensitivity analysis for TEFC induction motors," in *Second IEE International Conference on Power Electronics, Machines and Drives*, 2004, pp. 160–165.
- [42] A. Boglietti, E. Carpaneto, M. Cossale, S. Vaschetto, M. Popescu, and D. A. Staton, "Stator winding thermal conductivity evaluation: An industrial production assessment," *IEEE Trans. Ind. Appl.*, vol. 52, no. 5, pp. 3893–3900, Sep. 2016.
- [43] A. Boglietti, E. Carpaneto, M. Cossale, and S. Vaschetto, "Stator-Winding Thermal Models for Short-Time Thermal Transients: Definition and Validation," *IEEE Trans. Ind. Electron.*, vol. 63, no. 5, pp. 2713–2721, May 2016.
- [44] J. P. Holman, *Heat Transfer*. McGraw-Hill, 1999.
- [45] A. F. Mills, *Heat transfer*. Prentice Hall, 1999.
- [46] D. P. Kulkarni, G. Rupertus, and E. Chen, "Experimental investigation of contact resistance for water cooled jacket for electric motors and generators," *IEEE Trans. Energy Convers.*, vol. 27, no. 1, pp. 204–210, Mar. 2012.
- [47] "Motor-CAD Software by Motor Design - EMag, Therm and Lab." [Online]. Available: <https://www.motor-design.com/motor-cad-software/>.
- [48] K. Takahashi, H. Kuwahara, K. Kajiwara, and T. Obata, "Airflow and thermal conductance in a totally enclosed induction motor," *Heat Transf. - Asian Res.*, vol. 31, no. 1, pp. 7–20, Jan. 2002.
- [49] G. E. Luke, "The Cooling of Electric Machines," *Trans. Am. Inst. Electr. Eng.*, vol. 42, pp. 636–652, Jan. 1923.
- [50] A. DiGerlando and I. Vistoilli, "Thermal networks of induction motors for steady state and transient operation analysis," in *ICEM*, 1994, pp. 452–457.
- [51] E. S. (Essam S. . Hamdi, *Design of small electrical machines*. Wiley, 1994.
- [52] A. Boglietti and A. Cavagnino, "Analysis of the endwinding cooling effects in TEFC induction motors," *IEEE Trans. Ind. Appl.*, vol. 43, no. 5, pp. 1214–1222, 2007.
- [53] M. Markovic, L. Saunders, and Y. Perriard, "Determination of the Thermal Convection Coefficient for a Small Electric Motor," in *Conference Record of the 2006 IEEE Industry Applications Conference Forty-First IAS Annual Meeting*, 2006, vol. 1, pp. 58–61.
- [54] O. Meksi and A. O. Vargas, "Numerical and experimental determination of external heat transfer coefficient in small TENV electric machines," in *2015 IEEE Energy Conversion Congress and Exposition (ECCE)*, 2015, pp. 2742–2749.
- [55] A. Bejan and A. D. Kraus, *Heat Transfer Handbook*. John Wiley & Sons, 2003.
- [56] C. D. Jones and L. F. Smith, "Optimum Arrangement of Rectangular Fins on Horizontal Surfaces for Free-Convection Heat Transfer," *J. Heat Transfer*, vol. 92, no. 1, p. 6, 1970.

- [57] D. W. Van de Pol and J. K. Tierney, "Free Convection Nusselt Number for Vertical U-Shaped Channels," *J. Heat Transfer*, vol. 95, no. 4, p. 542, 1973.
- [58] I. Tari and M. Mehrtash, "Natural convection heat transfer from horizontal and slightly inclined plate-fin heat sinks," *Appl. Therm. Eng.*, vol. 61, no. 2, pp. 728–736, 2013.
- [59] I. Tari and M. Mehrtash, "Natural convection heat transfer from inclined plate-fin heat sinks," *Int. J. Heat Mass Transf.*, vol. 56, no. 1, pp. 574–593, 2013.
- [60] "Common Methods for Providing Cooling or Heat Dissipation in an Electric Motor | Kollmorgen." [Online]. Available: [https://www.kollmorgen.com/en-us/blogs/\\_blog-in-motion/articles/randy-wilson/common-methods-for-providing-cooling-or-heat-dissipation-in-an-electric-motor/](https://www.kollmorgen.com/en-us/blogs/_blog-in-motion/articles/randy-wilson/common-methods-for-providing-cooling-or-heat-dissipation-in-an-electric-motor/).
- [61] F. Kreith and D. Goswami, Eds., *The CRC Handbook of Mechanical Engineering, Second Edition*, vol. 20045273. CRC Press, 2004.
- [62] V. Matošević and Ž. Štih, "2D Magneto-thermal analysis of synchronous generator," *Przegľad elektrotechniczny*, vol. 2014, pp. 157–160, Mar. 2016.
- [63] Weili Li ; Junci Cao ; Fei Huo ; Jiafeng Shen, "Numerical analysis of stator-rotor coupled transient thermal field in induction motors with blocked rotor," in *Automation Congress, 2008, WAC 2008, World : date, Sept. 28 2008-Oct. 2 2008.*, 2008, pp. 1–6.
- [64] R.-J. Wang and G. C. Heyns, "Thermal analysis of a water-cooled interior permanent magnet traction machine," in *2013 IEEE International Conference on Industrial Technology (ICIT)*, 2013, pp. 416–421.
- [65] J. Driesen, R. Belmans, K. Hameyer, A. Arkkio, and T. Jokinen, "Efficient magnetic-thermal coupled simulation of electrical machines using a double combined FEM-circuit approach," in *International Conference on Electrical machines, ICEM'98, Istanbul, Turkey, 2-4 September, 1998*, 1998, pp. 1402–1407.
- [66] V. Hatzithanassiou, J. Xypteras, and G. Archontoulakis, "Electrical-thermal coupled calculation of an asynchronous machine," *Arch. für Elektrotechnik*, vol. 77, no. 2, pp. 117–122, Jan. 1994.
- [67] "Finite Element Method Magnetics: OctaveFEMM." [Online]. Available: <http://www.femm.info/wiki/octavefemm>.
- [68] R. Wrobel, P. H. Mellor, M. Popescu, and D. A. Staton, "Power loss analysis in thermal design of permanent magnet machines - A review," *IEEE Trans. Ind. Appl.*, vol. 52, pp. 1359–1368, 2015.
- [69] D. Eggers, S. Steentjes, and K. Hameyer, "Advanced iron-loss estimation for nonlinear material behavior," *IEEE Trans. Magn.*, vol. 48, no. 11, pp. 3021–3024, Nov. 2012.
- [70] A. Krings, S. Nategh, and A. Stening, "Measurement and modeling of iron losses in electrical machines," *Proc. 5th ...*, pp. 101–119, 2012.
- [71] B. Tekgun, "Analysis, Measurement and Estimation of the Core Losses in Electrical Machines," University of Akron, 2016.
- [72] M. J. Manyage and P. Pillay, "New Epstein frame for core loss measurements at high frequencies and high flux densities," in *Conference Record - IAS Annual Meeting (IEEE Industry Applications Society)*, 2008, pp. 1–6.
- [73] A. Belahcen and A. Arkkio, "Permanent magnets models and losses in 2D FEM simulation of electrical machines," in *19th International Conference on Electrical Machines, ICEM 2010*, 2010, pp. 1–6.

- [74] Y. Yang *et al.*, "Thermal management of electric machines," *IET Electr. Syst. Transp.*, vol. 7, no. 2, pp. 104–116, Jun. 2017.
- [75] W. M. Rohsenow, J. P. Hartnett, and Y. I. Cho, *Handbook of heat transfer*. McGraw-Hill, 1998.
- [76] A. Boglietti, A. Cavagnino, and D. A. Staton, "Thermal analysis of TEFC induction motors," in *38th IAS Annual Meeting on Conference Record of the Industry Applications Conference*, 2003, vol. 2, pp. 849–856.

## Acknowledgements

These PhD studies have been a truly life-changing experience for me that would not have been possible without the support and guidance that I received from many people.

First, I would like to extend my greatest thanks to my supervisors Prof. Anouar Belahcen and Dr Ants Kallaste who have always been ready to help and support me in research and life. Their excellent guidance and open attitude have encouraged me and shown how to go through this project.

For financial support, I would like to show my gratitude toward Estonia Research Council grant PUT (PUT1260) for financing my PhD study. Archimedes foundation (Dora Plus Program) and Doctoral School of Energy and Geotechnology III to provide the possibility to attend several conferences and courses.

All my colleagues from the Electrical Machine Group (EMG) and Tallinn University of Technology have earned my veneration for fruitful dissections and valuable ideas, which helped me to finalize the thesis.

I want to express my heartfelt thanks to my family and especially to my wonderful wife Fereshteh for always believing in me and encouraging me to follow my dreams.

Finally, I would like to thank all others who have helped me during the years but are not mentioned here.

## **Abstract**

### **Development of Thermal Analysis Tools for Synchronous Reluctance Motors**

The purpose of this thesis was to investigate the thermal behavior of the synchronous reluctance motors used in variable speed drive applications. The aim was to develop analytical and numerical thermal analysis tools to model the thermal behavior of the machine and apply them for design and optimization purposes.

There are various critical parameters in the thermal analysis of electrical machines, which affect the accuracy of the thermal models; most of them cannot be calculated by pure analytical or mathematical models. Consequently, in this thesis, the different critical parameters in the thermal analysis of the motor were considered, and the best solutions to overcome these problems are proposed.

An enormous part of heat is extracted by the convection phenomenon, the accurate determination of this factor during thermal analysis leads to higher accuracy of the thermal model. Accordingly, in the second part of this thesis, the different empirical correlations to evaluate the heat transfer coefficient from the different basic shapes during the active and passive cooling have been developed, and the most precise one was selected for each shape. The analytical calculation of the convection coefficient for the complex housing structure of the motor during the natural and forced cooling is described in detail based on the area-based composite correlation method.

In the next part of the thesis, the development of an analytical thermal analysis tool by using a lumped parameter thermal network is described in detail. Accordingly, all the heat transfer paths in the machine are modelled by using the thermal resistances, which represent conduction, convection, and radiation and the heat sources are presented as the current sources.

For the numerical part, the hybrid thermal model is proposed. This method consists of coupling the 2D finite element model of the active part of the machine with the lumped parameters thermal network of the end region of the machine to capture all the heat transfer paths in the machine by using the advantage of the finite element method and reducing the setup and computation time.

To validate and measure the accuracy of the analytical and numerical thermal tools, different experiments on a prototype synchronous reluctance motor were performed. The validation tests showed that the analytical, numerical, and experimental results are in good agreement, which proves the accuracy of the developed models.

The thesis research showed the importance of the thermal analysis for the estimation of the performance, efficiency, and reliability of the machine. The necessity of advanced future works on the topic is discussed and some tasks to develop the different options in the thermal analysis tools have been proposed.

## Kokkuvõte

### Soojusanalüüsi töövahendi väljaarendus sünkroon-reluktantsmootorile

Käesoleva töö eesmärgiks on uurida muutuva kiirusega ajamisüsteemides kasutatavate sünkroon-reluktantsmootorite soojuslikku käitumist. Eesmärgiks oli välja töötada analüütilistel ja numbrilistel meetoditel põhinevad temperatuuriarvutuse töövahendid, mille abil oleks võimalik modelleerida masina soojuslikke protsessi ning rakendada neid projekteerimise ja optimeerimise eesmärgil.

Elektrimasinate soojuslikes arvutustes esineb mitmeid kriitilisi parameetreid, mis mõjutavad soojuslikku mudeli täpsust ning enamikku neist ei saa määrata täpselt ainult analüütiliste või numbriliste arvutustega. Sellest lähtuvalt uuriti antud töös erinevaid kriitilisi elektrimasina soojuslikke parameetreid ning pakuti välja parimad lahendused, kuidas vajalikud väärtused leida.

Elektrimasina jahutamine toimub konvektsiooni ja soojuslikku kiirguse teel, mis tähendab, et ka antud parameetrite tegurite täpne määramine on oluline suure täpsusega soojuslikke arvutuste jaoks. Nende tegurite täpset määramist käsitletakse töö teises peatükis, kus uuritakse erinevaid olemasolevaid empiirilisi arvutusmeetodeid mainitud tegurite jaoks. Antud jahutustegureid uuritakse nii aktiiv- kui ka passiivjahutuse korral ning nende muutust vastavalt erinevatele põhipindadele. Vastavalt saadud tulemustele valiti välja kõige täpsemad arvutusmeetodid lähtudes jahutustingimustest ning põhipinnast. Lõpuks antakse keerulise kujuga elektrimootori korpuse pinna jaoks detailne kirjeldus konvektsiooniteguri analüütilisest arvutusest, lähtudes pindade liitkorrelatsiooni meetodist.

Töö järgmises osas töötatakse välja ning antakse detailne kirjeldus analüütilisest soojusarvutuse töövahendist, mis põhineb koondparameetrilisel soojusarvutusmeetodil. Vastavalt antud meetodile koostatakse aseskeem, mis koosneb soojuslikkest takistitest, mis omakorda kirjeldavad soojusjuhtivust, soojuslikku konvektsiooni ja soojuslikku kiirgust, ning soojusallikatest, mis esitatakse kui vooluallikad.

Numbriliste meetodite osas pakutakse välja hübriidne soojusarvutusmeetod. Antud meetod põhineb 2D lõplike elementide arvutusmeetodi ja koondparameetrilise soojusarvutusmeetodi kombineerimisel. 2D lõplike elementide arvutusmeetodit kasutatakse masina aktiivosa modelleerimiseks ning koondparameetrilist arvutusi kasutatakse laupühenduste modelleerimiseks. Antud hübriidmeetod võimaldab ära kasutada mõlema alammeetodi tugevaid külgi ning suurendab oluliselt elektrimasina soojuslikke arvutuste kiirust.

Kontrollimaks ning määramaks väljatöötatud temperatuuri tööriistade täpsused, viidi läbi erinevad katsed sünkroon-reluktantsmootori prototüübil. Valideerimiskatsed näitasid, et nii väljatöötatud analüütilised kui ka numbrilised arvutusmeetodid annavad hea tulemuse, mis tõestab väljatöötatud temperatuuriarvutustööriistade piisavat täpsust.

Lõputöö näitas soojuslikke arvutuste vajalikkust määramaks elektrimasina jõudlust, efektiivsust ja töökindlust. Töös on väljatoodud ka antud teemaga seotud olulised sammud, mis oleks vaja tulevikus teha ning on pakutud välja mõningad soovitusel antud tööriistade edasiarendamiseks.

# Appendix

## Publication I

P. Shams Ghahfarokhi, A. Belahcen, A. Kallaste, T. Vaimann, L. Gerokov, and A. Rassolkin, "Thermal Analysis of a SynRM Using a Thermal Network and a Hybrid Model," in *2018 XIII International Conference on Electrical Machines (ICEM)*, 2018, pp. 2682–2688.





# Thermal Analysis of a SynRM Using a Thermal Network and a Hybrid Model

P. Shams Ghahfarokhi, A. Belahcen, A. Kallaste, T. Vaimann, L. Gerokov, A. Rassõlkin

**Abstract** – This paper presents a lumped parameter thermal network and a hybrid model of a synchronous reluctance motor to predict the temperature of its different parts. The lumped parameter thermal network is developed and its parameters are calculated by simplified analytical correlations. The hybrid model consists of a 2D finite element model of the active part of the machine coupled with a lumped parameters thermal circuit of the end-winding region. A synchronous reluctance machine is used to validate the proposed approaches. The results from the proposed methods are compared with the experimental ones obtained from measurements on a prototype machine. The comparison shows a good agreement among the experimental result, analytical thermal network and hybrid model.

**Index Terms**—AC motors, Equivalent circuit, Finite element analysis, Lumped parameter network, Thermal analysis.

## I. INTRODUCTION

THE synchronous reluctance motor (SynRM) with transverse-laminated rotor construction is attracting the attention and interest of different users, due to its low cost, robustness, simple construction and manufacturing process [1], [2]. These types of motor are used in high torque, high speed and high dynamic applications, e.g., traction application.

According to the general expression of the torque in an electrical machine, the torque is proportional to the electrical loading and the magnetic loading [3]. In order to increase the torque, the electrical and magnetic loadings must be increased. However, due to the saturation of the stator iron in high flux density, the only practical way to increase the torque is by increasing the electrical loading, which can be achieved, by increasing the current density [3].

Higher current density means higher copper losses as well as the higher temperature of the motor. On the other hand, the lifetime of the insulation materials inside the slots highly depends on the temperature and is inversely proportional to it [4]. Therefore, the thermal design of the SynRM is more emphasized compared to other machine types.

The lumped parameter thermal network (LPTN) and the numerical analysis are the two main methods in thermal design and analysis of an electrical machine [5]. The LPTN is the common method to calculate the temperature of key components of the electrical machine. This method is a fast calculation method with an acceptable accuracy. The first LPTN was developed for the induction machine [6], [7] and [8]. In the following, Lindstrom in [9] developed the LPTN for a surface mounted permanent magnet synchronous machine (SPMSM). El-Refaie in [10], based on Lindstrom's work, developed an LPTN for an interior permanent magnet synchronous machine (IPMSM). In 2013, Nategh implemented an LPTN for a direct-cooled permanent magnet assisted synchronous reluctance motor (PMaSRM) [11].

The finite element analysis (FEA) and the computational fluid dynamic (CFD) are the two major numerical thermal design and analysis methods [5]. By using these two methods, any complex shape can be modeled. The FEA is suitable for accurate modeling of the heat losses distribution and thermal conduction in solid materials [12]. However, the convection and radiation phenomena are calculated by using the same empirical correlations as for the LPTN and they are implemented to the model as boundary condition [13]. The CFD is the most accurate method to model the heat transfer of an electrical machine. In addition to modeling the thermal conduction phenomenon in solid materials, it has an ability to model the fluid flow and convection phenomenon [11]. However, these two numerical methods need a high setup and computation time [14]. Therefore, using a hybrid thermal model, which is combining the advantages of the FEA and LPTN methods, can be an effective approach to model the heat transfer and analyze the thermal behavior of an electrical machine. In this approach, the active part of the electrical machine is modeled by an FE 2D method, and the end- region of the machine is modeled by an LPTN. Such a method leads to a reduced complexity of the model while achieving the benefit of the FEA in modeling the losses distribution and the thermal conduction phenomenon in the active part of the electrical machine.

---

This work was supported by the Estonian Research Council grant PUT (PUT1260).

Payam Shams Ghahfarokhi is with the Department of Electrical Power Engineering and Mechatronics, Tallinn University of Technology, Tallinn, Ehitajate tee 5, 19086 Estonia (e-mail: payam.shams@ttu.ee).

Anouar Belahcen is with the Department of Electrical Engineering and Automation, Aalto University, Espoo, 15500, 00076, Finland (e-mail: Anouar.Belahcen@aalto.fi).

Ants Kallaste is with the Department of Electrical Power Engineering and Mechatronics, Tallinn University of Technology, Tallinn, Ehitajate tee 5, 19086 Estonia (e-mail: ants.kallaste@ttu.ee).

Toomas Vaimann is with the Department of Electrical Power Engineering and Mechatronics, Tallinn University of Technology, Tallinn, Ehitajate tee 5, 19086 Estonia (e-mail: toomas.vaimann@ttu.ee).

Levon Gevorkov is with the Department of Electrical Power Engineering and Mechatronics, Tallinn University of Technology, Tallinn, Ehitajate tee 5, 19086 Estonia (e-mail: levon.gevorkov@ttu.ee).

Anton Rassõlkin is with the Department of Electrical Power Engineering and Mechatronics, Tallinn University of Technology, Tallinn, Ehitajate tee 5, 19086 Estonia (e-mail: anton.rassolkin@ttu.ee).

This paper focuses on the thermal analysis of a SynRM, which its cross-section illustrated in Fig. 1. Table I gives the design parameters of the motor and Table II presents the materials data. An LPTN of the machine is developed and the calculation of its parameters is thoroughly described. In hybrid method, a 2D FE model of the active part is developed and solved in parallel with an LPTN of the end region of the machine. In order to validate the LPTN and the hybrid models, a test bench is set up and measurements are conducted. The experimental results are then compared to these from both models.

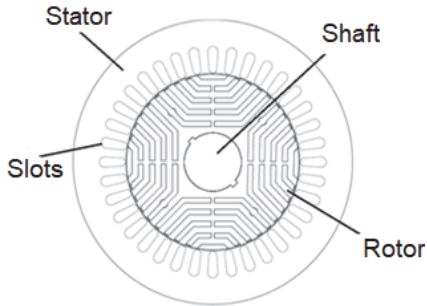


Fig. 1. The cross-section of the 11-kW transverse-laminated SynRM analyzed in this paper.

TABLE I  
DESIGN DATA OF THE TRANSVERSE- LAMINATED SYNRM

Parameter	Unit	Value
Rated power	<i>kW</i>	11
Rated speed	<i>rpm</i>	1500
Voltage	<i>V</i>	400
Pole pairs	-	2
Stator core length	<i>mm</i>	156
Stator outer diameter	<i>mm</i>	219
Number of slots	-	36
Air-gap height	<i>mm</i>	0.4
Rotor inner diameter	<i>mm</i>	45
Rotor outer diameter	<i>mm</i>	135.2
Coil height	<i>mm</i>	21
Slot filling factor	-	0.6
Slot area	<i>mm</i> <sup>2</sup>	130.1

TABLE II  
MATERIAL DATA OF THE TRANSVERSE- LAMINATED SYNRM

Machine part	Material	Thermal conductivity (W/mK)
Frame	Aluminum	230
Laminations	Electric steel	28
Winding	Copper	387
Impregnation	Resin	0.2
Air gap	Air	0.0257
Shaft	Steel	41

## II. LPTN METHOD

### A. LPTN Model

The SynRM with transverse laminated rotor referenced in the introduction part is used as the basis to develop the LPTN. To reduce the complexity of the model and increasing the computation speed, we introduced some simplifying hypothesis. The losses distribution is assumed uniform in the winding and the iron core. In the axial direction, the heat flux can only transfer through the shaft, end-winding and end regions of the machine. The heat flux distributions in both end regions of the machine are analogous.

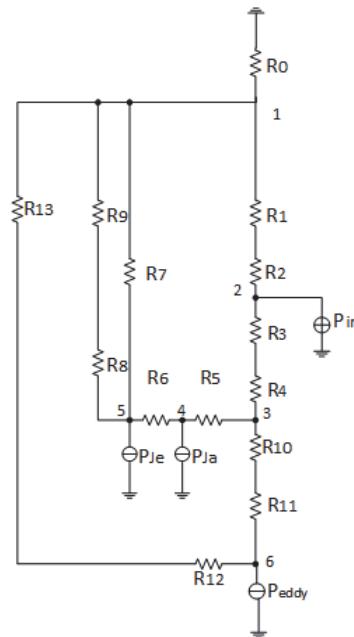


Fig. 2. The developed LPTN model of SynRM.

Figure 2 presents the steady-state LPTN developed for the machine under investigation. The model consists of six nodes and 14 thermal resistances, which capture all the key thermal parameters and temperature raises as well as the main thermal heat transfer paths. Table III gives the definition of the thermal model components of Fig. 2.

Since the SynRM has the same stator structure as an induction machine, the major difference between the developed LPTN in Fig. 2 and the thermal model of the induction machine proposed in [7] is the rotor part; precisely, the thermal resistances  $R_{11}$  and  $R_{12}$ . The detailed evaluation methods of the other thermal resistances in Table III can be found in [7] and is not described here.

TABLE III  
DEFINITION OF THE THERMAL MODEL COMPONENTS

Component	Description
$R_0$	Forced Convection and radiation thermal resistance from frame surfer to ambient
$R_1$	Interface gap conduction thermal resistance between the frame and the active part of the machine
$R_2$	Conduction thermal resistance of the upper half side of the stator yoke
$R_3$	Conduction thermal resistance of the lower half side of the stator yoke
$R_4$	Conduction thermal resistance of the stator teeth
$R_5$	Conduction thermal resistance between the stator winding and stator teeth
$R_6$	Conduction thermal resistance between the coil side and the end-windings
$R_7$	Conduction thermal resistance between the stator winding and the frame
$R_8$	Convection thermal resistances between the stator end-winding and the inner air of the end region
$R_9$	Convection thermal resistance between the inner air and the end cap
$R_{10}$	Convection thermal resistance of the air gap
$R_{11}$	Conduction thermal resistance of the upper half side of the rotor
$R_{12}$	Conduction thermal resistance of the lower half part of the rotor
$R_{13}$	Axial thermal conduction of the shaft
$P_{ir}$	Stator iron losses
$P_{Ja}$	Joule losses in the active part
$P_{Je}$	Joule losses in end-winding
$P_{eddy}$	Rotor iron losses

### B. Calculation of the Rotor Thermal Resistances

Figure 3 shows the geometry of a half of a pole of the SynRM rotor. The rotor construction consists of the iron laminations, which makes the magnetic flux paths and air gaps in the laminations, which are the magnetic flux barriers. Making the hypothesis that the heat transfer inside the flux barriers is carried out through natural convection and that the thermal conductivity of the rotor iron laminations is very high, we can neglect the heat transfer by the natural convection phenomenon from magnetic flux barriers. As a result, the total heat fluxes inside the rotor are transferred through the iron laminations.

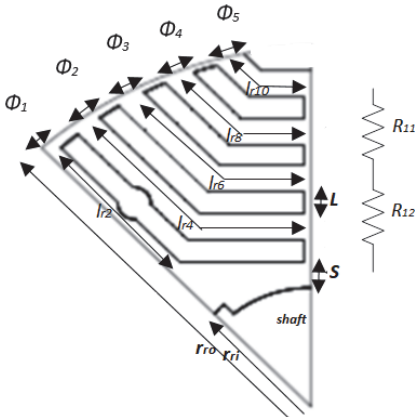


Fig. 3. Cross section of 1/8 of the rotor

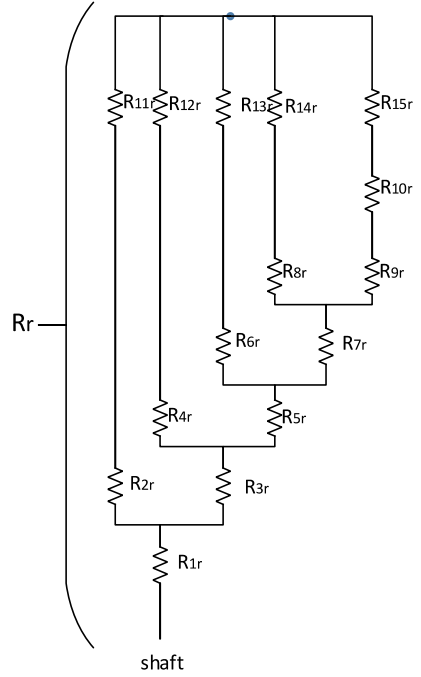


Fig. 4. The thermal equivalent circuit of the rotor

Figure 4 shows the equivalent thermal circuit for the calculation of the total thermal resistance from the rotor surface to the shaft, which is illustrated by  $R_r$ . Furthermore, the value of  $R_r$  is equal to the sum of the values of  $R_{11}$  and  $R_{12}$ . Accordingly,  $R_r$  consists of the series-parallel combinations of thermal resistances which the values of thermal resistances  $R_{11r}$  to  $R_{15r}$  are calculated by (2) and the rest are evaluated by (1). Finally, by using the series-parallel resistances law in the electrical circuit the value of  $R_r$  is calculated.

$$R = \frac{l}{\lambda \cdot A}, \quad (1)$$

$$R = \frac{\ln\left(\frac{r_o}{r_i}\right)}{\lambda \cdot L \cdot \phi}, \quad (2)$$

where  $l$  is the length of heat flux path (m),  $A$  is the cross-section area (m<sup>2</sup>),  $\lambda$  is the thermal conductivity of the material (W/m.K),  $r_o$  and  $r_i$  are the outer radius and the inner radius of a cylinder (m),  $L$  is the active length of the machine (m) and  $\phi$  is the angular span (rad).

### C. Solving the LPTN

For the steady-state thermal analysis, the final nodal temperatures of Fig. 2 can be calculated by the matrix inversion theory [15]. Accordingly, the nodal temperatures of the proposed thermal model are calculated as follow:

$$[T] = [G]^{-1}[P], \quad (3)$$

where  $[T]$  is the temperature column vector,  $[P]$  is the power column vector, which contains the losses at each node and  $[G]$  is the thermal conductance square matrix which is defined as:

$$G = \begin{bmatrix} \sum_{i=1}^n \frac{1}{R_{1,i}} & -\frac{1}{R_{1,2}} & \dots & -\frac{1}{R_{1,n}} \\ -\frac{1}{R_{2,1}} & \sum_{i=1}^n \frac{1}{R_{2,i}} & \dots & -\frac{1}{R_{2,n}} \\ \vdots & \vdots & \ddots & \vdots \\ -\frac{1}{R_{n,1}} & -\frac{1}{R_{n,2}} & \dots & \sum_{i=1}^n \frac{1}{R_{n,i}} \end{bmatrix}. \quad (4)$$

The  $G_{i,i}$  components in the main diagonal of the thermal conductance matrix are defined as the sum of the conductances connected to the  $i$ -th node and  $G_{i,j}$  is defined as the negative thermal conductances between nodes  $i$  and  $j$ .

### III. THE HYBRID THERMAL MODEL

The electrical machine can be modeled by the FEA in 2D and 3D format [16]. As mentioned, the 3D FEA is a time-consuming process and consist of several complex geometries setup e.g., end-windings, frame structures. Fig.5 shows the construction of the end region of the electrical machine. Accordingly, the machine construction is divided into two main sections: active and an end region. The 2D FEA can only model the heat transfer of the active part of the electrical machine and it does not take into account the effect of heat transfer from the end region of the electrical machine. Since the end region of electrical machine consists of the hottest spot, it has a great effect on the heat transfer. As a result, the 2D model cannot provide the correct view of heat transfer for the electrical machine. We implement a hybrid thermal model to remedy this problem and evaluate the amount of the heat power, which is transferred from the end region to the active part or vice-versa. The hybrid thermal model is constructed by coupling the 2D FE model with an LPTN model of the end region of the machine.

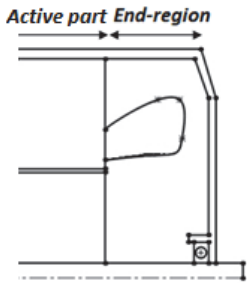


Fig. 5. Axial cross section of the machine

### A. The 2D FEA Thermal Model

In the hybrid thermal model of the electrical machine, the active part is modeled by using the 2D FEA. During the modeling process of the active part, we are facing two main challenges: first, defining the thermal conductivity of the slots and second implementing the convection and radiation phenomena into 2D FE model.

The slot of the electrical machine consists of several materials with different thermal conductivities e.g. copper conductors, the conductor insulation, the impregnation material and the slot insulation [5]. According to the small dimensions of slots and materials layer; it is impossible to model each material layer inside the slots. To solve this problem we define an equivalent thermal conductivity for the slot. The equivalent thermal conductivity of the slot is calculated by the analytical formulation from [17].

The heat is transferred from the exterior surface of the electrical machine to the ambient by the convection and radiation phenomena. These phenomena are implemented into the 2D FE model by defining the boundary layers on the outer surface of the model to describe the quality of the heat transfer from the outer surface of the machine to the ambient. Figure 1 shows the simplified cross-section of the machine, while its realistic cross-section consists of the axial cooling fins in the outer surface of the machine. In order to modify and implement the effect of the cooling fins; the equivalent heat transfer coefficient is calculated by the analytical formulation from [18].

### B. LPTN of End-Winding

To implement the effects of the end-windings on the total heat transfer of the machine as well as predicting the temperature of different parts of the SynRM, the equivalent thermal circuit of the end-winding is developed in parallel to the 2D FE Model.

Figure 6 shows the steady-state LPTN of the end-winding. This model consists of two nodes, five thermal resistance and one copper losses source, which capture all the key thermal parameters and temperature raises as well as the main thermal heat transfer paths in the end regions of the SynRM.

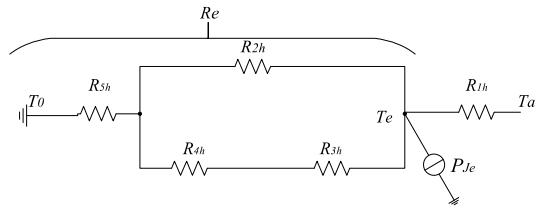


Fig. 6. LPTN of end winding.

Table III describes the definition of the thermal model components of Fig. 6. The value of the  $R_{th}$  is calculated by an analytical formulation from [9], [19]. The value of  $R_{2h}$  and  $R_{3h}$  are calculated by using the analytical correlations from [7].

TABLE IV  
DEFINITION OF END-WINDING THERMAL MODEL COMPONENTS

Component	Description
$R_{1h}$	Conduction thermal resistance between the midpoint of end-winding and the midpoint of coil side.
$R_{2h}$	Conduction thermal resistance between the stator winding and frame
$R_{3h}$	Convection thermal resistances between the stator end-winding and inner air of end region
$R_{4h}$	Convection thermal resistance between the inner air and end cap
$R_{5h}$	Total heat extraction thermal resistance from frame to ambient
$P_{Je}$	Stator end-winding joule losses
$T_a$	Average temperature of slots (from FE model)
$T_c$	Average temperature of end-windings (from LPTN model)

### C. Hybrid model calculation

We implement the hybrid thermal model to calculate and evaluate the temperature of the machine. In order to implement this method, the equivalent thermal circuit and the 2D FEA models must be coupled. For this purpose, we have defined the  $R_{1h}$ , which can be called the coupling resistance because connects the active part to the end region of the machine (Fig.6).

Figure 7 shows the final LPTN of the end-windings.

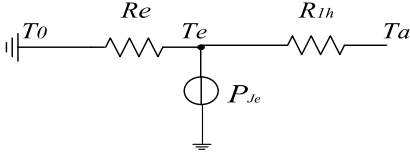


Fig. 7. Final LPTN of the end-winding.

According to Fig. 7, the temperature of the end-windings ( $T_c$ ), as well as the amount of the heat transfer from the end-windings to slots ( $P_{ex}$ ), are evaluated by applying the Kirchhoff current rule as follow:

$$T_e = \left( P_{Je} + \frac{T_0}{R_e} + \frac{T_a}{R_{1h}} \right) (R_{1h} + R_e) , \quad (5)$$

$$P_{ex} = \frac{T_e - T_a}{R_{1h}} . \quad (6)$$

Figure 8 shows the flowchart of the hybrid model calculation. In the first calculation step the average temperature of the slots  $T_a$  are calculated with the 2D FE model. Next  $T_c$  is calculated by using the value of  $T_a$  and (5). Finally, the amount of heat transfer  $P_{ex}$  from the end-windings to the slot is evaluated by (6). In the next calculation step, the amount of  $P_{ex}$  is added to the active copper losses and inserted into the 2D FE model. This loop will continue until the difference between  $T_c$  of the new step with previous one is less than the defined tolerance value  $\epsilon$  ( $\epsilon=0.01K$ ).

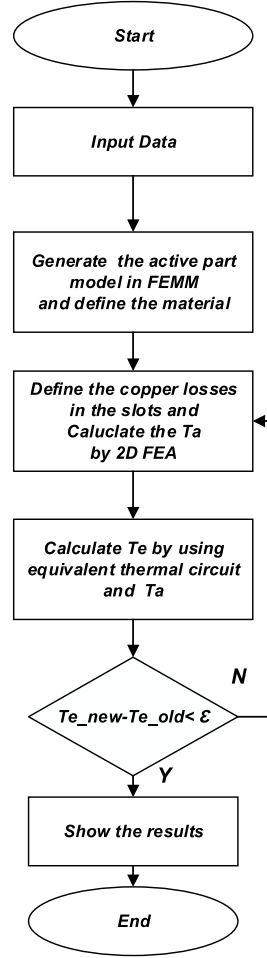


Fig. 8. The flow chart of hybrid model calculation.

## IV. EXPERIMENTAL METHODOLOGY

The objective of the experimental work is to validate both the LPTN and the hybrid model. In addition, the accuracy of each method to predict the temperature of different components of the machine is determined.

For the experimental work, the SynRM is operated under no load condition. For this purpose, the SynRM is synchronized to the grid with an induction machine, which is disconnected from the SynRM after synchronization. The purpose is to operate the SynRM under sinusoidal grid supply as to conserve the same voltage and thus the same iron losses.



Fig. 9. Test setup.

Figure 9 shows the experimental setup. During the experiment, the active power, RMS value of the current and voltage, temperature and power factor of each phase, are measured with a data acquisition system (Dewetron). The SynRM has been equipped with six PT100 thermal sensors. Three sensors have been located in the end winding section of each phase and three others have been installed inside the slots. The motor surface temperature has been measured by infrared laser digital thermometer.

## V. RESULTS AND DISCUSSION

In order to verify the developed LPTN and hybrid thermal model, the steady state temperature results are compared with the experimental results.

During the experiment, when the machine reached its steady-state mode, the outer frame surface and ambient temperatures and total input power have been measured. In the steady state mode, the input power was 220.5 (W) and the mean temperature of the frame surface was 26.7 (°C).

Table V shows the LPTN, hybrid model, and experimental results. Both the LPTN and the hybrid model results show good agreement with the experimental results, confirming the reliability of the proposed SynRM thermal models.

TABLE V  
ANALYTICAL LPTN, HYBRID MODEL AND EXPERIMENT RESULTS

Machine components	LPTN Results	Hybrid model Results	Experiment Results
Frame surface (°C)	25.9	29.1	26.7
Winding (°C)	34.1	33.2	33
End winding (°C)	35.9	33.7	33.6

The relative difference of LPTN results for the surface temperature, slot winding and end-winding are 3%, 3.3% and 6.8% respectively. These difference in the LPTN arise from the hypothesis of the uniform distribution of losses in the machine as well as from the fact that the LPTN model predicts the mean temperature of the machine component while in the experimental part, the thermocouples show the temperatures at given positions. This fact is illustrated in Fig. 10, which shows the temperature distribution over the frame surface of the SynRM in the steady-state mode. The picture is captured by a thermal camera. The figure gives a good overview of the temperature difference on the frame surface of the SynRM.

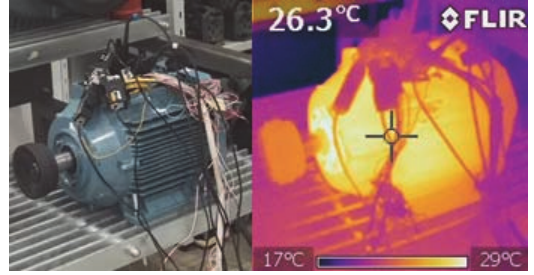


Fig. 10. Temperature distribution over the frame surface.

The relative difference of the same components by the hybrid thermal model are 9%, 0.6% and 0.3% respectively. Fig. 11 shows the temperature distribution in the active part of the machine. The relative difference in the surface temperature arises from the assumption that the mean temperature of the active part of the frame is assumed as the surface temperature.

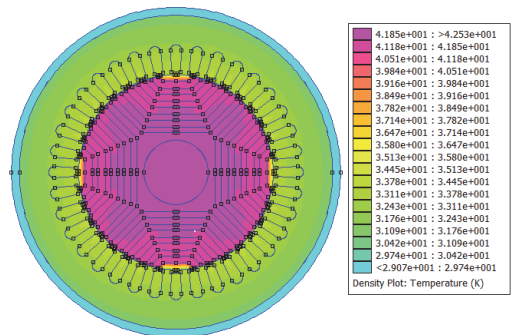


Fig. 11. Temperature distribution in the active part of the machine by using the hybrid model.

The comparison of the LPTN results with the hybrid model indicates that the accuracy of the hybrid model in predicting the slots and the end winding temperature is higher than that of the LPTN.

## VI. CONCLUSION

The focus of this paper has been to develop an LPTN and a hybrid thermal model. The LPTN has been developed through some simplifying hypotheses. The hybrid model consists of a 2D FE model for the active part of the machine and an LPTN for the end-region section, which makes it possible to predict the temperature rise of the different sections of the electrical machine e.g., end-windings, slots, rotor, stator teeth, and yoke.

The experimental results of the SynRM under no load operation have been compared to the LPTN predicted temperatures and hybrid model. The agreement between the LPTN temperatures and hybrid model temperatures and the measured ones seems to be very good. For the future job, the thermal model of the machine will be adjusted to predict the temperature of the machine under load and normal operation of the machine.

## VII. REFERENCES

- [1] N. Bianchi, "Synchronous Reluctance and PM Assisted Reluctance Motors," Springer, Cham, 2016, pp. 27–57.
- [2] A. Boglietti, A. Cavagnino, M. Pastorelli, D. Staton, and A. Vagati, "Thermal analysis of induction and synchronous reluctance motors," *IEEE Trans. Ind. Appl.*, vol. 42, no. 3, pp. 675–680, May 2006.
- [3] B. Mecrow, "Design of Machines and Drives," Newcastle upon tyne, 2011.
- [4] Y. C. Chong, "Thermal Analysis and Air Flow Modelling of Electrical Machines," University of Edinburgh, 2015.
- [5] P. S. Ghahfarokhi, A. Kallaste, A. Belahcen, T. Vaimann, and A. Rassolkina, "Review of thermal analysis of permanent magnet assisted synchronous reluctance machines," in *2016 Electric Power Quality and Supply Reliability (PQ)*, 2016, pp. 219–224.
- [6] P. H. Mellor, D. Roberts, and D. R. Turner, "Lumped parameter thermal model for electrical machines of TEFC design," *IEE Proc. B Electr. Power Appl.*, vol. 138, no. 5, p. 205, 1991.
- [7] A. Boglietti, A. Cavagnino, M. Lazzari, and M. Pastorelli, "A simplified thermal model for variable-speed self-cooled industrial induction motor," *IEEE Trans. Ind. Appl.*, vol. 39, no. 4, pp. 945–952, Jul. 2003.
- [8] G. Kylander, "Thermal modelling of small cage induction motors," Chalmers University of Technology, 1995.
- [9] J. Lindström, "Thermal Model of a Permanent-Magnet Motor for a Hybrid Electric Vehicle," CHALMERS UNIVERSITY OF TECHNOLOGY, Goteborg, 1999.
- [10] A. M. EL-Refaie, N. C. Harris, T. M. Jahns, and K. M. Rahman, "Thermal Analysis of Multibarrier Interior PM Synchronous Machine Using Lumped Parameter Model," *IEEE Trans. Energy Convers.*, vol. 19, no. 2, pp. 303–309, Jun. 2004.
- [11] S. Nategh, Z. Huang, A. Krings, O. Wallmark, and M. Leksell, "Thermal Modeling of Directly Cooled Electric Machines Using Lumped Parameter and Limited CFD Analysis," *IEEE Trans. Energy Convers.*, vol. 28, no. 4, pp. 979–990, Dec. 2013.
- [12] A. Boglietti, A. Cavagnino, and D. Staton, "Determination of critical parameters in electrical machine thermal models," *IEEE Trans. Ind. Appl.*, vol. 44, no. 4, pp. 1150–1159, 2008.
- [13] A. Boglietti, A. Cavagnino, and D. A. Staton, "TEFC induction motors thermal models: A parameter sensitivity analysis," *IEEE Trans. Ind. Appl.*, vol. 41, no. 3, pp. 756–763, May 2005.
- [14] S. Nategh, O. Wallmark, M. Leksell, and S. Zhao, "Thermal analysis of a PMaSRM using partial FEA and lumped parameter modeling," *IEEE Trans. Energy Convers.*, vol. 27, no. 2, pp. 477–488, Jun. 2012.
- [15] P. S. Ghahfarokhi, A. Kallaste, A. Belahcen, and T. Vaimann, "Steady state and transient thermal analysis of the stator coil of a permanent magnet generator," in *2017 18th International Scientific Conference on Electric Power Engineering (EPE)*, 2017, pp. 1–5.
- [16] V. Matošević and Ž. Štihi, "2D Magneto-thermal analysis of synchronous generator," *Przegľad elektrotechniczny*, vol. 2014, pp. 157–160, Mar. 2016.
- [17] M. Popescu, D. Staton, D. Dorrell, F. Marignetti, and D. Hawkins, "Study of the thermal aspects in brushless permanent magnet machines performance," in *2013 IEEE Workshop on Electrical Machines Design, Control and Diagnosis (WEMDCD)*, 2013, pp. 60–69.
- [18] V. Hatziaathanassiou, J. Xypteras, and G. Archontoulakis, "Electrical-thermal coupled calculation of an asynchronous machine," *Arch. für Elektrotechnik*, vol. 77, no. 2, pp. 117–122, Jan. 1994.
- [19] P. S. Ghahfarokhi, A. Kallaste, A. Belahcen, T. Vaimann, and A. Rassolkina, "Hybrid Thermal Model of a Synchronous Reluctance Machine," *Case Stud. Therm. Eng.*, May 2018.

## VIII. BIOGRAPHIES

**Payam Shams Ghahfarokhi** was born in Iran, in 1986. He received the B.Sc. degree in electrical power engineering from IAUN in 2010 and the M.Sc. degree in electrical power engineering from university of Newcastle upon Tyne in 2011. He is currently a Ph.D. student at Tallinn University of Technology. He has been the student IEEE member since 2017. His main field of interests is design of permanent magnet electrical machine and thermal design of electrical machine.

**Anouar Belahcen** (M13-SM15) received the M.Sc. (Tech.) and Doctor (Tech.) degrees from Helsinki University of Technology, Finland, in 1998, and 2004, respectively. He is now Professor of electrical machines at Tallinn University of Technology, Estonia and Professor of Energy and Power at Aalto University, Finland. His research interest are numerical modeling of electrical machines, magnetic materials, coupled magneto-mechanical problems, magnetic forces, magnetostriction, and fault diagnostics

**Ants Kallaste** was born in Pärnu, Estonia in 1980 and received his B.Sc., M.Sc., and Ph.D. degrees in electrical engineering from Tallinn University of Technology, Estonia, in 2004, 2006, and 2013, respectively. He is currently a Senior Researcher in Tallinn University of Technology, Department of Electrical Engineering and carrying out postdoctoral research at the Department of Electrical Engineering and Automation, Aalto University, Espoo, Finland. He has been working in several companies as an Electrical Engineer. Presently he is working at the Tallinn University of Technology, Department of Electrical Engineering holding the position of Head of Chair of Electrical Machines. He has been the IEEE member since 2013. His main research interests include permanent magnet machine design and wind turbines.

**Toomas Vaimann** (S'11-M'14) was born in Pärnu, Estonia, in 1984 and received his B.Sc., M.Sc., and Ph.D. degrees in electrical engineering from Tallinn University of Technology, Estonia, in 2007, 2009, and 2014, respectively. He is currently a Senior Researcher in Tallinn University of Technology, Department of Electrical Engineering and carrying out postdoctoral research at the Department of Electrical Engineering and Automation, Aalto University, Espoo, Finland. He has been working in several companies as an Electrical Engineer. He is the member of IEEE, Estonian Society of Moritz Hermann Jacobi and Estonian Society for Electrical Power Engineering. His main research interest is the diagnostics of electrical machines.

**Levon Gevorgov** is a researcher at Tallinn university of Technology. He was educated at the Ivane Javakishvili State University of Tbilisi, where he received the B.S. and M.S. degrees in radio-physics and electronics, in 2001 and 2003, respectively. In 2017 he received his PhD degree from Tallinn University of Technology. He has been working in several companies as an engineer. Presently he is working at the Tallinn University of Technology, Department of Electrical Power Engineering and Mechatronics as a research scientist. He has been IEEE member since 2016. Main scientific interests lay in the field of electric drives and pumping systems, machine vision and robotics

**Anton Rassõlkin** (S'12-M'16). was born in Tallinn, Estonia, in 1985 and received the BSc, MSc and PhD degrees in electric drives and power electronics from Tallinn University of Technology, Tallinn, Estonia, in 2008, 2010 and 2014, respectively. In 2010 received Dipl.-Ing. (FH) degree in automatic from University of Applied Science Giessen-Friedberg, Giessen, Germany. He has been working in several companies as an electrical engineer. Presently he is working at the Tallinn University of Technology, Department of Electrical Engineering as a research scientist. He is the member of IEEE The main research interests lay in the field of electric drives and its control systems as well as in the fields of electrical machines and electric transportation.





**Publication II**

P. Shams Ghahfarokhi, A. Kallaste, T. Vaimann, A. Rassolkin, and A. Belahcen, "Determination of natural convection heat transfer coefficient over the fin side of a coil system," *Int. J. Heat Mass Transf.*, vol. 126, pp. 677–682, Nov. 2018.





## Determination of natural convection heat transfer coefficient over the fin side of a coil system



Payam Shams Ghahfarokhi<sup>a,\*</sup>, Ants Kallaste<sup>a</sup>, Toomas Vaimann<sup>a</sup>, Anton Rassolkin<sup>a</sup>, Anouar Belahcen<sup>a,b</sup>

<sup>a</sup> Dept. Electrical Power Engineering and Mechatronics, Tallinn University of Technology, Tallinn, Estonia

<sup>b</sup> Dept. of Electrical Engineering and Automation, Aalto University, Finland

### ARTICLE INFO

#### Article history:

Received 15 August 2017

Received in revised form 9 April 2018

Accepted 14 May 2018

Available online 19 May 2018

#### Keywords:

Empirical correlation

Heat transfer

Natural convection

Plate fin array

### ABSTRACT

This paper presents a thermal study to define the appropriate correlations allowing the determination of the convective heat transfer coefficient over large parallel rectangular fins for a permanent magnet synchronous generator coil. For this purpose, an experimental setup is developed for both horizontal and vertical orientations and different input currents. The experimental results are compared with the analytical method, based on correlations proposed in the literature, which are generally limited for a small range of heat sinks. The results show that the analytical calculation based on Jones' correlation for the horizontal case and Tari's correlation for the vertical case, have good agreement with the experimental data. These correlations are experimentally validated for the calculation of the natural convection coefficients of large rectangular fins arrangement too.

© 2018 Elsevier Ltd. All rights reserved.

### 1. Introduction

The extended surface, which is called a fin is the preferred cooling method in the natural convection mode to enhance the heat transfer rate between the surface and the cooling fluid in electrical machines and other electrical devices. The fin and heat sink technologies are a subset of the passive cooling methods and have several advantages over the active ones, such as energy saving, affordability, reliability, and ease of manufacturing [1].

Rectangular cross section shaped plate fins on a flat base are the most common types of fins used in different electrical devices. In the natural convection mode, the characteristics of fins, e.g., length, height, and spacing between the fins play an important role on the maximum heat transfer rate. Therefore, there is a number of studies dedicated to find out the optimal parameters of the fin's geometry. Based on these findings, other studies have tried to define empirical correlations to determine the convection coefficient [2]. The parallel rectangular cross section fins on a flat base are generally used in vertical and horizontal configurations. There are many studies focused on finding the amount of natural heat transfer either experimentally or analytically. E.g., Jones and Smith [3], Van Del Pol and Tierney [4], Elenbaas [5], Rao [6], Baskaya [7] and Tari [2,8].

On the other hand, according to other studies, e.g., Rao [6], Ahmadi [1] and Boglietti [9], between 20 and 40% of the total heat transfer is extracted by the radiation phenomenon. Thus, the radiation heat extraction in parallel with the natural convection has a great effect on the total heat dissipation.

As mentioned above, there is a number of empirical correlations to calculate the natural heat transfer from parallel arrangement of rectangular cross section plate fins on a flat base in both horizontal and vertical configurations. Each of these correlations have been developed based on different ranges of Rayleigh number ( $Ra$ ), Prandtl number ( $Pr$ ) and fin's characteristics. Most of these correlations have been developed and used for small fins' size and spacing. In large electrical machines and devices, the fins' size and spacing are increasing. Therefore, it is important to find the appropriate correlation among the existing ones, which can describe the heat dissipation in these cases.

In this paper, we determine the appropriate correlations for large electrical machines with rectangular flat fin arrangements in horizontal and vertical orientations by means of analytical and experimental methods, based on the correlations proposed in the literature, which are generally limited to a small range of heat sinks. We also consider the impact of the fin on the natural heat transfer and the temperature of the plate fin array. For this purpose, one segment of the stator coil of a permanent magnet synchronous generator consisting of rectangular fin arrangements is investigated in both horizontal and vertical configurations.

\* Corresponding author.

E-mail address: [payam.shams@ttu.ee](mailto:payam.shams@ttu.ee) (P.S. Ghahfarokhi).

**2. Empirical correlations**

There are many empirical correlations for the rectangular fin arrangement with flat base. In this paper, the empirical correlations based on the scientific research of Jones and Smith [3], Van Del Pol and Tierney [4] and Tari [2,8] are discussed. According to Fig. 1, the configurations investigated are divided into two main categories: rectangular isothermal fins on a horizontal surface and rectangular isothermal fins on a vertical surface [10].

**2.1. Rectangular isothermal fins on a horizontal surface**

Fig. 1a shows rectangular fins on a horizontal surface. In 1970, Jones and Smith derived an empirical correlation to determine the natural heat transfer from horizontal fins [3]. They assumed the fins as U-shape horizontal channels and based on this assumption they developed their correlation by using the dimensionless Nusselt number

$$Nu = 0.00067 \cdot Gr \cdot Pr \cdot \left\{ 1 - e^{(-7640/Gr \cdot Pr)^{0.44}} \right\}^{1.7}, \tag{1}$$

where *Gr* is Grashof number and *Pr* is Prandtl number.

In this case, they have defined the fin space (*S*) as the characteristic length. According to (1), the Nusselt number is determined without considering the fins' size.

While in [8], Tari and Mehrtash defined an empirical correlation for the natural heat transfer from upward horizontal plate-fin heat sinks according to the fin characteristics. For this purpose, they defined a modified Grashof number as:

$$Gr' = Gr \cdot \left(\frac{H}{L}\right)^{0.5} \cdot \left(\frac{S}{H}\right)^{0.38}, \tag{2}$$

where *H* (m) and *L* (m) are respectively the fin height and length. The Nusselt number is then expressed as:

$$Nu = 0.0915 \cdot (Gr' \cdot Pr)^{0.436}. \tag{3}$$

**2.2. Rectangular isothermal fins on a vertical surface**

The rectangular isothermal fins on vertical base plate is the common heat sink configuration. A number of research have been published about calculating the natural heat transfer from this configuration. One of the earliest research about this configuration is back to Van De Pol research in 1973. In [4], he also described the vertical fin configuration as a U-shape vertical channel. In this case, the Nusselt number was defined as:

$$Nu = \frac{r}{H} \cdot \frac{Gr \cdot Pr}{Z} \cdot \left[ 1 - e^{-Z \cdot \left(\frac{0.5}{(\frac{r}{H})^2 \cdot Gr \cdot Pr}\right)^{0.75}} \right], \tag{4}$$

where *Z* is defined as:

$$Z = 24 \cdot \frac{1 - 0.483 \cdot e^{-0.17/Z}}{\left[ (1 + \alpha/2) \cdot (1 + (1 - e^{-0.83 \cdot \alpha}) \cdot (9.14 \cdot \sqrt{\alpha} \cdot e^{-465 \cdot S} - 0.61)) \right]^3}, \tag{5}$$

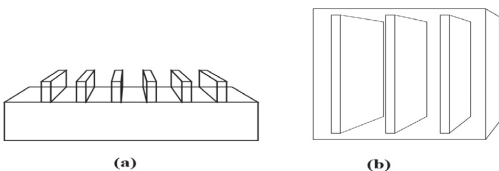


**Fig. 1.** Investigated configurations: (a) rectangular isothermal fins on a horizontal surface, (b) rectangular isothermal fins on a vertical surface.

$\alpha$  is the channel aspect ratio and *r* (m) the characteristic length.

In [2], Tari and Mehrtash introduced a new empirical correlation for the calculation of the Nusselt number from a vertical heat sink. They defined a new modified Grashof number as:

$$Gr' = Gr \cdot \left(\frac{H}{L}\right)^{0.5} \cdot \left(\frac{S}{H}\right), \tag{6}$$

and based on the modified Grashof number, they defined the Nusselt number as:

$$Nu = 0.0929 \cdot (Gr' \cdot Pr)^{0.5} \text{ for } Gr' \cdot Pr < 250, \tag{7a}$$

$$Nu = 0.2413 \cdot (Gr' \cdot Pr)^{1/3} \text{ for } 250 < Gr' \cdot Pr < 10^6. \tag{7b}$$

Finally, the natural convection coefficient *h<sub>c</sub>* is calculated from the Nusselt number as [11]:

$$h_c = \frac{Nu \cdot k}{L_c}, \tag{8}$$

where *k* (W/m K) is the fluid thermal conductivity and *L<sub>c</sub>* (m) is the characteristic length of the cooling surface.

**3. Experimental setup and procedure**

The objective of the experimental work in this paper is to assess the natural heat transfer coefficient from the fin section of the stator coil of a permanent magnet generator in the horizontal and vertical orientations. Yet another objective is to compare the analytical data to experimental data for finding the appropriate empirical correlation in both cases and verify the accuracy of these correlations.

From previous research works [12] and [13], the stator coil used in this investigation consists of six different faces as shown in Fig. 2. To consider the natural convection from the fin's side, the heat flux flow should be confined only to the fin side. To achieve this, we created an insulation box according to the dimensions of the coil by means of foam insulation boards with thickness of 10 cm. Fig. 3 shows the coil box and the fins' side of the coil in vertical and horizontal configurations. Since the foam insulation material has low thermal conductivity *k* = 0.3 (W/m K), the thermal flux flow is restricted to the open surface. Therefore, the box is operating as a semi-closed calorimeter. Another important point about the box is the temperature operation point; as the foam insulation board can handle temperatures up to 90 °C, during the experiment, the coil temperature should not exceed that temperature. Furthermore, in order to protect the test bench from external heating source and bulk fluid motion as well as increasing the accuracy of the results, the experimental setup is located in a closed room

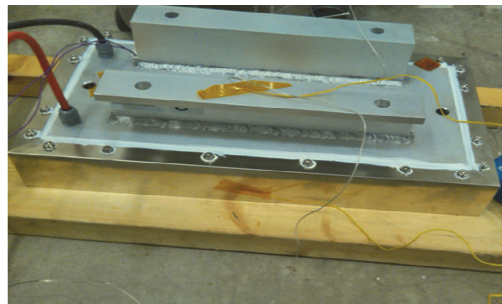


**Fig. 2.** The coil module used in the experimental work.

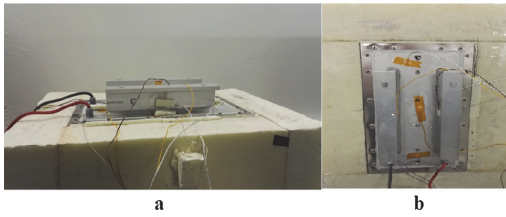


Fig. 3. The used configurations in the experiment: Coil module inside the coil box in (a) horizontal position (b) vertical position.

and the environment temperature of room is monitor by an extra thermocouple.

The fin side of the coil module is constructed from aluminum with a thermal conductivity of 171 (W/m K) and an emissivity of 0.5. The test bench is designed to measure the natural convection coefficient from the fin's side of the coil module. For this purpose, we use the DC test method. The DC test is a common experimental method for determining the convection coefficient of heat transfer. In this test, the loss of the coil is confined to the joule loss of the coil winding and the power can be easily calculated from the measured electric quantities. In the calculations, we accounted for the variations in the winding electrical resistance, as the winding resistivity is temperature dependent [12,14]. During the experiments, in addition to the power input to the coil module, the temperature of the fins side is measured at different locations. The Coil module is supplied through a digitally-controlled DC power supply. The voltage and the current are measured to determine the input power, which is equal to the heat power. Seven K-type thermocouples are installed by means of adhesive material in various locations on the fin side of the coil module. The ambient temperature is also measured by means of a K-type thermocouple. For the purpose of increasing the accuracy of the temperature measurement and minimizing the contact resistance between the thermocouple and the coil module surface, we used a commercial thermal paste. The average temperature of these seven thermocouples is assumed to be the mean temperature of the fin side of the coil module. This assumption is based on the observed measurements, where the mean difference between the temperatures of the seven thermocouples is 1% and is less than 0.5% in most cases. During the experiments, all the temperature data are collected by means of a Graphtec GL200 logger. The experiment has been carried out for each current input until the system reached its steady state condition. For each of the configurations, the experimental procedure is repeated for five different current inputs: 10, 12, 15, 17 and 20 Amps.

#### 4. The analysis method of experimental data

The total heat produced in the coil is equal to the total input power. Thus, the total heat in Watts (W) is defined as:

$$Q_T = V \cdot I, \quad (9)$$

where  $V$  (V) is the input voltage and  $I$  (A) the input current.

Accordingly, the total heat is extracted by means of the natural convection and radiation phenomena. Thus, the total heat can be described as:

$$Q_T = Q_c + Q_r, \quad (10)$$

where  $Q_c$  (W) is the amount of heat extracted by natural convection and  $Q_r$  (W) is the amount of heat extracted by radiation.

According to [15] and [16] the heat extraction coefficient  $h_e$  is calculated as:

$$h_e = \frac{Q_T}{(T_s - T_a) \cdot A}, \quad (11)$$

where  $T_s$  ( $^{\circ}\text{C}$ ) is the mean temperature of the fin side of the coil module,  $T_a$  ( $^{\circ}\text{C}$ ) is the ambient temperature and  $A$  ( $\text{m}^2$ ) is the fin side surface area.

The total heat extraction coefficient is defined as the sum of the convection  $h_c$  and radiation  $h_r$  coefficients:

$$h_e = h_c + h_r. \quad (12)$$

The radiation coefficient is defined as [16]:

$$h_r = \varepsilon \cdot \sigma \cdot (T_s^2 + T_a^2) \cdot (T_s + T_a), \quad (13)$$

where  $\varepsilon$  is the emissivity of the surface and  $\sigma = 5.67 \times 10^{-8}$  ( $\text{W}/\text{m}^2 \text{K}^4$ ) is the Stefan-Boltzmann constant.

#### 4.1. Uncertainty analysis of experimental results

In this section, we determined the total accuracy of experimental data according to the accuracy of the measurement instruments. During the experiment, the voltage and current are measured with the Tti QPX1200S. The accuracy of the voltage and current readings are 0.1% and 0.3% respectively. Furthermore, the standard accuracy of the K-type thermocouple is 0.75%. According to [1], the power uncertainty is evaluated as:

$$\omega_{Q_T} = \left[ \left( \frac{\partial Q_T}{\partial V} \cdot \omega_V \right)^2 + \left( \frac{\partial Q_T}{\partial I} \cdot \omega_I \right)^2 \right]^{0.5}, \quad (14)$$

where  $\omega_{Q_T}$ ,  $\omega_V$  and  $\omega_I$  are the uncertainties in the total input power, voltage and current.

This leads to the uncertainty for the computed convection coefficient as:

$$\omega_h = \left[ \left( \frac{\partial h}{\partial Q_T} \cdot \omega_{Q_T} \right)^2 + 2 \cdot \left( \frac{\partial h}{\partial T} \cdot \omega_T \right)^2 \right]^{0.5}, \quad (15)$$

where  $\omega_T$  is the uncertainty in the temperature measurement.

#### 5. Analytical calculation method

Fig. 4 shows the actual shape of the fin side of the coil module and the modified shape used in the theoretical calculations. The actual fin is divided into two sections; the fin section and the flat plate surface. The module consists of two fins spaced by  $S = 86$  mm. The fin's height is  $H = 62.7$  mm, its thickness is  $D_{fin} = 10$  mm, and its length is  $L_{fin} = 265$  mm. The width of the L-shaped plate on top of the fin is  $W_L = 38$  mm. The width of the coils module is  $W = 222$  mm and its length  $L_{coil} = 419$  mm. Therefore, the convection coefficient for each section is calculated separately and finally, the equivalent convection coefficient is calculated according to the area of each section. It should be noted that the actual setup consists of L-shaped fins. However, the upper part of the fin is for mechanical support purpose only. The effect of this part on the heat convection coefficient has been estimated through 2D finite element computations. It turns out that this part participated in the heat transfer, as it dissipated 13.8% of the total heat in average, resulting in a temperature difference of 3.7%. Therefore, this shape has been replaced in the experimental calculations by an equivalent increased length of the fins, so that the same amount of heat is dissipated through the additional length. However, this change in the length affected very little the calculation of the heat transfer coefficient (less than 1% difference, which is lower than the measurement uncertainty).

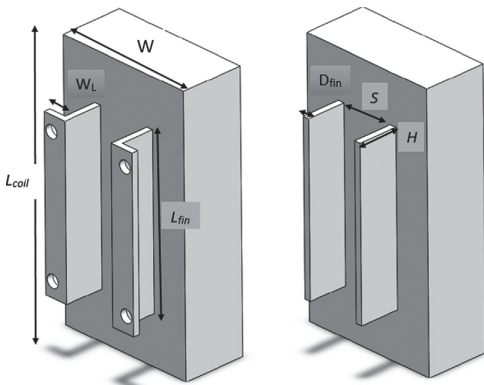


Fig. 4. Illustration of the investigated setup: (a) Actual module format (b) simplified format. The indicated dimensions are given in the text.

According to the theory of convection from a flat plate, the Nusselt number empirical correlations for the horizontal upward and vertical configurations are defined respectively as [17] and [18]:

$$Nu = 0.54(Gr \cdot Pr)^{0.25}, \tag{16}$$

$$Nu = \left\{ 0.825 + \frac{0.387(Gr \cdot Pr)^{0.25}}{[1 + (0.492/Pr)^{9/16}]^{8/27}} \right\}^2. \tag{17}$$

Therefore, the equivalent convection coefficient is defined as:

$$h_c = \frac{h_1 \cdot A_1 + h_2 \cdot A_2}{A_T}, \tag{18}$$

where  $h_1$  ( $W/m^2 C$ ) is the convection coefficient from fin section,  $h_2$  ( $W/m^2 C$ ) is the convection coefficient from the flat section,  $A_1$  ( $m^2$ ) is the surface area of the fin sections,  $A_2$  ( $m^2$ ) is the surface area of the flat plate.  $A_T$  ( $m^2$ ) is the total surface area.

6. Results and discussion

The validation of the empirical correlations is made by comparison with experimental data for the five input currents for both horizontal and vertical configurations. We present the analytical and experimental results according to the coils module's orientation.

In the experimental part, the fin side of the coil module is studied in both horizontal and vertical cases. To determine the convection coefficient from the experimental data; first, the total heat  $Q_T$  is calculated by Eq. (9), then according to the ambient and surface temperatures of the case study, the total heat extraction coefficient  $h_e$  and radiation coefficient  $h_r$  are determined respectively by Eqs. (11) and (13). Finally, the natural convection coefficient  $h_c$  is calculated by Eq. (12).

For the analytical part, according to the coil module orientation, the appropriate empirical correlations are used to calculate the natural convection coefficient  $h_c$ . The fin side of the coil module consists of two different sections: the flat part and the fin section. Therefore, the amount of the natural convection is calculated separately for each section. To calculate the natural convection coefficient  $h_1$  of the model, according to the model's configuration, the Nusselt number  $Nu$  for the fin section was calculated by Eqs. (1) and (3) in the horizontal case or Eq. (4), Eq. (7a) and Eq. (7b) in the vertical case. While for the calculation of the convection

coefficient  $h_2$  of the flat part, the Nusselt number is calculated by Eq. (16) or Eq. (17). Then,  $h_1$  and  $h_2$  are calculated by Eq. (8). Finally, the total natural convection coefficient  $h_c$  is calculated by Eq. (18).

For the ease of comparing the experimental and analytical results, the data for each configuration are plotted against the temperature difference between the ambient and the cooling surface. This plot is expected to help to choose the appropriate correlation depending on the configuration and the temperature range. It should be noted that the maximum uncertainty in the computed convection coefficients is 6.2%. The uncertainty values are displayed as error bars in Figs. 5 and 6.

Table 1 shows the experimental data for the horizontal configuration.

Tables 2 and 3 show the analytical data for the horizontal case for which the natural convection coefficients  $h_1$  for the fin section has been calculated based on Jones [3] and Tari [8] empirical correlations respectively.

Fig. 5 shows the variation of the total heat extraction coefficient  $h_e$  with the temperature difference for five different input currents in the horizontal configuration. The average relative difference of the analytical data based on Tari [8] in comparison with the experimental one is 8.1% and the maximum relative difference based on this correlation is 12.9%. The average relative difference for analytical data based on Jones [3] empirical correlation is 9.1% and the maximum relative difference for these data is 12.1%. However, according to Tables 1 and 2, it is clearly shown that by increasing the temperature, the relative difference of the analytical data based on Jones correlation compared with the experimental data decreases. For the temperature difference of 34.4 (°C) the relative difference is 9.5% with Jones correlation while in the same situation it is 11.5% with Tari correlation. Furthermore, Fig. 5 shows that

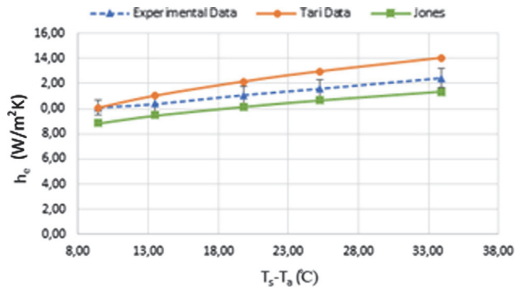


Fig. 5. Variation of the total heat extraction coefficient according to the temperature difference for the vertical orientation.

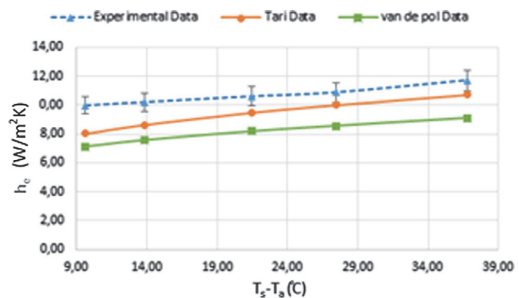


Fig. 6. Variation of the total heat extraction coefficient with the temperature difference for the horizontal orientation.

**Table 1**  
Experimental results for horizontal configuration.

$I$ (A)	$T_s$ (°C)	$T_a$ (°C)	$Q_r$ (W)	$h_e$ W/(m <sup>2</sup> K)	$h_r$ W/(m <sup>2</sup> K)	$h_c$ W/(m <sup>2</sup> K)
10	27.7	18.2	15.23	10.09	3.53	6.56
12	32.4	18.9	22.38	10.37	3.63	6.74
15	38.6	18.2	35.97	11.07	3.73	7.34
17	43.9	18.3	47.34	11.58	3.83	7.75
20	53.4	19	68.16	12.44	4.03	8.41

**Table 2**  
Analytical results for horizontal orientation based Jones empirical correlation.

$I$ (A)	$T_s$ (°C)	$T_a$ (°C)	$h_e$ W/(m <sup>2</sup> K)	$h_r$ W/(m <sup>2</sup> K)	$h_c$ W/(m <sup>2</sup> K)
10	27.7	18.2	8.87	3.53	5.34
12	32.4	18.9	9.47	3.63	5.84
15	38.6	18.2	10.16	3.73	6.43
17	43.9	18.3	10.66	3.83	6.83
20	53.4	19	11.36	4.03	7.33

**Table 3**  
Analytical results for horizontal orientation based Tari empirical correlation.

$I$ (A)	$T_s$ (°C)	$T_a$ (°C)	$h_e$ W/(m <sup>2</sup> K)	$h_r$ W/(m <sup>2</sup> K)	$h_c$ W/(m <sup>2</sup> K)
10	27.7	18.2	10.07	3.53	6.54
12	32.4	18.9	11.02	3.63	7.39
15	38.6	18.2	12.15	3.73	8.42
17	43.9	18.3	12.96	3.83	9.13
20	53.4	19	14.05	4.03	10.03

by increasing the temperature the analytical data curve based on Tari's correlation diverges from the experimental curve. It is interesting to note that the Jones empirical correlation has been developed without any dependence on the physical fin array's properties e.g., fin's height ( $H$ ) and fin's length ( $L_{fin}$ ).

Table 4 shows the experimental data for the vertical configuration.

Tables 5 and 6 show the analytical data for the vertical case for which the natural convection coefficients  $h_l$  for fin section has been calculated based on Van De Pol [4] and Tari [2] respectively.

Fig. 6 shows the variation of the total heat extraction coefficient ( $h_e$ ) with the temperature difference for five different input currents in the vertical orientation. Significant differences were found between the analytical data based on Van Del Pol [4] correlation and the experimental data. The mean relative difference of this empirical correlation is about 24% and the maximum one is 29%. The main reasons for this difference can be explained by the defined range for this correlation as well as by the fact that Van De Pol equations were derived for periodical channel whereas Tari's equation is valid for a single channel too. According to [4]

**Table 4**  
Experimental results for vertical configuration.

$I$ (A)	$T_s$ (°C)	$T_a$ (°C)	$Q_r$ (W)	$h_e$ W/(m <sup>2</sup> K)	$h_r$ W/(m <sup>2</sup> K)	$h_c$ W/(m <sup>2</sup> K)
10	28.6	19	15.31	9.97	3.56	6.41
12	33.1	19.3	22.44	10.20	3.65	6.55
15	40.7	19.2	36.28	10.60	3.79	6.81
17	45.9	18.4	47.65	10.88	3.87	7.00
20	55.4	18.6	68.66	11.70	4.07	7.63

**Table 5**  
Analytical results for vertical orientation based van de pol empirical correlation.

$I$ (A)	$T_s$ (°C)	$T_a$ (°C)	$h_e$ W/(m <sup>2</sup> K)	$h_r$ W/(m <sup>2</sup> K)	$h_c$ W/(m <sup>2</sup> K)
10	28.6	19	7.12	3.56	3.56
12	33.1	19.3	7.56	3.65	3.91
15	40.7	19.2	8.17	3.79	4.38
17	45.9	18.4	8.54	3.87	4.67
20	55.4	18.6	9.08	4.07	5.01

**Table 6**  
Analytical results for vertical orientation based Tari empirical correlation.

$I$ (A)	$T_s$ (°C)	$T_a$ (°C)	$h_e$ W/(m <sup>2</sup> K)	$h_r$ W/(m <sup>2</sup> K)	$h_c$ W/(m <sup>2</sup> K)
10	28.6	19	8.02	3.56	4.46
12	33.1	19.3	8.63	3.65	4.98
15	40.7	19.2	9.47	3.79	5.68
17	45.9	18.4	10.00	3.87	6.13
20	55.4	18.6	10.71	4.07	6.64

and [19], this correlation is fitted for rectangular fins in the range of  $0.33 < H/S < 4$  and  $42 < L_{fin}/S < 10.6$ . Our case-study is not located within these ranges. However, as Fig. 6 shows, the difference between the analytical data based on Tari's correlations and experimental data is significant at lower temperatures, but as the temperature difference increases, the analytical data curve converges toward the experimental one. Thus, the appropriateness of this correlation is better at high temperature raises. The mean relative difference for this correlation is 12%. The maximum relative difference occurred at low-temperature rise and it amounts to 29%.

Another interesting finding is achieved by simple comparison between natural convection coefficients of the corresponding currents, which proves that the natural convection coefficient in the horizontal configuration is higher than in the vertical one, which means that the horizontal flat plate fins topology provides better natural cooling than the vertical one and thus can reduce the amount of the cooling power consumption as well as the surface temperature.

## 7. Conclusion

The focus in this paper is on the determination of the natural convection heat transfer from parallel rectangular fins on a flat base plate of the coil of a large permanent magnet generator in both horizontal and vertical configurations, by means of experimental and analytical methods. For this purpose, a number of empirical correlations for both configurations was studied. Finally, according to a comparison of experimental data with empirical ones, the appropriate ones were selected. According to the selected correlations, the natural convection coefficients for both configurations were calculated and validated through an experimental test setup. The experimental data were collected for five different input currents corresponding to different temperature raises. All experiments were made at the steady state of the thermal system.

According to this study, it can be concluded that for the large rectangular fins in the horizontal configuration the results based on Jone's empirical correlation are in good agreement with the experimental one. In addition, the appropriateness of this correlation is enhancing with increasing temperature rise. For the vertical case, the analytical results based on Tari's empirical correlation have a good agreement with the experimental data.

## Acknowledgements

This research has been supported by the Estonian Research Council under grants PUT1260.

## Conflict of interests

None declared.

## References

- [1] M. Ahmadi, G. Mostafavi, M. Bahrami, Natural convection from rectangular interrupted fins, *Int. J. Therm. Sci.* 82 (2014) 62–71.
- [2] I. Tari, M. Mehrtash, Natural convection heat transfer from inclined plate-fin heat sinks, *Int. J. Heat Mass Transf.* 56 (1) (2013) 574–593.
- [3] C.D. Jones, L.F. Smith, Optimum arrangement of rectangular fins on horizontal surfaces for free-convection heat transfer, *J. Heat Transfer* 92 (1) (1970) 6.
- [4] D.W. Van de Pol, J.K. Tierney, Free convection nusselt number for vertical U-shaped channels, *J. Heat Transfer* 95 (4) (1973) 542.
- [5] W. Elenbaas, Heat dissipation of parallel plates by free convection, *Physica* 9 (1) (Jan. 1942) 1–28.
- [6] V.D. Rao, S.V. Naidu, B.G. Rao, K.V. Sharma, Heat transfer from a horizontal fin array by natural convection and radiation—A conjugate analysis, *Int. J. Heat Mass Transf.* 49 (19) (2006) 3379–3391.
- [7] S. Baskaya, M. Sivrioglu, M. Ozek, Parametric study of natural convection heat transfer from horizontal rectangular fin arrays, *Int. J. Therm. Sci.* 39 (8) (Sep. 2000) 797–805.
- [8] I. Tari, M. Mehrtash, Natural convection heat transfer from horizontal and slightly inclined plate-fin heat sinks, *Appl. Therm. Eng.* 61 (2) (2013) 728–736.
- [9] A. Boglietti, A. Cavagnino, M. Parvis, A. Vallan, Evaluation of radiation thermal resistances in industrial motors, *IEEE Trans. Ind. Appl.* 42 (3) (May 2006) 688–693.
- [10] F. Kreith, R. M. Manglik, M. Bohn, Principles of heat transfer, 7th ed. Global Engineering, 2011.
- [11] D.A. Staton, A. Cavagnino, Convection heat transfer and flow calculations suitable for electric machines thermal models, *IEEE Trans. Ind. Electron.* 55 (10) (Oct. 2008) 3509–3516.
- [12] Payam Shams Ghahfarokhi, Ants Kallaste, Anour Belahcen, Toomas Vaimann, Determination of forced convection coefficient over a flat side of coil, in: 58th International Scientific Conference on Power and Electrical Engineering of Riga Technical University (RTUCon), 2017, pp. 1–4.
- [13] P. Shams Ghahfarokhi, A. Kallaste, A. Belahcen, Determination of thermal convection coefficient from coil's flat plate side, in: 16th International Symposium Topical Problems in the Field of Electrical and Power Engineering and Doctoral School of Energy and Geotechnology III, 2017, pp. 130–132.
- [14] P.S. Ghahfarokhi, A. Kallaste, A. Belahcen, T. Vaimann, Steady state and transient thermal analysis of the stator coil of a permanent magnet generator, in: 2017 18th International Scientific Conference on Electric Power Engineering (EPE), 2017, pp. 1–5.
- [15] M. Markovic, L. Saunders, Y. Perriard, Determination of the thermal convection coefficient for a small electric motor, in: Conference Record of the 2006 IEEE Industry Applications Conference Forty-First IAS Annual Meeting, 2006, vol. 1, pp. 58–61.
- [16] O. Meksi, A.O. Vargas, Numerical and experimental determination of external heat transfer coefficient in small TENV electric machines, *IEEE Energy Convers. Cong. Exposition (ECCE)* 2015 (2015) 2742–2749.
- [17] F.P. Incropera, D.P. DeWitt, T.L. Bergman, A.S. Lavine, *Fundam. Heat Mass Transfer* (2007).
- [18] S.N. Long, Ch, *Heat Transfer*. Ventus Publication ApS, 2009.
- [19] W.M. Rohsenow, James P. Hartnett, Y.I. Cho, *Handbook of heat transfer*, McGraw-Hill, 1998.



**Publication III**

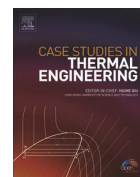
P. Shams Ghahfarokhi, A. Kallaste, A. Belahcen, T. Vaimann, and A. Rassõlkin, "Hybrid thermal model of a synchronous reluctance machine," *Case Stud. Therm. Eng.*, vol. 12, pp. 381–389, Sep. 2018.





Contents lists available at ScienceDirect

## Case Studies in Thermal Engineering

journal homepage: [www.elsevier.com/locate/csite](http://www.elsevier.com/locate/csite)

## Hybrid thermal model of a synchronous reluctance machine

Payam Shams Ghahfarokhi<sup>a,\*</sup>, Ants Kallaste<sup>a</sup>, Anouar Belahcen<sup>b</sup>, Toomas Vaimann<sup>a</sup>, Anton Rassõlkin<sup>a</sup><sup>a</sup> Electrical Power Engineering and Mechatronics, Tallinn University of Technology, Ehitajate tee 5, Tallinn, Estonia<sup>b</sup> Electrical Engineering and Automation, Aalto University, Espoo, Finland

## A B S T R A C T

This paper presents a hybrid thermal modeling methodology to analyze the temperature performance of radial flux electrical machines. For this purpose, the 2D finite element model of the active part of the machine is coupled with a lumped parameters thermal circuit of the end-winding region. A synchronous reluctance machine is used to validate the proposed approach. The results from the proposed method are compared with the experimental ones, which are obtained from a prototype machine. The computations show that the 2D FE model underestimates the temperature rise in the machine as it does not account for the power losses in the end-windings. The hybrid model accounts for these losses as well as for the heat dissipation in the end-winding region.

## 1. Introduction

According to the efforts to achieve higher torque and power density, higher energy efficiency and cost reduction in the design of new generation of electrical machines, the thermal design of electrical machine in parallel with the electromagnetic design has acquired a particular importance [1].

The thermal analysis of an electrical machine is divided into two groups; the lump parameters thermal network (LPTN) and the finite element analysis (FEA) [1,2]. The LPTN is a common method for thermal analysis of key components of the electrical machine. There are many reports from the literature on the thermal analysis of different electrical machines, e.g., [3–7]. The main advantage of this method over the FEA is the short calculation time with acceptable accuracy [2,8]. The FEA needs high setup and computational time, but it is considered to be more accurate in modeling the loss distribution and thus the temperature rise in the machines [2,8,9].

An electrical machine can be modeled with the FEA in a 2D or 3D approach [9]. Modeling the electrical machine by the 3D FEA is a very time-consuming process and consist of several complex geometry setups e.g., end-windings. Accordingly, in order to reduce the computation time and use the benefits of FEA for monitoring the thermal behavior of the electrical machine, the 2D FEA is usually implemented. There are many reports on the thermal modeling of electrical machines by 2D FEA [9–14], among others. However, there are some problems in the 2D FEA thermal models of electrical machines. As an example, in [10], the author neglected the axial heat flow from the end-winding to the active part of the machine and in [11], the paper presents a 2D FEA where the results are compared with a simplified LPTN which is not including the end-winding thermal effect. Since they applied the simplified assumption to neglect the heat transfer from the end-windings to the slots, they could not model the hottest spot of the electrical machine and the whole temperature distribution is underestimated. As a result, these models cannot provide a correct view of the heat transfer and thermal analysis for an electrical machine. In order to remedy this simplification, as well as using the advantages of the 2D FEA, we

\* Corresponding author.

E-mail address: [payam.shams@ttu.ee](mailto:payam.shams@ttu.ee) (P.S. Ghahfarokhi).

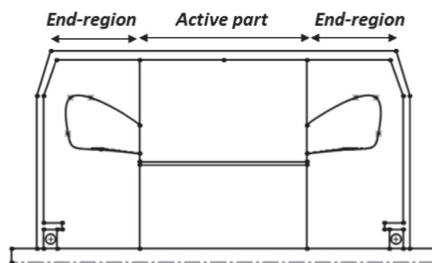


Fig. 1. The axial cross-section of the electrical machine.

propose a hybrid thermal model, which consist of coupling 2D FEA with the equivalent thermal circuit. Such an approach is very common in the electromagnetic analysis of electrical machines, where the end-winding impedance is added in the winding circuit equations and coupled with the 2D field equations.

The coupling methodology can be divided into two types; direct and indirect coupling. The direct coupling method requires access to the 2D system matrix assembly routine to add the circuit terms and solve all the equations simultaneously. Such an approach although fast is not possible to implement in a general purpose software unless one has access to the code. In this paper, we choose the indirect approach as explained in the methods section. We focus on the application of this method in the steady-state thermal analysis of a synchronous reluctance motor (SynRM). The temperature of the active part of the machine is modeled by means of a 2D FEA simulation software and the temperature effect of the end-winding region of the machine is evaluated by an equivalent thermal circuit. The two models are combined through an iterative procedure.

## 2. The hybrid thermal model details

Fig. 1 shows an illustration of the axial cross section of an electrical machine. According to this figure, the construction of the electrical machine is divided into two main sections, the magnetic active part of the machine and the end-winding region. The 2D FEA can model only the heat transfer within the active part of the machine. It does not take into account the effect of heat transfer between the end-winding region and these active parts. One possibility to tackle this issue is to include the power losses in the end-winding in the slot losses while compiling the 2D model of the machine. However, this would result in an overestimation of the temperatures, as a large part of the end-winding losses is flowing through the end-winding region and not transferred to the active parts. Yet a better approach is the proposed hybrid model. The hybrid thermal model is constructed by coupling the 2D FEA model of the active parts and the lumped parameters thermal network model of the end-winding region.

The hybrid thermal model described above is applied to a four poles 11 kW, 400 V, 50 Hz, transverse-laminated radial flux SynRM with F insulation class. Fig. 2 shows a CAD drawing of the machine and its cross section. Tables 1 and 2 give the geometrical and material data of the prototype SynRM.

### 2.1. The FEA thermal model

As mentioned, in the hybrid thermal calculation method, the active parts of the machine are modeled by using a 2D FEA software. In order to model the heat transfer of the active part of the machine, the FEMM package software is selected. This software has some advantages, e.g., free license software whit a Matlab toolbox called OctaveFEMM to provide a way for operating the FEMM solver via Matlab functions [15].

The main challenges with the FEA are how to define the thermal conductivity of the composite materials inside the slots such as the copper conductors, the conductor insulation, the impregnation material and the slot insulation [1]; and how to implement the convection and radiation phenomena.

The slot area consists of different materials with different thermal conductivities. Due to the small dimensions of the materials layer in the slot, it is not practical to model each material separately. To solve this problem, an equivalent thermal conductivity  $k_e$  of the slot area is defined as in [16]:

$$k_e = k_2 \frac{(1 + f_1)k_1 + (1 - f_1)k_2}{(1 - f_1)k_1 + (1 + f_1)k_2}, \quad (1)$$

where  $k_1$  is the thermal conductivity of the copper conductors,  $k_2$  is the thermal conductivity of the slot impregnation,  $f_1$  is the volume fraction of the conductor in the slot and  $f_2$  is the volume fraction of the impregnation in the slot (with  $f_1 + f_2 = 1$ ). The other insulation materials are assumed equivalent to the impregnation material, which is a well-justified assumption as explained in [16].

The heat is transferred from the exterior surface of the electrical machine to the ambient by the convection and radiation phenomena. These phenomena are implemented into the 2D FE model by defining the boundary condition on the outer surface of the model to describe the quality of the heat transfer from the outer surface of the machine to the ambient. In an actual machine, the outer surface consists of axial cooling fins, which can be modeled in the FEA analysis but this will result in a very dense mesh and thus

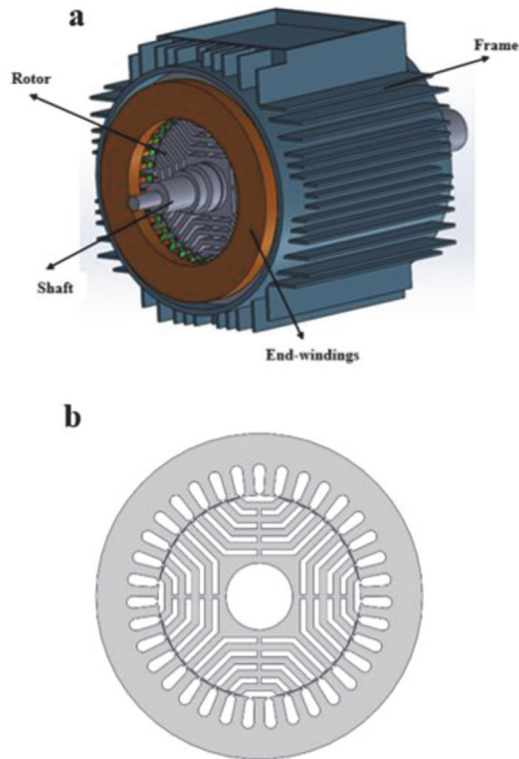


Fig. 2. Structure and Topology of transverse-laminated SynRM analyzed in this paper.

**Table 1**  
Geometrical data of the transverse- laminated SynRM.

Name	Symbol	Unit	Value
Stator core length	$L_s$	mm	156
Stator inner diameter	$D_{is}$	mm	136
Stator outer diameter	$D_{os}$	mm	219
Number of slots	$N_s$	-	36
Air-gap height	$h_{ag}$	mm	0.4
Rotor inner diameter	$D_{ir}$	mm	45
Rotor outer diameter	$D_{or}$	mm	135.2
Slot height	$h_l$	mm	21
Slot filling factor	$k_f$	-	0.6
Slot area	$S_s$	mm <sup>2</sup>	130.1

**Table 2**  
Material data of transverse- laminated SynRM.

Machine part	Material	Thermal conductivity symbols	Thermal conductivity (W/mK)
Frame	Aluminum	$k_{al}$	230
Laminations	Electric steel	$k_{ir}$	28
Winding	Copper	$k_{cu}$	387
Impregnation	Resin	$k_2$	0.2
Air gap	Air	$k_{air}$	0.0257
Shaft	Steel	$k_{st}$	41

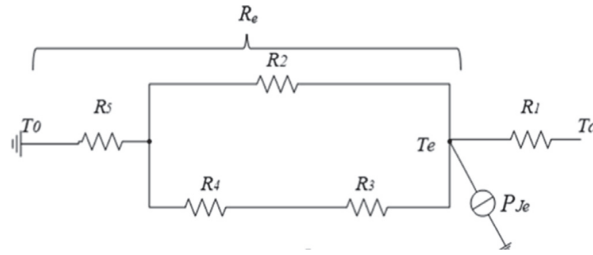


Fig. 3. The equivalent thermal circuit of the end-windings.

very slow computations. In order to reduce the model size, a modified smooth outer surface is used and the effect of the cooling fins is accounted for through an equivalent heat transfer coefficient  $h'$ , which is calculated as in [14]:

$$h' = \frac{s}{s'}h, \tag{2}$$

where  $h$  is the actual heat coefficient,  $s = 0.4 \text{ m}^2$  is the actual outer surface of the active part of the machine including the fins and  $s' = 0.11 \text{ m}^2$  is the simplified outer surface.

2.2. Lumped parameters thermal network

Since the 2D FEA does not take into account the effect of heat transfer through the end-winding region of the electrical machine a lumped parameters thermal network of these parts of the machine is developed and coupled with the FEA.

The developed lumped parameters thermal network is valid for the steady-state operation. It consists of thermal resistances and power sources as shown in Fig. 3. The main assumption for this construction is the fact that the power losses distribution is assumed uniform in the end-windings, which are represented as a toroidal structure. Yet another assumption is that the heat flux distribution in both end regions of the machine are analogous. This later assumption could be removed if one makes separate thermal models for each end-winding.

The variables in the LPTN of Fig. 3 are  $T_a$  and  $T_e$ , which represent the average temperatures of the slots and the end-windings respectively. The model consists of two nodes and five thermal resistances as well as the end winding copper losses as a heat source. Table 3 describes the definition of the thermal model components of Fig. 3.

The value of the thermal resistances of Table 3 are computed with an acceptable accuracy by the following analytical equations:

$$R_1 = \frac{l_{av}}{6N_s k_{cu} s_{cu}}, \tag{3}$$

$$l_a = L_s + 1.2\tau_p + l', \tag{4}$$

where  $l_{av} = 0.321 \text{ m}$  is the average conductor length of half a turn,  $N_s$  is the number of the stator slots,  $k_{cu}$  is the thermal conductivity of the copper,  $s_{cu} = 7.8 \times 10^{-5} \text{ m}$  is the total copper conductor cross-section area,  $\tau_p = 0.096 \text{ m}$  is the pole pitch, and  $l' = 0.05 \text{ m}$  is an empirically determined constant, depending on the size of the machine [4].

$$R_2 = \frac{1}{2\pi k_{air} (L_f - L_s)} \ln\left(\frac{r_{oy}}{r_{oy} - 0.5t_{sy}}\right), \tag{5}$$

where  $L_f = 0.222 \text{ m}$  is the frame length,  $L_s$  is the stator core length,  $r_{oy}$  is the outer stator yoke radius,  $t_{sy}$  is the stator radius height and  $k_{air}$  is the air conductivity [8].

$$R_3 = \frac{1}{s_{ew} h_{ew}}, \tag{6}$$

where  $s_{ew} = 0.03 \text{ m}^2$  is the total surface of the end-windings in contact with the inner air and  $h_{ew} = 15.5 \text{ W}/(\text{m}^2\text{K})$  is the convection

Table 3  
Definition and the values of the thermal model components.

Component	Value	Unit	Description
$R_1$	0.05	K/W	Conduction thermal resistance between the midpoint of end-winding and the midpoint of coil side
$R_2$	10.7	K/W	Conduction thermal resistance between the stator winding and the frame
$R_3$	2.3	K/W	Convection thermal resistances between the stator end-winding and inner air of the end region
$R_4$	0.8	K/W	Convection thermal resistance between the inner air and the end cap
$R_5$	0.6	K/W	Total heat extraction thermal resistance from the frame to the ambient
$P_{Je}$	98.3	W	Stator end-winding Joule losses

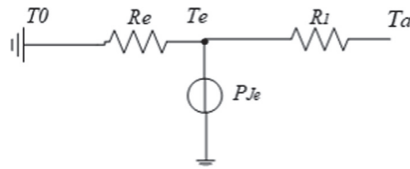


Fig. 4. The final equivalent thermal circuit after lumping \$R\_2\$ to \$R\_5\$ into \$R\_e\$.

coefficient for the air between the end-windings and the inner air, which are calculated as follow [4,8]:

$$s_{ew} = (L_f - L_s)2\pi r_{is}, \tag{7}$$

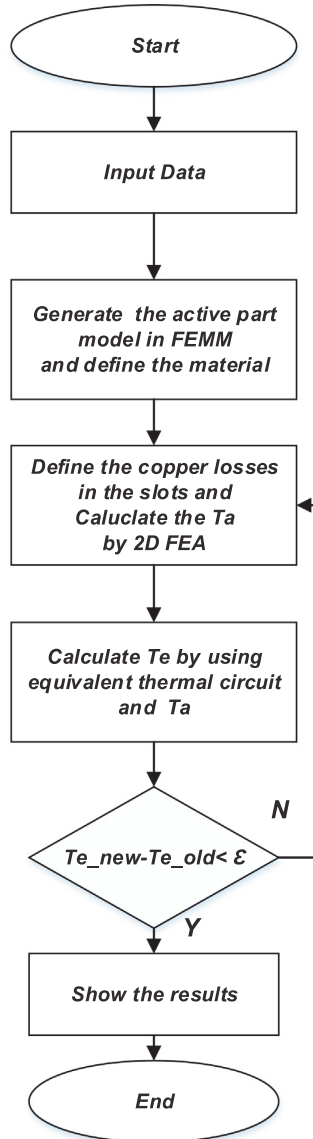


Fig. 5. The flow chart of hybrid model calculation.

$$h_{ew} = 15.5(0.29\nu+1) \tag{8}$$

$$\nu = r_{or}\omega\eta, \tag{9}$$

where  $r_{is}$  is the inner stator radius,  $\nu$  is the inner air speed,  $r_{or}$  is the outer rotor radius;  $\omega$  is the rotor angular speed and  $\eta$  is the fan efficiency and according to [3] it is equal to 0.5.

$$R_4 = \frac{1}{s_{ec}h_{ec}}, \tag{10}$$

where  $s_{ec} = 0.08 \text{ m}^2$  is the external surface of the two machine end-caps and  $h_{ec}$  is the convection coefficient between the inner air gap and the end-cap, which it is equal to the value of  $h_{ew}$  [4].

$$R_5 = \frac{1}{s_e h_e}, \tag{11}$$

where  $s_e = 0.22 \text{ m}^2$  is the lateral outer surface of the SynRM and  $h_e = 7.1 \text{ W}/(\text{m}^2\text{K})$  is the total heat extraction coefficient from the outer surface, which consists of the sum of the radiation and convection coefficients.

### 2.3. Hybrid model calculation

The LPTN of Fig. 3 is further simplified by combining the thermal resistances  $R_2$  to  $R_5$  in a single equivalent resistance  $R_e$  as:

$$R_e = \frac{(R_4 + R_5) \times R_2}{R_2 + R_3 + R_4} + R_5. \tag{12}$$

Fig. 4 shows the final LPNT used in the hybrid thermal model.

The end-windings and slot copper loss are evaluated from the total copper loss based on the volumes of the copper conductors in the slots and in the end-windings. The temperature of the end-windings  $T_e$ , and the amount of heat transfer from the end-windings to slots  $P_{ex}$ , are evaluated by applying the Kirchhoff current rule as follow:

$$T_e = \left( P_{e} + \frac{T_0}{R_e} + \frac{T_a}{R_1} \right) (R_1 + R_e), \tag{13}$$

$$P_{ex} = \frac{T_e - T_a}{R_1}. \tag{14}$$

where the temperature of the active parts  $T_a$  is evaluated by the FEA and  $P_{ex}$  is the amount of losses added to the slot losses in the FEA at each iteration. Note that  $P_{ex}$  can be negative in some cases.

Fig. 5 shows the flowchart of the hybrid model calculation. After the construction of the FE model and the definition of the materials, the copper power losses are inserted in the model. In the first iteration step, the FEA calculates the temperature of the active part of the machine and predicts the average value of the slot temperature  $T_a$ .  $T_e$  and  $P_{ex}$  are then calculated by (13) and (14) respectively. In the next iteration,  $P_{ex}$  is added to the active copper losses in the FE model. This iteration process will continue until the difference between the previous  $T_e$  and the new one is smaller than an arbitrary defined accuracy  $\mathcal{E}$ , which was 0.01 K in our case.

The FE model requires some parameters, such as the losses and the radiation and convection heat transfer coefficients at the outer surface. These parameters have been evaluated experimentally as explained in the following section.

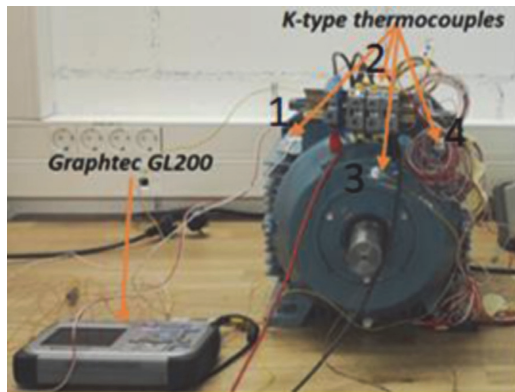


Fig. 6. Test setup.



### 3. Experimental methodology

The objective of the experimental work is to determine the heat extraction coefficient and the copper losses. The accuracy of the calculation based on the hybrid model is also evaluated by comparing the computation and measurement results.

The total heat extraction coefficient for the natural cooling is evaluated by using the DC stator test. In this test, the losses of the machine are confined to the Joule loss of the stator windings where the electric power can be easily measured. In the calculations, we accounted for the variations in the winding electrical resistance, as the winding resistivity is temperature dependent [7,17]. During the experiments, the DC power applied to the motor is measured as well as the surface temperature of the motor at different locations. Four K-type thermocouples are installed by means of adhesive material in various locations on the frame surface of the motor. The ambient temperature is also measured by means of a K-type thermocouple. For the purpose of increasing the accuracy of the temperature measurement and minimizing the contact resistance between the thermocouples and the frame surface of the motor, we used thermal paste. The average temperature of these four thermocouples is assumed to be the mean temperature of the motor frame surface. During the experiments, all the temperature data are collected by means of a Graphtec GL200 logger. The experiment has been carried in the thermal steady-state condition. The total heat extraction coefficient  $h_e$  is calculated as [18]:

$$h_e = \frac{P}{(T_s - T_0)S}, \tag{15}$$

where  $T_s$  is the frame surface temperature,  $T_0$  is the ambient temperature,  $S = 0.69 \text{ m}^2$  is the total surface area of the frame and  $P$  is the input electric DC power.

Fig. 6 shows the experimental setup and the different location of the surface frame K type thermocouples. In addition to the surface temperature, the temperature inside the machine was also measured. For this purpose, six different RTD PT100 have been installed inside the end-windings and slots of the stator. These measured temperatures are used to validate the hybrid thermal model results.

#### 3.1. Uncertainty analysis of experimental results

In this sub section, we determined the total accuracy of experimental data according to the accuracy of the measurement instruments. During the experiment, the voltage and current are measured with the TTi QPX1200S. The accuracy of the voltage and current readings are 0.1% and 0.3% respectively. Furthermore, the standard accuracy of the K-type thermocouple is 0.75%. According to [19], the power uncertainty is evaluated as:

$$\omega_{Q_T} = \left[ \left( \frac{\partial Q_T}{\partial V} \cdot \omega_V \right)^2 + \left( \frac{\partial Q_T}{\partial I} \cdot \omega_I \right)^2 \right]^{0.5}, \tag{16}$$

where  $\omega_{Q_T}$ ,  $\omega_V$  and  $\omega_I$  are the uncertainties in the total input power, voltage and current.

This leads to the uncertainty for the computed convection coefficient as:

$$\omega_h = \left[ \left( \frac{\partial h}{\partial Q_T} \cdot \omega_{Q_T} \right)^2 + 2 \cdot \left( \frac{\partial h}{\partial T} \cdot \omega_T \right)^2 \right]^{0.5}, \tag{17}$$

where  $\omega_T$  is the uncertainty in the temperature measurement.

It should be noted that the maximum uncertainty in the computed convection coefficients is 6.2%.

### 4. Results and discussion

The hybrid model is applied for the same operating condition as in the experiment, i.e. DC test. The comparison is carried out for the hybrid model, the experimental results, and a simple 2D model that does not account for the end-windings.

As Fig. 6 shows, each sensor is marked with a number. Accordingly, Table 4 shows the measured temperature by the thermocouples which have been install on the outer surface of the SynRM.

The experimental test resulted in a frame surface mean temperature of 61.2 °C for a DC input power of 191.1 W, while the ambient temperature was 21.8 °C. The standard deviation of the frame temperature as calculated from the four sensors was  $\pm 2.2$  °C. Fig. 7 shows the temperature distribution around the frame surface. From these values, the total heat extraction coefficient calculated by (15) is 7.1 W/Km<sup>2</sup>. The equivalent thermal conductivity of the slot and its modified total heat extraction coefficient, calculated by (1) and (2) respectively, are 0.79 W/(Km) and 27 W/(Km<sup>2</sup>). The evaluated copper losses produced in the slots and end-windings are 92.8 W and 98.3 W respectively. These values were used in the FE part of the hybrid model.

**Table 4**  
surface temperature of the SynRM.

	1 (°C)	2 (°C)	3 (°C)	4 (°C)
Surface temperature of the SynRM	61.7	64.4	58.7	60.3

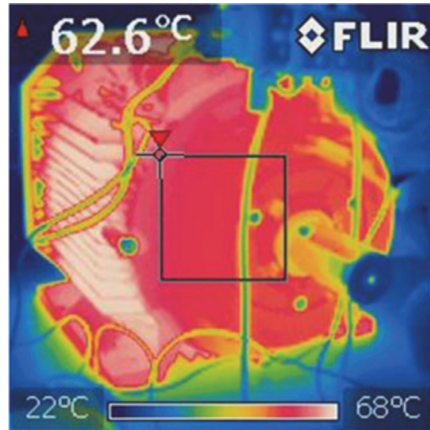


Fig. 7. Temperature distribution over the frame surface.

**Table 5**  
Measured and calculated temperatures.

	Hybrid Model (°C)	2D FEA (°C)	Experimental (°C)
Slot	72.9	51.9	74 ± 2.2
End-winding	78.5	–	78 ± 0.15

Table 5 shows the steady-state temperature results of the end-windings and slots from the three methods;

According to Table 5, there is a significant difference in the predicted temperature between the hybrid thermal model and the simple 2D FE model, around 21 °C. Furthermore, the hybrid thermal model results are in a good agreement with the experimental ones. This proves that the proposed method can be implemented to predict the temperatures of the machine with a high accuracy.

Figs. 8 and 9 show the temperature distribution in the active part of the machine computed with the hybrid thermal model and 2D FEA respectively. The hottest parts of the machine's active part are the slots as would be expected. The two distributions look alike, except that the results from the hybrid model are around 21 °C higher than for the FE Model. This is due to the fact that part of the end-winding heat is flowing to the slots.

The results of this study indicate that the 2D FEA cannot be used alone for heat transfer modeling unless additional considerations are given to the end-windings and possibly to the shaft. The computations with the hybrid model show that a considerable amount of heat (61.98% of the end-windings losses) is transferred from the end-windings to the slots.

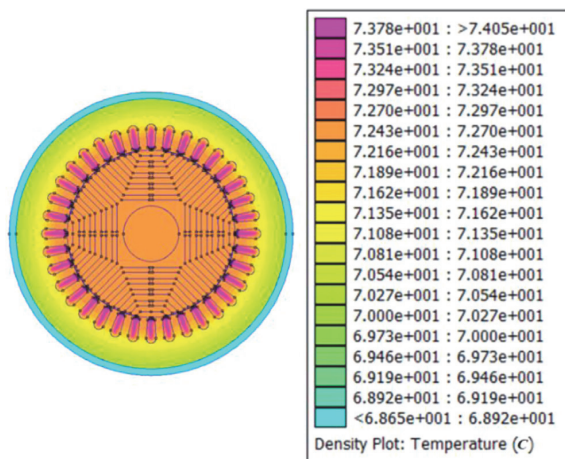


Fig. 8. Temperature distribution in the active part of the machine by using the hybrid model.

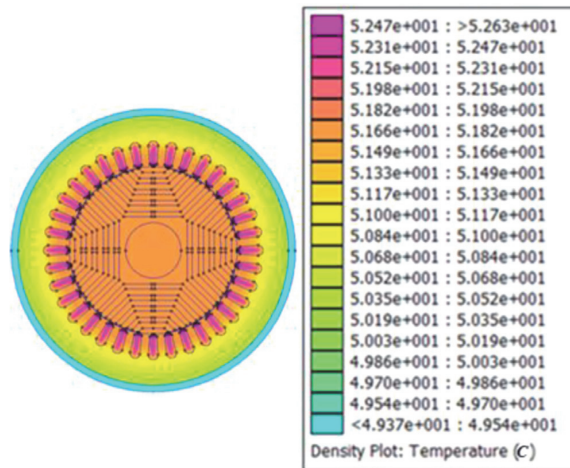


Fig. 9. Temperature distribution in the active part of the machine by using the only 2D FEA and simplifying assumption.

## 5. Conclusion

The focus of this paper has been to develop a hybrid thermal model, which consists of a 2D FE model for the active part of the machine and a Lumped Parameters Thermal Network for the end-region section. This model makes it possible to predict the temperature rise of the different sections of the electrical machine e.g., end-windings, slots, rotor, stator teeth, and yoke, with a higher accuracy than the simple 2D FE model alone. This hybrid model is a good alternative to the 3D FE models, which require high and unaffordable computation time. The accuracy of the model is still good as the results of the model are in good agreement with the experimental setup.

## Acknowledgments

This research has been supported by the Estonian Research Council under grant PUT1260.

## References

- [1] P.S. Ghahfarokhi, A. Kallaste, A. Belahcen, T. Vaimann, A. Rassolkin, Review of thermal analysis of permanent magnet assisted synchronous reluctance machines, *Electr. Power Qual. Supply Reliab.* (2016) 219–224.
- [2] A. Boglietti, A. Cavagnino, D. Staton, M. Shanel, M. Mueller, C. Mejuto, Evolution and modern approaches for thermal analysis of electrical machines, *IEEE Trans. Ind. Electron.* 56 (3) (2009) 871–882.
- [3] P.H. Mellor, D. Roberts, D.R. Turner, Lumped parameter thermal model for electrical machines of TEFC design, *IEE Proc. B Electr. Power Appl.* 138 (5) (1991) 205.
- [4] A. Boglietti, A. Cavagnino, M. Lazzari, M. Pastorelli, A simplified thermal model for variable-speed self-cooled industrial induction motor, *IEEE Trans. Ind. Appl.* 39 (4) (2003) 945–952.
- [5] J. Lindström, Thermal Model of a Permanent-Magnet Motor for a Hybrid Electric Vehicle, Chalmers university of technology, Goteborg, 1999.
- [6] A.M. EL-Refaei, N.C. Harris, T.M. Jahns, K.M. Rahman, Thermal analysis of multibarrier interior PM synchronous machine using lumped parameter model, *IEEE Trans. Energy Convers.* 19 (2) (2004) 303–309.
- [7] P.S. Ghahfarokhi, A. Kallaste, A. Belahcen, T. Vaimann, Steady state and transient thermal analysis of the stator coil of a permanent magnet generator, in: *Proceedings of the 18th International Scientific Conference on Electric Power Engineering (EPE)*, 2017, pp. 1–5.
- [8] A. Boglietti, A. Cavagnino, D. Staton, Determination of critical parameters in electrical machine thermal models, *IEEE Trans. Ind. Appl.* 44 (4) (2008) 1150–1159.
- [9] V. Matošević, Ž. Štih, 2D Magneto-thermal analysis of synchronous generator, *Przeglad Elektrotech.* 2014 (2016) 157–160.
- [10] Weili Li Junci Cao Fei Huo Jiafeng Shen, Numerical analysis of stator-rotor coupled transient thermal field in induction motors with blocked rotor. in: *Proceedings of the Automation Congress, 2008, WAC 2008 World*: date, Sept. 28 2008–Oct. 2 2008. 2008 pp.1–6.
- [11] R.-J. Wang, G.C. Heyns, Thermal analysis of a water-cooled interior permanent magnet traction machine, in: *Proceedings of the IEEE International Conference on Industrial Technology (ICIT)*, 2013, pp. 416–421.
- [12] J. Driesen, R. Belmans, K. Hameyer, A. Arkkio, T. Jokinen, Efficient magnetic-thermal coupled simulation of electrical machines using a double combined FEM-circuit approach, in: *Proceedings of the International Conference on Electrical machines, ICEM'98, Istanbul, Turkey, 2–4 September 1998*, 1998, pp. 1402–1407.
- [13] S. LIPIŃSKI, K. Grunt, J. Zawilak, 2D steady-state thermal analysis of a line-start, permanent magnet synchronous motor, *PRZEGLAD Elektrotech.* 1 (3) (2017) 183–186.
- [14] V. Hatzithanassiou, J. Xypteras, G. Archontoulakis, Electrical-thermal coupled calculation of an asynchronous machine, *Arch. für Elektro.* 77 (2) (1994) 117–122.
- [15] Finite Element Method Magnetics: OctaveFEMM. [Online]. Available: <<http://www.femm.info/wiki/octavefemm>>.
- [16] M. Popescu, D. Staton, D. Dorrell, F. Marignetti, and D. Hawkins, “Study of the thermal aspects in brushless permanent magnet machines performance,” in: *Proceedings of the IEEE Workshop on Electrical Machines Design, Control and Diagnosis (WEMDCD)*, 2013, pp. 60–69.
- [17] A.R.PayamShams. Ghahfarokhi, Ants Kallaste, Anouar Belahcen, Toomas Vaimann, Determination of Forced Convection Coefficient Over a Flat Side of Coil, in: *Proceedings of the 58th International Scientific Conference on Power and Electrical Engineering of Riga Technical University (RTUCON)*, 2017, pp. 1–4.
- [18] P. shams Ghahfarokhi, A. Kallaste, and A. Belahcen, Determination of thermal convection coefficient from coil's flat plate side. in: *Proceedings of the 16th International Symposium Topical Problems in the Field of Electrical and Power Engineering and Doctoral School of Energy and Geotechnology III*. 2017, pp. 130–132.
- [19] M. Ahmadi, G. Mostafavi, M. Bahrami, Natural convection from rectangular interrupted fins, *Int. J. Therm. Sci.* 82 (2014) 62–71.



**Publication IV**

P. Shams Ghahfarokhi, A. Kallaste, T. Vaimann, A. Rassolkin, and A. Belahcen, "Steady-State Thermal Model of a Synchronous Reluctance Motor," in 2018 IEEE 59th International Scientific Conference on Power and Electrical Engineering of Riga Technical University (RTUCON), 2018, pp. 1–5.



# Steady-State Thermal Model of a Synchronous Reluctance Motor

Payam Shams Ghahfarokhi, Ants Kallaste,  
Toomas Vaimann, Anton Rassolkin  
Dept. Electrical Power Engineering and Mechatronics  
Tallinn University of Technology  
Tallinn, Estonia  
payam.shams@ttu.ee

Anouar Belahcen  
Dept. Electrical Power Engineering and Mechatronics  
Tallinn University of Technology  
Tallinn, Estonia  
Dept. of Electrical Engineering and Automation  
Aalto University  
Finland

**Abstract**— This paper presents an analytical thermal model of a synchronous reluctance motor (SynRMs) to predict the temperature of its different parts. For the analytical calculation, a lumped parameter thermal network (LPTN) is developed and analyzed. To validate the developed model, measurements are carried out on an experimental setup including the analyzed machine. Finally, the test results are compared with the analytical results to assess the accuracy of the model.

**Keywords**—ac motors; lumped parameter thermal network; Synchronous reluctance motor; thermal analysis; thermal model

## I. INTRODUCTION

Recently, there has been a growing interest in SynRMs due to its low cost and simple structure as well as simple construction and manufacturing process [1]. This topology is presented as the right choice for traction and high-speed applications. A number of efforts has been done to achieve higher torque and power density, higher energy efficiency, and cost reduction. To achieve these goals, the thermal analysis of the electrical machine in parallel with the electromagnetic design is necessary.

The thermal analysis of an electrical machine is divided into two categories; analytical LPTN and finite element analysis (FEA) [2],[3]. The FEA has an ability to model complex shapes as well as accurate conduction heat transfer and heat loss distribution inside solid materials [2], [4] However, it is a time-consuming method and the convection boundaries are evaluated by means of the same empirical and analytical correlations which are applied for the LPTN[4], [5].

Some advantages of LPTN compared to the FEA are the fast calculation time with an acceptable accuracy. The thermal designers of electrical machines apply this method to evaluate the temperature of the key components of the electrical machine. There is a number of reports for LPTN analysis of the electrical machines [5]-[10]. Most of these reports deal with LPTN of the induction [6]-[9] and permanent magnet synchronous machines [5],[10]. In some models e.g., the proposed thermal model in [6], the heat transfer paths have

been developed in both radial and axial directions. As a result, the network complexity in terms of model details such as the number of nodes and thermal resistances and the calculation time has been increased. In order to tackle the mentioned problems, Boglietti in [9], presented a simplified thermal network for an induction motor. Accordingly, the number of the thermal nodes has been reduced to six and the axial heat transfer paths have been confined to the shaft and the end-windings.

There has been a small number of reports describing the thermal model of the SynRMs. e.g., in [11], Rasid mainly focused on the heat transfer inside the stator slots and proposed a thermal model for the active part of the machine. In [1], Boglietti used the FEA for modeling these active parts of the machine.

This paper presents a simplified LPTN for a SynRM based on the proposed thermal model in [9]. This model has been specially developed for steady-state thermal analysis of a totally enclosed fan cooled (TEFC) transverse-laminated SynRM.

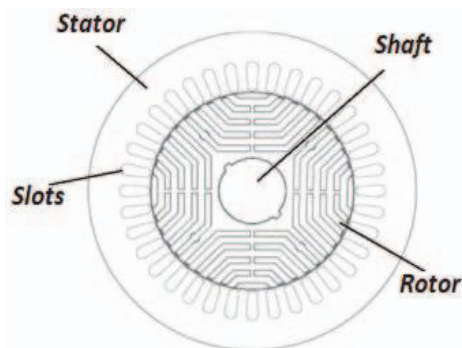


Fig. 1. The cross-section of the 11-kW transverse-laminated SynRM analyzed in this paper.

This work was supported by the Estonian Research Council grant PUT (PUT1260).

## II. THERMAL MODEL DETAILS

## A. Thermal Model Equivalent Circuit

The thermal model developed in this paper is intended for a four poles 10 kW, 400 V, 50 Hz, transverse-laminated SynRM with F insulation class, which its cross-section is shown in Fig. 1. Table I and II show the geometrical and material data of the experimental SynRM.

TABLE I. GEOMETRICAL DATA OF TRANSVERSE- LAMINATED SYNRM

Name	Unit	Value
Stator core length	mm	156
Stator inner diameter	mm	136
Stator outer diameter	mm	219
Number of slots	-	36
Air-gap height	mm	0.4
Rotor inner diameter	mm	45
Rotor outer diameter	mm	135.2
Coil height	mm	21
Slot filling factor	-	0.6
Slot area	mm <sup>2</sup>	130.1

TABLE II. MATERIAL DATA OF TRANSVERSE- LAMINATED SYNRM

Machine part	Material	Thermal conductivity (W/mK)
Frame	Aluminum	230
Laminations	Electric steel	28
Winding	Copper	387
Impregnation	Resin	0.2
Air gap	Air	0.0257
Shaft	Steel	41

To model the steady-state thermal behavior of the machine with the LPTN method, the different heat transfer paths and thermal losses of the machine are represented by means of impedances and power sources respectively. During this process, we implement some hypotheses to reduce the complexity of the thermal model. E.g., the heat losses distribution is assumed to be uniform, the heat flux can only transfer in the axial direction through the shaft, end-winding and end regions of the machine, the heat flux distribution in both end regions of the machine are analogous.

Figure 2 presents the developed LPTN of the machine. The thermal model consists of five nodes and 13 thermal resistances, which capture all the key thermal parameters and temperature raises as well as the main thermal heat transfer paths. Table III gives the definition of the thermal model components of Fig. 2.

Since the SynRM has the same stator structure as an induction machine, the only difference between the developed thermal model in Fig. 2 with the thermal model of the induction machine proposed in [9] is the rotor model. Precisely, the only thermal resistances which will be different from the proposed model in [9] are  $R_{10}$  and  $R_{11}$ . The detailed evaluation methods of the other thermal resistances in Table III can be found in [9] and are not described here.

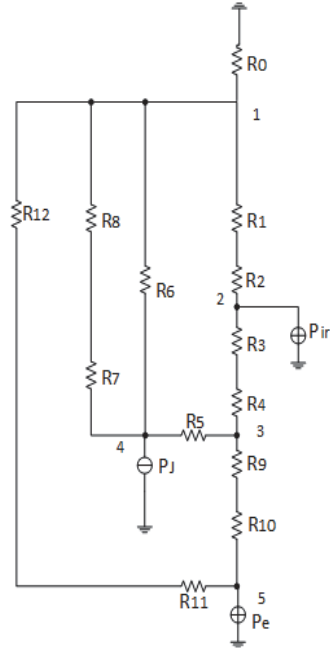


Fig. 2. The developed LPTN model of SynRM.

TABLE III

DEFINITION OF THERMAL MODEL COMPONENTS

Component	Description
$R_0$	Natural Convection and radiation thermal resistance from frame surfer to ambient
$R_1$	Interface gap conduction thermal resistance between the frame and active part of the machine
$R_2$	Conduction thermal resistance of the upper half side of the stator yoke
$R_3$	Conduction thermal resistance of the lower half side of the stator yoke
$R_4$	Conduction thermal resistance of the stator teeth
$R_5$	Conduction thermal resistance between the stator winding and stator teeth
$R_6$	Conduction thermal resistance between the stator winding and frame
$R_7$	Convection thermal resistances between the stator end-winding and inner air of end region
$R_8$	Convection thermal resistance between the inner air and end cap
$R_9$	Convection thermal resistance of the air gap
$R_{10}$	Conduction thermal resistance of upper half side of the rotor
$R_{11}$	Conduction thermal resistance the lower half part of the rotor
$R_{12}$	Axial thermal conduction of the shaft
$P_{ir}$	Stator iron losses
$P_j$	Stator joule losses
$P_e$	Rotor iron losses



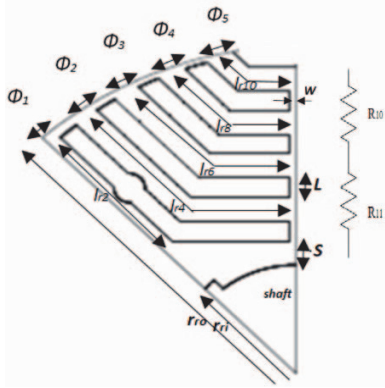


Fig. 3. Cross section of 1/8 of the rotor.

**B. Calculation of Rotor Thermal Resistances**

Figure 3 shows the geometry of a half a pole of the SynRM rotor. The rotor construction consists of the iron laminations, which makes the magnetic flux paths and air gaps in the laminations, which are the magnetic flux barriers. By using the hypothesis that the heat transfer inside the flux barriers is carried out through natural convection and also due to the high thermal conductivity of the rotor iron laminations; we eliminate the heat transfer by the natural convection phenomenon from magnetic flux barriers. As a result, the total heat fluxes inside the rotor are transferred from the iron laminations.

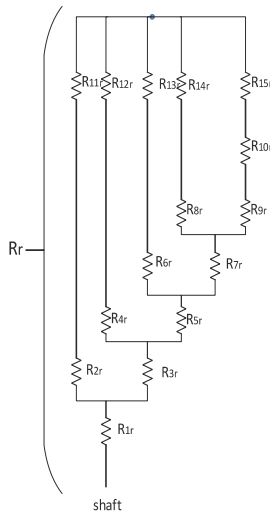


Fig. 4. The thermal equivalent circuit of the rotor.

Figure 4 shows the equivalent thermal circuit for the calculation of the total thermal resistance from the rotor surface to the shaft, which is illustrated by  $R_r$ . Furthermore, the value of  $R_r$  is equal to the sum of the values of  $R_{10}$  and  $R_{11}$ . Accordingly,  $R_r$  consists of the series-parallel combinations of thermal resistances which the values of thermal resistances  $R_{11r}$  to  $R_{15r}$  are calculated by (2) and the rest are evaluated by (1). Finally, by using the series-parallel resistances law in the electrical circuit the value of  $R_r$  is calculated.

$$R = \frac{l}{\lambda \cdot A}, \tag{1}$$

$$R = \frac{\ln\left(\frac{r_o}{r_i}\right)}{\lambda \cdot L \cdot \phi}, \tag{2}$$

where  $l$  is the length of heat flux path (m),  $A$  is the cross-section area (m<sup>2</sup>),  $\lambda$  is the thermal conductivity of the material (W/m.K),  $r_o$  and  $r_i$  are the outer radius and the inner radius of cylinder (m),  $L$  is the active length of the machine (m) and  $\phi$  is the angular span (rad).

**C. Analytical Nodal Temperature Calculation**

For the steady-state thermal analysis, the final nodal temperatures of Fig. 2 can be calculated by the matrix inversion theory [12]. Accordingly, the nodal temperatures of the proposed thermal model are calculated as follow:

$$[T] = [G]^{-1} [P], \tag{3}$$

where  $[T]$  is the temperature column vector,  $[P]$  is the power column vector which contains the losses at each node and  $[G]$  is the thermal conductance square matrix which is defined as:

$$G = \begin{bmatrix} \sum_{j=1}^n \frac{1}{R_{1,j}} & -\frac{1}{R_{1,2}} & \dots & -\frac{1}{R_{1,n}} \\ -\frac{1}{R_{2,1}} & \sum_{j=1}^n \frac{1}{R_{2,j}} & \dots & -\frac{1}{R_{2,n}} \\ \vdots & \vdots & \ddots & \vdots \\ -\frac{1}{R_{n,1}} & -\frac{1}{R_{n,2}} & \dots & \sum_{j=1}^n \frac{1}{R_{n,j}} \end{bmatrix} \tag{4}$$

The  $G_{i,i}$  components in the main diagonal of the thermal conductance matrix are defined as the sum of the conductances connected to the  $i$ -th node and  $G_{i,j}$  is defined as the negative thermal conductances between nodes  $i$  and  $j$ .

### III. EXPERIMENTAL METHODOLOGY

The objective of the experimental work in the natural cooling mode is to determine the value of the natural convection and radiation thermal resistance ( $R_\theta$ ) as well as the accuracy of the analytical calculation based on the LPTN model.

According to [9], the value of the resistance  $R_\theta$  is evaluated by using DC stator test. The DC stator test is a common experimental method for determining the value of the resistance  $R_\theta$ . In this test, the loss of SynRM is confined to the joule loss of the stator coil windings where the electric power can be easily measured. In the calculations, we accounted for the variations in the winding electrical resistance, as the winding resistivity is temperature dependent [12],[13]. During the experiments, the DC power applied to the motor is measured as well as the surface temperature of the motor at different locations. The SynRM is supplied through a digital DC power supply, since the forced cooling air speed is zero and the motor is cooled by natural convection, the motor is supplied with 40% -70% of its nominal current for overheat protection. Four K-type thermocouples are installed by means of adhesive material in various locations on the frame surface of the motor. The ambient temperature is also measured by means of a K-type thermocouple. For the purpose of increasing the accuracy of the temperature measurement and minimizing the contact resistance between the thermocouple and the frame surface of the motor, we used thermal paste. The average temperature of these four thermocouples is assumed to be the mean temperature of the motor frame surface. During the experiments, all the temperature data are collected by means of a Graphtec GL200. The experiment has been carried out until the system reached its steady-state condition. The resistance  $R_\theta$  is then calculated as [14]:

$$R_\theta = \frac{T_s - T_a}{P}, \quad (5)$$

where  $T_s$  is the frame surface temperature (□),  $T_a$  is the ambient temperature (□) and  $P$  is the input DC power (W).

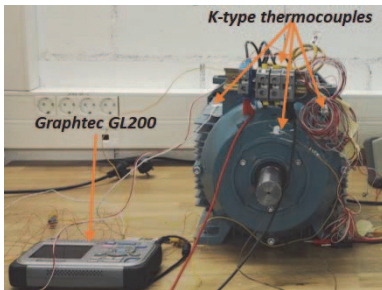


Fig. 5. SynRM test setup.

Figure 5 shows the experimental setup and different location of the surface frame thermocouples. In addition to the

surface temperature, the temperature inside the machine was also measured. For this purpose, six different thermocouples have been installed inside the end-windings and slots of the stator. Finally, all measured temperature values are used to validate the developed thermal model.

### IV. RESULTS AND DISCUSSION

The DC measurements were carried out at current equals to 40% of the nominal current of the machine, i.e. 8.71 (A). It then took about seven hours to reach the steady-state thermal behavior.

In the steady state mode, the input power was 191.16 (W), the mean temperature of the frame surface was 61.2 (□) and the ambient temperature was 21.8 (□). Finally, the evaluated value of  $R_\theta$  by using (5) was 0.2056 (□/W).

TABLE IV

Analytical and Experimental Temperature of Motor Components		
Machine components	Analytical thermal model	Experimental mean temperature
Frame surface (□)	59.4	61.2
Winding (□)	70.8	74
End winding (□)	76.7	78

To validate the developed thermal model, the analytically calculated temperatures are compared with the experimental data. We present the analytical and experimental results in Table IV. Accordingly, the analytical results are in good agreement with those obtained by the experimental method. The mean difference in the temperature between the analytical and experimental results is around 3%. This difference arises from the hypothesis of the uniform distribution of losses in the machine as well as from the fact that the analytical LPTN model predicts the mean temperature of the machine component while in the experimental part, the thermocouples show the temperatures at given positions. This fact is illustrated in Fig. 6, which shows the temperature distribution over the frame surface of the SynRM in the steady-state mode. The picture is captured by a thermal camera. The figure gives a good overview of the temperature difference on the frame surface of the SynRM. however, The result shows that the presented thermal model can be applied for temperature prediction of the SynRM.

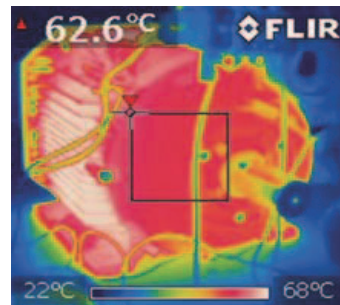


Fig. 6. The surface temperature of SynRM.

## V. CONCLUSION

A steady-state LPTN of a transverse-laminated SynRM has been presented. It makes it possible to predict the temperature of the important parts of the machine. We have implemented some simplification hypothesis to reduce the complexity of the model to decrease the computation time without compromising the accuracy of the temperature prediction.

The experimental results of the SynRM under DC stator test have been compared to the LPTN predicted temperatures. The agreement between the analytical temperature and the measured ones seems to be very good. For the future job, the thermal model of the machine will be adjusted to predict the temperature of the machine under forced cooling and normal operation of the machine. For this reason, a radiation thermal resistance and a forced convection thermal resistance parallel to the natural convection one will be in the thermal model.

## REFERENCES

- [1] A. Boglietti, A. Cavagnino, M. Pastorelli, D. Staton, and A. Vagati, "Thermal analysis of induction and synchronous reluctance motors," *IEEE Trans. Ind. Appl.*, vol. 42, no. 3, pp. 675–680, May 2006.
- [2] P. S. Ghahfarokhi, A. Kallaste, A. Belahcen, T. Vaimann, and A. Rassolkin, "Review of thermal analysis of permanent magnet assisted synchronous reluctance machines," in 2016 Electric Power Quality and Supply Reliability (PQ), 2016, pp. 219–224.
- [3] A. Boglietti, A. Cavagnino, D. Staton, M. Shanel, M. Mueller, and C. Mejuto, "Evolution and Modern Approaches for Thermal Analysis of Electrical Machines," *IEEE Trans. Ind. Electron.*, vol. 56, no. 3, pp. 871–882, Mar. 2009.
- [4] A. Boglietti, A. Cavagnino, and D. Staton, "Determination of Critical Parameters in Electrical Machine Thermal Models," *IEEE Trans. Ind. Appl.*, vol. 44, no. 4, pp. 1150–1159, 2008.
- [5] A. M. EL-Refaie, N. C. Harris, T. M. Jahns, and K. M. Rahman, "Thermal Analysis of Multibarrier Interior PM Synchronous Machine Using Lumped Parameter Model," *IEEE Trans. Energy Convers.*, vol. 19, no. 2, pp. 303–309, Jun. 2004.
- [6] P. H. Mellor, D. Roberts, and D. R. Turner, "Lumped parameter thermal model for electrical machines of TEFC design," *IEE Proc. B Electr. Power Appl.*, vol. 138, no. 5, p. 205, 1991.
- [7] A. Boglietti, A. Cavagnino, M. Popescu, and D. Staton, "Thermal Model and Analysis of Wound-Rotor Induction Machine," *IEEE Trans. Ind. Appl.*, vol. 49, no. 5, pp. 2078–2085, Sep. 2013.
- [8] O. I. Okoro, "Steady and Transient States Thermal Analysis of a 7.5-kW Squirrel-Cage Induction Machine at Rated-Load Operation," *IEEE Trans. Energy Convers.*, vol. 20, no. 4, pp. 730–736, Dec. 2005.
- [9] A. Boglietti, A. Cavagnino, M. Lazzari, and M. Pastorelli, "A simplified thermal model for variable-speed self-cooled industrial induction motor," *IEEE Trans. Ind. Appl.*, vol. 39, no. 4, pp. 945–952, Jul. 2003.
- [10] J. Lindström, "Thermal Model of a Permanent-Magnet Motor for a Hybrid Electric Vehicle," *CHALMERS UNIVERSITY OF TECHNOLOGY*, Goteborg, 1999.
- [11] M. A. H. Rasid, A. Ospina, K. El Kadri Benkara, and V. Lanfranchi, "Thermal model of stator slot for small synchronous reluctance machine," in 2014 International Conference on Electrical Machines (ICEM), 2014, pp. 2199–2204.
- [12] P. S. Ghahfarokhi, A. Kallaste, A. Belahcen, and T. Vaimann, "Steady state and transient thermal analysis of the stator coil of a permanent magnet generator," in 2017 18th International Scientific Conference on Electric Power Engineering (EPE), 2017, pp. 1–5.
- [13] P. S. Ghahfarokhi, A. Kallaste, A. Belahcen, T. Vaimann, "Determination of Forced Convection Coefficient Over a Flat Side of Coil," in 58th International Scientific Conference on Power and Electrical Engineering of Riga Technical University (RTUCON), 2017, pp. 1–4.
- [14] A. Boglietti, A. Cavagnino, and D. A. Staton, "Thermal analysis of TEFC induction motors," in 38th IAS Annual Meeting on Conference Record of the Industry Applications Conference, 2003., vol. 2, pp. 849–856.

## BIOGRAPHIES

**Payam Shams Ghahfarokhi** was born in Iran, in 1986. He received the B.Sc. degree in electrical power engineering from IAUN in 2010 and the M.Sc. degree in electrical power engineering from Newcastle University in 2011. He is currently a Ph.D. student at Tallinn University of Technology. He has been the student IEEE member since 2017. His main field of interests is design of permanent magnet electrical machine and thermal design of electrical machine.

**Anouar Belahcen** (M13-SM15) received the M.Sc. (Tech.) and Doctor (Tech.) degrees from Helsinki University of Technology, Finland, in 1998, and 2004, respectively. He is now Professor of electrical machines at Tallinn University of Technology, Estonia and Professor of Energy and Power at Aalto University, Finland. His research interest are numerical modeling of electrical machines, magnetic materials, coupled magneto-mechanical problems, magnetic forces, magnetostriction, and fault diagnostics

**Ants Kallaste** was born in Pärnu, Estonia in 1980 and received his B.Sc., M.Sc., and Ph.D. degrees in electrical engineering from Tallinn University of Technology, Estonia, in 2004, 2006, and 2013, respectively. He is currently a Senior Researcher in Tallinn University of Technology, Department of Electrical Engineering and carrying out postdoctoral research at the Department of Electrical Engineering and Automation, Aalto University, Espoo, Finland. He has been working in several companies as an Electrical Engineer. Presently he is working at the Tallinn University of Technology, Department of Electrical Engineering holding the position of Head of Chair of Electrical Machines. He has been the IEEE member since 2013. His main research interests include permanent magnet machine design and wind turbines.

**Toomas Vaimann** (S'11-M'14) was born in Pärnu, Estonia, in 1984 and received his B.Sc., M.Sc., and Ph.D. degrees in electrical engineering from Tallinn University of Technology, Estonia, in 2007, 2009, and 2014, respectively. He is currently a Senior Researcher in Tallinn University of Technology, Department of Electrical Engineering and carrying out postdoctoral research at the Department of Electrical Engineering and Automation, Aalto University, Espoo, Finland. He has been working in several companies as an Electrical Engineer. He is the member of IEEE, Estonian Society of Moritz Hermann Jacobi and Estonian Society for Electrical Power Engineering. His main research interest is the diagnostics of electrical machines.

**Anton Rassõlkin** (S'12-M'16). was born in Tallinn, Estonia, in 1985 and received the BSc, MSc and PhD degrees in electric drives and power electronics from Tallinn University of Technology, Tallinn, Estonia, in 2008, 2010 and 2014, respectively. In 2010 received Dipl.-Ing. (FH) degree in automatic from University of Applied Science Giessen-Friedberg, Giessen, Germany. He has been working in several companies as an electrical engineer. Presently he is working at the Tallinn University of Technology, Department of Electrical Engineering as a research scientist. He is the member of IEEE The main research interests lay in the field of electric drives and its control systems as well as in the fields of electrical machines and electric transportation.



**Publication V**

P. Shams Ghahfarokhi, A. Kallaste, T. Vaimann, and A. Belahcen, "Natural convection from flat side's of coil system," in 2018 19th International Scientific Conference on Electric Power Engineering (EPE), 2018, pp. 1–5.



# Natural Convection From Flat Side's of Coil System

Payam Shams Ghahfarokhi, Ants Kallaste, Toomas Vaimann  
Dept. Electrical Power Engineering and Mechatronics  
Tallinn University of Technology  
Tallinn, Estonia  
payam.shams@ttu.ee

Anouar Belahcen  
Dept. Electrical engineering and Automation  
Aalto University  
Espoo, Finland

**Abstract**—This paper presents a thermal study to determine the convective heat transfer coefficient over the flat side of a permanent magnet synchronous generator coil in horizontal and vertical directions by using the empirical correlations. To validate the results, an experimental setup is developed for both horizontal and vertical orientations and different input currents. The experimental results are compared with the analytical method, based on correlations proposed in the literature. The results show that the analytical calculation based on empirical correlation for the horizontal case and Mac Adams as well as Churchill I correlations for the vertical case have a good agreement with the experimental data.

**Keywords**— empirical correlation; flat plate; heat transfer; natural convection.

## I. INTRODUCTION

According to the increased demand for high efficiency, high power density and high torque as well as small size and cost reduction of an electrical machine; the thermal design and analysis of an electrical machine has started to receive more attention.

The lumped parameter thermal network (LPTN) and the finite element (FE) analysis are two common methods in thermal design and analysis of electrical machine, which can simulate the heat transfer phenomenon to predict the temperature of electrical machine components[1],[2].

In the electrical machine with the natural cooling system, the most important phenomenon, which has a great effect on the accuracy of the model, is natural convection from the machine housing to the ambient[3]. This phenomenon depends on many factors e.g., surface temperature, ambient properties and shape of surfaces. The simplest housing of the electrical machine consists of the smooth blocks. The natural convection coefficients from these types of housing are calculated by using empirical dimensionless correlations for flat plates[3]. Fortunately, there are different correlations for convection heat transfer over flat plate surface in the horizontal and the vertical orientations.

This paper presents the determination of the natural convection coefficient over the flat plate surface in the horizontal and the vertical orientations theoretically and experimentally. Finally, the theoretical result compare to experimental ones to validate the results and detect the accuracy-

-of each correlation to find a consensus which of them is more exact to calculate the natural convection over flat plate surface especially for the smooth blocked housing of electrical machine.

## II. NATURAL CONVECTION DIMENSIONLESS ANALYSIS

The natural convection phenomenon is the heat transfer processes due to the buoyancy forces[4]. From the molecular point of view, the warmer molecules that are lighter displace the cooler fluid molecules that are heavier[5].

The value of the natural convection coefficient is calculated by means of three dimensionless numbers: Nusselt number (Nu), Grashof number (Gr) and Prandtl number (Pr)[1]. These dimensionless numbers are calculated as follow[4], [6]:

$$\text{Nu} = a(\text{GrPr})^b, \quad (1)$$

$$\text{Gr} = \frac{\beta g \Delta T \rho^2 L^3}{\mu^2}, \quad (2)$$

$$\text{Pr} = \frac{c_p \mu}{k}, \quad (3)$$

Where  $a$  and  $b$  are constant,  $\beta$  is coefficient of volume expansion [1/K];  $g$  is the gravitational acceleration [m/s<sup>2</sup>];  $\Delta T$  is temperature difference between the surface and fluid [C];  $\rho$  is fluid density [kg/m<sup>3</sup>];  $L$  is the characteristic length of the surface [m];  $\mu$  is the fluid dynamic viscosity [kg/(s.m)];  $c_p$  is fluid specific heat capacity [kJ/(kg °C)] and  $k$  is fluid thermal conductivity [W/(m °C)].

Finally, the amount of natural convection coefficient ( $h$ ) is evaluated as:

$$h = \frac{\text{Nu}k}{L}, \quad (4)$$

In the natural convection, there is another dimensionless number, which is called Rayleigh number (Ra). This number is defined as to multiplication of the Gr, and Pr [1]. It is used to determine fluid flow mode (laminar or turbulent)[4].

According to (2) and (3), to calculate the dimensionless numbers, the fluid properties play a key role. As all these parameters are temperature dependent and the value of these parameters are changing by the temperature. As the fluid in our case study is air, the fluid properties are calculated by using correlations, which has been provided in [7].

This work was supported by the Estonian Research Council grant PUT (PUT1260).

### III. EMPIRICAL CORRELATIONS

The empirical correlations for theoretical calculation of the natural convection coefficient over the flat surface by means of dimensionless number in both horizontal and the vertical orientations are presented in this section

#### A. Flat Plate in Horizontal Direction

The empirical correlations for flat plate in the horizontal direction according to hot plate status are divided into two main categories (Fig. 1): upper face and lower face [8].

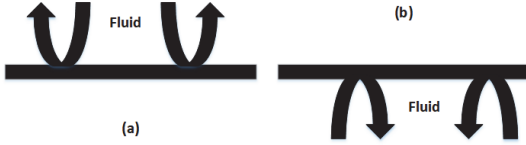


Fig. 1. Natural convection on the horizontal flat a) hot surface facing up and b) hot surface facing down.

The empirical correlations for the upper face hot surface in the laminar and turbulent mode are respectively as [8]:

$$Nu = 0.54(GrPr)^{0.25}, \quad (5)$$

$$Nu = 0.15(GrPr)^{0.33}, \quad (6)$$

The empirical correlation for the lower hot surface is:

$$Nu = 0.27(GrPr)^{0.25}, \quad (7)$$

Moreover, the characteristic length for the horizontal surface is calculated as [8]:

$$L = \frac{A}{p}, \quad (8)$$

where A is the surface area of the flat plate and p is perimeter.

#### B. Flat Plate in Vertical Direction

There are different empirical correlations for the calculation of average Nusselt number for the vertical flat plate. One of the first correlations to calculate the Nusselt number, which covers laminar and turbulent, has been introduced by Mc Adams in 1954 as follow [9]:

$$Nu = 0.59(GrPr)^{0.25}, \quad (9)$$

$$Nu = 0.10(GrPr)^{0.33}, \quad (10)$$

However, Churchill and Chu in 1975 have found the new correlation that can be applied to an entire range of Ra [9]:

$$Nu = \left\{ 0.825 + \frac{0.387(GrPr)^{1/6}}{[1+(0.492/Pr)^9/16]^{8/27}} \right\}^2, \quad (11)$$

Moreover, they recommended the correlation for laminar mode as follow [9]:

$$Nu = 0.68 + \frac{0.67(GrPr)^{1/4}}{[1+(0.492/Pr)^9/16]^{4/9}}, \quad (12)$$

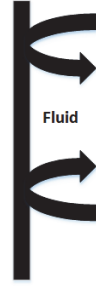


Fig. 2. Natural convection on vertical plate

### IV. EXPERIMENTAL SETUP AND PROCEDURE

The objective of the experimental work in this paper is to assess the natural heat transfer coefficient from the flat side of the stator coil of a permanent magnet generator in the horizontal and vertical orientations. Yet another objective is to compare the analytical data to experimental data for finding the appropriate empirical correlation in both cases and verify the accuracy of these correlations.

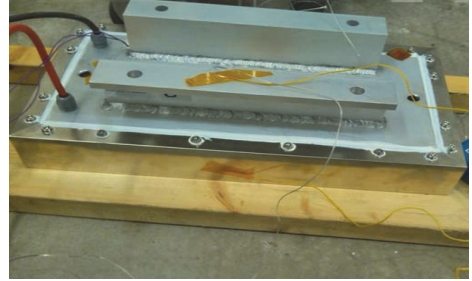


Fig. 3. Coil module

#### A. Experimental Procedure

According to our previous research work [10], the stator coil under study consists of six different faces (Fig. 3). To consider the natural convection from the flat side, the heat flux flow should be confined only to the flat side. To achieve this, we created an insulation box according to the dimensions of the coil by means of foam insulation boards with a thickness of 10 cm. Figure 4 shows the coil box and the flat side of the coil in. Since the foam insulation material has low thermal conductivity  $k=0.3$  (W/m K), the thermal flux flow is restricted to the open surface. Therefore, the box is operating as a closed calorimeter. Another important point about the box is the temperature operation point; as the foam insulation board can handle temperatures up to 90 °C, during the experiment, the coil temperature should not exceed that temperature.

The test bench is designed to measure the natural convection coefficient from the flat's side of the coil module. For this purpose, we use the DC test method. The DC test is a common experimental method for determining the convection coefficient of heat transfer. In this test, the loss of the coil is



confined to the DC copper loss of the coil winding and the power can be easily calculated from the measured electric voltage and current. In the calculations, we accounted for the variations in the winding electrical resistance, as the winding resistivity is temperature dependent [10], [11]. During the experiments, in addition to the power input to the coil module, the temperature of the flat side is measured at different locations. Six K-type thermocouples are installed by means of adhesive material in various locations on the fin side of the coil module. The ambient temperature is also measured by means of a K-type thermocouple.

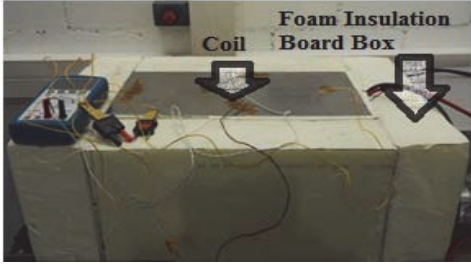


Fig. 4. The used configurations in the experiment

### B. Analysis Method of Experimental Data

The total heat produced in the coil is equal to total input power. Thus, the total heat in Watts (W) is defined as:

$$Q_T = V \cdot I, \quad (13)$$

where  $V$  (V) is the input voltage and  $I$  (A) the input current.

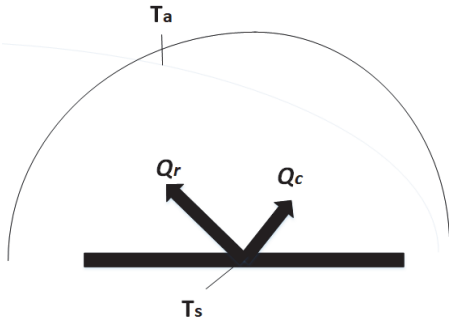


Fig. 5. Physical system

As Fig. 5 shows, during the natural cooling, the total heat is extracted from flat surface of the coil to the ambient by the natural convection and radiation phenomena. Thus, the total heat described as:

$$Q_T = Q_c + Q_r, \quad (14)$$

where  $Q_c$  (W) is the amount of heat extracted by natural convection and  $Q_r$  (W) is the amount of heat extracted by radiation.

According to [12] and [2], the heat extraction coefficient  $h_e$  is calculated as:

$$h_e = \frac{Q_T}{(T_s - T_a) \cdot A}, \quad (15)$$

where  $T_s$  (°C) is the mean temperature of the fin side of the coil module,  $T_a$  (°C) is the ambient temperature and  $A$  (m<sup>2</sup>) is the fin side surface area.

The total heat extraction coefficient is defined as the sum of the convection  $h_c$  and radiation  $h_r$  coefficients:

$$h_e = h_c + h_r. \quad (16)$$

The radiation coefficient is defined as [2]:

$$h_r = \varepsilon \cdot \sigma \cdot (T_s^2 + T_a^2) \cdot (T_s + T_a), \quad (17)$$

where  $\varepsilon$  is the emissivity of the surface and  $\sigma = 5.67 \times 10^{-8}$  (W/m<sup>2</sup> K<sup>4</sup>) is the Stefan-Boltzmann constant.

## V. RESULTS AND DISCUSSION

The validation of the empirical correlations is made by comparison with experimental data for the five input currents for both horizontal and vertical configurations. We present the analytical and experimental results according to the coil module's orientation.

In the experimental part, the flat side of the coil module is studied in both horizontal and vertical cases. To determine the convection coefficient from the experimental data; first, the total heat  $Q_T$  is calculated based on the measured values of the current and voltage by (13), then according to the ambient and surface temperatures of the case study, the total heat extraction coefficient  $h_e$  and radiation coefficient  $h_r$  are determined respectively by (15) and (17). Finally, the natural convection coefficient  $h_c$  is calculated by (16).

For the analytical part, according to the coil module orientation, the appropriate empirical correlations are used to calculate the natural convection coefficient  $h_c$ .

### A. Horizontal Direction

Tables I and II show the experimental and analytical data for horizontal configuration, respectively.

TABLE I. EXPERIMENTAL RESULTS FOR HORIZONTAL CONFIGURATION

$I$ (A)	$T_s$ (°C)	$T_a$ (°C)	$Q_T$ (W)	$h_e$ W/(m <sup>2</sup> K)	$h_r$ W/(m <sup>2</sup> K)	$h_c$ W/(m <sup>2</sup> K)
10	40	23	15.76	10.09	3.53	6.56
12	46.6	23	23.47	10.37	3.63	6.74
15	60.3	23	38.64	11.07	3.73	7.34
17	71.6	24	51.68	11.58	3.83	7.75
18	77.3	24	59.33	12.44	4.03	8.41

TABLE II. ANALYTICAL RESULTS FOR HORIZONTAL CONFIGURATION

$I$ (A)	$T_s$ (°C)	$T_a$ (°C)	$h_e$ W/(m <sup>2</sup> K)	$h_r$ W/(m <sup>2</sup> K)	$h_c$ W/(m <sup>2</sup> K)
10	40	23	9.22	3.53	5.37
12	46.6	23	9.78	3.63	5.80
15	60.3	23	10.70	3.73	6.44
17	71.6	24	11.30	3.83	6.79
18	77.3	24	11.58	4.03	6.94

Figure 6 shows the variation of the total heat extraction coefficient  $h_e$  with the temperature difference for five different input currents in the horizontal configuration. The average relative difference of the analytical data in comparison with the experimental one is 6% and the maximum relative difference based on this correlation is 9%. However, according to Table I and II, it is clearly shown that by increasing the temperature, the relative difference of the analytical data compared with the experimental data decreases.

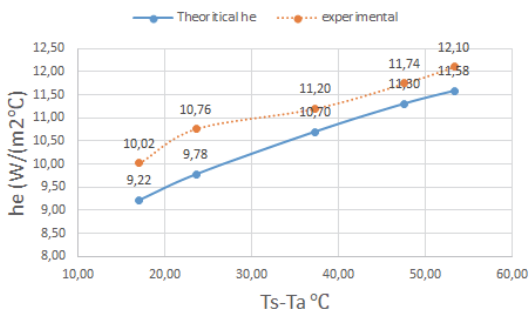


Fig. 6. Variation of total heat extraction coefficient with temperature difference for the horizontal direction.

**B. Vertical Direction**

Tables III shows the experimental data for vertical configuration.

TABLE III. EXPERIMENTAL RESULTS FOR VERTICAL CONFIGURATION

$I$ (A)	$T_s$ (°C)	$T_a$ (°C)	$Q_r$ (W)	$h_e$ W/(m <sup>2</sup> K)	$h_r$ W/(m <sup>2</sup> K)	$h_c$ W/(m <sup>2</sup> K)
10	42.3	24	15.89	8.81	3.91	5.48
12	49.6	24	23.62	9.98	4.05	5.93
15	62.4	24	38.90	10.94	4.32	6.62
17	74.3	24	52.21	11.22	4.58	6.64
18	81.0	25	59.78	11.54	4.75	6.79

Tables IV, V, and VI show the analytical data for the vertical case for which the natural convection coefficients have been calculated based on Mac Adams, Churchill I and II respectively.

TABLE IV. ANALYTICAL RESULTS FOR VERTICAL CONFIGURATION BASED ON MAC ADAMS CORRELATION

$I$ (A)	$T_s$ (°C)	$T_a$ (°C)	$h_e$ W/(m <sup>2</sup> K)	$h_r$ W/(m <sup>2</sup> K)	$h_c$ W/(m <sup>2</sup> K)
10	42.3	24	8.42	3.91	4.45
12	49.6	24	8.90	4.05	4.86
15	62.4	24	9.67	4.32	5.35
17	74.3	24	10.25	4.58	5.67
18	81.0	25	10.54	4.75	5.79

TABLE V. ANALYTICAL RESULTS FOR VERTICAL CONFIGURATION BASED ON CHURCHILL I CORRELATION

$I$ (A)	$T_s$ (°C)	$T_a$ (°C)	$h_e$ W/(m <sup>2</sup> K)	$h_r$ W/(m <sup>2</sup> K)	$h_c$ W/(m <sup>2</sup> K)
10	42.3	24	8.22	3.91	4.31
12	49.6	24	8.76	4.05	4.71
15	62.4	24	9.55	4.32	5.23
17	74.3	24	10.16	4.58	5.58
18	81.0	25	10.45	4.75	5.70

TABLE VI. ANALYTICAL RESULTS FOR VERTICAL CONFIGURATION BASED ON CHURCHILL II CORRELATION

$I$ (A)	$T_s$ (°C)	$T_a$ (°C)	$h_e$ W/(m <sup>2</sup> K)	$h_r$ W/(m <sup>2</sup> K)	$h_c$ W/(m <sup>2</sup> K)
10	42.3	24	8.17	3.91	4.26
12	49.6	24	8.66	4.05	4.60
15	62.4	24	9.36	4.32	5.04
17	74.3	24	9.92	4.58	5.34
18	81.0	25	10.20	4.75	5.45

Figure 7 shows the variation of the total heat extraction coefficient ( $h_e$ ) with the temperature difference for five different input currents in a vertical orientation. Significant differences were found between the analytical data based Churchill II correlation and the experimental data. The mean relative difference of this empirical correlation is about 12% and the maximum one is 14%. However, the amount of the mean difference of the analytical results based on Mac Adams correlation is less than the analytical results based on the Churchill I correlation. The average relative difference based on the mentioned correlations are 9% and 10% respectively.

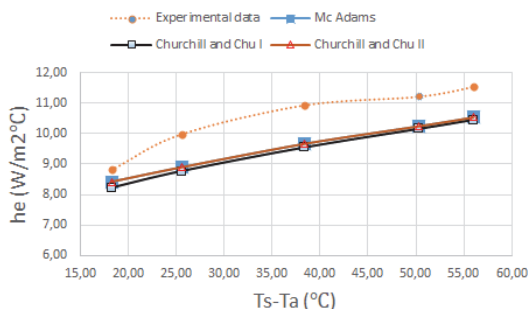


Fig. 7. Variation of total heat extraction coefficient with temperature difference for the vertical direction.

Another interesting finding is achieved by simple comparison between natural convection coefficients of the corresponding currents. Accordingly, the natural convection coefficient in the horizontal configuration is higher than in the vertical one, which means that the horizontal flat plate provides better natural cooling than the vertical one and thus can reduce the amount of the copper power loss as well as the surface temperature. Therefore, the experimental data were collected for five different input currents corresponding to different temperature raises. All experiments were made at the steady state of the thermal system.

## VI. CONCLUSION

This paper presented the determination of the natural convection over the flat plate for both horizontal and vertical orientations by using different empirical correlations. In order to validate and evaluate the accuracy of each correlation, the experimental setup has been developed. Therefore, the experimental data were collected for five different input currents corresponding to different temperature raises. Accordingly, the analytical data are in good agreement with the experimental one.

According to this study, it can be concluded that flat plate in the horizontal configuration provides better cooling condition rather than vertical manner. Moreover, for the vertical case, the Mac Adams and Churchill I have good agreement with experimental one.

## REFERENCES

- [1] P. S. Ghahfarokhi, A. Kallaste, A. Belahcen, T. Vaimann, and A. Rassolkin, "Review of thermal analysis of permanent magnet assisted synchronous reluctance machines," in 2016 Electric Power Quality and Supply Reliability (PQ), 2016, pp. 219–224.
- [2] O. Meksi and A. O. Vargas, "Numerical and experimental determination of external heat transfer coefficient in small TENV electric machines," in 2015 IEEE Energy Conversion Congress and Exposition (ECCE), 2015, pp. 2742–2749.
- [3] A. Boglietti, A. Cavagnino, and D. Staton, "Determination of critical parameters in electrical machine thermal models," IEEE Trans. Ind. Appl., vol. 44, no. 4, pp. 1150–1159, 2008.
- [4] D. A. Staton and A. Cavagnino, "Convection Heat Transfer and Flow Calculations Suitable for Electric Machines Thermal Models," IEEE Trans. Ind. Electron., vol. 55, no. 10, pp. 3509–3516, Oct. 2008.
- [5] J. Pyrhönen, T. Jokinen, and V. Hrabovcová, Design of Rotating Electrical Machines. Wiley, 2008.
- [6] P. S. Ghahfarokhi, A. Kallaste, A. Belahcen, and T. Vaimann, "Thermal analysis of electromagnetic levitation coil," in 2016 17th International Scientific Conference on Electric Power Engineering (EPE), 2016, pp. 1–5.
- [7] A. Boglietti, A. Cavagnino, M. Lazzari, and M. Pastorelli, "A simplified thermal model for variable-speed self-cooled industrial induction motor," IEEE Trans. Ind. Appl., vol. 39, no. 4, pp. 945–952, Jul. 2003.
- [8] Y. A. Cengel, Heat Transfer: A Practical Approach. New York: McGraw-Hill, 2004.
- [9] A. D. K. Adrian Bejan, Heat Transfer Handbook. John Wiley & Sons, 2003.
- [10] A. R. Payam Shams Ghahfarokhi, Ants Kallaste, Anouar Belahcen, Toomas Vaimann, "Determination of Forced Convection Coefficient Over a Flat Side of Coil," in 58th International Scientific Conference on Power and Electrical Engineering of Riga Technical University (RTUCON), 2017, pp. 1–4.
- [11] P. S. Ghahfarokhi and A. Kallaste, "Steady State and Transient Thermal Analysis of the Stator Coil of a Permanent Magnet Generator," in 2016 17th International Scientific Conference on Electric Power Engineering (EPE), 2017, pp. 1–7.
- [12] M. Markovic, L. Saunders, and Y. Perriard, "Determination of the Thermal Convection Coefficient for a Small Electric Motor," in Conference Record of the 2006 IEEE Industry Applications Conference Forty-First IAS Annual Meeting, 2006, vol. 1, pp. 58–61.
- [13] G. Eason, B. Noble, and I. N. Sneddon, "On certain integrals of Lipschitz-Hankel type involving products of Bessel functions," Phil. Trans. Roy. Soc. London, vol. A247, pp. 529–551, April 1955. (references)
- [14] J. Clerk Maxwell, A Treatise on Electricity and Magnetism, 3rd ed., vol. 2. Oxford: Clarendon, 1892, pp.68–73.
- [15] I. S. Jacobs and C. P. Bean, "Fine particles, thin films and exchange anisotropy," in Magnetism, vol. III, G. T. Rado and H. Suhl, Eds. New York: Academic, 1963, pp. 271–350.
- [16] K. Elissa, "Title of paper if known," unpublished.
- [17] R. Nicole, "Title of paper with only first word capitalized," J. Name Stand. Abbrev., in press.
- [18] Y. Yorozu, M. Hirano, K. Oka, and Y. Tagawa, "Electron spectroscopy studies on magneto-optical media and plastic substrate interface," IEEE Transl. J. Magn. Japan, vol. 2, pp. 740–741, August 1987 [Digests 9th Annual Conf. Magnetism Japan, p. 301, 1982].
- [19] M. Young, The Technical Writer's Handbook. Mill Valley, CA: University Science, 1989.



**Publication VI**

P. Shams Ghahfarokhi, A. Kallaste, T. Vaimann, A. Rassolkin, and A. Belahcen, "Determination of forced convection coefficient over a flat side of coil," in 2017 IEEE 58th International Scientific Conference on Power and Electrical Engineering of Riga Technical University (RTUCON), 2017, pp. 1–4.



# Determination of Forced Convection Coefficient Over a Flat Side of Coil

Payam Shams Ghahfarokhi, Ants Kallaste, Toomas Vaimann, Anton Rassolkin  
Dept. Electrical Power Engineering and Mechatronics  
Tallinn University of Technology  
Tallinn, Estonia  
payam.shams@ttu.ee

Anouar Belahcen  
Dept. Electrical Power Engineering and Mechatronics  
Tallinn University of Technology  
Tallinn, Estonia  
Dept. of Electrical Engineering and Automation  
Aalto University  
Finland

**Abstract**—The paper presents analytical and experimental determination of the forced convection heat transfer coefficients over the flat side of a permanent magnet synchronous generator coil. In the analytical part, the forced convection coefficients at different wind speeds are calculated based on various known equations of the forced convection heat transfer coefficient with unheated starting length. The experimental part consists of loading the coil with DC current and measurements of the coil temperatures with thermal sensors while it was inside a wind tunnel. Based on the measurement, the convection coefficients were found. In the final part, the experimental and analytical results are compared. It is shown that the accuracy of the analytical results is more precise in high turbulent flows.

**Keywords**—forced convection heat transfer coefficient; flat surface; laminar and turbulent flow.

## I. INTRODUCTION

Permanent magnet machines are popular types of electrical machines in different industries. These types of machine are widely used in the aerospace and automotive industry and in wind turbines. In these applications, customer demands are high: machines require higher torque and power density, higher energy efficiency and cost reduction. To achieve the customer demands, thermal analysis of the electrical machine in parallel with electromagnetic design is gaining more attention.

Nowadays, two different high energy rare earth magnetic materials are employed in these machines, namely the Neodymium Iron Boron (NdFeB) and the Samarium Cobalt (SmCo)[1]. The operation point of these rare earth magnetic materials are inversely proportional to the temperature. The thermal stress inside the electrical machines leads to the temperature rise in the permanent magnet, which may eventuate to irreversible demagnetization of the magnets. Therefore, an appropriate cooling method is necessary for these machines [1]. The thermal stress inside the electrical machine is produced by the losses. An important source of loss in these types of machine is the stator coils, but some losses are also produced in the iron core of the machines and in permanent magnets[1].

A significant part of heat is dissipated with the convection phenomenon, which can be divided into two parts: natural and

forced convection [2]. In this phenomenon, the amount of the heat transfer between the cooling surface and the coolant fluid is directly proportional to the fluid's velocity. In the natural form of the convection, the velocity of the fluid is low and it is more appropriate for low power electrical machines. However, for higher heat transfer from the surface, higher velocity is necessary to increase the flow rate of fluid. This is achieved by applying a fan or a blower [3]. Another effective way for increasing the fluid motion is to implement a distinct cooling system, e.g., a wind tunnel technology for wind miles can be implemented instead of extra equipment in the machine for increasing the coolant speed.

A serious challenge in the thermal analysis of an electrical machine under forced convection is to determine the forced convection coefficient from the cooling surface as the accuracy of this coefficient has a direct effect on the accuracy of the temperature prediction of any thermal model.

The aim of the paper is to determine analytically and experimentally the influence of the fluid flow on the heat transfer coefficient on the permanent magnet synchronous stator coil and propose a methodology to account for it in lumped parameters thermal modelling.

## II. FORCED CONVECTION EMPIRICAL CORRELATIONS

According to the fluid flow, the forced convection is classified into two categories: external and internal forced convection [3],[4].

### A. External Forced Convection

In the external forced convection, the flow boundary layers develop without any physical limitation, e.g., the fluid flow over a flat plate [3], [4]. Our focus will be on this kind of forced convection as our interest is in the forced convection from the flat side of the stator coils. There are various empirical correlations for this problem as reported in [5].

In these correlations, the forced convection coefficient is calculated based on fluid dynamics dimensionless numbers such as Reynolds number (Re), Prandtl number (Pr) and Nusselt number (Nu). Furthermore, the fluid mode, which can be either laminar or turbulent, is determined by the Reynolds

---

This work was supported by the Estonian Research Council grant PUT (PUT1260).

number. The Prandtl and Reynolds Numbers are calculated respectively as:

$$\text{Pr} = c_p \cdot \mu / k, \quad (1)$$

$$\text{Re} = \rho \cdot v \cdot L / \mu, \quad (2)$$

where  $c_p$  is the fluid specific heat capacity [kJ/(kg °C)],  $\mu$  is the fluid dynamic viscosity [kg/(m s)],  $k$  is the fluid thermal conductivity [W/(m °C)],  $\rho$  is the fluid density [kg/m<sup>3</sup>],  $v$  is the fluid velocity [m/s] and  $L$  is the characteristic length of the cooling surface [m] [6].

According to the heat transfer textbooks, e.g. [4], the Nusselt number for an isothermal flat plate in the laminar mode is calculated as:

$$\text{Nu} = 0.664 \cdot \text{Re}^{0.5} \cdot \text{Pr}^{1/3}, \quad (3)$$

and in the turbulent mode it is defined as:

$$\text{Nu} = (0.037 \cdot \text{Re}^{0.8} - A) \cdot \text{Pr}^{1/3}, \quad (4)$$

where  $A$  is the constant determined by the critical Reynolds number ( $\text{Re}_{xc}$ ) [4].

$$A = 0.037 \cdot \text{Re}_{xc}^{0.8} - 0.664 \cdot \text{Re}_{xc}^{0.5}, \quad (5)$$

In cases where the length ( $X_c$ ) over which the transition from laminar to turbulent flow occurs is smaller than the characteristic length ( $X_c/L > 0.95$ ), the Nusselt number is calculated as:

$$\text{Nu} = 0.037 \cdot \text{Re}^{0.8} \cdot \text{Pr}^{1/3}. \quad (6)$$

Finally, the forced convection coefficient ( $h$ ) is calculated as:

$$h = \text{Nu} \cdot k / L. \quad (7)$$

So far we have considered situations where the entire plate is heated over the whole length. In many situations, the flat plates involve an unheated part  $0 < x < \xi$ , as shown in Fig 1. This part consists of insulated materials and there is no heat generation beneath it. In such case, the velocity boundary layer starts to develop from  $x=0$  but the thermal boundary layer starts to develop from  $x=\xi$  [3], [7].

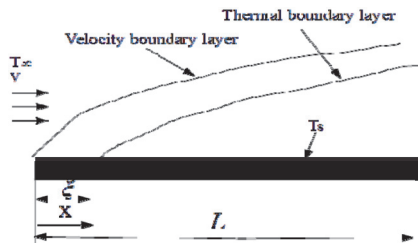


Fig. 1. Illustration of the coolant flow over a flat plate with an unheated part.

The local Nusselt number for this situation under laminar mode is calculated based on the following correlation [7]:

$$\text{Nu}_x = \frac{0.332 \cdot \text{Re}_x^{0.5} \cdot \text{Pr}^{1/3}}{\left[1 - \left(\frac{\xi}{x}\right)^{3/4}\right]^{1/3}}, \quad (8)$$

and for the turbulent mode it is calculated as [7]:

$$\text{Nu}_x = \frac{0.0296 \cdot \text{Re}_x^{0.8} \cdot \text{Pr}^{1/3}}{\left[1 - \left(\frac{\xi}{x}\right)^{9/10}\right]^{1/9}}, \quad (9)$$

This results in an average forced convection coefficient over the flat plate with an unheated part, which is calculated in the laminar mode as:

$$h = 2 \cdot \frac{1 - \left(\frac{\xi}{L}\right)^{3/4}}{1 - \left(\frac{\xi}{L}\right)} \cdot h_{x=L}, \quad (10)$$

and for the turbulent mode as:

$$h = 1.25 \cdot \frac{1 - \left(\frac{\xi}{L}\right)^{9/10}}{1 - \left(\frac{\xi}{L}\right)} \cdot h_{x=L}. \quad (11)$$

### B. Internal Forced Convection

In the internal forced convection, the fluid flows inside a confined space, e.g., a cylinder, tube or duct. In this case the coolant fluid is completely bounded by the inner surface and the boundary layer cannot expand freely [3], [4]. In this situation, the Reynolds number is defined as:

$$\text{Re} = v \cdot D / \vartheta, \quad (12)$$

where  $D$  is the hydraulic diameter of the internal flow [m] and  $\vartheta$  is the kinematic viscosity of the fluid [m<sup>2</sup>/s] [3].

In the internal forced convection, the laminar and turbulent modes of flow are determined by the Reynolds number too. For  $\text{Re} < 2300$ , the fluid flow is laminar, for  $2300 \leq \text{Re} \leq 10^4$ , the fluid is in a transient mode, and for  $10^4 < \text{Re}$ , the fluid flow is turbulent [3],[4].

### III. EXPERIMENTAL SETUP

The objective of the experimental work is to assess the effects of air fluid flow speed over the flat side of the stator coil on the estimation of the convection coefficient. As Fig. 2a shows the stator coil consists of six different faces. To consider the forced convection from the flat side, the heat flux flow should be confined only to the flat side. To achieve this, we created an insulation box according to the dimensions of the coil by means of foam insulation boards. Fig. 2b shows the coil box and the flat side of the coil. In this case, since the foam insulation board materials have low thermal conductivity ( $k = 0.3 \text{ W/(m °C)}$ ), the thermal flux outflow cannot transfer from the other sides. Therefore, the box is operating as a closed



calorimeter. Another important point about the box is the temperature operation point as the foam insulation board can handle temperatures up to 90 °C, during the experiment, the coil temperature should not exceed that temperature.

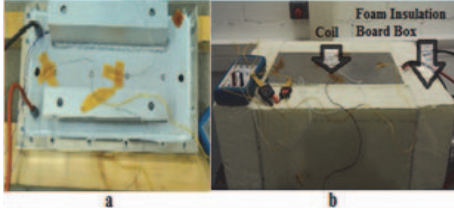


Fig. 2. a) shows the stator coil b) shows the stator coil inside coil box.

According to Fig.3, the test bench for considering the forced convection over flat side of the stator coil is constructed from different sections such as a wind tunnel and an induction motor actuated fan. The induction motor is controlled with a frequency converter to regulate the coolant flow. Further, the coil insulation box is used as a calorimeter and a DC power-source is used to heat up the coil, which temperature is measured by thermocouples and controlled via a temperature controller.

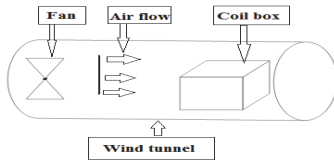


Fig. 3. Schematic diagram of the main part of the experimental setup.

#### A. Wind Tunnel

The experiment was performed inside a wind tunnel made of a cylindrical steel duct at the length of which is 300 cm and the diameter is 80 cm.

#### B. Fan Section

A four pole 7.5 kW squirrel cage induction motor is connected to the fan blades as the fan section. It is placed in front of the wind tunnel to blow the air through the tunnel and provide airflow at different speed ranges.

#### C. DC Test Setup

The DC test is a common experimental method for determining the convection coefficient heat transfer. In this test the loss of the stator coil is confined to joule loss of the coil winding and the amount of power can be easily measured. In the calculations, we accounted for the variations in the winding electrical resistance, as the winding resistivity is temperature dependent. Accordingly, the convection coefficient is determined when the coil reaches its final temperature and the steady state situation is achieved. The total heat extraction coefficient ( $h_e$ ) is calculated as:

$$h_e = \frac{P}{(T_s - T_a) \cdot S}, \quad (13)$$

where  $P$  is the coil winding Joule loss [W],  $S$  is the total exterior surface of the coil flat plate [m<sup>2</sup>],  $T_s$  is the surface temperature [K] and  $T_a$  is the ambient temperature [K] [8].

The total heat extraction coefficient is defined as the sum of the convection coefficient ( $h_e$ ) and the radiation coefficient ( $h_r$ ) [9], which leads to the forced convection coefficient as:

$$h_c = h_e + h_r, \quad (14)$$

The radiation coefficient is calculated analytically by the following correlation:

$$h_r = \varepsilon \sigma_c (T_s + T_a)(T_s^2 + T_a^2), \quad (15)$$

where  $\varepsilon$  is the emissivity coefficient and  $\sigma_c$  is the Stefan-Boltzmann constant  $\sigma_c = 5.67 \times 10^{-8}$  [W/(m<sup>2</sup> K<sup>4</sup>)] [8].

#### D. Thermocouples and Thermal controller

As Fig. 4 shows, to measure the surface temperature of the coil flat side, 5 K-Type thermocouples (chromel–alumel) were mounted on different locations of the coil flat side surface.

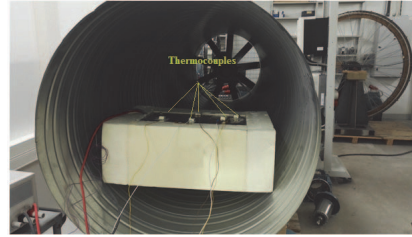


Fig. 4. Coil box inside the wind tunnel and location of the thermocouples.

## IV. RESULTS AND DISCUSSION

The investigations were carried out analytically and experimentally to determine the forced convection coefficient over the flat side of coil, which is located inside the wind tunnel.

Table I shows experimental data for the case study under fixed current equal to 28 amps with different wind speeds. During the test, the wind speed was measured by means of hot wire anemometer, which was fixed in the middle of the coil box's framework. The total heat extraction coefficients were calculated by using (13). Also the radiation coefficients were calculated analytically by using (15), finally the forced convection coefficients were calculated based on (14).

TABLE I. EXPERIMENTAL RESULTS

$V$ (m/s)	$T_s$ (°C)	$T_a$ (°C)	$P_{loss}$ (W)	$h_e$ W/(m <sup>2</sup> C)	$h_r$ W/(m <sup>2</sup> C)	$h_c$ W/(m <sup>2</sup> C)
4.1	62.7	18.6	137.4	33.70	4.22	29.48
6.1	52.4	18.5	133.0	42.36	4.01	38.36
7.1	50.5	18.7	131.7	44.80	3.97	40.83
8.2	47.2	18.3	130.2	48.96	3.90	45.05
10.5	43.5	18.3	128.4	55.09	3.83	51.26

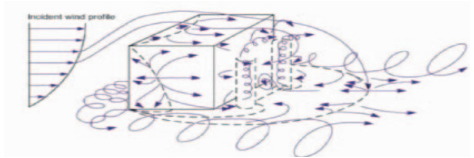


Fig. 5. Three dimensional wind flow around the rectangular box [10].

In the analytical calculation, as the coil box is located inside the wind tunnel, its boundary layer cannot develop such as the free stream mode. In this situation the characteristic of the wind tunnel directly affect to fluid flow mode over the plate. As Fig. 4 shows, the coil box was located in the outlet of wind tunnel. According to [11], the turbulent and transition mode occur away from the entrance of the tunnel. Furthermore, as Fig. 5 illustrates, the coil box itself accelerates the wind speed and increase the turbulent situation. Accordingly, the critical Reynold number for our case study is defined based on the critical Reynolds number in the internal flow. As results, the fluid flow is in the turbulent mode.

TABLE II. ANALYTICAL RESULTS

$V$ (m/s)	$T_s$ (°C)	$T_a$ (°C)	$h_{cL}$ W/(m <sup>2</sup> C)	$h_{cT}$ W/(m <sup>2</sup> C)
4.1	63	18.0	13.94	21.95
6.1	52	18.0	17.07	30.63
7.1	50	18.0	18.42	34.65
8.2	47	18.0	19.82	42.01
10.5	43	18.0	22.45	46.15

As Fig. 4 shows, the flat plat has been started by unheated part with the specification of  $\xi=0.1$  m and  $L=0.32$ m. Table II shows the analytical data for laminar ( $h_{cL}$ ) and turbulent ( $h_{cT}$ ) modes, which the analytical values are calculated by using (10), (11) in different wind speed ranges.

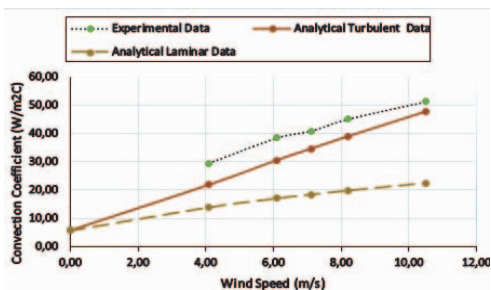


Fig. 6. Convection heat transfer coefficient according to wind speeds.

Fig. 6 shows the variations of the convection heat transfer with the wind speed based on experimental and analytical data. From the graph in Fig. 6, it is apparent that the convection coefficient heat transfer is proportional to wind speed and it will be increased by increasing the speed. Accordingly, the graph proves the importance of accurate comprehensive of fluid flow mode during forced convection heat transfer

calculation. As expected, the fluid flow was in the turbulent mode. One interesting finding base on analytical data is the linear correlation between convection coefficient and wind speed. Another important finding was the convection coefficient at zero speed is not zero, which can be attributed to the natural convection. Fig. 6 shows that by increasing the wind speed the experimental data converge toward turbulent analytical results. Thus, it can be expected the precision of analytical calculation is enhanced in high wind speed with high turbulent flow. However, in forced convection coefficient calculation, 15% difference between the analytical and experimental data is an acceptable error [4].

V. CONCLUSIONS

Focus in this paper is on the forced convection heat transfer over a flat plat with unheated part, especially for a flat part of a permanent magnet synchronous stator’s coil located inside a wind tunnel, analytically and experimentally.

As the experimental and analytical analysis have shown, the coil’s box is generally operated in the turbulent flow. According to the analytical results, forced convection has a linear relation with speed and it starts to increase by increasing the speed. However the analytical calculation shows a great precision at the high turbulent flow but the accuracy is decreased at low turbulences.

REFERENCES

- [1] M. Popescu, D. Staton, D. Dorrell, F. Marignetti, and D. Hawkins, “Study of the thermal aspects in brushless permanent magnet machines performance,” in 2013 IEEE Workshop on Electrical Machines Design, Control and Diagnosis (WEMDCD), 2013, pp. 60–69.
- [2] P. S. Ghahfarokhi, A. Kallaste, A. Belahcen, T. Vaimann, and A. Rassolkin, “Review of thermal analysis of permanent magnet assisted synchronous reluctance machines,” in 2016 Electric Power Quality and Supply Reliability (PQ), 2016, pp. 219–224.
- [3] Y. A. Cengel, Heat Transfer: A Practical Approach. New York : McGraw-Hill, 2004.
- [4] F. P. Incropera, D. P. DeWitt, T. L. Bergman, and A. S. Lavine, Fundamentals of Heat and Mass Transfer. 2007.
- [5] E. Sartori, “Convection coefficient equations for forced air flow over flat surfaces,” Sol. Energy, vol. 80, no. 9, pp. 1063–1071, 2006.
- [6] D. A. Staton and A. Cavagnino, “Convection Heat Transfer and Flow Calculations Suitable for Electric Machines Thermal Models,” IEEE Trans. Ind. Electron., vol. 55, no. 10, pp. 3509–3516, Oct. 2008.
- [7] F. Kreith and D. Goswami, Eds., The CRC Handbook of Mechanical Engineering, Second Edition, vol. 20045273. CRC Press, 2004.
- [8] O. Meksi and A. O. Vargas, “Numerical and experimental determination of external heat transfer coefficient in small TENV electric machines,” in 2015 IEEE Energy Conversion Congress and Exposition (ECCE), 2015, pp. 2742–2749.
- [9] P. shams Ghahfarokhi, A. Kallaste, and A. Belahcen, “Determination of Thermal Convection Coefficient from Coil’s Flat Plate Side,” in 16th International Symposium Topical Problems in the Field of Electrical and Power Engineering and Doctoral School of Energy and Geotechnology III”, 2017, pp. 130–132.
- [10] G. C. Woo, J. A. Peterku, J. E. Germuk, and C. M. Space, “Wind-Tunnel Measurements N the Wakes of Structures Administration,” Fort Collins, CO, United States, 1977.
- [11] S. M. Ghiaasiaan, Convective heat and mass transfer. Cambridge University Press, 2011.

**Publication VII**

P. Shams Ghahfarokhi, A. Kallaste, A. Belahcen, and T. Vaimann, "Steady state and transient thermal analysis of the stator coil of a permanent magnet generator," in 2017 18th International Scientific Conference on Electric Power Engineering (EPE), 2017, pp. 1–5.



# Steady State and Transient Thermal Analysis of the Stator Coil of a Permanent Magnet Generator

Payam Shams Ghahfarokhi, Ants Kallaste

Dept. Electrical Power Engineering and Mechatronics  
Tallinn University of Technology  
Tallinn, Estonia  
payam.shams@ttu.ee

Anouar Belahcen, Toomas Vaimann

Dept. Electrical Power Engineering and Mechatronics  
Tallinn University of Technology  
Tallinn, Estonia  
Dept. of Electrical Engineering and Automation  
Aalto University  
Finland

**Abstract**—this paper presents the analytical thermal analysis of a permanent magnet generator stator coil. The analytical analysis consists of a lump parameter thermal network (LPTN) to predict the steady state and transient temperature of the coil module. In the steady state part the average temperature of different parts of the network are estimated by using the matrix inversion and an iterative loop. In the transient state, the temperature behavior of each node is calculated by the Runge-Kutta 4<sup>th</sup> order iteration method. In the final part, the experimental and analytical results are compared to each other.

**Keywords**—Lump parameter thermal network, iterative method, temperature, stator coil.

## I. INTRODUCTION

Permanent magnet machines are gaining more popularity in different part of industry such as aerospace, automotive, wind turbines etc. This has led to higher customer demands on this type of machines, i.e. the machines require higher torque/power density, higher efficiency and lower price. From the thermal point of view, increasing the machine torque density will result in higher thermal stress in the machine. Furthermore, the remanence of permanent magnet materials is inversely proportional to the temperature and their performance is reduced by the temperature rise. Therefore, the accurate thermal analysis in parallel with the electromagnetic design is necessary especially for that type of machines.

In the electrical machine design, two types of methods are used for thermal calculations: analytical lump parameter thermal network (LPTN) and numerical methods, mainly finite elements [1]. The analytical method is a fast calculation method with acceptable accuracy; this is a common method in the thermal analysis of electrical machines [1]. One of the most accurate LPTNs for electrical machines was developed by Mellor in 1991. This thermal network accounted for the heat transfer in both radial and axial directions [2]. In 2003, Boglietti suggested using a simplified assumption by neglecting the heat transfer in the axial part of the electrical machine. The accuracy of this model depends on the accuracy of the calculation of the heat resistance from the machine surface to the ambient [3].

A serious challenge in the thermal calculation is to find or calculate the heat extraction coefficients related to the convection and radiation. This becomes more significant under forced convection since most of the heat is extracted from the machine to the ambient through the convection phenomenon [4]. However, in the natural convection, the heat extracted by radiation is also quite large and cannot be neglected in the calculation [5].

The heat extraction coefficients can be determined by experimental tests. One of the simplest methods is the long time DC test [6]. This test has the advantage of limiting the losses in the machine to the copper DC losses, which can be easily measured. The drawback for this test is that it will give both convection and radiation coefficients together and it is not easy to separate them. However other tests are available to determine only the radiation coefficient, but they require particular facilities such as a vacuum chamber, which is not easy to acquire [7].

The aim is to study, the steady state and transient thermal analysis for the machine stator coil of a permanent magnet generator. The LPTN of the coil module is built and an analytical calculation is carried out to analyze its behavior. The coil module is also built and tested with a long time DC test and the thermal coefficients are extracted from the measurement data. Finally, the analytical calculation and experimental results are compared.

## II. THERMAL MODEL

In this paper a coil module is investigated, which is meant for the stator of a surface mounted permanent magnet synchronous generator with slotless configuration. The machine stator design consists of a number of separate coils. For the thermal calculation, the LPTN was developed for one coil module. The model can be later extended for the full machine stator. Figure. 1 shows the coil module design, which consists of the coil itself, the resin, the back iron, the frame, the cooling fins, and the cover of the coil.

### A. Lump Parameter Thermal Network

Building the LPTN model of the coil module is based on the Boglietti's simplified model[3]. The LPTN model is similar to an electrical circuit where the temperature of each node

---

This work was supported by the Estonian Research Council grant PUT (PUT1260).

corresponds to the voltage in the electrical circuit, the power loss source is represented by a current source, thermal resistances and thermal capacitances are similar to the electrical resistances and capacitances.

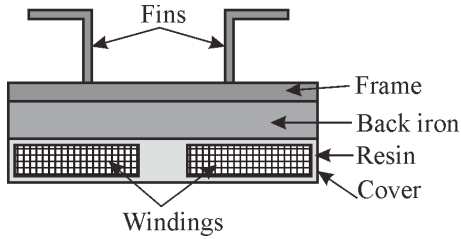


Fig 1. Stator coil module construction.

For calculating the equivalent circuit parameters, the thermal conduction resistance for all materials can be calculated as:

$$R = \frac{l}{kA}, \quad (1)$$

where  $l$  is the length (m) of a given part,  $k$  the thermal conductivity ( $W/(m \cdot K)$ ) of the material of that part and  $A$  is its cross section area ( $m^2$ ).

The thermal convection and radiation resistances, which are for the thermal flux extraction from the stator coil module to the ambient is calculated as:

$$R = \frac{1}{hS}, \quad (2)$$

where  $h$  is the convection or radiation coefficient ( $W/(m^2 \cdot K)$ ) and  $S$  is surface area ( $m^2$ ) in contact with the ambient air.

With the above given resistances, it is possible to build the LPTN for solving the steady state situation. To find the transient behavior of the temperature additionally the thermal capacitances has to be added into the model. The thermal capacitances are calculated as follow [8]:

$$C = c_p \rho V, \quad (3)$$

where  $C$  is the thermal capacitance (J/K),  $c_p$  is the specific heat capacity ( $J/(kg \cdot K)$ ),  $\rho$  is the mass density ( $kg/m^3$ ) and  $V$  is volume ( $m^3$ ).

According to the Fig. 1. and the symmetric situation; the LPTN is developed for the quarter part of coil module. The LPTN was developed where the quarter part of coil module was divided into 6 nodes as it can be seen from Fig. 2. 1 represents the frame upper part, 2 represents the back iron, 3 represents the top resin and the top half part of the coil, 4 represents the active part of the coil to long side, 5 represented the end winding part of the coil module and 6 represents the bottom resin and the steel cover. The thermal model consists of 11 thermal resistances where R1, R8, R10 and R11 represent convection and radiation resistances from the coil module surface and the others represent the conduction of the materials.  $P_j$  represents the joule loss ( $P_j=108.8$  W).

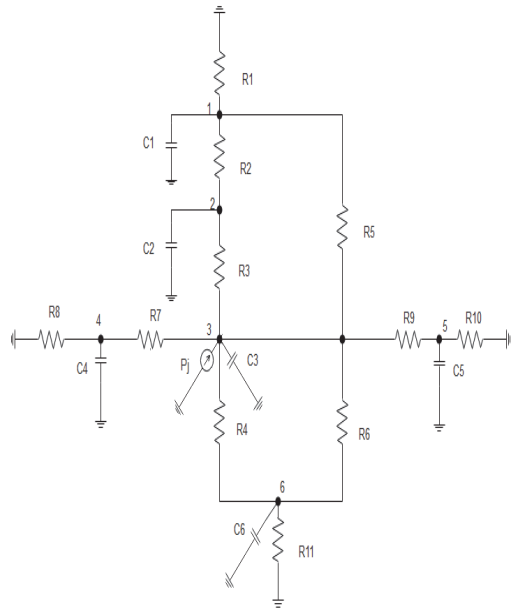


Fig 2. LPTN of a stator coil module.

TABLE I. THERMAL CAPACITANCES AND THERMAL RESISTANCES VALUES

Thermal capacitances	Value (J/K)	Thermal resistances	Value (K/W)
C <sub>1</sub>	1614	R <sub>1</sub>	3.5283
C <sub>2</sub>	214	R <sub>2</sub>	0.0589
C <sub>3</sub>	214	R <sub>3</sub>	0.1821
C <sub>4</sub>	31	R <sub>4</sub>	0.1821
C <sub>5</sub>	562	R <sub>5</sub>	3.0687
C <sub>6</sub>	18	R <sub>6</sub>	0.1822
		R <sub>7</sub>	3.4718
		R <sub>8</sub>	7.8041
		R <sub>9</sub>	2.9131
		R <sub>10</sub>	14.1819
		R <sub>11</sub>	5.4179

### III. ANALYTICAL CALCULATION

One of the most useful simulation softwares for analytical thermal calculations of the steady state and transient is MATLAB [9]. In the steady state analysis, the final nodal temperatures are calculated by the Gauss-Siedel iterative methods and the matrix inversion theory. For the transient

analysis the temperature raise of each node during time is describe by a first order differential equation, which can be solved by different iterative mathematical methods such as the implicit Adams-Moulton method of 2nd order (trapezoid rule) or the Runge-Kutta 4th order method [10], [11]. As the Runge-Kutta 4th order method has the highest accuracy compared with other iterative methods, it is the preferred methods for solving the transient differential equations [12], [13]. In this paper, for the analytical calculation, the MATLAB software is used and the equations are solved by the Runge-Kutta 4th order method.

For calculating the nodal temperature, the differential equation related to each node is developed. As it was described in the previous section the LPTN consist of 6 nodes therefore in transient state, the model consists of 6 first order differential equations and each differential equation will be the model for the thermal transient behavior of the corresponding node. According to these note, the differential equations for the transient analysis of all the nodes are as follow:

$$P_1 = C_1 \frac{dT_1}{dt} + \frac{1}{R_1}(T_1 - T_0) + \frac{1}{R_2}(T_1 - T_2) + \frac{1}{R_5}(T_1 - T_5), \quad (4a)$$

$$P_2 = C_2 \frac{dT_2}{dt} + \frac{1}{R_2}(T_2 - T_1) + \frac{1}{R_3}(T_2 - T_3), \quad (4b)$$

$$P_3 = C_3 \frac{dT_3}{dt} + \frac{1}{R_3}(T_3 - T_2) + \frac{1}{R_4}(T_3 - T_6) + \frac{1}{R_5}(T_3 - T_6) + \frac{1}{R_6}(T_3 - T_6) + \frac{1}{R_7}(T_3 - T_4) + \frac{1}{R_9}(T_3 - T_7), \quad (4c)$$

$$P_4 = C_4 \frac{dT_4}{dt} + \frac{1}{R_7}(T_4 - T_3) + \frac{1}{R_8}(T_4 - T_0), \quad (4d)$$

$$P_5 = C_5 \frac{dT_5}{dt} + \frac{1}{R_9}(T_5 - T_3) + \frac{1}{R_{10}}(T_5 - T_0), \quad (4e)$$

$$P_6 = C_6 \frac{dT_6}{dt} + \frac{1}{R_4}(T_6 - T_3) + \frac{1}{R_6}(T_6 - T_3) + \frac{1}{R_{11}}(T_6 - T_0), \quad (4f)$$

where  $P_i$  is the power loss in node  $i$ ,  $T_i$  is the temperature in node  $i$ ,  $C_i$  is the thermal capacitance in node  $i$  and  $R_i$  is the thermal resistance.

The above differential equations are converted to the matrix format for transient thermal model as follow[14]:

$$\frac{d}{dt}[\mathbf{T}] = [\mathbf{C}]^{-1}[\mathbf{P}] - [\mathbf{C}]^{-1}[\mathbf{G}][\mathbf{T}], \quad (5)$$

where  $[\mathbf{T}]$  is the temperature column vector,  $[\mathbf{C}]$  is the thermal capacitance diagonal matrix and  $[\mathbf{G}]$  is the thermal conductance square matrix.

The thermal conductance for each node are defined as:

$$G_{1-1} = G_1 + G_2 + G_5, \quad (6a)$$

$$G_{2-2} = G_2 + G_3, \quad (6b)$$

$$G_{3-3} = G_3 + G_4 + G_5 + G_6 + G_7 + G_9, \quad (6c)$$

$$G_{4-4} = G_7 + G_8, \quad (6d)$$

$$G_{5-5} = G_9 + G_{10}, \quad (6e)$$

$$G_{6-6} = G_4 + G_6 + G_{11}, \quad (6f)$$

where  $G_i$  for instance is the inverse of  $R_i$  and  $G_{i-j}$  for instance is the sum of the conductance connected to the node  $i$ .

For the steady state analysis, the temperature variation with time can be neglected and the system will be in a steady state. In this manner, the steady state matrix format is defined as [1]:

$$[\mathbf{T}] = [\mathbf{G}]^{-1}[\mathbf{P}] \quad (7)$$

#### IV. EXPERIMENTAL SETUP

To verify the calculation results, experimental tests were carried out. For this, an experimental setup was built as shown in Fig. 3. In this test the coil module surface temperature was measured at 5 different points and also the coil inner temperature and ambient temperature were measured. The temperature in the coil was produced by loading the winding with a DC current, which was measured together with the supply voltage. Several tests were carried out with different constant DC currents. All the tests started at the point where the coil temperature was at ambient temperature and lasted until the coil reached to the steady state temperature.

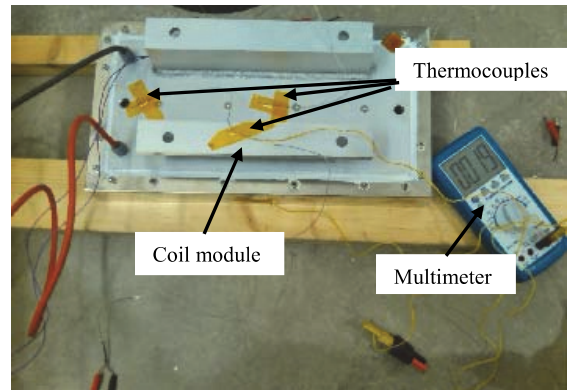


Fig 3. DC test setup for the coil module.

The DC load was used because in this manner the only source of temperature will be the coil winding Joule losses and the amount of power can be easily calculated. In these calculations, we accounted for the winding electrical resistance variation as the winding resistivity is temperature dependent. This aspect is important in the transient temperature test and the related calculation as when loading the winding with DC current the power supplied to the coil is increasing with the temperature.

### V. ANALYTICAL AND EXPERIMENTAL RESULTS

As it was presented in the analytical calculation part, the solutions of the LPTN leads to algebraic and differential equations that describe the temperature behavior of each node in the steady state and transient analysis and finally all these equations were written in a matrix format.

The analytically computed and experimental temperature of the each node at the steady state are presented in Table II.

TABLE II. STEADY STATE RESULTS

Node	Analytical temperature (°C)	Experimental temperature (°C)
Node 1	62.97	57
Node 2	63.64	—
Node 3	65.70	69.24
Node 4	51.62	—
Node 5	57.91	58
Node6	64.94	58

The analytical and experimental transient temperature within the coil module and on the coil module’s frame are shown respectively in figure 4 and figure 5.

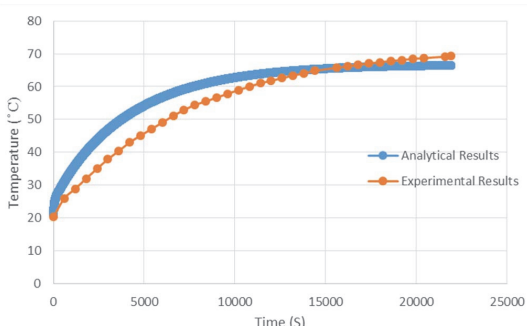


Fig 4. Transient temperature within the coil module.

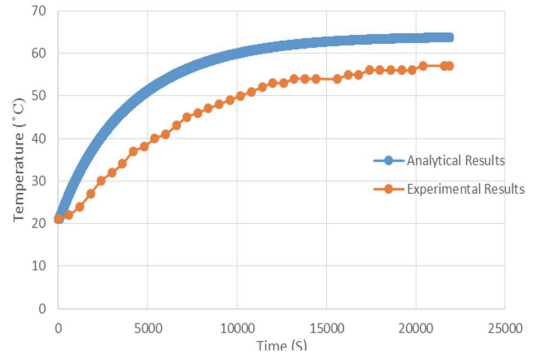


Fig 5. Transient temperature of surface.

AS can be seen from Fig. 4 and 5 there are some difference between the measured and calculated values. The analytical calculation method predicts the average temperature of the nodes while in the reality the sensors measure the nodal temperature. Furthermore, in the analytical method, the power loss is assumed to be distributed uniformly in the system while in the reality the power loss is not distributed uniformly. Another important point is about measuring the inside coil module’s temperature. For measuring purposes, the thermocouple is connected to the end winding part, which is the hottest part of the coil. So the measured and predicted temperatures have some differences. Further, some simplifications were used in the developing LPTN such as neglecting the middle section of winding and the thin layer of resin between the aluminum bars of the windings. The effect of these simplifications partly leads to the temperature differences observed between the analytical calculation and the experimental results of the nodes 1, 3 and 6.

### VI. CONCLUSION

In this paper, simplified lumped parameter thermal networks for predicting the steady state and transient temperatures of the stator coil module of a slotless permanent magnet generator were developed. All the equations related to steady state and transient LPTN were expanded and solved through accurate iteration methods. The comparison between the analytical and experimental results shows that that the model can predict the nodal temperature with an acceptable accuracy. The important point about this work is the ability to define the transient temperature behavior of the coil base on Runge- Kutta 4<sup>th</sup> order iteration method and MATLAB software. There is still some work to be done to improve the LPTN by adding some thermal resistances and capacitances of some parts and finding the exact characteristics of the materials used in the construction of the coil module.



## REFERENCES

- [1] P. S. Ghahfarokhi, A. Kallaste, A. Belahcen, T. Vaimann, and A. Rassolkin, "Review of thermal analysis of permanent magnet assisted synchronous reluctance machines," in 2016 Electric Power Quality and Supply Reliability (PQ), 2016, pp. 219–224.
- [2] P. H. Mellor, D. Roberts, and D. R. Turner, "Lumped parameter thermal model for electrical machines of TEFC design," IEE Proc. B Electr. Power Appl., vol. 138, no. 5, p. 205, 1991.
- [3] A. Boglietti, A. Cavagnino, M. Lazzari, and M. Pastorelli, "A simplified thermal model for variable-speed self-cooled industrial induction motor," IEEE Trans. Ind. Appl., vol. 39, no. 4, pp. 945–952, Jul. 2003.
- [4] P. S. Ghahfarokhi, A. Kallaste, A. Belahcen, and T. Vaimann, "Thermal analysis of electromagnetic levitation coil," in 2016 17th International Scientific Conference on Electric Power Engineering (EPE), 2016, pp. 1–5.
- [5] A. Boglietti, A. Cavagnino, M. Parvis, and A. Vallan, "Evaluation of radiation thermal resistances in industrial motors," IEEE Trans. Ind. Appl., vol. 42, no. 3, pp. 688–693, May 2006.
- [6] A. Boglietti, A. Cavagnino, and D. A. Staton, "Thermal analysis of TEFC induction motors," in 38th IAS Annual Meeting on Conference Record of the Industry Applications Conference, 2003., vol. 2, pp. 849–856.
- [7] A. Boglietti, E. Carpaneto, M. Cossale, and S. Vaschetto, "Stator-Winding Thermal Models for Short-Time Thermal Transients: Definition and Validation," IEEE Trans. Ind. Electron., vol. 63, no. 5, pp. 2713–2721, May 2016.
- [8] R. Wrobel, N. McNeill, and P. H. Mellor, "Performance Analysis and Thermal Modeling of a High-Energy-Density Prebiased Inductor," IEEE Trans. Ind. Electron., vol. 57, no. 1, pp. 201–208, Jan. 2010.
- [9] "MATLAB - MathWorks - MATLAB & Simulink." [Online]. Available: <https://se.mathworks.com/products/matlab.html>.
- [10] G. Kylander, "Thermal modelling of small cage induction motors," Ph.D.thesis, Chalmers University of Technology, Goteborg, Sweden, 1995.
- [11] O. Okoro, "Dynamic and thermal modelling of induction machine with non-linear effects," Ph.D. thesis, Kassel University, Kassel, Germany, 2002.
- [12] O. I. Okoro, "Steady and Transient States Thermal Analysis of a 7.5-kW Squirrel-Cage Induction Machine at Rated-Load Operation," IEEE Trans. Energy Convers., vol. 20, no. 4, pp. 730–736, Dec. 2005.
- [13] O. T. Ogunsola and L. Song, "Review And Evaluation of Using R-C Thermal Modeling of Cooling Load Prediction For HVAC System Control Purpose," 2012, pp. 1–9.
- [14] S. T. Lee, H. J. Kim, J. hee Cho, D. Joo, and D. kyong Kim, "Thermal analysis of interior permanent-magnet synchronous motor by electromagnetic field-thermal linked analysis," J. Electr. Eng. Technol., vol. 7, no. 6, pp. 905–910, 2012.



**Publication VIII**

P. Shams Ghahfarokhi, A. Kallaste, A. Belahcen, T. Vaimann, and A. Rassolkin, "Review of thermal analysis of permanent magnet assisted synchronous reluctance machines," in 2016 Electric Power Quality and Supply Reliability (PQ), 2016, pp. 219–224.



# Review of Thermal Analysis of Permanent Magnet Assisted Synchronous Reluctance Machines

Payam Shams Ghahfarokhi, Ants Kallaste, *Member, IEEE*, Anouar Belahcen, *Senior Member, IEEE*,  
Toomas Vaimann, *Member, IEEE*, and Anton Rassõlkin, *Member, IEEE*

**Abstract**—This paper presents a review of the losses and thermal analysis of permanent magnet assisted synchronous reluctance motors. Various types of solutions for critical parts of heat extractions and different empirical correlation for determination of each part are presented in details. Finally the experimental methods for determination of the critical parameters are presented. In this paper has tried to give advices how to calculate the critical parameter for constructing more accurate lumped parameter thermal network.

**Index Terms**—convection, radiation, conduction, core losses, magnet losses, computational fluid dynamic, finite-element analysis, lumped-parameter thermal network, Permanent Magnet Assisted Synchronous Reluctance Machines.

## I. INTRODUCTION

The permanent magnet synchronous machines (PMSM) with new types of permanent magnet material that consist of rare earth material like Neodymium Iron Boron (NdFeB) and Samarium Cobalt (SmCo) have many advantages for instance high efficiencies, high power factor and high power densities. However, due to the price increase of rare earth materials and the fact that 80% of the rare earth materials are located in China, the designers have started to find new topologies to reduce the usage and the amount of rare earth permanent magnet materials in their designs. They started by developing the synchronous reluctance motor (SynRM); in this topology there is no permanent magnet in the rotor configuration therefore the positive point about this topology is the low cost. On the other hand the power density, efficiency and power factor are very low in comparison with PMSMs. The designers have noticed that if they add some permanent magnet inside the rotor configuration of SynRM it will have a huge effect on the efficiency, saliency ratio and power factor of the motor. This new topology was called Permanent Magnet Assisted Synchronous Reluctance Machines (PMA SynRM). This topology has several advantages, for instance high saliency ratio, high power factor, high efficiency and possible exploitation of less expensive ferrites magnets. This topology forms a combination of the synchronous reluctance and interior PM machine topologies and is very popular in electric vehicle traction applications [1], [2].

The use of permanent magnet materials in this type of electrical machine and due to the possible irreversible demagnetization

of these types of material under thermal stress, it is very importance to investigate the thermal design of PMASynRM. The thermal stress is produced by the electrical machine losses, which appear in the form of heat energy and increasing temperature of the permanent magnet materials. For protecting the PMs from high temperature, two different ways exist. The first one is considering how to reduce the losses by optimized electromagnetic design of different parts of machine. The second one is about the thermal analysis of machine and the choice of appropriate cooling system for dissipating the losses from the electrical machine [3].

Nowadays due to the increasing demand of the customers for highly efficient, small size and compact electrical machine, the thermal design of electrical machine become more challenging for the designers. In the past the thermal design of electrical machine did not look very important and it was easy to realize. This is noticed by comparison of the number of papers published about the electromagnetic design and thermal design of electrical machine. The reason is clear; the electrical machine designers are the electrical engineering but the thermal design field is related to the mechanical engineering. The thermal analysis of electrical machine is also more complicated than the electromagnetic design. The thermal model of an electrical machine has direct correlation with the manufacturing process and in comparison with electromagnetic design the thermal analysis of electrical machine is always a 3-dimensional problem. In some thermal phenomena, the thermal behavior of an electrical machine cannot be described by pure mathematical correlations [3], [4].

The main objective of this paper is to introduce the losses in PMASynRM and the modern approaches for calculating and analyzing the critical part of the machine based on the analytical lumped parameter method and using the experience from other electrical machine thermal analysis.

## II. LOSSES

The main losses in PMASynRM are divided into three categories consisting of: Stator copper losses, Iron losses and Magnet losses [3].

### A. Copper Losses

The highest amount of losses in PMASynRM is generated by the stator copper losses. This type of losses consist of two segments, namely the AC segment and the DC segment. The DC segment includes the effect of the temperature on increasing the resistances of the winding. The AC part includes the skin and proximity effects. This part of losses become more significant in high-speed electrical machines and machines with form-windings supplied with a

---

This work was supported by the Estonian Research Council grant PUT (PUT1260).

P. Shams Ghahfarokhi, A. Kallaste, A. Belahcen, T. Vaimann, and A. Rassõlkin are with the Department of Electrical Engineering, Tallinn University of Technology, Ehitajate tee 5, 19086 Tallinn, Estonia (e-mail: Payam.Shams@tu.ee, Ants.Kallaste@tu.ee, Anouar.Belahcen@tu.ee, Toomas.Vaimann@tu.ee, Anton.Rassolkin@tu.ee).

frequency converters. There are different ways to reduce the amount of the AC copper losses like twisting the wire or dividing the conductors into sub conductors [3], [5], [6]. According to [6] the total amount of the copper losses in a winding of  $m$  phases is calculated as:

$$P_{cu} = ml^2 R, \quad (1)$$

where  $R$  is the resistance of the phase winding, which is calculated as:

$$R = K_R \frac{Nl_{av}}{\sigma S_c}, \quad (2)$$

where  $K_R$  is the skin effect factor,  $N$  is the number of turns,  $l_{av}$  is the average length of a turn,  $S_c$  is the cross section area of the copper wire and  $\sigma$  is the specific conductivity of the copper. It should be noted that (2) lumps the DC and AC losses together through the  $K_R$  factor and does not segregate between skin and proximity effects.

### B. Iron Loss

The iron loss problematic is much more complex and it's handling is a subject of many research till now. The most common methodologies are the 3 terms and the two terms approaches, which are both based on early work of Steinmetz [22] and Bertotti [23]. The two terms approach divide the iron losses into two categories; the hysteresis loss (static loss) and the eddy current loss (dynamic loss) [3], [6], and [24]. They are calculated as:

$$P_{Fe} = P_h + P_e = K_h B^n f + K_e B^2 f^2, \quad (3)$$

where  $K_h$  and  $K_e$  are the hysteresis and eddy current loss coefficients and  $B$  is the pick value of the flux density (Tesla), considered as sinusoidal in time.  $n$  varies between 1.5 and 2.5 depending on the material, and  $f$  is frequency (Hertz). In the Bertotti's approach,  $n$  is set to 1 and an additional term named excess losses is added to (3). This term is given as

$$K_{exc} B^{1.5} f^{1.5}. \quad (4)$$

### C. Magnet Loss

The magnet loss is produce by the eddy currents induced in the magnets due to the magnetic flux high harmonics produced by the slotting, the supply or other geometrical effects. It can be estimated as:

$$P_m \approx \frac{V_m b_m^2 B_m^2 f^2}{12 \rho_m}, \quad (5)$$

where  $f$  is frequency (Hertz),  $\rho_m$  is the magnet resistivity,  $V_m$  is total volume of magnets  $B_m$  is magnetic flux density in the air gap and  $b_m$  is the magnet width.

The magnet loss is negligible for the ferrite magnet material due to its high resistivity while it becomes significant in the high energy PMs like NdFeB and SmCo which have low resistivity [3], [7].

## III. THERMAL ANALYSIS METHODS

The thermal analysis of an electrical machine is divided into two main categories; analytical lump circuit methods and the numerical thermal analysis methods [4].

### A. Thermal Analysis Based on Lumped Parameter Network

Lumped parameter thermal network (LPTN) analysis method is used for calculating heat transfer and flow from different parts of the machine. The positive point about the analytical method is that it is a fast calculation method; therefore, it takes very short time to calculate the temperature of different parts of the thermal circuit. The accuracy in the determination of the heat transfer paths plays an important role. In heat transfer calculation, the components with nearly the same temperature are lumped and represented with one node. Main heat transfer ways are displayed by the thermal resistance among the nodes. For instance the heat is flowing through some conduction resistances from the coil to the teeth then to the core and the frame and finally transferred by means of convection and radiation resistances from the frame to the ambient After drawing all main heat transfer paths the model looks as a network of heat resistances and sources. The thermal equivalent circuit is similar to an electrical circuit, where the temperature operates like a voltage, the power losses display as current sources and the thermal resistances are analogue to electrical resistances [4]. The nodes temperatures are calculated by solving the network matrix and by using iterative methods whenever needed.

$$[T] = [G]^{-1} [P], \quad (6)$$

where  $[T]$  is the temperature matrix,  $[G]$  is the thermal conduction matrix, and  $[P]$  is the loss matrix.

One of the early papers about the implementation of the LPTN was written by Mellor in 1991 [8]. According to [8], this model was too complicated as it was applied to display the heat transfer in both axial and radial directions. Therefore, complicated mathematical correlations were applied for resolving the different thermal phenomena. Afterward, in 2003 Boglietti developed a simplified model by applying some simplifications and assumptions about the heat flux paths. For instance, the heat extracts only in radial direction and the power loss distribution is uniform in every component. A comparison of Boglietti's and Mellor's models showed that the results were very similar [9], which removed the need for most of the axial components of the network.

### B. Numerical Thermal Analysis

The numerical analysis is divided in to two types: the finite element analysis (FEA) and the computational fluid dynamics (CFD) [4], [10].

The FEA analysis is the usual method for calculating electromagnetic design in both 2-D and 3-D models. According to the importance of the thermal design therefore this part is added to the FEA software. It is a very accurate method for calculating the conduction inside the motor. However, for calculating the contact, convection, and radiation resistances, it needs the empirical correlations and calculations used in LPTNs too. Unlike LPTNs, in the FEA, the power loss distribution can be determined accurately and it is not uniformly distributed inside the machine. This is very time-consuming method, it takes a lot of time to construct the model therefore it is applied in a very complicated geometry that cannot be calculated by LPTNs [4].

The CFD method is a complex method. In addition to heat transfer calculation, it has the ability of fluid flow prediction. Therefore, the designer should have knowledge

about fluid flow and heat flow. From a practical point of view, this method is applied when empirical correlations and usual formula cannot be applied for predicting the heat transfer behavior, for instance in the end winding and end caps area. This method is also applied for calculating the convection heat transfer coefficients [11].

#### IV. HEAT EXTRACTION

The heat is extracted from electrical machines by three phenomena: conduction, convection and radiation [6].

##### A. Conduction

Two different mechanisms exist for the heat transfer through the conduction. The first one is defined by the molecule interaction and molecule vibration and the second one is defined according to the free electron in the materials [6].

The conduction resistance is calculated easily by the correlation:

$$R_{th} = \frac{l}{kA}, \quad (7)$$

where  $l$  is the path length (m),  $k$  is the thermal conductivity [W/(m °C)] and  $A$  is the heat transfer area (m<sup>2</sup>).

According to (7), the conduction resistance depends mainly on the material's thermal conductivity and the material's dimensions. The conduction resistance is reduced when the conducting material has high thermal conductivity or the ratio between the area and length is high [5].

Two regions are critical in the calculation of conduction resistance; the first one is related to the stator slot and the second one is related the interface between different materials, or contact resistance [3], [6], and [12].

In the slot area the copper conductor, the conductor insulation (conductor enamel), the slot insulation, and the impregnation materials all to gather have different thermal conductivity. Usually the electrical conductive materials also are good thermal conductors but the conductivity of the insulations and impregnation materials are lower. Therefore, these materials cannot transfer the heat energy to the teeth effectively. To overcome this modelling issue, the designers use the concept of equivalent thermal conductivity. For calculating the slot's equivalent thermal conductivity in the LPTN, different types of analytical solution exist, for instance cuboidal winding concept, layered winding model and equivalent insulation [13].

The equivalent thermal conductivity can be estimated by the Hashin and Shtrikman expression [14]. The Hashin and Shtrikman correlation can be applied for two materials while the slot consist of at least three components. To overcome this issue two different simplifying assumptions exist. The one that is applied in this paper assumes that the conductor insulation has the same thermal conductivity as the impregnation. In this case, the equivalent thermal conductivity is determined as:

$$K_e = K_2 \frac{(1 + f_1)K_1 + (1 - f_1)K_2}{(1 - f_1)K_1 + (1 + f_1)K_2}, \quad (8)$$

where  $K_1$  is the thermal conductivity of the conductor and  $K_2$  is the thermal conductivity of the slot impregnation,  $f_1$  is the volume ratio of the conductor in the slot and  $f_2$  is the volume ratio of the impregnation in slot so that  $f_1 + f_2 = 1$  [3], [14].

For the experimental determination and evaluation of the equivalent thermal conductivity of the stator winding, two different test methods exist: the thermal steady-state condition test and the short-time thermal transient test [9], [13]. These two experimental methods are appropriated for electrical machine with distributed windings [13].

In the steady-state test, the 3-phase distributed stator windings are connected in series or parallel to a DC power supply. In this situation, the PMASynRM loss is the stator copper loss. As the rotor speed is zero, for thermal safety reasons the DC current is limited to 50–70% of the rated current. It is a long time test as it takes several hours to reach the steady state thermal condition.

The short-time thermal transient test was introduced by Boglietti and the whole procedure is described in [15]. Unlike the steady state test, in a short-time thermal transient test, the 3-phase stator winding is connecting to a DC supply with current equal to rated current. In this method, the stator lamination is assumed to be in the isothermal state with constant temperature. The test is finished when the temperature of the stator lamination increase by 1 °C, which reduces the test period to few minutes.

The second critical issue in the determination of the conduction resistance refers to the contact or interface gap between two materials. Different types of contact resistance exist in thermal analysis of electrical machine for instance the frame to stator yoke, the slot liner to lamination and the permanent magnet to the rotor lamination. The interface gap occurs due to imperfections and irregularities in contact surfaces, surface softness and smoothness, and air pressure. The most important contact resistance is related to the interface gap between the frame and the stator lamination. Most of the heat lows through this area and thus accurate calculation of the contact resistance in this area leads to accurate temperature determination [10], [12]. The interface gap resistance is calculate by the formula

$$R_g = \frac{l_g}{2K_{air} \pi r_{oy} L_s}, \quad (9)$$

where  $l_g$  is the interface gap,  $K_{air}$  is air thermal conductivity,  $r_{oy}$  is the outer stator yoke radius and  $L_s$  is stator core length.

The important part of the correlation (9) is how to estimate the length of interface gap. Lindstrom in [16] introduced a table base on the material of the frame and the power rang of the motor. Boglietti in [10] tried to find an empirical correlation for determining the interface gap but finally he did not any correlation that can describe the behavior of the interface gap. He observed that the length of the interface gap for the same motors of same company is not uniform. Therefore, he end up to the conclusion that the interface gap not only depends on the frame material but it also depends on the manufacturing process and the surface condition. At the end, he suggested to use an average interface gap as a first estimation.

##### B. Convection

The convection is the most significant method of heat transfer. It happens due to the cooling fluid motion. Two different types of convection exist: the natural convection and the forced convection. The natural convection occurs when the object is placed in the fluid at a different temperature. Its physical definition is the buoyancy force. In the

forced convection, the fluid motion occurs due to external forces like fans, pumps or blowers [6], [17].

The convection heat resistance is calculate by the correlation:

$$R_{th} = \frac{1}{hA}, \quad (10)$$

where  $h$  is the convection heat transfer coefficient [W/(m<sup>2</sup>°C)], and  $A$  convection surface area (m<sup>2</sup>).

The most significant part of the convection resistance calculation is to define the convection heat transfer coefficient. Fortunately, due to the simple shapes of the different parts of electrical machines like flat plate, circle and cylinder, there are many empirical correlations for calculating this coefficient. For calculating both the natural and forced convection coefficient, the empirical correlation are defined by dimensionless numbers. The correlation for natural convection is such as:

$$Nu = a(GrPr)^b, \quad (11)$$

for forced convection the correlation is such as:

$$Nu = a(Re)^b(Pr)^c, \quad (12)$$

where  $Nu$  is Nusselt number,  $Gr$  is Grashof number,  $Pr$  is Prandtl number,  $Re$  is Reynolds number, and  $a$ ,  $b$ , and  $c$  are constants.

The  $Gr$ ,  $Pr$ , and  $Re$  are calculated as :

$$Gr = \frac{\beta g \Delta T \rho^2 L^3}{\mu^2}, \quad (13)$$

$$Pr = \frac{C_p \mu}{k}, \quad (14)$$

$$Re = \frac{\rho v L}{\mu}, \quad (15)$$

where  $\mu$  is the fluid viscosity [kg/(s.m)],  $\rho$  the fluid density (kg/m<sup>3</sup>),  $C_p$  the fluid specific heat capacity [kJ/(kg°C)],  $v$  the fluid velocity (m/s),  $\Delta T$  the temperature difference between the fluid and the cooling surface (°C),  $L$  the characteristic length of the surface (m),  $\beta$  the fluid coefficient of the cubical expansion (1/k), and  $g$  the gravitational acceleration (m/s<sup>2</sup>) [12], [17], [18].

The relation between the convection heat transfer coefficient and the Nusselt number is defined as [12], [17]

$$h = \frac{Nu k}{L}. \quad (16)$$

In the natural convection, the magnitude of  $Gr.Pr$  is used to determine if the flow is laminar or turbulent whereas in the forced convection the magnitude of  $Re$  is used for this purpose [17].

Three critical regions exist in the calculation of convection resistance. The first one is about the open fin in exterior surface of the machine. The next one is related to the end space of the machine and the last one is related to heat transfer through the air gap.

The calculation of the heat transfer coefficient for smooth surface is rather easy, but for the calculation of the heat transfer coefficient of surfaces with axial and radial fin, more complex correlations are needed. Therefore, the area

based composite correlations are used for calculation of complex fin shapes. In this method, each complex fin geometry is calculated based on the combination of horizontal and vertical flat plate, cylinder, and other geometries [12].

The end space is the most difficult part for determination of the convection coefficient. The end space contains the end winding, end cap and in some cases simple fan. Some authors for instance Mellor, pal, and Schubert did research on cooling of end winding. The most useful formula for calculation of heat convection coefficient in end space is:

$$h = k_1(1 + k_2 V^{k_3}), \quad (17)$$

where  $k_1$ ,  $k_2$ , and  $k_3$  are curve fitting coefficients and  $V$  is the velocity of local fluid (m/s). The first term of the above correlation represents the natural convection and the second term represent the forced convection [12].

The last critical part is related to the calculation of convection coefficient of the airgap. The first correlation was introduced by Taylor in 1935 and then it was expanded by Gazley in 1958. The correlation is such as

$$Ta = \frac{\rho^2 \Omega^2 r_m \delta^3}{\mu^2}, \quad (18)$$

where  $Ta$  is Taylor number,  $\Omega$  is rotor's angular velocity,  $r_m$  is average radius of rotor and the stator and  $\delta$  is the radial air-gap length [6], [12].

By using Becker and Kaya correlation, the Nusselt number for  $Ta < 1700$  is equal to 2 and for  $1700 < Ta < 10^4$  it is calculated by the correlation:

$$Nu = 0.128 Ta^{0.367}. \quad (19)$$

For  $10^7 > Ta > 10^4$  the Nusselt number is calculated as [6]:

$$Nu = 0.409 Ta^{0.241}. \quad (20)$$

### C. Radiation

Radiation is a thermal transfer phenomenon that does not need a medium for heat transferring. In this phenomenon, the heat is transferred by electromagnetic waves. The radiation resistance is determined as

$$R = \frac{1}{h_r A}, \quad (21)$$

where  $h_r$  is the radiation coefficient and  $A$  is the radiating surface area [4], [6].

The radiation depends directly on the emissivity and the view factor. Both factors are changed in the range of one to zero. The radiation coefficient is calculated as

$$h_r = \sigma \varepsilon F_{1-2} \frac{(T_1^4 - T_2^4)}{(T_1 - T_2)}, \quad (22)$$

where  $\sigma = 5.67 \cdot 10^{-8}$  [W/(m<sup>2</sup>.K<sup>4</sup>)],  $\varepsilon$  is the emissivity of the surface that for most of the electrical motor is equal to 0.85,  $F_{1-2}$  is the view factor for dissipating surface to the absorbing surface, and  $T_1$  and  $T_2$  are the temperatures of the surface 1 and surface 2 (K). The view factor can be calculated according to the surface shape. There are many text book that explain this calculation, for instance [19] and [20] are suitable ones.



The radiation occurs inside and outside of the electrical motor and the calculation of the view factor is a difficult problem. For instance, it is quite difficult to calculate view factor of the end winding and winding. Another problem about radiation is that it occurs in parallel with convection and it is so difficult to separate these two phenomena through measurements. Practically specific equipment is used to measure the radiation coefficient. This equipment is called vacuum chamber. This facility is not very common in laboratories. The radiation becomes more significant when it is parallel with the natural convection but the radiation can be neglected in the case of forced convection. In this case, the radiation resistance is much larger than the forced convection resistance [10], [21].

## V. CONCLUSION

This paper is a review of the thermal analysis of permanent magnet assisted synchronous reluctance motor. Therefore, the significant losses in the PMASynRM has been presented. The different types of thermal analysis methods including the analytical and numerical Analysis have been compared with each other. The advantages and disadvantages of each method has been considered. This paper deeply goes through the analytical Lump parameter thermal network method. It describes the empirical correlations for different heat transfer phenomena and reports on the critical thermal analysis parameters in electrical machine. For each critical parameter, different solutions and empirical correlation have been presented. Finally, the experimental method to obtain each critical parameter has been described.

## REFERENCES

- [1] M. Obata, S. Morimoto, M. Sanada, and Y. Inoue, "Performance of PMASynRM with ferrite magnets for EV/HEV applications considering productivity," *IEEE Trans. Ind. Appl.*, vol. 50, no. 4, pp. 2427–2435, Jul./Aug. 2014.
- [2] P. Lazari, J. Wang, and B. Sen, "3-D effects of rotor step-skews in permanent magnet assisted synchronous reluctance machines," *INTERMAG 2015*.
- [3] M. Popescu, D. Staton, D. Dorrell, F. Marignetti, and D. Hawkins, "Study of the thermal aspects in brushless permanent magnet machines performance," *IEEE-WEMDCD*, pp. 60–69, 11–12 Mar. 2013.
- [4] A. Boglietti, A. Cavagnino, D. Staton, M. Shanel, M. Mueller, and C. Mejuto, "Evolution and modern approaches for thermal analysis of electrical machines," *IEEE Trans. Ind. Appl.*, vol. 56, no. 3, pp. 871–881, Mar. 2009.
- [5] M. Popescu, D. Staton, A. Boglietti, A. Cavagnino, D. Hawkins, and J. Goss, "Modern heat extraction systems for electrical machines – A review," *IEEE-WEMDCD*, pp. 289–296, 26–27 Mar. 2015.
- [6] J. Pyrhönen, T. Jokinen, and V. Hrabovcova, *Design of Rotating Electrical Machines*. John Wiley & Sons, Ltd., 2008.
- [7] R. Deeb, "Calculation of eddy current losses in permanent magnets of servo motor," *Electroscope*, 2011.
- [8] P. Mellor, D. Roberts, and D. Turner, "Lumped parameter thermal model for electrical machines of TEFC design," *Proc. Inst. Elect. Eng.*, pt. B, vol. 138, no. 5, Sep. 1991.
- [9] A. Boglietti, A. Cavagnino, M. Lazzari, and M. Pastorelli, "A simplified thermal model for variable-speed self-cooled industrial induction motor," *IEEE Trans. Ind. Appl.*, vol. 39, no. 4, pp. 945–952, Jul./Aug. 2003.
- [10] A. Boglietti, A. Cavagnino, and D. Staton, "Determination of critical parameters in electrical machine thermal models," *IEEE Trans. Ind. Appl.*, vol. 44, no. 4, pp. 1150–1159, Jul./Aug. 2008.
- [11] D. Staton, S. J. Pickering, and D. Lampard, "Recent advancement in the thermal design of electric motors," in *Proc. SMMA—Fall Tech. Conf.*, Durham, NC, Oct. 3–5, 2001.
- [12] D. Staton, A. Boglietti, and A. Cavagnino, "Solving the more difficult aspects of electric motor thermal analysis, in small and medium size industrial induction motors," *IEEE Trans. Energy Convers.*, vol. 20, no. 3, pp. 620–628, Sep. 2005.
- [13] A. Boglietti, M. Cossale, E. Carpaneto, S. Vaschetto, M. Popescu, and D. Staton, "Stator winding thermal conductivity evaluation: an industrial production assessment," *IEEE-ECCE*, pp. 4865–4871, Sep. 2015.
- [14] N. Simpson, R. Wrobel, and P. H. Mellor, "Estimation of equivalent thermal parameters of impregnated electrical windings," *IEEE Trans. Ind. Appl.*, vol. 49, no. 6, pp. 2505–2515, Nov./Dec. 2013.
- [15] A. Boglietti, E. Carpaneto, M. Cossale, A. Lucco Borlera, D. Staton, and M. Popescu, "Electrical machine first order short-time thermal transient model: measurements and parameters evaluation," *IEEE-IECON*, pp. 555–561, 2014.
- [16] J. Lindström, *Thermal Model of a Permanent-Magnet Motor for a Hybrid Electric Vehicle*. Licentiate thesis, Chalmers University of Technology, Göteborg, Sweden, Apr. 1999.
- [17] A. Cavagnino and D. Staton, "Convection heat transfer and flow calculations suitable for analytical modelling of electric machines," in *Proc. IEEE IECON*, Paris, France, Nov. 2006, pp. 4841–4846.
- [18] J. P. Holman, *Heat Transfer*. New York: Mc Graw-Hill, 1997.
- [19] S. N. Rea and S. E. West, "Thermal radiation from finned heat sinks," *IEEE Trans. Parts, Hybrids, Packag.*, vol. PHP-12, no. 2, pp. 115–117, Jun. 1976.
- [20] M. F. Modest, *Radiative Heat Transfer*. New York: Academic, 2003.
- [21] A. Boglietti, A. Cavagnino, M. Parvis, and A. Vallan "Evaluation of radiation thermal resistances in industrial motor," *IEEE Trans. Ind. Appl.*, vol. 42, no.3, pp. 688–693, May/Jun. 2006.
- [22] C. Steinmetz, "On the law of hysteresis," *AIEE Transactions*, vol. 9, pp. 3–64, 1892.
- [23] G. Bertotti, "General properties of power losses in soft ferromagnetic materials," *IEEE Trans. Magn.*, vol. 24, no. 1, pp. 621–630, 1988.
- [24] D. Eggers, S. Steentjes, and K. Hameyer, "Advanced iron-loss estimation for nonlinear material behavior," *IEEE Trans. Magn.*, vol. 48, no. 11, pp. 3021–3024, Nov.2012.



**Payam Shams Ghahfarokhi** was born in Iran, in 1986. He received the B.Sc. degree in electrical power engineering from IAUN in 2010 and the M.Sc. degree in electrical power engineering from university of Newcastle upon Tyne in 2011.

He is currently a Ph.D. student at Tallinn University of Technology. His main field of interests is design of Permanent Magnet electrical machine and thermal design of electrical machine.



**Ants Kallaste** was born in Pärnu, Estonia in 1980 and received his B.Sc., M.Sc., and Ph.D. degrees in electrical engineering from Tallinn University of Technology, Estonia, in 2004, 2006, and 2013, respectively. He is currently a Senior Researcher in Tallinn University of Technology, Department of Electrical Engineering and carrying out postdoctoral research at the Department of Electrical Engineering and Automation, Aalto University, Espoo, Finland.

He has been working in several companies as an Electrical Engineer. Presently he is working at the Tallinn University of Technology, Department of Electrical Engineering holding the position of Head of Chair of Electrical Machines. He has been the IEEE member since 2013. His main research interests include permanent magnet machine design and wind turbines.



**Anouar Belahcen** (SM) was born in Morocco, in 1963. He received the B.Sc. degree in physics from the University Sidi Mohamed Ben Abdellah, Fes, Morocco, in 1988 and the M.Sc. (Tech.) and Doctor (Tech.) degrees from Helsinki University of Technology, Finland, in 1998 and 2004, respectively.

From 2008 to 2013, he has been working as Adjunct Professor in the field of coupled problems and material modelling at Aalto University, Finland. Since 2011 he is Professor of electrical machines at Tallinn University of Technology, Estonia and in 2013 he became Professor of Energy and Power at Aalto University. His research interest are numerical modelling of electrical machines, especially magnetic material modelling, coupled magnetic and mechanical problems, magnetic forces, and magnetostriction.



**Toomas Vaimann** was born in Pärnu, Estonia, in 1984 and received his B.Sc., M.Sc., and Ph.D. degrees in electrical engineering from Tallinn University of Technology, Estonia, in 2007, 2009, and 2014, respectively. He is currently a Senior Researcher in Tallinn University of Technology, Department of Electrical Engineering and carrying out postdoctoral research at the Department of Electrical Engineering and Automation, Aalto University, Espoo, Finland.

He has been working in several companies as an Electrical Engineer. He is the member of IEEE (S'11-M'14), Estonian Society of Moritz Hermann Jacobi and Estonian Society for Electrical Power Engineering. His main research interest is the diagnostics of electrical machines.



**Anton Rassõlkin** was born in Tallinn, Estonia, in 1985 and received the B.Sc., M.Sc., and Ph.D. degrees in electric drives and power electronics from Tallinn University of Technology, Tallinn, Estonia, in 2008, 2010, and 2014, respectively. In 2010 received Dipl.-Ing. (FH) degree in automatic from University of Applied Science Giessen-Friedberg, Giessen, Germany.

He has been working in several companies as an Electrical Engineer. Presently he is working at the Tallinn University of Technology, Department of Electrical Engineering as a Research Scientist.

He has been the IEEE student member since 2012 and IEEE member since 2016. The main research interests lay in the field of electric drives and its control systems as well as in the fields of electrical machines and electric transportation.

**Publication IX**

P. Shams Ghahfarokhi, A. Kallaste, A. Belahcen, and T. Vaimann, "Thermal analysis of electromagnetic levitation coil," in 2016 17th International Scientific Conference on Electric Power Engineering (EPE), 2016, pp. 1–5.



# Thermal Analysis of Electromagnetic Levitation Coil

Payam Shams Ghahfarokhi, Ants Kallaste  
Department of Electrical Engineering,  
Tallinn University of Technology,  
Tallinn, Estonia  
payam.shams@ttu.ee

Anouar Belahcen, Toomas Vaimann  
Department of Electrical Engineering and Automation,  
Aalto University,  
Espoo, Finland

**Abstract**—This paper presents analytical and numerical thermal analysis of three different toroidal coils levitated on an aluminum plate. The analytical method consists of a network of thermal resistances that make it possible to estimate the average temperature of the coils. In the numerical method, by using the FEM thermal and magnetic analysis, the average temperature of the coils and the amount of the in-rush levitation current are calculated. All the numerical and analytical results are compared with experimental results and they show very good agreement. The effects of optimization parameters on the levitation system are considered.

**Keywords**—coil; electromagnetics; levitation; optimization; thermal analysis.

## I. INTRODUCTION

The research institutes and the industries in industrial countries like Germany and Japan have a special look on the magnetic levitation theory. This theory has multiple applications from transportation and magnetic bearings of flywheel to levitation melting of conductive metals.

In the general view, the magnetic levitation can be divided into two main categories, attractive and repulsive. The simple example for attractive manner is a piece of steel attracted to a permanent magnet. In this category the levitation force is the result of the interaction between the DC magnetic field that is produced by a DC current or a permanent magnet and the magnetization field inside the ferromagnetic material [1], [2].

The repulsive manner or electromagnetic levitation (EML) theory was introduced for the first time by Muck in 1923 [3]. According to EML theory, an alternating magnetic field generates eddy current in the conductive body that is placed in the magnetic field. The levitation happens when the force due to the interaction of the current induced magnetic field and the eddy-current inducing magnetic field overcomes the gravity force of the levitated body. The toroidal coil that is carrying the alternating current and aluminum sheet is good example for EML [1], [2].

When the current flows inside the coils it produces resistive losses, the resistive losses appear in the form of heat energy inside the coils and increases the coil temperature. The coil is covered by some epoxy material as insulation. If the applied current is more than the maximum current, the coil is overheated and it destroys the insulation. In this case, for stable levitation and preventing the coil from overheating it is important to carry

out the thermal analysis to calculate the maximum amount of the current and the temperature time constant.

The aim of this paper is to use the analytical and the numerical methods for finding the thermal analysis based optimal parameters for the levitation of toroidal coils.

## II. ELECTROMAGNETIC LEVITATION THEORETICAL ASPECT

The induction principle is one of the basic rules of electromagnetic levitation. When the current is applied to the toroidal coil, according to the Ampere's circuit law the current produces a magnetic field, which can be calculated from the following equation:

$$\oint H dl = \int J dA, \quad (1)$$

where  $H$  is the magnetic field intensity (A/m) and  $J$  is the current density (A/m<sup>2</sup>).  $A$  is the cross section area of the current carrying coil (m<sup>2</sup>).

According to the Faraday's law, when the aluminum plate is placed in the time varying magnetic field, this field induces an electric field ( $E=\sigma J$ ) and thus a circulating or eddy-current inside the plate. The generated eddy-current in the plate is calculated according to the relation:

$$\frac{1}{\sigma} \oint J dl = -\frac{d}{dt} \int B dA, \quad (2)$$

where  $B$  is the magnetic flux density (T),  $\sigma$  is the specific conductivity of the copper (S/m). According to the Lenz law, this current creates the magnetic field opposite to the first magnetic field. According to the Lorentz force law, the magnetic force will be generated when the current flows in area within the existence of the magnetic flux [1], [2].

Another important parameter for generating the magnetic field is defined by the penetration depth or skin depth ( $\delta$ ), this parameter determines the minimum thickness of aluminum plate in which the eddy-current is generated and is given by:

$$\delta = \sqrt{\frac{1}{\pi f \mu \sigma}}, \quad (3)$$

where  $f$  is the AC current frequency and  $\mu$  is the permeability of the plate [1], [2], [4]. In our case  $f=50$  Hz,  $\mu=4\pi \times 10^{-7}$  (H/m) and  $\sigma=3.8 \times 10^7$  (S/m), which results in  $\delta=11.55$  mm.

This work was supported by the Estonian Research Council grant PUT (PUT1260).

The electromagnetic levitation of the toroidal coil over the aluminum sheet consists of two systems: electromagnetic system and mechanical system [4].

#### A. Electromagnetic System

For better understanding and calculation of an electromagnetic levitation coil, the model is replaced by the simplified electrical circuit. The electric equivalent circuit in Fig. 1 represents the simplified electric circuit of the levitation system.

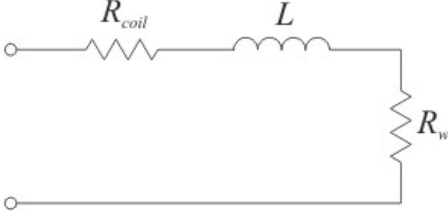


Fig. 1. Electric equivalent circuit.

In this circuit,  $R_{coil}$  represents the resistance of the toroidal coil,  $L$  represents the inductance of the toroidal coil and  $R_w$  represents the losses due to eddy-current in the plate. It should be noted that  $R_w$  is not a real resistance but rather a fictitious resistance representing the power transmitted by the coil to the plate. The schematic of the model is shown in Fig. 2.

The coil inductance is calculated by formula:

$$L = N^2 R_1 \mu \left( \ln \left( \frac{8R_1}{D} \right) - 2 \right), \quad (4)$$

where  $N$  is the number of turns,  $R_1$  is the mean radius of the toroidal coil and  $D$  is the diameter of the cross section area of the coil.

The electromagnetic force is calculated by the formula:

$$F_m = \frac{B^2 A}{2\mu_0}, \quad (5)$$

where  $A$  is the aluminum sheet surface area and  $\mu_0 = 4\pi \times 10^{-7} (H/m)$ .

The aluminum sheet surface area is calculated as  $A = \pi(R_1 - h)^2$  [5], where  $h$  is the levitation height.

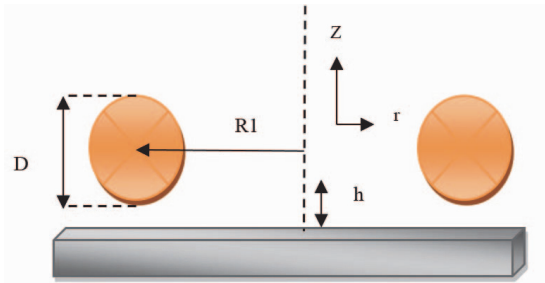


Fig. 2. Schematic of the model.

#### B. Mechanical System

The mechanical part considers the acting forces in the system and the motion of the coil. The gravity force ( $F_g$ ) and the electromagnetic force ( $F_m$ ) are the cause of vertical motion of the toroidal coil. The electromagnetic force is always acting in the direction of the  $z$ -axis and the gravity force is constant downward [4]:

$$F_g = -mge_z, \quad (6)$$

where  $m$  is the mass of the coil and  $g$  is the acceleration due to the gravity (9.81 m/s). When the electromagnetic force is higher than the gravity force, the coil starts to lift from the aluminum sheet.

#### III. LOSSES

The resistive losses in the conductors of the toroidal coil produce heat inside the coil. The amount of this loss is calculated as:

$$P_{cu} = I^2 R_{coil}, \quad (7)$$

where  $R_{coil}$  is the AC resistance of the toroidal coil, which is calculated as:

$$R_{coil} = K_R \frac{N l_{av}}{\sigma S_C}, \quad (8)$$

where  $K_R$  is the skin effect factor,  $N$  is the number of turns,  $l_{av}$  is the average length of a turn,  $S_C$  is the cross section area of the copper wire and  $\sigma$  is the specific conductivity of the copper.

The electrical resistance is changing by the temperature due to the specific conductivity and the resistivity ( $\rho = 1/\sigma$ ), which both are temperature dependent. The resistivity at a different temperature  $T$  is determined by the formula:

$$\rho(T) = \rho(T_0)(1 + \alpha\Delta T), \quad (9)$$

where  $\alpha$  is the temperature coefficient. For better comparison, it is better to replace the current by the current density ( $J = I/S$ ). The resistive losses will be redefined as:

$$P_{cu} = \frac{K_R}{\rho\sigma} N J^2 m_{cu}, \quad (10)$$

where  $p$  is the mass density of the conductor and  $m_{cu}$  is the mass of conductors [6]. Usually the skin effect in the low frequency will be negligible and  $K_R = 1$ .

#### IV. HEAT FLOW ANALYSIS

The second law of thermodynamics indicates that the heat naturally transfers from the higher temperature to the lower temperature. In the toroidal levitation coil, the thermal behavior of the coil plays an important role to determine the maximum current that can be applied to the coil to levitate it over the plate. If the applied current to the coil is more than the maximum current, the coil will be overheated. This heat will be removed mainly by convection. The heat removed by the radiation is not

very significant and it can be neglected, because the temperature difference between the surfaces is small.

#### A. Natural Convection Dimensionless Analysis

The convection is the most significant method of heat transfer. By this method, the heat will be removed from inside the coil to the surface of the coil and then transferred to the ambient due to fluid motion. Natural convection occurs when the object is placed in the fluid at different temperature, according to its physical definition it happens due to buoyancy force [7]. The convection coefficient is calculated by using empirical correlation and dimensionless numbers [7]. In this situation, the empirical relation is:

$$Nu = c(Gr Pr)^m, \quad (11)$$

where  $c$  and  $m$  are constant,  $Nu$  is the Nusselt number,  $Gr$  is the Grashof number and  $Pr$  the Prandtl number [8].

The convection coefficient is calculated by correlation:

$$h = \frac{NuK}{L}, \quad (12)$$

where  $h$  is the heat transfer coefficient,  $L$  the characteristic length and  $K$  the fluid thermal conductivity.

The thermal resistance of convection is

$$R_{th} = \frac{1}{hS}, \quad (13)$$

where  $S$  is the surface area of the coil [7].

#### B. Temperature Time Constant

The temperature time constant ( $\tau$ ) is defined as the time when the temperature reaches 63.2% of its maximum value or final temperature and it is determined by:

$$T(\tau) = T_0 + (T_f - T_0) * 0.632 \quad (14)$$

When the current flows inside the coil, it takes the time for the coil to reach its final temperature, which is approximately equal to 3 times the temperature time constant. By using (14) and knowing the final temperature, the time required for any temperature between ambient temperature and final temperature can be evaluated by [9]:

$$T = T_0 + (T_f - T_0)e^{-\frac{t}{\tau}} \quad (15)$$

#### V. COIL MODELS

Three different copper coils with parameters in Table I are modeled and built. An 8 cm thick aluminum plate is used for levitating the coil.

TABLE I. COIL PARAMETERS

	Number of turns	Winding diameter (mm)	Outer diameter (cm)	Inner diameter (cm)	Average diameter (cm)	Filling factor
<b>Coil A</b>	100	0.82	18.60	16.05	17.325	0.40
<b>Coil B</b>	150	0.82	18.75	16.20	17.475	0.45
<b>Coil C</b>	200	0.82	18.73	16.40	17.567	0.53

For considering and predicting the thermal behavior of the coils, two different methods are used: analytical and numerical methods. In the analytical methods power loss, resistance and temperature are evaluated by the analytical formulas (7), (8). For the numerical method, the FEM analysis is used. At the end, all analytical and numerical results will be compared to the experimental results.

#### A. Analytical Method

For the analytical part, the formulas and some empirical correlations are gathered to predict the thermal behavior of the coil. The coil is divided to three nodes. The first node is located in the center of cross section area (T1), the second node is placed in the surface of the coil (T2) and the third node is in the ambient that presented ambient temperature ( $T_0=20^\circ\text{C}$ ). Average thermal conductivity for inside the coil is calculated by an empirical equation. Fig. 3 shows the nodes location.

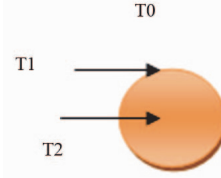


Fig. 3. Nodes location.

The nodes temperatures are calculated by solving the matrix below using iterative methods.

$$[T]=[G]^{-1}[P] \quad (16)$$

Here  $T$  is the temperature matrix,  $G$  is the thermal conduction matrix, and  $P$  is the loss matrix. Table II shows the thermal analytical results.

TABLE II. COILS ANALYTICAL RESULTS

	$R_0(\Omega)$	$R(\Omega)$	$P_{Cu}(W)$	Temperature ( $^\circ\text{C}$ )
<b>Coil A</b>	1.7581	2.1199	20.3726	78.13
<b>Coil B</b>	2.6197	3.3037	24.0840	87.56
<b>Coil C</b>	3.5113	4.5269	28.2931	83.29

#### B. Numerical Method

In the numerical part, the models are considered by using the Finite Element Analysis (FEA). Fig. 4 proves ELM theory that the AC current produces the eddy-current inside of the aluminum plate, but in DC the magnetic flux easily moves through the aluminum plate. There is no current induced inside the plate, which means in this manner there is no magnetic field to generate opposite magnetic field.

## VI. ANALYSIS AND DISCUSSION

The comparison between the analytical resistances results and experimental results shows less than 10% difference. This difference may be caused in the analytical calculation by using the average length of the coil to calculate the total wire length. Also, by increasing the number of turns, the amount of the resistances has increased. This increasing has happened because the length of the wire has increased.

As the copper loss is proportional to the resistances, also the amount of copper loss has been increased. As the results show, by increasing the power loss the amount of the heat inside coils are increased. The comparison between temperature prediction results with the experimental results show small differences. These are caused by the some assumption and simplification in calculation of convection coefficient, such as cross section area of the coil. In the analytical calculation, it is assumed to be circular and symmetrical but in reality it appears to be square and asymmetrical.

Comparison between coils B and C shows that the average temperature of coil B is higher than the one of coil C. As it is shown in Table IV, the amount of the power loss in coil C is bigger than in coil B, but the average temperature of coil B is higher than the one of coil C. This is caused by the difference between the filling factors. The filling factor of coil C is bigger than the one of coil B. This means, that the thickness of air layer between the turns of coil C is smaller than in coil B. Since the air has low thermal conductivity, the rate of transmission of thermal flux to the surface of coil C is faster than in coil B. As a result the internal temperature of coil C is lower than of coil B. Another effect of the filling factor is on the amount of magnetic flux going through the plate. In the coil with higher filling factor, the distance between its center and the surface of the plate is shorter. It means, that the amount of the flux going through the plate has been increased. The result is the increasing amount of eddy-current and the levitation force.

The final point is about temperature time constant. According to the Table V, by increasing the number of turns, the temperature time constant is increased. This means, that the coil can be levitated for a longer time before it reaches its temperature limitation. According to this, the coil with higher number of turns and good filing factor can levitate better, also by adding some insulation like resin instead of the air, the thermal flux transmission is improved.

## VII. CONCLUSIONS

The simple case of electromagnetic levitation system has been presented in this paper and this paper has been focused mainly on the thermal behavior and losses dissipation. Two different methods consisting of analytical and numerical methods have been presented for predicting the average temperature of the levitation coils.

In the analytical analysis, by using some empirical equations, it has been tried to evaluate the convection coefficient to predict the average temperatures of a coil. By using the FEM analysis, the average temperatures and starting levitation currents have been estimated. Results have been presented for three toroidal coils and both analytical and numerical results have been compared with the experimental results to find the factors for

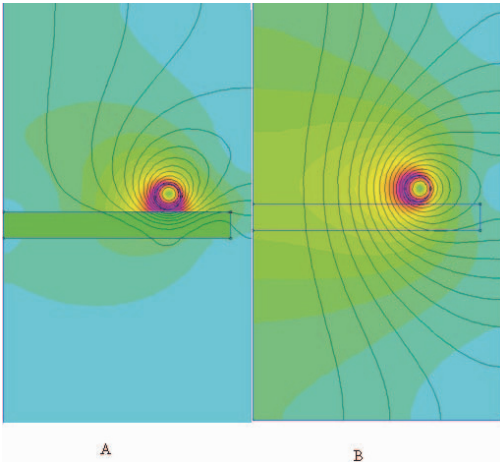


Fig. 4. A) Magnetic field in coil by current with  $f = 50$  Hz and B) Magnetic field in the coil by DC current

Table III shows the numerical thermal and magnetic analysis for the coils

TABLE III. COILS NUMERICAL RESULTS

	Average Temperature (C°)	Starting levitation current (A)
Coil A	74.3216	12.4
Coil B	86.7110	10.4
Coil C	83.5236	8.8

### C. Experimental Results

In the magnetic levitation experimental part, coils are connected to an auto transformer that works with 50 Hz, 220 V. By measuring the voltage and current of the coil and using the Ohm's law and power formula, the amount of the resistance and copper losses are determined. Table IV shows amount of resistances and copper losses

TABLE IV. COILS EXPERIMENTAL RESULTS

	$R_0$ ( $\Omega$ )	$R$ ( $\Omega$ )	$P_{Cu}$ (W)
Coil A	1.700	2.0640	19.9662
Coil B	2.560	3.2140	23.6041
Coil C	3.525	4.3944	27.6853

Table V shows the average temperatures, temperature time constant and starting levitation current.

TABLE V. TEMPERATURE AND LEVITATION RESULTS

	Average Temperature (C°)	Temperature time constant (min)	Starting levitation current (A)
Coil A	77.35	7.5	11
Coil B	86.97	8.75	10.9
Coil C	84.90	11.25	8



making the optimal levitation coil. These factors consist of number of turns and filling factor. The effects of these factors on the thermal behavior and magnetic behavior of the coils have been considered.

#### REFERENCES

- [1] M. T. Thompson, "Eddy Current Magnetic Levitation Models and Experiments," IEEE Potentials, Feb., vol.19, 2000, pp. 40-44
- [2] M. T. Thompson, "Electrodynamic Magnetic Suspension—Models, Scaling Laws, and Experimental Results," IEEE Trans. Ed., vol. 43, no. 3, pp. 336-342, Aug. 2000.
- [3] W. Nan, X. Wen-Jun, W. Bing-Bo, "Physical Characteristics of Electromagnetic Levitation processing", Chin. Phys. Soc., vol. 8, no.7, July. 1999.
- [4] D. J. Jackson, "Electromagnetic Levitation of a Solid Metallic Torus," MSc thesis, University of Toronto, Canada, 2000.
- [5] H. Mölder, "Electromagnetic Levitation Coil," [online]. Available: [http://www.eope.ee/\\_download/euni\\_repository/file/475/H6ljuk.html](http://www.eope.ee/_download/euni_repository/file/475/H6ljuk.html)
- [6] J. Pyrhönen, T. Jokinen, V. Hrabovcova, Design of Rotating Electrical Machines. John Wiley & Sons, Ltd., 2008 .
- [7] D. A. Staton, A. Cavagnino, "Convection Heat Transfer and Flow Calculations Suitable for Electric Machines Thermal Models," IEEE Trans. Ind. Elect., vol. 55, no. 10, pp. 3509-3516, Oct. 2008.
- [8] J. P. Holman, Heat Transfer. New York: Mc Graw-Hill, 1997.
- [9] Thermal time constant, Technical Note, [online]. Available: <http://www.ohizumi-mfg.jp/english/product/technote1.html>

# Curriculum vitae

## Personal data

Name: Payam Shams Ghahfarokhi  
Date and place of birth: 19.09.1986, Iran  
Nationality: Iran  
E-mail: payam.shams@taltech.ee

## Education

2015–... Ph.D. studies, Tallinn University of Technology, Tallinn  
2015–2011 MSc Electrical Power ENG, Newcastle University, Newcastle Upon Tyne  
2005–2010 BSc Electrical Power ENG, University of Najafabad (IAUN), Isfahan  
2000–2004 Adab High school, Isfahan

## Language competence

Persian	Native (Mother's tongue)
English	Fluent
Estonian	A2

## Professional employment

2018–... Early Stage Researcher, Tallinn University of Technology  
2015 Junior Researcher, Tallinn University of Technology  
2012–2013 Working in a research group of knowledgebase company  
2011–2012 Private tutor, teaching electrical machine  
2009 Engineer, Akhtar Niroo Naghshe Jahan Co.

## Honours & Awards

- 2019, Payam Shams Ghahfarokhi, Most Active Participant Award from 18th International Symposium "Topical Problems in the Field of Electrical and Power Engineering" and "Doctoral School of Energy", Estonia, January 14-19.
- 2017, Payam Shams Ghahfarokhi, Most Active Participant Award from 58th International Scientific Conference on Power and Electrical Engineering of Riga Technical University (RTUCON), Latvia, October 12-14.
- 2016, Payam Shams Ghahfarokhi, a Ph.D. course on Permanent magnet technology: Materials, Machines and Numerical Analysis at Aalto University with Excellent Level, Finland, May 29 to June 2.
- 2015, Payam Shams Ghahfarokhi, State Financed doctoral study place at Tallinn University of Technology, Estonia.
- 2011, Payam Shams Ghahfarokhi, MSc distinction (cum laude) from Newcastle University, UK, November 3.

**Field of research**

- Natural Sciences and Engineering; Electrical Engineering and Electronics; Electrical engineering
- Natural Sciences and Engineering; Electrical Engineering and Electronics; Thermal engineering, applied thermodynamics

**Projects**

- Lep18080 "Analytic thermal model for ABB generators type AMG0630, AMG0560 and AMG0500", Tallinn University of Technology, School of Engineering, Department of Electrical Power Engineering and Mechatronics.
- PSG137 "Additive Manufacturing of Electrical Machines", Tallinn University of Technology, School of Engineering, Department of Electrical Power Engineering and Mechatronics.
- PUT1260 "Lifecycle Influenced Optimization Methodology for Electrical Motor-Drives", Tallinn University of Technology, School of Engineering, Department of Electrical Power Engineering and Mechatronics.

# Elulookirjeldus

## Isikuandmed

Nimi: Payam Shams Ghahfarokhi  
Sünniaeg ja -koht: 19.09.1986, Iraan  
Kodakondsus: Iraan  
E-post: payam.shams@taltech.ee

## Hariduskäik

2015–... Ph.D., Tallinna Tehnikaülikool, Tallinn  
2015–2011 MSc Electrical Power ENG, Newcastle'i ülikool, Newcastle  
2005–2010 BSc Electrical Power ENG, Najafabadi ülikool (IAUN), Isfahan  
2000–2004 Adab keskkool, Isfahan

## Keelteoskus

Pärsia keel	Kõrgtase
Inglise keel	Kõrgtase
Eesti keel	A2

## Teenistuskäik

2018–... Nooremteadur, Tallinn Tehnikaülikool  
2015 Nooremteadur, Tallinn Tehnikaülikool  
2012–2013 Töötamine teadmistebaasiühingu uurimisrühmas  
2011–2012 Eraõpetaja, Elektrimasinate alal  
2009 Insener, Akhtar Niroo Naghshe Jahan OÜ

## Teaduspreemiad ja tunnustused

- 2019, Payam Shams Ghahfarokhi, 18. Kõige aktiivsema osaleja auhind "Energia doktorikool", Eesti, 14. jaanuar
- 2017, Payam Shams Ghahfarokhi, Kõige aktiivsema osaleja auhind 58. rahvusvahelisest teaduslikust konverentsist Riia Tehnikaülikooli (RTUCON), Läti, 12.-14. oktoober
- 2016, Payam Shams Ghahfarokhi, Ph.D. kestva magnetitehnoloogia kursus: materjalid, masinad ja arvuline analüüs Aalto Ülikoolis suurepärase tasemega, Soome, 29. mai - 2. juuni
- 2015, Payam Shams Ghahfarokhi, riigi rahastatud doktorikraadi koht Tallinna Tehnikaülikoolis
- 2011, Payam Shams Ghahfarokhi, MSc eristus (cum laude) Newcastle'i ülikoolist, 3. november.

## **Teadustöö põhisuunad**

- Loodusteadused ja tehnika; Elektrotehnika ja elektroonika; Elektrotehnika
- Loodusteadused ja tehnika; Elektrotehnika ja elektroonika; Soojustehnika, rakendatav termodünaamika

## **Jooksvad projektid**

- PSG137 "3D prinditud elektrimasinad", Tallinna Tehnikaülikool, Inseneriteaduskond, Elektroenergeetika ja mehhatroonika instituut.
- PUT1260 "Elutsüklit arvestav elektrimootorajamite optimeerimismetodoloogia", Tallinna Tehnikaülikool, Energeetikateaduskond, Tallinna Tehnikaülikool, Inseneriteaduskond, Elektroenergeetika ja mehhatroonika instituut.
- Lep18080 "Anaütiline temperatuuri mudel ABB generaatoritele AMG0630, AMG0560 ja AMG0500", Tallinna Tehnikaülikool, Inseneriteaduskond, Elektroenergeetika ja mehhatroonika instituut.